UiO **: University of Oslo**

Nico König

Structure and Exchange Kinetics of Nanocrystalline Micelles, Telechelic Hydrogels and Self-Assembling Antimicrobial Peptides

Thesis submitted for the degree of Philosophiae Doctor

Department of Chemistry
Faculty of Mathematics and Natural Sciences
University of Oslo, Norway

in cooperation with
Jülich Centre for Neutron Science (JCNS)
Forschungszentrum Jülich GmbH, Germany

JÜLICH
Forschungszentrum

2020

Daß ich erkenne, was die Welt
Im Innersten zusammenhält

So that I may perceive whatever holds
The world together in its inmost folds

—Johann Wolfgang von Goethe
Faust. Eine Tragödie.

Preface

This thesis is submitted in partial fulfillment of the requirements for the degree of *Philosophiae Doctor* at the University of Oslo. It comprises five scientific articles, three of which have already been published in peer-reviewed journals. The research project was supervised by Prof. Reidar Lund and Dr. Lutz Willner and took place from March 2017 to May 2020. It was conducted in equal parts at the Jülich Center for Neutron Science (Forschungszentrum Jülich GmbH, Germany) and the Department of Chemistry (University of Oslo, Norway). In addition, experiments were carried out at external large-scale facilities, mainly at Heinz Maier-Leibnitz Zentrum (MLZ) in Garching, Germany, and ISIS Neutron and Muon Source in Didcot, United Kingdom.

Acknowledgments

First of all, I would like to thank my two awesome supervisors, Lutz and Reidar. Thank you for giving me the opportunity to pursue this project. I enjoyed the last three (and a bit) years greatly and it wouldn't have been half as fun (or successful) without you. Thank you for always lending an ear, for your patience, your ideas and support and for never neglecting the fun part of it. The best supervisors are those you can spend a night drinking with!

Furthermore, I'd like to thank my great colleagues, both in Jülich and Oslo. The Kaffeerunde was always a nice place to take a break, vent one's anger about shitty data or failed experiments, share some sweets or cake and simply have a good laugh together. I particularly enjoyed our dinner trips to Aachen, Cologne and Jülich! The Young Softies made me feel welcome in Oslo from the very beginning. Det var alltid morsomt å spise mat sammen, diskutere sære ting ved norsk kultur og språk, og klage over hvor distré sjefen er. Og bilturen vår til Aarhus er uforglemmelig!

This work would not have been possible without the help of the beamline scientists supporting our scattering experiments.Thank you for your dedication, for your patience with us annoying users who call in the middle of the night because a cuvette is leaking, and simply for making things possible!

Außerdem geht ein großer Dank an meine Jungs. Wir sehen uns zwar leider nicht mehr so häufig, wie ich gerne hätte, aber wenn ich dann nach Hause komme, ist es umso schöner, mal wieder ein paar Bier zu heben und die Wissenschaft Wissenschaft sein zu lassen. Danke, dass ihr all die Jahre für mich da wart!

Auch an meine Freunde aus dem Physikstudium möchte ich hier meinen Dank richten. Selbst wenn sich unsere Wege nach dem Studium getrennt haben, habt ihr doch maßgeblich dazu beigetragen, dass ich jetzt an diesem Punkt in meinem Leben stehe. Aber am Ende sind es natürlich doch bloß alles bürgerliche Kategorien...

Zum Schluss geht mein tiefster Dank an meine Familie. Danke für eure Unterstützung in den letzten dreißig (!) Jahren und, dass es immer einen Ort gab, an den ich zurückkehren konnte. Danke, dass ihr mir den Rücken gestärkt habt, dass ihr mich aufgebaut habt, wenn es mal nicht so gut lief, und dass ihr dabei wart, wenn es etwas zu feiern gab.

Im Übrigen bin ich der Meinung, dass Lena gedankt werden sollte!

So long, and thanks for all the fish!

Nico König
Oslo, May 2020

Scope

The overall aim of the present doctoral thesis was to investigate the fundamental laws governing molecular self-assembly and the consequences of these relations. To this end, we employed well-defined model systems and attempted to extrapolate the gained insight to more complex systems. Since the studied assemblies have characteristic structural features on the nanometer scale, small-angle scattering techniques were the natural choice for our experiments. With these studies, we shed light on the relationship between molecular interaction, self-assembled structure and molecular exchange kinetics.

The PhD project builds on previous studies of polymeric micelles in our group, particularly the introduction of poly(ethylene oxide)-mono-n-alkyl ethers, C_n-PEO, as micellar model system. The core-forming alkyl blocks of these molecules are truly monodisperse, which, in combination with time-resolved small-angle neutron scattering experiments, provided enhanced experimental insight into the molecular exchange kinetics between polymeric micelles in solution. In the present work, we continue these studies. Exploiting the advantages of C_n-PEO as a model system, we use (time-resolved) small-angle X-ray and neutron scattering experiments to shine light on the interplay of crystallization, co-assembly, molecular architecture and exchange kinetics. The alkyl chains crystallize below a certain temperature, allowing us to study the impact of crystallinity on micellar morphology and molecular exchange between micelles. We successfully tune the crystallization by co-assembling polymers of different length and observe the consequences for micelle behavior. Furthermore, we investigate the exchange mechanism in micelles formed by telechelic copolymers. With our profound insight about molecular self-assembly, we aim to transfer this knowledge to more complex topics. Thus, we set out to structurally characterize filaments formed by self-assembling antimicrobial peptides, a potential new antibiotic material, and measure the exchange kinetics between the assemblies. In the end, though, we reveal the exceptional physical integrity of the assembled peptide structures.

The thesis is organized as follows: First, the scientific output of the PhD project is summarized. Then, Chapter 1 gives an introduction to the field of Soft Matter and Self-Assembly, provides background information for the topics covered in the thesis and presents the state of science. Chapter 2 briefly introduces the samples under investigation, their synthesis and characterization. Thereafter, Chapter 3 includes a detailed recapitulation of small-angle scattering as the main experimental method of this work and describes the data evaluation. Experiments using complementary techniques are shortly outlined. In Chapter 4, the research results of the PhD project are summarized and discussed in their scientific context. Finally, Chapter 5 contains a brief conclusion of the thesis and lists remaining open questions for future studies. The dissertation is based on five scientific articles which are attached at the end. Three of which are already published in peer-reviewed journals while the other two are manuscripts to be submitted shortly.

Contents

Abbreviations and Symbols

3W62	$K_3W(QL)_6K_2$ peptide
A(Q)	scattering amplitude
AFM	atomic force microscopy
AMP	antimicrobial peptide
b	scattering length
c	mass-per-volume concentration
CAC	critical association concentration
CD	circular dichroism spectroscopy
CDSA	crystallization-driven self-assembly
CMC	critical micelle concentration
C_n-PEOx	poly(ethylene oxide)-mono-n-alkyl ether with n the number of alkyl carbon atoms and x the PEO molecular weight in kg/mol
CnFXX	blend of C_n-PEO5 and C_n-PEO10-C_n with XX vol% telechelic molecules
cryoTEM	cryogenic transmission electron microscopy
$\frac{d\sigma}{d\Omega}$	differential scattering cross-section
$\frac{d\Sigma}{d\Omega}$	macroscopic differential scattering cross-section
d	density / distance / thickness
D	thickness of the micellar corona
Đ	polydispersity
DLS	dynamic light scattering
DMF	dimethylformamide
DSC	differential scanning calorimetry
EO	ethylene oxide
eV	electron volt $(1.602 \times 10^{-19}\,\text{J})$

f_{tel}	volume fraction of telechelic molecules
G	Gibbs free energy
$I(t)$	(integrated) scattering intensity
k	rate constant
k_B	Boltzmann constant (1.381×10^{-23} J/K)
k_{exch}	microscopic molecular exchange rate constant
k_{rheo}	macroscopic rheological relaxation rate constant
KZAC	kinetic zero-average-contrast
m	degree of polymerization of the hydrophilic block
MIC	minimum inhibitory concentration
MW	molecular weight
n	degree of polymerization of the hydrophobic block
N_{A}	Avogadro constant (6.022×10^{23} mol^{-1})
N_{agg}	aggregation number
NMR	nuclear magnetic resonance spectroscopy
P-3W62	PEGylated K$_3$W(QL)$_6$K$_2$ peptide
P-W362	PEGylated WK$_3$(QL)$_6$K$_2$ peptide
$P(Q)$	form factor
PB	polybutadiene
PDMA	poly(*N,N*-dimethylacrylamide)
PE	polyethylene
PEG	poly(ethylene glycol)
PEO	poly(ethylene oxide)
PEP	poly(ethylene-*alt*-propylene)
PLA	polylactide
PMMA	poly(methyl methacrylate)
PnBMA	poly(*n*-butyl methacrylate)
PP	polypropylene
PPO	poly(propylene oxide)
PS	polystyrene

PVL	poly(δ-valerolactone)
PVP	poly(2-vinylpyridine)
$\vec{Q}, Q = \left|\vec{Q}\right|$	scattering vector, momentum transfer
R	universal gas constant ($8.314\,\mathrm{J/mol/K}$)
R_c	micellar core radius
R_m	overall micellar radius
$R(t)$	relaxation function of molecular exchange
$S(Q)$	structure factor
SAAMP	self-assembling antimicrobial peptide
SAS	small-angle scattering
SANS	small-angle neutron scattering
SAXS	small-angle X-ray scattering
SLD	scattering length density
t	time
T	absolute temperature
TEM	transmission electron microscopy
TR-SANS	time-resolved small-angle neutron scattering
w	weight fraction
W362	$WK_3(QL)_6K_2$ peptide
WAXS	wide-angle X-ray scattering
XRD	X-ray diffraction
ZAC	zero-average contrast
Å	Ångström ($10^{-10}\,\mathrm{m}$)
2θ	scattering angle
γ	interfacial tension (between micellar core and corona)
λ	wavelength
ρ	scattering length density
τ_0	time constant in Arrhenius law, "attempt time"
ϕ	volume fraction
χ	Flory-Huggins interaction parameter

Publications

Paper I

Nico König, Lutz Willner, Göran Carlström, Thomas Zinn, Kenneth D. Knudsen, Frode Rise, Daniel Topgaard and Reidar Lund:
"Spherical micelles with a non-spherical core: the effect of core crystallization".
Manuscript

N.K., L.W. and R.L. initially devised the study. The idea for the NMR experiments originates from a discussion between R.L. and D.T. L.W. and Matthias Amann (Jülich Center for Neutron Science, Forschungszentrum Jülich GmbH; deceased) synthesized and characterized the polymers. N.K. and L.W. prepared the samples. T.Z. performed the WAXS experiments which were evaluated by N.K. F.R. and N.K. conducted the ^{1}H NMR measurements while N.K. analyzed the data. D.T. proposed the ^{13}C NMR experiments which were performed by N.K., G.C. and D.T. N.K. analyzed the data under guidance of D.T. K.D.K. conducted a first SANS study. L.W. carried out additional test measurements before N.K. conducted the definitive SANS experiment. N.K. also performed the SAXS measurements and evaluated all SAS experiments including the development of the scattering model. N.K. drafted the manuscript (incl. figures and literature review) with input from R.L. and D.T. The manuscript was further developed by all authors together.

Paper II

Nico König, Lutz Willner and Reidar Lund:
"Structure and thermodynamics of mixed polymeric micelles with crystalline cores: tuning properties via co-assembly".

The idea for the work was conceived by all authors together. L.W. synthesized and characterized the polymers. N.K. and L.W. prepared the samples. Bente A. Breiby (Department of Pharmacy, University of Oslo) performed the DSC measurements which N.K. evaluated. N.K. executed the density and SAXS experiments and analyzed the data. N.K. developed the scattering model, based on a previously existing one. N.K. conducted all data analysis under supervision of R.L. N.K. mainly performed the literature review with input from L.W. and R.L. N.K. prepared all figures and wrote the first draft of the manuscript which was finalized by all authors together. Revisions after peer review were also done collectively.

Paper III

N.K., L.W. and R.L. designed the study. T.Z. carried out preliminary work. L.W. synthesized and characterized the polymers. N.K. and L.W. prepared the samples. N.K. performed the SANS experiments with the help of L.W., V.P. and Matthias Amann (Jülich Center for Neutron Science, Forschungszentrum Jülich GmbH; deceased). Matthias Amann introduced N.K. to SANS experiments, while V.P. as local contact provided technical support and L.W. assisted with lab issues. N.K. performed the data analysis. N.K. furthermore carried out and evaluated the SAXS and density measurements while Bente A. Breiby (Department of Pharmacy, University of Oslo) did the DSC measurements which N.K. analyzed. R.L. provided guidance in data interpretation. Thereupon, N.K. prepared all figures and wrote the first draft of the manuscript. It was further developed together with R.L. and L.W. and finalized by all authors. N.K., L.W. and R.L. took responsibility for the revisions after peer review.

Paper IV

N.K., L.W. and R.L. designed the study. L.W. synthesized and characterized the polymers. N.K. and L.W. prepared the samples. N.K. performed the SANS experiments with the help of L.W., V.P. and N.M. V.P. and N.M. as local contacts provided technical support and L.W. assisted with lab issues. N.K. performed the SANS data analysis. Bente A. Breiby (Department of Pharmacy, University of Oslo) carried out the DSC measurements which N.K. analyzed. R.L. provided guidance in data interpretation. N.K. developed the kinetic model with input from L.W. and R.L. L.W. created the micelle sketches and N.K. produced the data plots. N.K. and L.W. jointly wrote the first draft of the manuscript and performed the literature review. The manuscript was further developed in collaboration with R.L. and finalized by all authors. N.K., L.W. and R.L. took responsibility for the revisions after peer review.

Paper V

Nico König, Josefine E. Nielsen, Lutz Willner, Su Yang, Ari Benjamin, Martha Dunbar, Aurel Radulescu, Najet Mahmoudi, Sinan Keten, He Dong and Reidar Lund:
"Exceptional physical stability of beta-sheet nanofibers formed by self-assembly of a *de novo* antimicrobial peptide".
Manuscript

N.K. and R.L. designed the study. S.Y. synthesized the peptides and conjugated them with polymers synthesized by L.W. N.K. and J.E.N. prepared the samples and performed the SAXS experiments. N.K. took responsibility for the SANS experiments and received help from J.E.N., L.W. and R.L. N.M. and A.R. as local contacts provided technical support. N.K. analyzed all scattering data and developed the geometrical scattering model with input from J.E.N. and R.L. S.Y. carried out the CD measurements. A.B. began the MD simulations under the guidance of S.K. and R.L. M.D. finalized the simulations and ran CRYSOL/CRYSON to obtain computed scattering curves. N.K. merged all results and wrote a first draft of the manuscript. J.E.N., S.Y. and H.D. provided relevant literature references. H.D. and S.Y. wrote the synthesis paragraph. M.D. wrote about the MD simulations and their results. N.K. prepared all figures except for the simulation snapshot, which M.D. created. The manuscript was further developed by N.K., J.E.N., S.Y., M.D., H.D. and R.L.

Not included in this thesis:

Josefine E. Nielsen, Nico König, Maximilian W.A. Skoda, Armando Maestro, He Dong, Marité Cardenas and Reidar Lund:
"Lipid membrane interactions of self-assembling antimicrobial nanofibers: effect of PEGylation".
Manuscript

Conference Contributions and Popular-Scientific Outreach

End of Cooperativity − Chain Exchange Kinetics in Mixed Polymeric Micelles with Partially Crystalline Cores
Oral contribution at the "15th Nordic Workshop on Scattering from Soft Matter" held in Lund, Sweden, on 17th to 18th January 2018

End of Cooperativity: Chain Exchange Kinetics in Mixed Polymeric Micelles
Poster contribution at the "Spring Meeting of the German Physical Society" held in Berlin, Germany, on 11th to 16th March 2018

End of Cooperativity: Chain Exchange Kinetics in Mixed Polymeric Micelles with Partially Crystalline Cores
Poster contribution at the workshop "Time, Work and Function: Time-resolved synchrotron and neutron techniques for studies of soft, biological and hard matter" held in Oslo, Norway, on 13th to 15th June 2018

End of Cooperativity − Chain Exchange Kinetics in Mixed Polymeric Micelles with Partially Crystalline Cores
Participant contribution in the "14th European Summer School on 'Scattering Methods Applied to Soft Condensed Matter'" held in Bombannes, France, on 19th to 26th June 2018

On the Cooperativity during Melting and Molecular Exchange in Micelles with Crystalline Cores
Oral contribution at the "21st National Meeting of the Norwegian Chemical Society" held in Lillestrøm, Norway, on 16th to 18th October 2018

Molecular Exchange in Self-Assembling Systems
Participant contribution in the "Yearly Meeting of the Network for Young Nordic Neutron Scatterers (NYNNeS)" held in Copenhagen, Denmark, on 22nd to 23rd October 2018

The Art of Making Tiny Boxes − Controlled transport of drug molecules
Popular-scientific talk at the "Kjemi Grand Prix" of the Department of Chemistry, University of Oslo, Norway, on 31st January 2019
Voted 2nd place by the audience

Effects of co-assembly and core crystallization on the structure of n-alkyl-poly(ethylene oxide) micelles
Poster contribution at the "16th Nordic Workshop on Scattering from Soft Matter" held in Aarhus, Denmark, on 9th to 10th January 2019

End of Cooperativity: Chain Exchange Kinetics in Mixed Polymeric Micelles
Poster contribution at "The Geilo School 2019: 'Evolving Soft Matter: Shape, Dynamics and Functionality'" held in Geilo, Norway, on 11th to 21st March 2019

The Art of Making Tiny Boxes — Controlled transport of drug molecules
Popular-scientific talk for new students at the Department of Chemistry, University of Oslo, Norway, on 12th August 2019

Nanomedicine — At the interface of physics, chemistry and biology
Popular-scientific talk for science teachers in the course of the "Subject-Pedagogical Day" at the University of Oslo, Norway, on 31st October 2019

A Tale of Two Tails — Exchange Kinetics in Telechelic Polymer Micelles
Oral contribution at the "17th Nordic Workshop on Scattering from Soft Matter" held in Linköping, Sweden, on 14th to 15th January 2020
Talk given by Reidar Lund because Nico König was unavailable due to illness
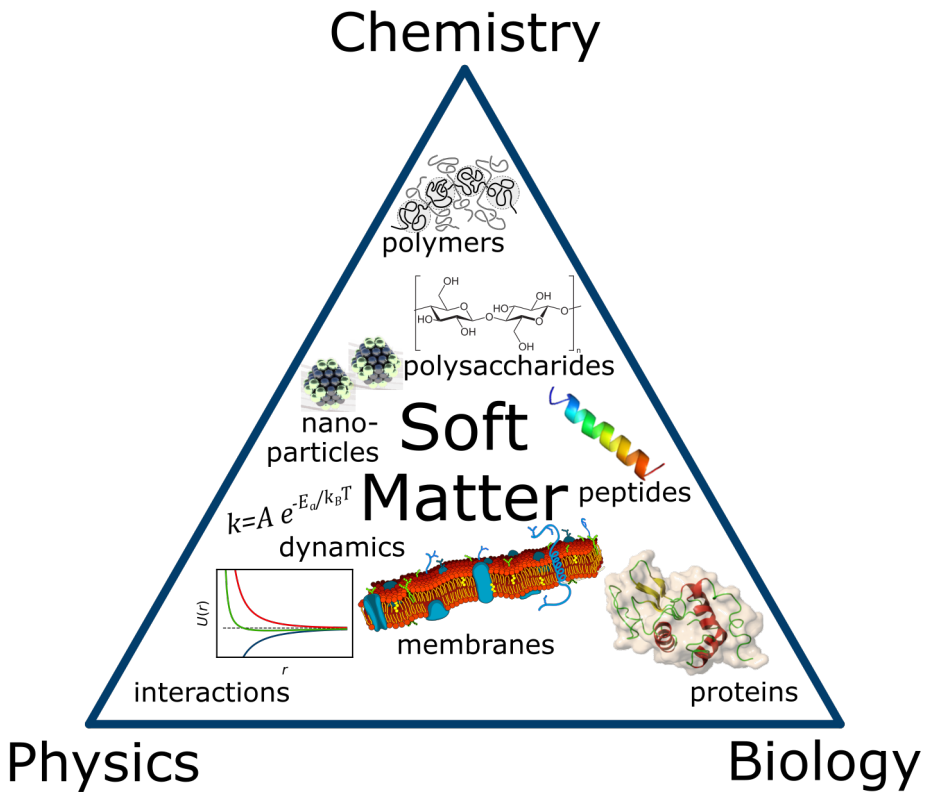
Chapter 1

Introduction

Soft (Condensed) Matter is a subfield within Condensed Matter. It is called "soft", in contrast to "hard" condensed matter, because the materials under investigation are literally soft. This can be illustrated with a rough estimation: The hardness of a material is often described by its shear modulus which has the dimension of energy per volume. In a conventional molecular crystal, typical bonding energies are in the range of $E_{\mathrm{mol}} \sim 1\,\mathrm{eV}$ (i.e., $\gg k_B T$) and bond lengths in the range of $d_{\mathrm{mol}} \sim 1\,\text{Å}$. In colloidal crystals, a typical Soft Matter system, on the other hand, interactions are usually in the order of the thermal energy $k_B T$, which is much weaker ($E_{\mathrm{col}} < 0.1\,\mathrm{eV}$), and at the same time interparticle distances are substantially longer, $d_{\mathrm{col}} \sim 1\,\mathrm{\mu m}$, because the colloidal particles are much larger than molecules. With these numbers, the shear module can be roughly estimated by calculating how much energy per unit volume, E/d^3, is needed to break the crystal bonds when the material is sheared. The result is that typical Hard Matter shear modules are 10^{13} times larger than Soft Matter shear modules! Even though the given values are very rough estimates, it still exemplifies how "soft" Soft Matter materials are.[1]

Soft Matter is a very interdisciplinary field, at the interface of physics, chemistry and biology, as illustrated in Figure 1.1, and also has direct relevance for material science and medicine. Typical examples of Soft Matter systems are dispersion colloids, self-assembling amphiphiles, polymers, proteins, membranes and many more. According to Jones [2], all these systems share three main characteristics:

- Thermal fluctuations play a key role in their behavior. Since relevant energy levels are on the order of $k_B T$, these systems are constantly affected by thermally activated, structural fluctuations. This is also one reason for their "softness".

- The structures that define the overall material properties are mesoscopic: Larger than the constituting microscopic, molecular building blocks, yet smaller than the overall macroscopic sample size.

- These mesostructures arise from spontaneous self-assembly of the molecular building blocks into hierarchical superstructures, driven by thermodynamic interactions.

The present doctoral thesis deals mainly with structures arising from self-assembly and how molecular exchange — induced by thermal fluctuations — takes place between them.

Figure 1.1: Illustration of Soft Matter at the interface of physics, chemistry and biology. Some graphics were taken from https://commons.wikimedia.org/ under Creative Commons license.

This chapter gives an introduction into the scientific topics covered by the thesis and presents the state of science. After some general notes on the use of the term "self-assembly" in the field of Soft Matter, a prime example will be discussed: polymeric micelles. Particular focus will be on crystallization phenomena in these self-assembled structures and their molecular exchange kinetics. Furthermore, we will introduce the polymeric model system, C_n-PEOx, which we employed in large parts of this work. Finally, the last section of this chapter introduces another self-assembling system, antimicrobial peptides, and presents the specific example treated in this thesis, self-assembling $K_x(QL)_yK_z$ peptides.

1.1   Self-Assembly in Soft Matter

The term self-assembly applies to many different phenomena and has been used extensively, triggering Whitesides and Grzybowski to ask "Is Anything Not Self-Assembly?".[3] Therefore, Grzybowski et al. later tried to define self-assembly as "the spontaneous formation of organized structures from many discrete components that interact with one another directly [...] and/or indirectly, through their environment [...]".[4] They further introduced the concepts of "static" or "equilibrium" self-assembly and "dynamic" self-assembly, where the former describes stable structures in thermodynamical equilibrium whereas the latter is applied to more flexible and active systems that dissipate energy.[3, 4] These definitions, though, are still very general and can be applied to phenomena at all length scales, from molecules to galaxies.

In the scope of the present work, however, we will only refer to equilibrium self-assembly in the context of Soft Matter research, where microscopic molecules, driven by the appropriate thermodynamic potential, spontaneously form superstructures on the mesoscopic scale which define the macroscopic properties of the material. But even under this constraint, there are still manifold aspects

self-assembly		
characteristics	systems	applications
▪ *nanostructures*	▪ surfactants	▪ tissue engineering
▪ weak driving forces	▪ *synthetic polymers*	▪ drug delivery
▪ thermal fluctuations	▪ lipids	▪ oil recovery
▪ colloidal interactions	▪ biopolymers	▪ nanolithography
▪ *molecular exchange*	▪ *peptides*	▪ nanoreactors
▪ susceptible to stimuli	▪ proteins	▪ personal care

Figure 1.2: Overview over the concept of self-assembly in the context of Soft Matter research. Topics treated in the present thesis are highlighted.

to the concept which are (non-exhaustively) presented in Figure 1.2. The most basic topic is probably the quest for ever new morphologies created via molecular self-assembly which triggers research regarding the underlying driving forces or application of external stimuli. Of course, systems can only attain their thermodynamic equilibrium if there is molecular exchange. But also kinetically trapped systems offer unique opportunities. Therefore, control over the exchange kinetics is a another goal. Furthermore, the particular building blocks under investigation are limitless: from simple surfactants and synthetic polymers over membrane-forming lipids to polypeptide chains constituting proteins. And finally, all these systems find various applications in medicine (tissue engineering [5, 6], drug delivery [7, 8]), industry (oil recovery [9, 10], nanolithography [11, 12], nanoreactors [13]) or everyday life products (personal care [14], viscosity modification [15]).

In the following, the focus will lie on the particular topics treated in this thesis: polymeric micelles and how they and their exchange kinetics are affected by crystallization as well as self-assembling antimicrobial peptides.

1.2 Polymeric Micelles

Beside being a paramount example for molecular self-assembly, polymeric micelles have been the subject of extensive research because of their enourmous versatility.[16, 17] When block copolymers are dispersed in a solvent that is selective for one of the blocks, micellar aggregates form. However, there are no limits to possible solvent/copolymer systems which leads to a zoo of different morphologies, dynamics and functionalities. Therefore it is not surprising that polymeric micelles have found application in the unlikeliest fields, from subterranean crude oil recovery to nano-sized electric wires. The following section shines light on different aspects of polymeric micelles that are relevant for the present thesis.

1.2.1 Micellization

Whenever amphiphilic molecules like amphiphilic block copolymers are dispersed in water, the common understanding is that the hydrophobic moieties will aggregate to minimize the interaction with water molecules.[1] In fact, though, it is the other way round, as Charles Tanford described in his classical textbook *The Hydrophobic Effect*.[18] Actually, the attraction between hydrophobic moieties is too weak to drive the aggregation since it is mostly van-der-Waals forces. Nevertheless, the dispersed hydrophobic groups disturb the hydrogen bond network of water which is highly dynamic and thus has a high degree of entropy. But the water molecules in contact with a hydrophobic surface can only establish a reduced number of hydrogen bonds. This constrains their orientational freedom

---

[1]This concept is in principle also valid for other solvophobic/solvophilic systems, but here we will only discuss the concept of hydrophobic/hydrophilic, because water is the only solvent used in the present thesis.
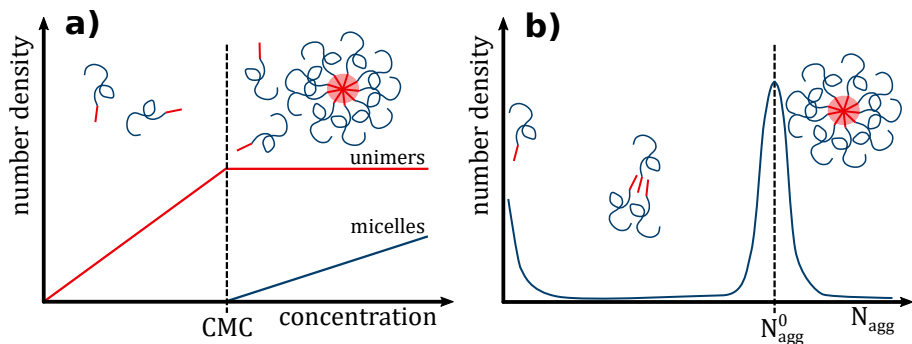
Figure 1.3: The concept of micellization: a) The number density of unimers and micelles vs. the overall polymer concentration. b) Distribution of aggregation numbers well above the CMC.

and reduces the entropy substantially, which drives the minimization of contact area between water and hydrophobic groups, leading to aggregation of the latter. This process can be described as a mesoscopic phase separation. Yet, the aggregation cannot continue infinitely because of packing restrictions inside the hydrophobic domain as well as the presence of the hydrophilic moieties which favor solvent contacts. So, instead of macroscopic phase separation, mesoscopic equilibrium structures are formed, so-called *micelles*. They can take the form of spheres, ellipsoids, disks, cylinders or worms — but all these morphologies share a hydrophobic core surrounded by a water-swollen hydrophilic shell.[19, 20]

As illustrated in Figure 1.3a), this process of micellization only happens above a certain threshold concentration: the critical micelle concentration (CMC). Below the CMC, the amphiphilic molecules are dispersed as unimers. Even though the contact area between hydrophobic groups and water is in principle thermodynamically unfavorable, mixing entropy averts micellization at low concentrations. With increasing amphiphile concentration, however, the contribution from the disturbed water network starts to dominate and micellization sets in. In the classical theory, based on the seminal works of Leibler et al. [21], this system is described through its Gibbs free energy

$$G_{\text{system}} = G_{\text{mic}} + G_{\text{mix}} - TS_m, \tag{1.1}$$

where G_{mic} is the free energy (per molecule) of a micelle, G_{mix} is the mixing term of unimers and water and S_m is the translational entropy. In the so-called *pseudo-phase approximation*, the micelles and unimers are considered as distinct phases and the CMC is the amphiphile concentration at which the two phases are in equilibrium.[22] However, the interfacial tension between hydrophobic groups and water is typically high, so that the CMC is rather low and there is only an insignificant amount of unimers present in solution. In that case, G_{mix} and S_m become negligible and it is sufficient to consider the micellar free energy

per molecule G_{mic} to derive micellar properties. It consists of three terms:

$$G_{\text{mic}} = G_{\text{int}} + G_{\text{core}} + G_{\text{shell}}. \tag{1.2}$$

The unfavorable enthalpy G_{int} of hydrophobic-hydrophilic interfaces drives the aggregation but it is countered by the terms G_{core} and G_{shell} which describe stretching, spatial restrictions and entropic penalties arising from aggregation in the hydrophobic and hydrophilic moieties, respectively. The resulting overall micellar free energy G_{mic} depends on the number of molecules per micelle, N_{agg}, and has a minimum at a certain equilibrium aggregation number N_{agg}^0. Yet, these micelles are no static structures. Since they are not covalently bound, they are subject to constant thermal fluctuations — as it is typical for Soft Matter systems — which can lead to exchange of molecules between micelles. This is the principal mechanism to reach thermodynamic equilibrium and the time scale on which molecular exchange takes place depends mainly on temperature and hydrophobicity, see Section 1.5 on page 14.[2] This leads to an aggregation number distribution as sketched in Figure 1.3b). Most micelles contain N_{agg}^0 amphiphiles but due to thermal fluctuations, there is a certain distribution $\Delta N_{\text{agg}}/N_{\text{agg}} \propto N_{\text{agg}}^{3/2}$ around it.[21] In addition, there is a number of unimeric amphiphiles corresponding to the CMC and finally some sub-micelles with aggregation numbers in between which are only transient as they are thermodynamically unstable.

However, this thesis focuses on spherical micelles in thermodynamic equilibrium, formed by amphiphilic block copolymers, which will be treated in the next section. Therefore, the topic of micellization is not discussed further here and the interested reader is referred to the literature.[19–21, 23, 24]

1.2.2 Morphology

There have been a number of theoretical studies to predict the equilibrium structure of polymeric micelles which can be divided into two groups. Firstly, there are models based on Flory-type mean-field theories.[21, 22, 25, 26] These theories require a homogeneous core and shell, though, which is a good approximation for thin shells but not applicable to micelles with extended shells where the local polymer concentration is expected to decrease further from the core. Here, scaling approaches are more suitable which exploit the self-similar properties of polymers in solution.[27–30]

The micellar systems presented in this thesis exhibit an extended spherical shell because the hydrophilic block is much larger than the hydrophobic one. These kinds of micelles are also called *star-like* micelles due to their resemblance to starpolymers. The most established model for spherical, star-like micelles is that of Halperin and Alexander [27, 28] which builds on the ideas of Daoud and Cotton [31]. The model assumes a homogeneous, solvent-free core comprising the hydrophobic blocks which is surrounded by a shell of swollen hydrophilic

---

[2]If molecular exchange is slower than the experimental time scale, one speaks of kinetically trapped systems.

blocks, the so-called *corona*. Based on the self-similar properties of the swollen hydrophilic blocks, the local polymer concentration in the corona is supposed to decrease $\propto r^{-4/3}$ with the distance r from the core. Later, the model was extended by Zhulina et al. to also accomodate swelling of the core and non-spherical morphologies.[32, 33] According to these scaling theories, the micellar size is mostly determined by the degree of polymerization of the hydrophobic block n, the degree of polymerization of the hydrophilic block m and the interfacial tension γ between hydrophobic core and water-swollen corona. By minimizing the micellar free energy G_{mic}, Equation (1.2), Zhulina et al. [32] found that the aggregation number of spherical, star-like micelles scales as

$$N_{\mathrm{agg}} \propto \gamma^{6/5} n^{4/5}. \tag{1.3}$$

With a solvent-free, spherical core, this immediately leads to a core radius of

$$R_{\mathrm{c}} \propto \gamma^{2/5} n^{3/5}. \tag{1.4}$$

Furthermore, by assuming water is a good solvent for the hydrophilic block (Flory exponent $\nu = 0.588 \approx 3/5$ [34]), the thickness of the corona scales as

$$D \propto \gamma^{6/25} n^{4/25} m^{3/5}. \tag{1.5}$$

In addition, there is also a geometrical approach to derive how the aggregation number N_{agg} scales with the length of the hydrophobic block n. In the so-called *super-strong segregation limit* (SSSL) [35], i.e., when γ is very high, one can infer that the corona blocks are packed as densely as possible on the core surface to minimize the surface area per molecule, $s = 4\pi R_{\mathrm{c}}^2 / N_{\mathrm{agg}}$. In this case, s would equal the monomer cross-section a^2, with the monomer size a. A simple geometrical consideration then yields $4\pi R_{\mathrm{c}}^2 = N_{\mathrm{agg}} a^2$ and $4\pi R_{\mathrm{c}}^3 / 3 = N_{\mathrm{agg}} n a^3$, which results in [36]

$$N_{\mathrm{agg}} \propto n^2. \tag{1.6}$$

This behavior is usually found for low-molecular-weight surfactant micelles.[23, 36]

1.2.3 Mixed Polymeric Micelles

As discussed above, the (structural) properties of polymeric micelles depend on different factors, most importantly the chemical nature of the constituting polymer blocks as well as their respective degree of polymerization. For specific applications, exact control over these parameters is crucial and this can pose a severe challenge in the synthesis process. Even though the advance of living ionic and controlled radical polymerization have improved the accuracy of polymer synthesis tremendously [37], exactly controlled polymerization is still difficult and inherently the products have a (small) Poisson-distributed polydispersity. Fortunately, the blending of block copolymers has turned out to be a facile and efficient method for fine-tuning micellar properties. In fact, this concept has already proven its worth both in natural (e.g., lipid mixtures in

biological membranes) and artificial systems (e.g., personal care products). Hence, copolymer blending has also attracted research interest. For instance, it has been exploited to tune thermodynamic properties and the rheological response of polymeric micelles [38–41], to improve the physical stability and enhance loading capacities for drug delivery applications [42–45] or to create completely novel morphologies [46–50]. In addition to this intentional blending, the polydispersity inherent to polymerization techniques can also be understood as a form of mixture. It was even postulated that, under certain conditions, polydispersity increases the micelle stability and leads to a narrower size distribution.[51] Therefore it is important to investigate the effect of blending different block lengths on the micellar properties. Accordingly, a lot of computational and experimental studies have been performed which will be discussed in more detail in Section 4.2.2 on page 69, in the discussion of the results of the present work.

There have also been theoretical treatments of the topic.[52–54] Shim et al. have studied copolymers with soluble blocks of the same chemical nature but different lengths and insoluble blocks of the same length but a different chemical nature.[52] They found two possible scenarios when the overall polymer concentration is gradually increased, depending on the ratio of the two species in solution. Either mixed micelles are formed immediately upon crossing the (common) CMC or one species micellizes first and then the other species is incorporated into these micelles gradually. Sens et al. extended this work and investigated copolymer mixtures of the same chemical nature but where all block lengths of both hydrophobic and hydrophilic blocks are varied.[53] They reported a somewhat different finding: If the difference between the copolymer blocks are "not too large", mixed micelles are formed. With larger differences, though, pure micelles of the larger block coexist with mixed micelles. In the context of the present thesis, it is particularly interesting that they predict identical core blocks with moderately mismatched corona blocks to always form mixed micelles, whereas only a slight mismatch in the core blocks with identical corona blocks can already prohibit mixed micelles. They concede, however, that this might only be true for asymptotically long polymers and in reality might be blurred by the inherent polydispersity. Yet, for the work presented here, the theory of Borovinskii and Khokhlov is probably most suitable as they analyzed copolymer blends with very long, identical corona blocks and mismatched core blocks.[54] They identified five concentration regimes: At very low overall concentration, only unimers are present in solution. Upon crossing the longer blocks' CMC, these micellize first while the shorter blocks mostly stay unimeric. Then, even though still below the shorter blocks' CMC, these start to be incorporated into the existing micelles. When the concentration is increased over the shorter blocks' CMC, a part of the shorter copolymers is incorporated in the longer blocks' micelles and the excess short chains form a population of pure short-block micelles. Finally, well above the CMC of both species, mixed micelles of approximately equal size and composition dominate as long as the difference between the core blocks is "not so great" [54]. Otherwise, this last regime cannot be observed. These theoretical predictions will be compared with the results of the present work and other experimental findings in Section 4.2.2 on page 69.
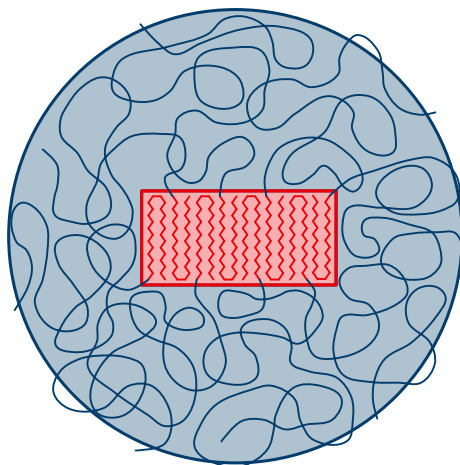
Figure 1.4: Illustration of the Vilgis and Halperin model for core-crystalline micelles.

1.3 Crystallinity in Polymeric Micelles

So far, we mainly discussed the hydrophobic effect [18] as driving force behind micellization — or, more general, the selectivity of the solvent towards one of the copolymer blocks. But there are also other interactions that can trigger aggregation. One example that has attracted significant attention in recent years is crystallization. The so-called *crystallization-driven self-assembly* (CDSA) approach allows for unprecedented control over the micellar morphology and opens up many new applications.[55–57] It will be discussed in the following section. Crystalline micellar cores also have effects on possible applications. In micelles employed for drug delivery, for instance, it was shown that core crystallization can retard the drug release [58] but at the same time reduces the micellar loading capacity [59]. Moreover, crystallization affects the molecular exchange kinetics between micelles.[60, 61]

Theoretically, the topic has been treated by Vilgis and Halperin who proposed a model for micelles with crystalline cores.[62] In this model, the hydrophobic blocks undergo chain-fold crystallization as depicted in Figure 1.4 and form cylindrical or disk-like cores. The hydrophilic blocks are grafted on the basal planes of the core and, in the limit of long hydrophilic blocks, form an extended corona that would be nearly spherical, despite the aspherical core. Surprisingly, these assumptions lead to the same scaling laws as those for star-like micelles, Equations (1.3) to (1.5) on page 7, which can be partly explained by the fact that the enthalpy gain upon crystallization is independent of the aggregation number and thus does not influence the aggregation behavior.

1.3.1 Crystallization-Driven Self-Assembly

As mentioned above, CDSA has introduced unprecedented control over micellar structures.[55–57] Conventional micellar (self-)assembly routes have difficulties producing low-dimensional structures like cylinders or platelets. They often only coexist with other morphologies and/or occur only in limited regions of the phase diagram. In contrast, CDSA has excelled in producing such structures. For example, the groups of Ian Manners and Mitchell A. Winnik [63–66] as well as Rachel K. O'Reilly [67, 68] have presented remarkable works.

Even though crystallization can be the sole driving force behind self-assembly in a common solvent, it usually acts together with solvent selectivity. The common understanding is that CDSA is a two-step process: The selectivity of the solvent drives the initial aggregation of solvophobic blocks which then crystallize and determine the final micellar shape. The origin of CDSA can be traced back to 1998, when Massey et al. reported the formation of cylindrical micelles driven by core-crystallization.[69] The concept was further evolved into *living* CDSA, starting with the work of Wang et al.[70] Like in living polymerization techniques, the micellar ends remain "active" and micellar growth can continue when more material is added to the solution, allowing defined structures up to the multi-micrometer range. These structures might find applications in different fields, from drug and gene delivery over nanomotors to optoelectronic devices.[57]

1.3.2 Crystallization in Micellar Confinement

Nonetheless, crystallization in the confined space of a micellar core exhibits several peculiarities [71, 72], which will be addressed in the following. Common techniques to investigate the crystalline nature of a material are X-ray diffraction (XRD) and/or wide-angle X-ray scattering (WAXS). Yet, when the crystallites, i.e., the coherently scattering crystalline domains, are very small, the diffraction peaks become broadened. This effect was first described by Paul Scherrer in 1918 [73]:

$$\Delta(2\theta) \gtrsim \frac{K\,\lambda}{d\,\cos\left(2\theta/2\right)}, \tag{1.7}$$

where $\Delta(2\theta)$ is the peak width, $K \approx 1$ a shape factor, λ the X-ray wavelength, d the crystallite size and 2θ the scattering angle. Thus, Bragg peaks can become non-distinguishably broad in the case of nanometer-sized crystallites such as in micellar cores. In addition, the fact that the hydrophobic blocks are tethered to the core-corona interface limits the achievable crystallinity. This was found by Nojima et al. who in a clever experiment prepared poly(δ-valerolactone)-polystyrene (PVL-PS) diblock copolymers which formed spherical PVL domains in a PS matrix.[74] The gist of the experiment, however, was that the block junction was photocleavable. So they could directly compare the crystallization behavior of tethered PVL blocks in the PS matrix with free PVL chains in the same matrix and found that the former displayed a reduced crystallinity. This was shortly after verified via Monte Carlo simulations by Cai et al.[75] They confirmed that the grafting sites reduced the achievable crystallinity but at the same time

the chain stretching caused by the tethering to the core-matrix interface allowed for faster crystallization. In addition, Das et al. reported that block length polydispersity can further reduce the crystallinity in micellar cores.[76] Thus, reported degrees of crystallinity in polymeric micelles are typically in the range of $30-50\,\%$.[77–79]

Another interesting aspect refers to the mechanism of crystallization. Due to their smallness, micellar cores are practically devoid of impurities which would serve as crystallization seeds. Hence, crystallization can only occur homogeneously and takes place independently in every single micelle.[80] But also surface freezing has been proposed as principal nucleation mechanism.[81] Nevertheless, each micellar core crystallizes independently which means that the crystallites, which are highly imperfect due to the spatial confinement, also exhibit different melting points. Despite being individually sharp, the superposition of all micellar melting transitions thus leads to broadened melting ranges of the macroscopic sample.[82] Another consequence of homogeneous crystallization in micellar cores is that tremendous undercooling is necessary to induce crystallization. For example, in the study mentioned above, Nojima et al. reported that they observed crystallization of the PVL blocks about $80\,\mathrm{K}$ below the melting point.[74] However, a part of the melting/crystallization point suppression can also be explained by the Gibbs-Thomson effect. Under nanometer confinement, the surface-to-volume ratio of the confined material is greatly increased and, because the surface creates an excess energy for the solid phase, the equilibrium is shifted towards the liquid phase.[83–85] Petrov and Furo gave the melting point depression as [84]

$$\Delta T_m = T_m^0 - T_m = \frac{V_M \, \gamma \, T_m^0}{\Delta H_m} \frac{\partial S}{\partial V}, \tag{1.8}$$

where T_m^0 is the bulk melting temperature, T_m the melting point in confinement, V_M the material's molar volume, γ the interfacial tension, ΔH_m the molar melting enthalpy, S the pore surface and V the pore volume. Thus, the factor $\partial S/\partial V$ depends on the pore geometry. For spherical pores with radius R_c, one obtains

$$\Delta T_m = \frac{V_M \, \gamma \, T_m^0}{\Delta H_m} \frac{2}{R_c}. \tag{1.9}$$

1.3.3   Crystallization of *n*-Alkanes

A significant part of this thesis deals with micelles where n-alkyl groups form the hydrophobic block. Therefore, the particular crystallization behavior of n-alkanes will be briefly reviewed in the following.[3] Despite their chemical simplicity, alkanes exhibit a surprisingly rich phase diagram.[86] A well-known example is the odd-even effect: The melting points of alkanes with an even

---

[3]Throughout this thesis, we only treat linear n-alkanes. To avoid confusion with the index n, denominating the number of carbon atoms in an alkane C_n, we will in the following omit the leading n in n-alkanes and still refer exclusively to linear alkanes.
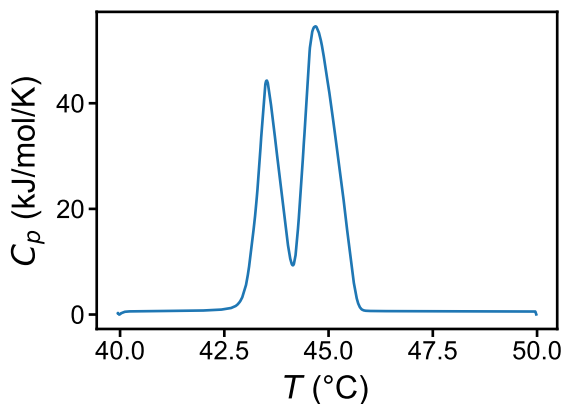
Figure 1.5: Melting curve of pure docosane (C_{22}) measured with DSC at a scan rate of 0.5 K/min. (unpublished data)

number of carbon atoms are systematically higher than those of alkanes with an odd number of carbon atoms because even-numbered alkanes can form crystals of higher order. However, the effect flattens out among longer alkanes. Another interesting feature is the existence of so-called *rotator phases*. They are intermediate phases between the solid crystalline and liquid phase where the alkane molecules retain their longitudinal order but gain a rotational degree of freedom around their axes. Figure 1.5 shows a DSC melting curve of pure docosane (C_{22}) which clearly reveals two transitions: from the crystalline phase to the rotator phase and then to the melt. Interestingly, alkanes of all lengths are completely miscible in the melt state but tend to de-mix in the solid phase if the length mismatch is too large. The associated mixing rules have been determined by Kravchenko: For instance, alkanes with a length mismatch $\Delta n \geq 4$ are immiscible in the solid phase if $n < 28$.[86, 87] These rules have been confirmed experimentally in a number of cases.[88–90]

The crystallization behavior of alkanes under confinement has been extensively studied by the group of Dujin Wang.[81] They prepared nearly monodisperse, alkane-containing microcapsules with diameters of $1-5\,\mu m$ and investigated the alkane crystallization with DSC, XRD and NMR. Beside the phenomenon of surface freezing, which they propose as principal nucleation mechanism in confinement, they also studied the behavior of alkane mixtures under confinement. Interestingly, they found that phase separation of length-mismatched alkanes in the solid phase was suppressed in microcapsules because the main separation mechanisms, lamellar ordering and longitudinal diffusion, are restrained under confinement.

The results of the present thesis shed light on the crystallization behavior of alkanes under even stronger confinement: in nanometer-sized micellar cores,

using the C$_n$-PEOx model system presented in the following section. We also investigated how core crystallization affects the micellar morphology — with possible implications for CDSA.

1.4 C$_n$-PEOx as a Model System

In the context of this thesis, micelles formed from poly(ethylene oxide)-mono-n-alkyl ethers, C$_n$-PEOx, with relatively long alkyl blocks, $n \geq 16$, serve as model system. To better understand complex phenomena, it is customary to employ simpler, well-defined model systems for which C$_n$-PEOx is a prime example. Here, the index n denotes the number of carbon atoms in the alkyl block and x the PEO molecular weight in kg/mol. When dissolved in water, these molecules typically form well-defined micellar entities which have been used to investigate the fundamental properties of non-ionic amphiphilic block copolymers. The highly hydrophobic, core-forming alkyl blocks represent the simplest hydrocarbons and are usually monodisperse. The hydrophilic, corona-forming PEO blocks, on the other hand, are relatively inert and can be synthesized with very low polydispersities ($Đ < 1.05$) by living polymerization techniques.

Commercially, a number of C$_n$-PEOx derivatives are available under the trade name "Brij" and have found several applications, among others in the pharmaceutical sector.[91–96] Due to its archetypical features, C$_n$-PEOx has been extensively employed to study micellar aggregation [97–103] and rheological response [40, 104]. Furthermore, it has proven to be particularly suited to study the molecular exchange kinetics between polymeric micelles — see Section 1.5.2 on page 15. The exchange rates depend exponentially on the length of the hydrophobic block and thus the inherent polydispersity of conventional polymers has rendered quantitative studies difficult. But since the alkyl blocks of C$_n$-PEOx are truly monodisperse, it allowed for precise interpretation of experimental data.[61, 105, 106] Finally, C$_n$-PEOx also exhibits (partial) core crystallization [77, 107, 108], making it an interesting model system to study alkyl crystallization under nanometer confinement with implications for CDSA. For example, Zinn et al. reported that the alkyl blocks in C$_n$-PEOx micelles exhibit a melting point suppression according to the Gibbs-Thomson effect, Equation (1.8) on page 11.[108] In another study, Plazzotta et al. found that core freezing led to size segregation in a mixture of C$_{18}$-PEO1 and C$_{18}$-PEO5, even though the core blocks were identical.[109] The same group later exploited core freezing to trigger the release of a hydrophobic cargo from the micellar core.[110]

In the context of the present thesis, C$_n$-PEOx was employed to investigate the crystallization behavior of alkyl groups in micellar cores and how crystallization affects both micellar morphology and exchange kinetics as well as related phenomena.
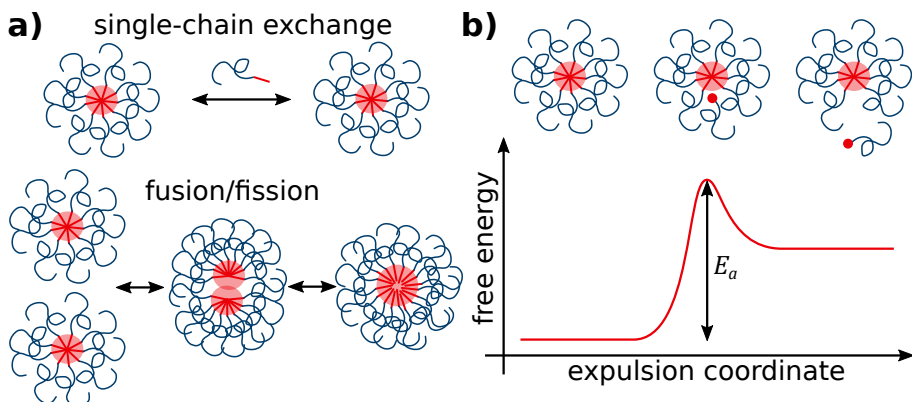
Figure 1.6: a) Two possible mechanisms for the exchange of molecules between micelles. b) Expulsion of a molecule as pictured in the Halperin-Alexander theory.

1.5 Molecular Exchange Kinetics in Polymeric Micelles

As mentioned in the previous section, C_n-PEOx is an excellent model system to investigate the molecular exchange kinetics in polymeric micelles and is used to that end also in parts of the present work. Molecular exchange is the key process for polymeric micelles to attain thermodynamic equilibrium structures. When amphiphilic copolymers are dispersed in a selective solvent, they rapidly assemble in non-equilibrium micelles first which then equilibrate by exchanging unimers.[111]

1.5.1 Theory of Molecular Exchange

In principle, one can think of two possible mechanisms to exchange molecules and attain equilibrium micelles [112], which are depicted in Figure 1.6a): Either micelles fuse and fission and thereby shift molecules or individual molecules are exchanged via free unimeric diffusion. Although fusion and fission has been observed in surfactant micelles [113, 114], it does usually not occur in polymeric micelles with long hydrophilic blocks because the extended coronas sterically hinder fusion events. Instead, the dominant exchange mechanism is unimeric exchange.[115]

Based on the works of Aniansson and Wall [116, 117], Halperin and Alexander developed a theory to describe that mechanism.[115, 118] Based on an estimation of the respective activation energies, they concluded that in polymeric micelles unimer exchange is the dominant mechanism. They then derived an expression for the corresponding relaxation rate by adopting Kramers' rate theory [119, 120] to polymeric micelles. The main difference is that in polymeric micelles the passage through the corona slows down the process and becomes the rate-determining step in the expulsion process. Thus, they pictured the expulsion as

a two-step process — compare Figure 1.6b): First, the core block forms a "bud" at the core-corona interface and then the whole molecule diffuses through the corona. The re-insertion into another micelle, on the other hand, is expected to be very rapid since it is enthalpically favorable. Therefore, the expulsion process is the rate-limiting step in molecular exchange between polymeric micelles and Halperin and Alexander found the associated rate constant to scale as

$$k \propto \exp\left(-\frac{n^{2/3}\,\gamma\,a^2}{k_B T}\right), \tag{1.10}$$

where a is the monomer size of the core block. Thus, the time scale of molecular exchange is very sensitive to the length of the core block n and the interfacial tension γ between core and corona. All other parameters influence the expulsion rate in a non-exponential fashion.

According to the theory described above, the exchange of molecules between polymeric micelles is a thermally activated process with a single-exponential relaxation function

$$R(t) = \exp(-kt), \tag{1.11}$$

where the rate constant k depends on an activation energy E_a in an Arrhenius relation

$$k = \frac{1}{\tau_0} \exp\left(-\frac{E_a}{k_B T}\right). \tag{1.12}$$

The activation energy $E_a \propto n^{2/3}\gamma$ is mainly determined by the enthalpic penalty arising from the newly created hydrophobic surface in the budding step. To account for non-spherical "buds" as well as other correction factors, the activation energy was later re-formulated as [121]

$$E_a = \alpha\,\gamma\,(36\pi)^{1/3}\,a^2\,n^\beta. \tag{1.13}$$

The exponent β depends on the bud shape ($2/3 < \beta < 1$: for a spherical shape $\beta = 2/3$ and for an elongated shape $\beta = 1$) and α allows for further corrections, e.g., relating to the bud-corona interaction and deviations in shape.

1.5.2 Experimental Work on Exchange Kinetics

The experimental observation of polymer exchange kinetics, however, proved to be difficult. There were promising experiments using ultrasonic absorption [122, 123] but in the end it was concluded that the observed relaxation processes could not be identified with molecular exchange.[123] Other techniques like non-radiative energy transfer [124] or fluorescence quenching [125–128] require bulky labels with unknown influence on the kinetics. Even transmission electron microscopy (TEM) was employed [129, 130] but was of course limited to very long observation times. More successful were temperature-jump light scattering experiments which extensively investigated the exchange kinetics in poly(ethylene oxide)–poly(propylene oxide)–poly(ethylene oxide) (PEO-PPO-PEO) triblock copolymer micelles.[122, 131, 132]

The actual breakthrough in the observation of micellar equilibrium exchange kinetics, though, came with the advent of kinetic zero-average-contrast (KZAC) neutron scattering experiments.[133] In short, it is a hydrogen/deuterium labeling scheme that allows to monitor the equilibrium molecular exchange without disturbance with down to millisecond time resolution.[4] Even though this new scheme provided excellent experimental data, it was still difficult to align them with the Halperin-Alexander theory. The molecular weight (MW) polydispersity inherent to synthetic polymers in combination with the strong sensitivity of the exchange rate to the block length hindered correct data evaluation. In 2006, Lund et al. performed a KZAC study on star-like poly(ethylene-propylene)-poly(ethylene oxide) (PEP-PEO) micelles in water/DMF mixtures.[134] In contrast to the single-exponential relaxation function predicted by the Halperin-Alexander theory, they found a logarithmic decay. Even though they considered the effect of polydispersity via convolution with a MW distribution $P(n)$,

$$R(t) = \int_1^\infty P(n)\,\exp(-k(n)\,t)\,\mathrm{d}n, \tag{1.14}$$

with the exchange rate $k(n)$ according to the Halperin-Alexander model, Equation (1.10), they could not explain their data satisfactorily. But some time later, Choi et al. studied a similar system, polystyrene-poly(ethylene-propylene) (PS-PEP) in squalane, and succeeded in describing their data with a slightly adjusted version of Equations (1.10) and (1.14).[135] Like Lund et al., they found a logarithmic decay of the relaxation function. But instead of a Poisson MW distribution, they assumed a Schulz-Zimm distribution. The decisive factors, however, were that they used $\beta = 1$ instead of $\beta = 2/3$ — compare Equations (1.10) and (1.13) — and allowed slight adjustments of the Flory-Huggins interaction parameter χ and the polydispersity index $Đ$.[5] By only adjusting these two parameters, they achieved a good description of their experimental $R(t)$. While χ mostly affected the time scale of the exchange, $Đ$ had a tremendous effect on the shape of the relaxation function: Already a moderate polydispersity broadened the expected single-exponential $R(t)$ into a logarithmic shape. In the light of these results, Lund et al. re-analyzed their data, adjusting the parameter α in Equation (1.13), and also achieved good agreement with their data, now in line with the Halperin-Alexander theory.[136] These works underlined the strong sensitivity of micellar exchange kinetics on both the core block length n and the interfacial tension γ / interaction parameter χ due to the double-logarithmic dependence of the relaxation function.

Li and Dormidontova performed computer simulations of monodisperse diblock copolymers and indeed detected a single-exponential relaxation function with $k \propto \exp(\chi\,n)$.[137] Yet, they observed not only single-chain exchange but also exchange of smaller aggregates as well as fusion/fission. But since they only simulated very short chains, the steric repulsion of extended coronas might

---

[4]It will be presented in more detail in Section 3.1.5 on page 47.
[5]The Flory-Huggins interaction parameter χ corresponds to the interfacial tension γ in Equation (1.13).

not have been strong enough to stop fusion events. Nevertheless, convincing experimental evidence for the Halperin-Alexander model was presented by Zinn et al. in 2012.[105] They employed C_n-PEO4 with truly monodisperse alkyl core blocks in a KZAC neutron scattering experiment and in fact observed a single-exponential relaxation function with a strong dependence on the alkyl block length. Even though the Halperin-Alexander theory appeared to be confirmed by then, Garcia Daza et al. later presented a simulation study where they surprisingly reported a logarithmic exchange despite simulating monodisperse polymers.[138] They explained it by a degeneracy of the energy states in the micellar core which would be broken upon chain expulsion and therefore lead to a broad distribution of activation energies. However, the logarithmic decay was only observed in a rather limited range, $0.9 > R(t) > 0.6$, and experimental evidence is missing to date.

Further experimental work investigated the effect of micellar morphology on the molecular exchange kinetics. Lund et al. studied PEP-PEO cylindrical micelles that irreversibly changed to a spherical shape upon heating or addition of DMF.[139] Instead of a Poisson MW distribution, which would be theoretically appropriate for polymers synthesized via living anionic polymerization, they employed a Schulz-Zimm distribution to account for side reactions and incomplete polymerization and that way successfully reproduced their data with Equations (1.12) to (1.14). Interestingly, they found the exchange in spherical micelles to be marginally but significantly faster compared to cylindrical micelles and explained it with the slightly decreased corona density in the spherical geometry. A similar result was found by Zhao et al. who prepared micelles of different sizes from the exact same copolymer, using two different preparation protocols.[140] The exchange in the larger micelles was significantly slower, supposedly due to the higher surface density of PEO chains on the core, retarding the expulsion process. The effect of corona density has also been addressed in other publications. Choi et al. observed a significant slowdown of exchange at elevated polymer concentration.[141] The effect set in above the micellar overlap concentration, when all sample volume is occupied by the micelles. Therefore, expulsed chains do not escape into the free solvent anymore but remain inside a spatially constrained, coronal environment and the entropic penalty slows down the kinetics. This work prompted Halperin to extend the classical kinetic theory by two corrections factors: a free energy penalty for the presence of the bud in the corona and the altered micellar free energy G_{mic}, Equation (1.2) on page 6, due to the removal of one chain.[118] In addition, Lu et al. created an analogous situation by adding PEP homopolymer to a solution of PS-PEP micelles in squalane, resulting in the same effect of retarded exchange because of coronal crowding.[142] Another interesting question refers to the length of the hydrophilic block. While there is consensus about the effect of the hydrophobic block length n, the effect of the hydrophilic block length m is still somewhat disputed. The original Halperin-Alexander theory [115] postulated increased exchange rates with shorter corona chains because the passage through the corona is shortened. This was confirmed by Zinn et al. using C_{27}-PEOx with varying PEO molecular weight [106] and also agrees with the previously

mentioned studies on micellar morphology [139, 140]. In contrast, both Li and Dormidontova and Wang et al. observed accelerated molecular exchange in micelles with longer corona blocks.[137, 143] They proposed that the longer chains experience a greater entropic penalty in the micellized state, lowering the free energy gain of micellization and thus facilitating expulsion. A unifying explanation for these contradictive findings has yet to be found.

Moreover, the effect of the Flory-Huggins interaction parameter was discussed in the literature. According to the Halperin-Alexander theory [115], the activation energy of chain expulsion depends linearly on χ / γ — see Equation (1.13) on page 15 — and this was confirmed by the simulations of Li and Dormidontova [137]. By blending two different solvents, Ma and Lodge systematically varied χ in poly(methyl methacrylate)-poly(n-butyl methacrylate) (PMMA-PnBMA) micelles.[144] Yet, their data were not commensurable with the Halperin-Alexander model and therefore they proposed a more elaborate χ dependence, inspired by the classical Flory-Huggins theory. The modification mainly corrects the behavior of E_a at low χ, whereas at high χ it approaches the classical linear dependence. Wang et al. later aimed to test the modified χ dependence by using another block copolymer, PS-PEP, and found a similar relationship, indicating that the model proposed by Ma and Lodge might be universally valid.[145]

As outlined in Section 1.2.3 on page 7, mixed micelles have attracted increased research interest and hence their exchange kinetics has been explored as well. It was addressed by Lu et al. in two publications where they investigated PS-PEP micelles with length-mismatched core blocks.[146, 147] Exploiting a smart labeling scheme, they monitored the molecular exchange of both species individually and found that they are independent. The exchange rate of the shorter/longer species was the same in both pure and mixed micelles. Very recently, Prhashanna and Dormidontova reported the same phenomenon in computer simulations of mixed micelles comprising linear copolymer chains.[148] However, they observed that copolymers with different architectures, namely linear and tadpole polymers, did affect each other's exchange rates when blended in the same micelle. In general, the effect of polymer architecture on the exchange kinetics has been investigated lately [148–151] but this is the topic of Section 1.5.3.

Furthermore, it remains a rather open question how core crystallization influences the molecular exchange. Kastantin et al. employed fluorescence quenching to monitor the exchange rates in lipid-PEO micelles. The lipid core of these micelles exhibited a solid-liquid transition and, interestingly, the activation energy of the process was significantly reduced in the liquid phase compared to the solid phase. Although the lipid tails did not adopt a thorough crystalline phase below the melting point, the results still point towards an additional free energy barrier imposed by the solidification. As mentioned above, also the cores of C_n-PEOx micelles crystallize partially. Zinn et al. hypothesized that the melting enthalpy might be added to the activation energy, Equation (1.13) on page 15, arising from the extra hydrophobic surface upon chain expulsion but some more experimental work was necessary.[61, 104] This missing work is part of the present thesis, shining more light on the interplay of crystallization and

molecular exchange in polymeric micelles.

Finally, we would like to remark that molecular exchange is not exclusively triggered by thermal fluctuations. Many micellar systems are in fact kinetically trapped, meaning that the thermal energy is not sufficiently high to overcome the free energy barrier for chain expulsion. These systems are therefore stuck in non-equilibrium states and the observed micellar structures highly depend on the preparation route.[140, 152, 153] In these kinetically trapped systems, molecular exchange can still be provoked by mechanical agitation. Murphy et al. presented an interesting work where they monitored molecular exchange between kinetically trapped poly(butadiene)-poly(ethylene oxide) (PB-PEO) micelles in water, using the KZAC TR-SANS scheme.[154] They reported that vortex mixing efficaciously triggered chain exchange and the kinetics were linear with respect to the agitation time. Therefore, they suggested that the exchange mechanism involved exchange of molecules via the air-water interface.

1.5.3 Exchange Kinetics in Triblock Copolymer Micelles

Also the block copolymer architecture has a strong effect on the molecular exchange kinetics. In the previous section it was pointed out that already minor changes in the coronal density, caused by different micelle morphologies, lead to different exchange rates. Thus, more pronounced changes to the corona are expected to affect the exchange kinetics even more. A particularly strong effect can be seen in triblock copolymers where one hydrophobic block is sided by two hydrophilic blocks. In comparison to diblock copolymer micelles of the same hydrophobic block length and aggregation number, this would lead to a doubled polymer density in the corona. Therefore, these triblock copolymers gain less free energy from micellization and typically exhibit lower aggregation numbers compared to their diblock counterparts.[150, 151] But this also entails that the activation energy for chain expulsion is significantly decreased and these micelles exhibit greatly accelerated molecular exchange which was confirmed by both experiment [149] and computer simulations [150, 151]. In case the hydrophobic block length is doubled as well, on the other hand, so that the triblock molecule simply resembles two conjoint diblock molecules, differences between diblock and triblock micelles are less severe. For example, Lund et al. studied the structure and exchange kinetics of PB10-PS10 diblock and PB10-PS20-PB10 triblock copolymer micelles in aliphatic solvents, where the numbers denote the approximate molecular weight in kg/mol and PS formed the micellar cores.[155] SANS experiments revealed a nearly identical structure of the two micellar species but the molecular exchange kinetics of triblock micelles monitored by TR-SANS was strongly retarded compared to the diblock micelles. The phenomenon could partly be explained by the doubled length of the PS block, compare the Halperin-Alexander theory in Section 1.5.1 on page 14, but the authors also found indications for topological effects, i.e., entanglement of PS chains in the core.

The micellar morphology and exchange kinetics are, however, even more affected by the inverse polymer architecture: when one hydrophilic block is

sided by two hydrophobic blocks. These kinds of triblock copolymers fall into the category of telechelic polymers. Telechelic polymers are defined as "a di-end-functional polymer where both ends possess the same functionality" [156] and often simply refer to hydrophilic polymers which are hydrophobically end-functionalized. The common understanding is that at low concentrations — but still above the CMC — these polymers mainly form "flower-like" micelles. This means that both hydrophobic groups of a molecule are buried in the same micellar core while the looped hydrophilic backbone forms a coronal "petal". In addition, there can be free hydrophobic groups in the solvent, so-called *dangling ends*. At higher concentrations, the molecules form clusters where the backbone block bridges between different micellar cores and at some point a percolating network is formed.[157–159] This rich range of structures allows for several applications, among others in drug delivery [160, 161], tissue engineering [162] and manipulation of micellar interaction [163, 164].

Figure 1.7 illustrates the different possible structures of micelles comprising both telechelic and monofunctional (i.e., diblock) molecules, where f_{tel} is the mass fraction of telechelic polymers in the blend. Conventional, monofunctional polymers at low concentration form freely diffusing micelles as described in Section 1.2. At higher concentration, they cannot diffuse freely anymore and soft colloidal crystals arise. As soon as telechelic molecules are added, though, two scenarios can occur: Either the telechelic chains bend back and form flower-like micelles or one hydrophilic group stays in solution and star-like micelles with dangling ends are created.[6] At higher concentrations, transient clusters are formed with telechelic molecules bridging between hydrophobic cores and, above a certain threshold concentration, these clusters develop a percolating network which macroscopically corresponds to a physical hydrogel.[165, 166]

Such structures have extensively been treated by both theory [167] and experiment, using various techniques like fluorescence [98, 158], light scattering [98, 158, 168–170] or neutron and X-ray scattering [102, 149, 159, 165, 166, 171, 172]. Yet, the investigation of the low-to-intermediate concentration range proved to be non-trivial. It was theoretically predicted that non-percolating clusters tend to phase-separate [173] and later also shown experimentally [168, 174]. Fortunately, Laflèche et al. found that telechelic micelles in solution can be stabilized by blending in monofunctional molecules as depicted in Figure 1.7.[98, 170] Nonetheless, the existence of actual flower-like micelles in solution was long disputed. In 2011, de Graaf et al. reported convincing evidence of flower-like micelles employing light scattering in combination with NMR spectroscopy.[175] Furthermore, Ghelichi and Qazvini presented an interesting computer experiment: They simulated telechelic polymers with a chargeable middle block. When the backbone was neutral, they observed flower-like micelles. But when the backbone was charged, its rigidity was consequently increased and micellar clusters were formed instead.[176] From a thermodynamic point of view, the prevalence of flower-like or clustered micelles can be estimated from the free energy.[158, 177] The opposing forces are the enthalpy gain of burying a hydrophobic group in a

---

[6]Of course, also behavior in between, with both looping and dangling chains, can occur.
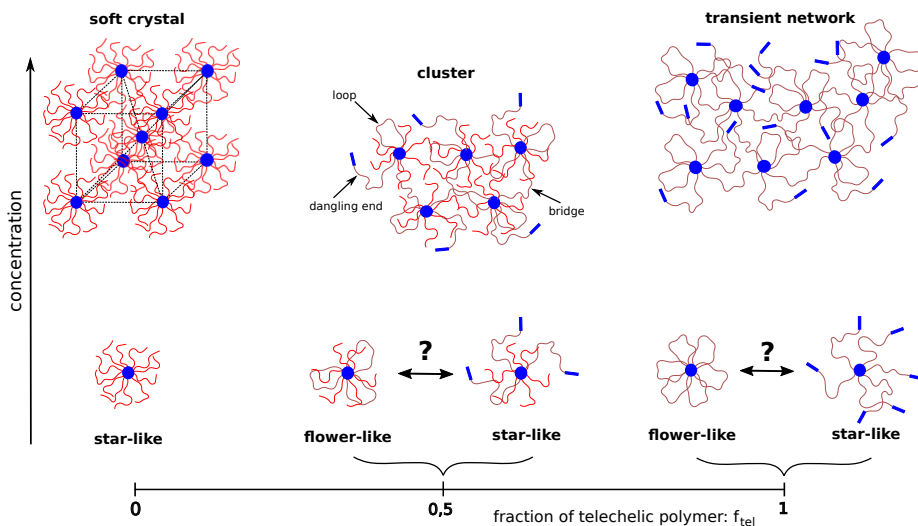
Figure 1.7: Possible structures formed by telechelic and monofunctional molecules in solution, well above the CMC. Reprinted with permission from Reference [102]. Copyright © 2017 American Chemical Society.

micellar core and the entropy penalty of loop formation. With long hydrophobic blocks, the enthalpy gain dominates and flower-like micelles are produced. But when the core blocks are short, the looping entropy is higher and dangling ends are thermodynamically tolerable so that clusters can form. This was confirmed experimentally by Zinn et al.[102] They studied mixed micelles comprising C_n-PEO10-C_n and C_n-PEO5 (to prevent phase separation) with DLS and SANS and found that longer alkyl blocks led to flower-like micelles whereas shorter hydrophobic blocks promoted clustering, in agreement with the free energy estimations of Alami et al. and Maiti and Chatterji.[158, 177] Another interesting study on the behavior of telechelic polymer micelles was presented by Abebe et al., who investigated PLA-PEO-PLA micelles with TR-SANS.[172] Polymers with optically pure D-lactide or L-lactide repeat units formed stable micellar solutions with active molecular exchange. But as soon as these two solutions were mixed, stereocomplexes of D-lactide and L-lactide formed, locking the molecular exchange and leading to a physical gel.

However, the most interesting feature of telechelic polymers is their rich rheological behavior.[157–159, 165, 170, 171, 173, 178–180] Due to their ability to form non-covalent bridges between hydrophobic entities, they exhibit phenomena like non-Newtonian flow behavior and are immensely used as associative thickeners in industrial applications. In their classical transient network theory, Tanaka and Edwards have related the macroscopic relaxation rate of telechelic gels measured by rheology k_{rheo} to the microscopic network relaxation rate k_{exch}, i.e., the dissociation rate of molecular bridges.[181] While the observation of the macroscopic k_{rheo} is straight-forward, it is not trivial to measure the

microscopic k_{exch} and experimental studies are scarce. Zinn et al. measured k_{rheo} of a C_{22}-PEO10-C_{22}/C_{22}-PEO5 1:1 mixture ($f_{\mathrm{tel}} = 0.5$) and compared it to the molecular exchange rate k_{exch} of C_{22}-PEO5 ($f_{\mathrm{tel}} = 0$) determined by KZAC TR-SANS.[104] In agreement with the Tanaka-Edwards theory [181], they found the same activation energy for both k_{rheo} and k_{exch}. Even though the absolute time scale was highly dependent on the polymer concentration, this result indicates that the relaxation mechanism of the telechelic network involves the release of only a single hydrophobic block at a time. If both hydrophobic blocks were released simultaneously in the relaxation mechanism, the activation energy would be doubled compared to the diblock exchange. However, Zinn et al. did not measure the molecular exchange rate of the telechelic C_{22}-PEO10-C_{22} directly.

To the best of our knowledge, the only direct measurement of k_{exch} of telechelic molecules so far was achieved by Lu et al.[149] They investigated PS-PEP-PS and PEP-PS-PEP triblock copolymers in squalane, a selective solvent for the PEP block, using the KZAC neutron scattering scheme. They found the PEP-PS-PEP molecules to exchange much faster than the corresponding PEP-PS diblock polymers and explained it by the additional entropy gain from the second corona block upon chain expulsion. The PS-PEP-PS molecules, on the other hand, exchanged much slower than the corresponding diblocks. This is reasonable considering that there are two hydrophobic blocks that both need to be expelled from the micellar core. Yet, the exchange was faster than what would have been expected for the simultaneous release of two PS blocks which, as mentioned above, would require twice the activation energy of the respective diblock. Thus, Lu et al. suggested a consecutive release mechanism. Unfortunately, they did not propose a quantitative explanation. This issue will be addressed in the present thesis.

There is, however, a quantitative study on the exchange kinetics of telechelic block copolymers in melt, i.e., without solvent: Yokoyama and Kramer prepared thin films of (partly deuterium-labeled) PVP-PS-PVP triblock and PS-PVP diblock copolymers and measured polymer diffusion with forward recoil spectrometry (FRES). The polymers assembled into a bcc structure of spherical domains consisting of the PVP blocks embedded in a PS matrix. The authors measured both tracer-diffusion (triblock diffusion in a diblock matrix) and self-diffusion (triblock diffusion in a triblock matrix). In both cases, the diffusion coefficient followed an exponential decay $\exp(-\chi n)$ where χ is the Flory-Huggins interaction parameter and n is the degree of polymerization of the core-forming PVP block. This agrees with the Halperin-Alexander theory of molecular exchange of polymer micelles in solution, compare Equations (1.12) and (1.13) on page 15, and suggests that only one PVP block is "activated" at a time. Yokoyama and Kramer coined the term *walking diffusion* for this mechanism, where the triblock diffuses by step-wise shifting one PVP block from one node to another. Even though the activation energies of diblock diffusion, triblock tracer diffusion and triblock self-diffusion were the same, the triblock self-diffusion was still significantly slower, supposedly due to topological constraints, i.e., molecular knots of the PS backbones. When the spacing between the

PVP domains was increased, though, the triblock diffusion coefficient scaled as $\exp(-2\chi n)$ at elevated temperatures (lower χ), indicating a "double activation" of both PVP blocks simultaneously, because the PS block was not long enough for bridging anymore and the gain in entropy of the PS block compensated the enthalpy loss in the PVP blocks upon expulsion. These interpretations were shortly after confirmed by computer simulations [183] and inspired our interpretation of the exchange mechanism in flower-like telechelic micelles in solution — compare Section 4.3.2.

1.6   Self-Assembling Antimicrobial Peptides

Previously, we have used well-defined polymeric model systems like C_n-PEOx to investigate the fundamental laws governing self-assembly and molecular exchange, including the works constituting this thesis. But we also aimed to transfer this knowledge to more complex systems and confirm that the observed fundamental relations still hold. As a biologically and medically relevant example, we chose a self-assembling antimicrobial peptide which, in collaboration with He Dong from the University of Texas at Arlington, we studied in terms of self-assembled structure and molecular exchange. Therefore, the following section will briefly introduce (self-assembling) antimicrobial peptides and review recent works on the specific peptide studied in the present thesis.

Increasing bacterial resistance against conventional antibiotics is one of humankind's greatest challenges in the 21st century.[184] As soon as a new antibiotic enters the market, the "development of resistance is not a matter of *if* but only a matter of *when*".[185] Most conventional small-molecule antibiotics act on specific molecular targets within bacteria, which are often involved in critical processes like cell wall synthesis, protein synthesis, or DNA replication and repair. By exploiting biochemical differences between prokaryotic and eukaryotic cells, selectivity towards the bacterial pathogen is ensured, so that the antibiotic has minimal side effects for the host. Yet, the mode of action of an antibiotic substance can be ineffective in mutated individuals.[185] Since microbial infections involve large numbers of bacteria and they reproduce at a high rate, mutants with antibiotic-resistant attributes occur relatively quickly and they soon dominate the colony because of their evolutionary advantage over non-resistant neighbors. If these infections are not cured completely, the resistant bacteria strain can spread. Thus, the lifetime of any antibiotic substance is inherently limited. In addition, the spread of resistant bacteria is accelerated by inappropriate and excessive use of antibiotics and, in the worst case, bacterial strains develop resistance against multiple antibiotics. These multi-drug-resistant pathogens are a severe threat in today's hospital environments.[184] To fight them, problematic antibiotics like Colistin, which had been abandoned due to their adverse side effects, have been re-introduced as last-resort measures [186], but even they face increasing resistance.[184] Therefore, beside a more mindful use of antibiotics, health systems worldwide rely on the development of new therapeutics.

A viable alternative to conventional small-molecule antibiotics are antimicrobial peptides (AMPs): short cationic amphiphilic peptides, which have immunostimulatory or direct antimicrobiotic capabilities.[187, 188] They have been part of the innate immune system of a multitude of organisms for millions of years, without evolution of widespread bacterial resistance — in contrast to what we currently observe with clinical antibiotics.[188, 189] Peschel and Sahl argued that AMPs and bacterial resistance mechanisms have co-evolved, leading to a "transient host-pathogen balance".[188] Typical bacterial responses to host-issued AMPs include enzymatic proteolysis, immobilization by excreted proteins, active extrusion or changes in the membrane composition.[188] However, these measures seem to be less effective against AMPs compared to small-molecule antibiotics, because AMPs typically have multiple modes of action, target unspecific yet essential parts of the pathogen like the cell membrane and act in concert with other AMPs as well as other parts of the immune system.[187–190]

Unfortunately, in terms of clinical application, AMPs also exhibit a number of drawbacks, in addition to their comparatively high production costs. Particularly peptides based on L-amino acids are susceptible to proteolytic degradation, limiting their lifetime *in vivo*. Moreover, AMPs are often poorly hemocompatible and toxic towards host cells.[191] Yet, some of these deficits can be mitigated through the formation of AMP superstructures via self-assembly.[192–194]

1.6.1 Effects of Self-Assembly

For a long time, most focus has been on the charge (distribution) and secondary structure of individual AMP molecules and how they relate to antimicrobial activity. Only rather recently, the potential of superstructures formed from self-assembling AMPs (SAAMPs) has been spotlighted.[192–194] The driving forces of AMP self-assembly are non-covalent interactions, typical for Soft Matter systems: hydrogen bonds, electrostatic and hydrophobic interaction as well as π-π stacking. Once an AMP self-assembles, its antimicrobial activity is inevitably affected because the (surface) charge density distribution changes compared to the unimeric state. In the extreme cases, self-assembly can infer antimicrobial effects on an otherwise ineffective peptide or, conversely, a unimerically active AMP can lose its efficacy in the assembled state [195]. In most cases, however, some intermediate effect is observed. Very often, self-assembly does not create antimicrobial activity by itself, but enhances already existing properties of the unimeric AMP: Most importantly, SAAMPs exhibit decreased toxicity towards host cells [196, 197] as well as increased selectivity and general antimicrobial efficacy [197–199]. For instance, Liu et al. presented an SAAMP derived from a human immunodeficiency virus (HIV) protein, functionalized with cholesterol to promote self-assembly.[198] The resulting peptide micelles possess a broad spectrum of antimicrobial activities and an increased therapeutic index in animal models compared to the unimeric peptide. In addition, they were shown to cross the blood-brain barrier, allowing the treatment of brain infections. In these cases, strong intermolecular interactions are desirable to stabilize the structure. Particularly if the peptides are to be administered systemically, which means

they will be highly diluted, it is important that the SAAMP structure remains intact to increase the serum circulation time.

Even if self-assembly mitigates the peptide's antimicrobial activity, it still offers unique advantages. As mentioned in the previous section, AMPs are very susceptible to proteolytic degradation, limiting the life time *in vivo*. But assembly into superstructures has been shown to protect potential enzymatic cleavage sites, so even if they are less effective or not antimicrobial at all, they can serve as unimer depot with sustained release kinetics.[192, 195] For example, Tu et al. reported a *de novo* lytic peptide which in the unimeric state was prone to enzyme digestion.[195] In the assembled state, on the other hand, the peptide was resistant to enzymatic degradation but at the same time lost its lytic capabilities. Yet, active peptide unimers were slowly released from the self-assembled fibers. By tuning the intermolecular interaction, one could adjust the release rate of such peptide depots. This principle in addition allows for responsive peptide assemblies. Assembly and disassembly can be triggered by environmental stimuli like pH, ionic strength or the presence of specific ions or enzymes.[195, 200, 201] In the case of the lytic SAAMP of Tu et al., this could be exploited to locally release active peptide unimers in the acidic environments of cancerous tissue, while under physiological pH in the bloodstream the assembled peptides remain dormant.[195]

A third feature of SAAMPs is that they can induce bacterial aggregation and thus localize an infection and restrain it from spreading.[193] Human α-defensin 6 (HD6), for instance, though not bactericidal itself, forms fibrils and nanonets that immobilize pathogens in the small intestine, exposing them for treatment by other components of the immune system.[202] In contrast, the precursor peptide proHD6 does neither self-assemble nor induce bacteria aggregation.[203]

In terms of morphology of SAAMPs, creativity knows no boundaries. Beside the already mentioned micellar nanoparticles [198], there are reports about hollow, virus-like capsids [204] or nanotubes [205]. Schnaider et al. took a very minimalistic approach, using only a dipeptide: They investigated fibers formed from diphenylalanine which permeate bacterial membranes and hence induce cell death.[199] Due to the extraordinary chemical simplicity, they propose diphenylalanine filaments as an antimicrobial platform for further modification and development. In general, peptide filaments, often based on beta sheets, are the most common structural pattern for SAAMPs.[195, 197, 199–201] These can be utilized to form antimicrobial biomaterials like hydrogels. Salick et al. created SAAMP-fibril-based injectable gels which can easily be administered via syringes due to their shear-thinning properties.[201] The gels showed bactericidal activity against methicillin-resistant *Staphylococcus aureus* and are thus interesting for applications in wound healing and medical implants. To summarize, self-assembly offers various advantageous features for AMPs, like boosted antimicrobial efficacy, protection against enzymatic degradation, induction of bacteria aggregation and formation of antimicrobial biomaterials.

Yet, there are still many open questions. Can self-assembled superstructures act on internal targets? When self-assembly enhances the antimicrobial activity, does the principle mode of action differ from the unimeric peptide? Does the

peptide morphology change upon contact with the bacterial membrane? Which role does the physical stability of the assembly play? Particularly the last question has been addressed in the course of this PhD project, on the example of a peptide family presented in the following.

1.6.2 $K_x(QL)_yK_z$ Peptides

In the last years, the Dong group reported on a family of highly effective, self-assembling AMPs based on the $K_x(QL)_yK_z$ motif [7], abbreviated as *XYZ*, with astounding hemocompatibility.[206–212] Using TEM, SAXS and circular dichroism (CD) spectroscopy, they showed that these peptides self-assemble into elongated filaments consisting of two sandwiched beta sheets held together by hydrophobic interaction of the Leucine residues [207–211], as shown in Figure 1.8. The chemical structure is also depicted in Figure 2.6 on page 35. The assembly is the result of a delicate balance between attractive (hydrogen bonds between peptide molecules and hydrophobic interaction between Leucine residues) and repulsive forces (electrostatic repulsion of terminal Lysine residues). For example, $K_2(QL)_6K_2$ (262) forms well-defined filaments while $K_2(QL)_4K_2$ (242) does not because it has a shorter $(QL)_y$ block and thus less hydrophobic interaction and hydrogen bonds but the same number of repulsive Lysine residues.[207] Electrostatic repulsion also limits the filament growth so they do not precipitate. The critical association concentration (CAC) of peptides with six QL repeat units are on the order of $1-10\,\mu M$, which corresponds to $\sim 10^{-3}-10^{-2}\,mg/mL$. Above the CAC, there are almost no unimeric peptide molecules left in solution due to autocatalytic growth of the filaments.[209–211] While the self-assembled filaments have also been considered as vehicles for other active ingredients [207, 212], the main body of research focused on their inherent bactericidal capabilities. In solution, minimal inhibitory concentrations (MIC) against common pathogens like *Escherichia coli*, *Pseudomonas aeruginosa*, *Staphylococcus epidermidis* and *Staphylococcus aureus* are in the range of $10-100\,\mu M$, i.e., well above the peptides' CAC.[208–211] This already indicates that the filaments themselves are the bactericidal moieties and not the unimeric peptide molecules for which the filaments merely serve as vehicle. While it was clear from scanning electron micrographs early on, that the mode of action involves disruption of the bacterial membranes [209], it was later confirmed by solid-state NMR spectroscopy that the mode of action indeed involves the assembled filament in direct contact with the membrane [211]. Furthermore, Xu et al. found that *E. coli* colonies developed no resistance to $^DW^DK_3(QL)_6^DK_2$ (D-W362) after ten passages, whereas significant resistance against conventional penicillin V already emerged after four passages.[211] As mentioned before, this is a typical phenomenon for AMPs owed to rather unspecific membrane interaction.

Interestingly, Xu et al. found that the antimicrobial efficacy of $K_x(QL)_yK_z$ AMPs strongly depends on the internal ordering of the central beta

---

[7]K: Lysine, hydrophilic, charged below pH 10.5; Q: Glutamine, hydrophilic; L: Leucine, hydrophobic

Peptide	N-terminus	Sequence	C-terminus
242	CH₃CO-	KK **QLQLQLQL** KK	-CONH₂
262	CH₃CO-	KK **QLQLQLQLQLQL** KK	-CONH₂
W262	CH₃CO-	WKK **QLQLQLQLQLQL** KK	-CONH₂
W362	CH₃CO-	WKKK **QLQLQLQLQLQL** KK	-CONH₂
D-W362ᵃ	CH₃CO- ᴰWᴰKᴰKᴰK **QLQLQLQLQLQL** ᴰKᴰK	-CONH₂
3W62	CH₃CO-	KK **KWQLQLQLQLQLQL** KK	-CONH₂
P-W362	PEG-	WKKK **QLQLQLQLQLQL** KK	-CONH₂
P-3W62	PEG-	KK **KWQLQLQLQLQLQL** KK	-CONH₂

ᵃ Right-handed amino acid enantiomers are marked by ᴰ.

Table 1.1: Peptide sequences mentioned in this section. The central hydrophilic-hydrophobic motif is highlighted in bold.
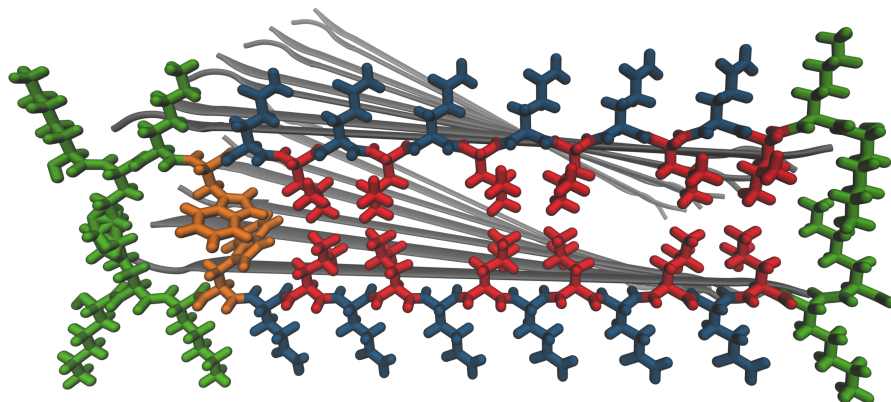
Figure 1.8: The peptide filaments consist of two sandwiched beta sheets, here on the example of the 3W62 derivative. The individual strands (grey) are connected via hydrogen bonds. The two antiparallel beta sheets are held together by hydrophobic interaction between the Leucine (L, red) and Tryptophan (W, orange) residues, while the charged Lysine (K, green) residues have a repulsive effect. Hydrophilic Glutamine residues (Q, blue) constitute the top and bottom of of the filament. Figure created in VMD [213]. The detailed chemical structure of 3W62 is shown in Figure 2.6 on page 35.

sheets.[209] The CD spectra of $K_3W(QL)_6K_2$ (3W62), $WK_3(QL)_6K_2$ (W362) and $WK_2(QL)_6K_2$ (W262)[8] revealed a clear beta sheet structure of W262 while W362 exhibited a significant portion of alpha helical and random coil content. Apparently, the additional Lysine residue disturbed the delicate balance of attractive and repulsive interactions. On the other hand, 3W62 consisted of clear beta sheets again because the repulsive contribution of the extra K was countered by the generated KW pair that extends the hydrophilic-hydrophobic motif of the six QL units. The content of ordered beta sheets was anticorrelated with the MICs against *E. coli*, *P. aeruginosa*, *S. epidermidis* and *S. aureus*: Highly ordered W262 exhibited the least bactericidal activity while W362 was most potent. The authors proposed that intercalation into the bacterial membrane is eased when the peptide filaments are more flexible internally. Surprisingly, the relation is inverted at higher concentration where the filaments form an elastic hydrogel.[208] Here, AMP derivatives with increased internal order exhibited a higher efficacy against *S. aureus* which was also positively correlated with the storage modulus of the hydrogel measured by oscillatory rheology. Obviously, a regular beta sheet structure led to hydrogels with higher viscosity and enhanced antimicrobial efficacy. The authors argued that the reason behind is an alternate mode of action: In hydrogel form, the filaments do not permeate the bacterial membrane but immobilize the pathogens via their high surface charge and the retention is improved with increased network stability.

Similar to what was described in the previous section, self-assembly also grants a number of advantages to $K_x(QL)_yK_z$ peptides. Assembled peptides were less prone to digestion by Trypsin and Chymotrypsin and the degree of protection increased with higher internal order of the filaments.[209] Self-assembly was also found to be key to enhance the AMP selectivity. While unimeric peptide molecules were clearly toxic for murine bone-marrow-derived monocytes (mBMDMs), assembled filaments showed no adverse effect.[209, 211] The authors moreover tested the hemocompatibility of $K_x(QL)_yK_z$ filaments. In hemolytic assays, incubation with D-W362 and peptide hydrogels had only a weak effect on red blood cells (RBCs).[208, 211] However, erythrocyte lysis is not the only effect that needs to be considered in terms of possible systemic application of SAAMPs. Therefore, Xu et al. investigated peptide-related eryptosis in RBCs and found that both W362 and 3W62 incurred significant damage to erythrocytes.[210] The damage caused by 3W62 was more severe, possibly because of its higher degree of internal order so that the charge domains were more defined and hence harmful for RBCs.

To increase the hemocompatibility of 3W62 and W362, Xu et al. PEGylated[9]

---

[8]W: Tryptophan, hydrophobic, fluorescent; has been introduced to the peptide sequence for accurate concentration measurement

[9]Chemically, poly(ethylene glycol) (PEG) and poly(ethylene oxide) (PEO) are the same polymer. But with lower degrees of polymerization, when the terminal hydroxyl group contributes significantly to the polymer characteristics, usage of PEG is more common, whereas with high degrees of polymerization, the hydroxyl group is not decisive anymore, so one simply uses PEO. With respect to C_n-PEOx polymers with relatively high MW, we therefore use the term PEO. In biochemistry, though, PEG is more common and therefore we use that term when discussing peptides.

the peptide molecules, denoted as P-W362 and P-3W62, respectively.[210] Due to its "stealth effect", PEGylation has become a popular tool in drug formulation since its introduction in the 1970s.[214] It increases the circulation time *in vivo*, reduces enzymatic degradation and retards or even eliminates immune response, because the polymer shields the active ingredient from degrading agents and other undesirable interactions.[215] Xu et al. found both the CACs of P-W362 and P-3W62 as well as their efficacy against *E. coli*, *P. aeruginosa* and *S. aureus* to be unchanged compared to the respective unPEGylated peptides.[210] SAXS and TEM experiments also confirmed that filaments were still the predominant morphology. Yet, CD measurements revealed that the conjugation with PEG perturbed the internal beta sheet structure. While 3W62 consisted almost exclusively of antiparallel beta sheets, the content was reduced in P-3W62 and the already slightly disordered W362 exhibited even higher amounts of alpha helices in the PEGylated P-W362 form. The decreased stability of the PEGylated sheets was also reflected in the TEM images where generally shorter filaments were observed and P-W362 even formed unspecific, spherical aggregates. Apparently, the attractive forces inside 3W62 were strong enough to maintain the filament morphology despite the entropic repulsion of the PEG chains. But, on the other hand, PEGylation had an enormous effect on the hemocompatibility. For 3W62 and W362, hemolytic activity was found to be dose-dependent, while for P-3W62 and P-W362 it was low and concentration-independent. In terms of eryptosis, PEGylation had no effect on W362 but the harmfulness of 3W62 for RBCs was tremendously decreased by the conjugation with PEG. As explained above, the compact charge interface of 3W62 is likely damaging RBCs whereas less ordered W362 filaments are less harmful. On the other hand, PEG effectively shields 3W62 charges while this concept fails with the more diffuse charge distribution of W362.

Very recently, Nielsen et al. investigated the membrane interaction of 3W62 and P-3W62 on supported lipid bilayers by using neutron reflectometry (NR).[216] In agreement with the findings of Xu et al., assembled 3W62 filaments showed markedly stronger interaction with the model membranes than unimeric 3W32 molecules. The filaments apparently adhered to the charged lipid headgroups by electrostatic interaction with the Lysine residues at the short edge of the filament — compare Figure 1.8. Surprisingly, they also found a significant amount of peptide inside the bilayer and proposed two possible explanations: The interaction with the membrane might disturb the balance of attractive and repulsive forces within the peptide structure, leading to filament destabilization and insertion of unimeric molecules into the bilayer. Or whole filaments could be incorporated, with the inserted Lysine residues in close proximity to the lipid headgroups at the bottom of the supported bilayer. Unfortunately, these two possibilities could not be definitely distinguished without further experiments. Furthermore, Nielsen et al. found that PEGylation led to decreased membrane affinity of P-3W62 compared to 3W62, which on the one hand contrasts that Xu et al. [210] observed the same antimicrobial efficacy but on the other hand explains the reduced hemolytic activity. Analogous to 3W62, Nielsen et al. detected intact P-3W62 filaments on top of the bilayer where the interaction with the

lipid headgroups was supposedly conveyed by both PEG chains and Lysine residues. Surprisingly, though, they also observed partial insertion of P-3W62 into the membrane. As it is unlikely that the bulky PEG chains are inserted, this rather points towards incorporation of unimeric molecules or fragmented filaments so that the PEG blocks remain in an hydrophilic environment. The filament destabilization might be caused by the strong membrane interaction of PEG due to preferential hydrogen bonding with the lipid headgroups.

In summary, the $K_x(QL)_yK_z$ motif represents a potent SAAMP platform where the balance between structure, stability, cytotoxicity and antimicrobial activity can be tuned by small adjustments of the amino acid sequence. In addition to the advantageous effects of PEGylation on the hemocompatibility, it also allows to study the physical integrity of peptide filaments and their exchange kinetics by KZAC TR-SANS experiments, similar to polymeric micelles — compare Sections 1.5 and 3.1.5 on page 14 and on page 47, respectively. These investigations are important because the mode of action of $K_x(QL)_yK_z$ peptides involves assembled filaments, calling for a high stability of the latter.

Chapter 2

Materials

In this chapter, we introduce the materials examined in the present doctoral thesis, namely C_n-PEOx polymers and 3W62 peptides as well as their respective derivatives. Since synthesis and characterization were not part of the present work, we will treat them only briefly here. More details on synthesis, characterization and sample preparation are given in the respective manuscripts.

2.1 C_n-PEOx

As outlined in Section 1.4 on page 13, C_n-PEOx is an excellent model system for many different aspects of polymer self-assembly. Some derivatives are commercially available under the trade name "Brij" — mostly C_{12}-, C_{16}- and C_{18}-PEOx with varying PEO length. But here we used in-house synthesized polymers to have a wider choice of alkyl block lengths and for a better control over the PEO polymerization. Moreover, deuterated and partly deuterated polymers, C_n-dPEOx and C_n-hdPEOx, with almost identical molecular characteristics were synthesized for contrast-variation neutron scattering experiments. Both polymers cannot be easily purchased from commercial polymer suppliers.

C_n-PEOx was synthesized via ring-opening living anionic polymerization of ethylene oxide (EO) in toluene — see Figure 2.1. Commercially available n-alkanols (C_nH_{2n+1}-OH, $n = 12, 14, 16, 22, 28$) in a 80:20 mixture with their respective potassium n-alkanolates served as initiator system. At 95 °C, all chemicals were completely soluble and together with a fast proton exchange between alkanols and alkanolates, this ensured homogeneous polymerization conditions and therefore a narrow molecular weight distribution of the product. After the EO monomer was consumed, the polymerization was terminated with acetic acid, leaving a hydroxyl group at the PEO terminus. Beside the ordinary proteated C_n-hPEOx, deuterated and partly deuterated polymers were synthesized following the same synthetic protocol. Fully deuterated C_n-dPEOx was prepared from deuterated dEO monomers and partly deuterated C_{28}-hdPEO5 from a 82 / 18 molar mixture of d- and hEO, leading to a random
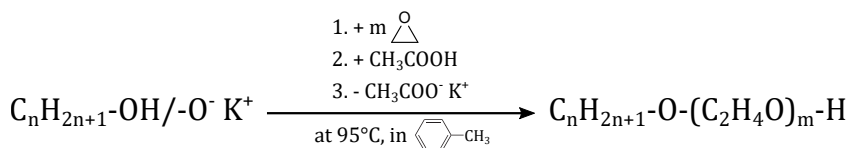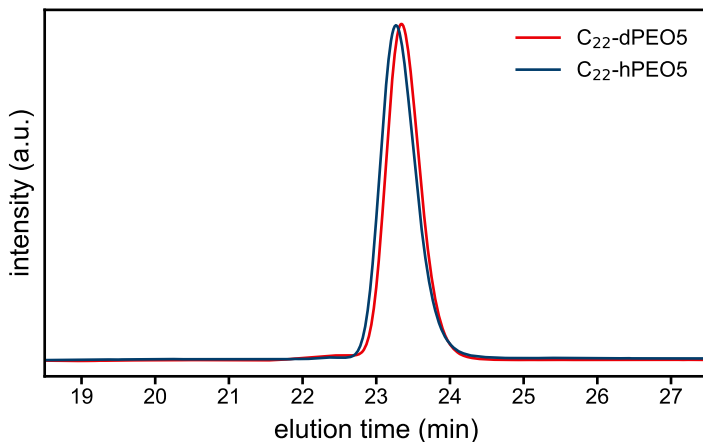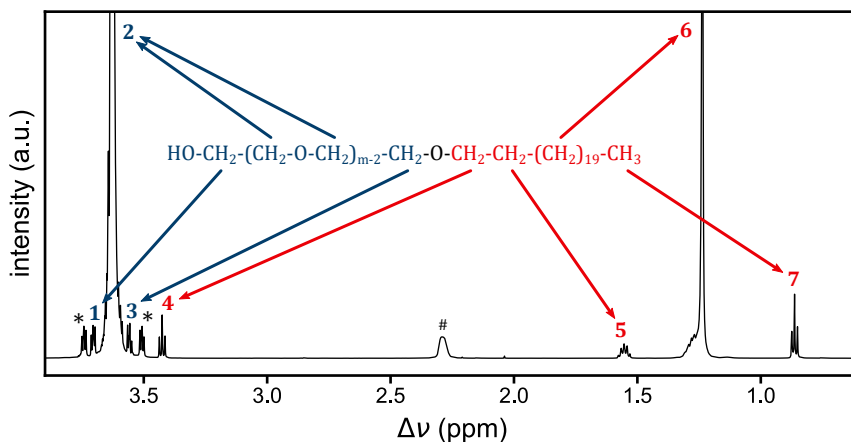
$$C_nH_{2n+1}\text{-OH/-O}^- \text{K}^+ \xrightarrow[\text{at 95°C, in }\langle\hexagon\rangle\text{-CH}_3]{\substack{1. + m \triangle\text{O} \\ 2. + CH_3COOH \\ 3. - CH_3COO^- K^+}} C_nH_{2n+1}\text{-O-}(C_2H_4O)_m\text{-H}$$

Figure 2.1: Reaction scheme of the C_n-PEOx synthesis.

Figure 2.2: SEC chromatograms of C_{22}-PEO5.

Figure 2.3: ^{1}H NMR spectrum of C_{22}-hPEO5 in CDCl$_3$. # marks the residual H$_2$O signal and * marks ^{13}C satellites.

distribution of monomers along the PEO chains. More details about the synthesis can be found in References [100] and [217].

The products were characterized by size-exclusion / gel-permeation chromatography (SEC/GPC), using a multidetector chromatographic set-up consisting of autosampler, isocratic pump (both Agilent Technologies, Series 1260 infinity), a column oven (Shimadzu CTO-20A), a refractive index (RI) detector (Optilab rEX), and an 18-angle light scattering detector (DAWN HELEOS-II),

both detectors from Wyatt Technologies. The SEC instrument was equipped with three consecutive GPC columns with continuous pore size distribution (Agilent PlusPore) which ensured high resolution. To suppress interaction effects, a mixture of tetrahydrofuran, *N,N*-dimethylacetamide and acetic acid (85:14:1 vol%) was used as eluent at a flux rate of 1 mL/min and a temperature of 40 °C. An accurate analysis of the chromatograms was done with ASTRA Software from Wyatt Technologies, yielding the apparent molecular weight characteristics, M_n and M_w as well as the polydispersity $Đ = M_w/M_n$. As an example, Figure 2.2 shows RI traces of C_{22}-hPEO5 and -dPEO. Both polymers show a single narrow peak at almost identical elution volumes, indicating a successful polymer synthesis and identical molar volumes of the two differently labeled polymers. The polydispersities were determined as $Đ \approx 1.02$ for both polymers.

In addition, we characterized proteated specimens by proton nuclear magnetic resonance (^{1}H NMR) spectroscopy to determine the degree of polymerization of the PEO block, m. The spectrum of C_{22}-hPEO5 is depicted in Figure 2.3. The degree of polymerization m was calculated by relating the integrals of the known number of *n*-alkyl protons (signals **4**–**7**) to the integral intensity of the main PEO peak at 3.6 ppm (signal **2**). In the given example, the integral of the peak yields $m - 2 = 109$. By comparing the SEC traces, the degree of polymerization of C_{22}-dPEO5 could therewith be estimated as $m = 107$. M_n determined by NMR and SEC are in excellent agreement. Characterization results of individual polymers employed in the present thesis are given in the respective publications (Papers I to III).

2.2 C_n-PEO$2x$-C_n

For the study presented in Paper IV, di-alkyl-functionalized PEOs, C_n-PEO$2x$-C_n, were synthesized by intermolecular coupling of the respective monofunctionalized PEOs, C_n-PEOx. The terminal hydroxyl groups of the PEO chains formed an ether linkage by reacting with tosyl chloride (TsCl) in the presence of solid potassium hydroxide as described in Reference [102]. SEC data of the raw product revealed higher molecular weight impurities and residual uncoupled C_n-PEOx polymer. Thereupon, a purification was carried out by fractionating with chloroform/heptane as solvent/non-solvent pair for PEO. After several fractionation steps, the product still contained $\sim 10\%$ residual monofunctional PEO as can be seen in the SEC traces in Figure 2.4a). However, as explained in Section 1.5.3 on page 19, the difunctional polymer was anyhow blended with its monofunctional counterpart to stabilize the micelles in solution. Thus, a certain amount of additional C_n-PEOx was added to the product to reach the desired volume fraction of telechelic molecules, f_{tel}, in the blend. These blends are denoted as CnFXX, where XX is the volume percentage of telechelic molecules. As an example, Figure 2.4b) shows the SEC traces of C22F50 blends, consisting of C_{22}-PEO5 and C_{22}-PEO10-C_{22} with $f_{\text{tel}} = 50\%$. In addition, the proteated samples were characterized with ^{1}H NMR in the same fashion as for monofunctional C_n-PEOx, confirming the successful linking reaction.
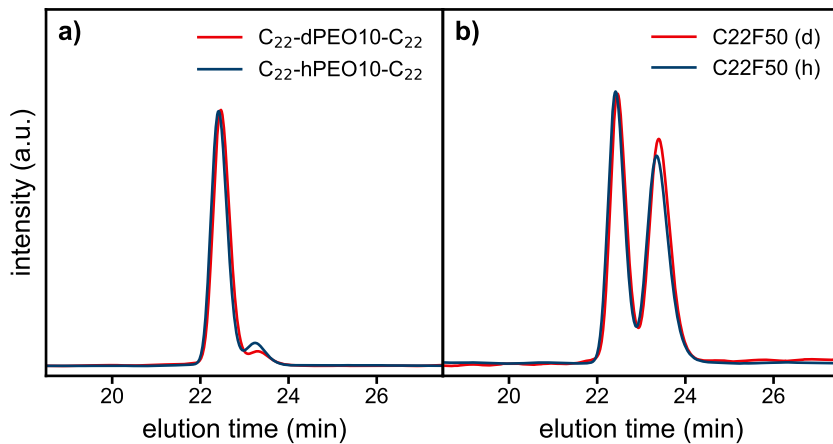
Figure 2.4: SEC chromatograms of a) the C_{22}-PEO10-C_{22} synthesis products and b) blended C22F50.
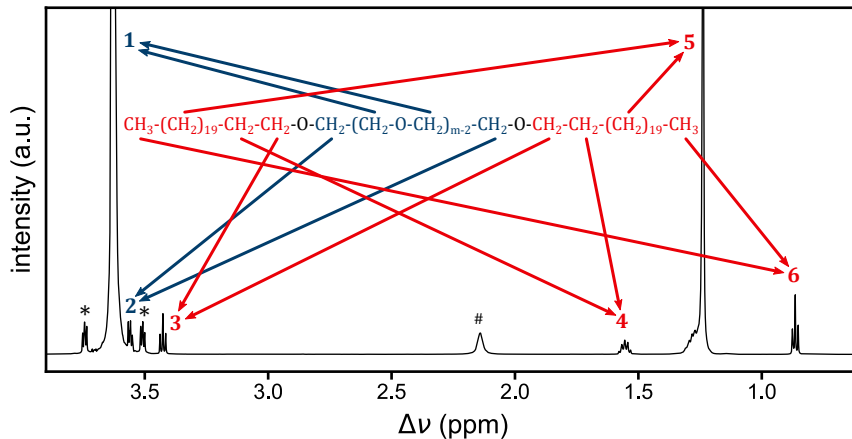

Figure 2.5: ^{1}H NMR spectrum of C_{22}-hPEO10-C_{22} in CDCl$_3$. # marks the residual H$_2$O signal and * marks ^{13}C satellites.

The spectrum shown in Figure 2.5 yields $m = 226$ — note the missing signal from the methylene group next to the hydroxyl terminus at 3.7 ppm (signal **1** in Figure 2.3). A slight mismatch of the PEO degree of polymerization was observed arising from the fractionation steps such that it slightly deviates from twice the PEO chain length in the monofunctional material.

2.3 3W62

In Paper V, we investigated self-assembled filaments formed by an antimicrobial peptide with the sequence $K_3W(QL)_6K_2$, or 3W62 for short. This peptide is part of a peptide family based on the $K_x(QL)_yK_z$ motif which is studied in the group of He Dong at the University of Texas at Arlington. The peptides used in the present work were synthesized by standard Fmoc-solid phase peptide synthesis, see Paper V and References [209, 210] for details. To avoid unwanted reactions at the N-terminal amino group, the latter was acetylated. Finally, the peptide was cleaved off the synthesis resin, leaving an amide group at the C-terminus. The final chemical structure of the product is given in Figure 2.6a).
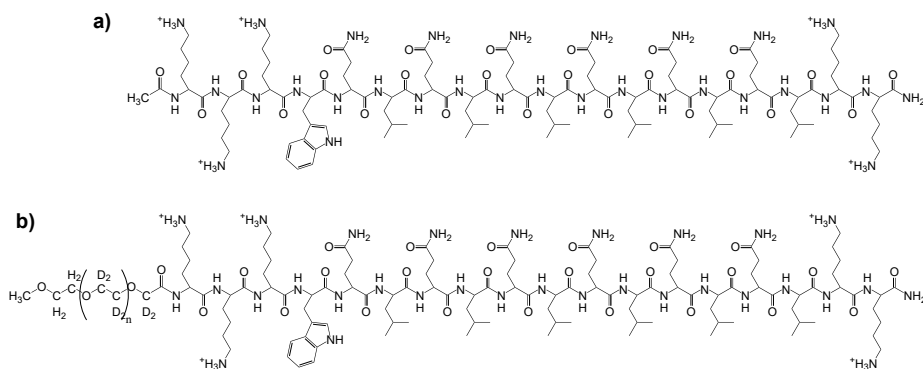
Figure 2.6: Chemical structure of a) 3W62 and b) dP-3W62.

As outlined in Section 1.6.2 on page 26, PEGylation[1] significantly improves the hemocompatibility of 3W62 without derogating the antimicrobial efficacy. At the same time, it allows to monitor the molecular exchange between filaments by KZAC neutron scattering experiments, as explained in Section 3.1.5 on page 47. To this end, 3W62 was functionalized with proteated (hP-3W62) and deuterated (dP-3W62) PEG2 at the N-terminus as shown in Figure 2.6b). While proteated hPEG2 was bought from Sigma-Aldrich, deuterated dPEG2 was synthesized by the same procedure as for C_n-PEOx described in Section 2.1, using methoxyethanol / potassium methoxyethanolate as initiator system. The terminal hydroxyl groups of both PEG species were converted to carboxyl groups

---

[1]With respect to the peptide-polymer conjugates treated in this thesis, the polymer is denoted as poly(ethylene glycol) (PEG) instead of poly(ethylene oxide) (PEO) — see Section 1.6.2 on page 26.

via oxidation which allowed a linking condensation reaction with the N-terminal amino group of 3W62, which in this case was not acetylated. Then, the polymer-peptide conjugate was cleaved off the resin, leaving the same amino C-terminus as in the unPEGylated 3W62.

Chapter 3

Experimental Methods

This chapter covers all experimental aspects involved in the present doctoral thesis. As the majority of results were obtained from small-angle scattering, we will recapitulate this particular family of experimental techniques in some detail. The auxiliary methods, on the other hand, will be treated only briefly. After a short introduction of the respective method, the focus will be on the specific experiments performed in the context of the thesis. For detailed reviews and theoretical background of the individual techniques, the reader is referred to standard textbooks.

3.1 Small-Angle Scattering

The present work aims to shed more light on structures arising from self-assembly of molecular building blocks and their exchange kinetics. The size of such mesoscopic structures is typically on a length scale $10-100$ nm and therefore particularly suited to be studied by small-angle scattering (SAS) techniques. One distinguished advantage of SAS over other characterization methods is that it allows self-assembled structures to be investigated *in situ*, i.e., in solution without complex sample preparation protocols which, for instance, are necessary for TEM experiments. In this section, we first present the general theory underlying SAS experiments and then some practical considerations. SAS experiments can in principle be performed by any kind of radiation but the prevailing techniques are small-angle X-ray (SAXS), neutron (SANS) and light (SALS) scattering. Since the latter was not employed in the present work, only the special features of SAXS and SANS will be discussed in the following. For more details and references, the reader is referred to relevant textbooks like [218] or [219].

3.1.1 General Theory of Small-Angle Scattering

The basic principle underlying any scattering experiment is the interaction between the incident radiation and the sample. In case of SAXS, X-ray photons interact with the atomic electron shell, whereas in SANS, neutrons interact with the nucleus. A basic sketch of the scattering geometry is depicted in Figure 3.1. The sample is illuminated by collimated, monochromatic radiation (neutrons or X-rays) and the scattering pattern is recorded by a 2D detector. In terms of scattering experiments, it is more practical to describe the radiation as waves instead of particles. Since the source-sample and sample-detector distances are large compared to the dimensions of the sample, the radiation can be considered as plane waves in Fraunhofer approximation, i.e., far-field approximation. The incident radiation is described by the wave vector $\vec{k}$ and the scattered radiation
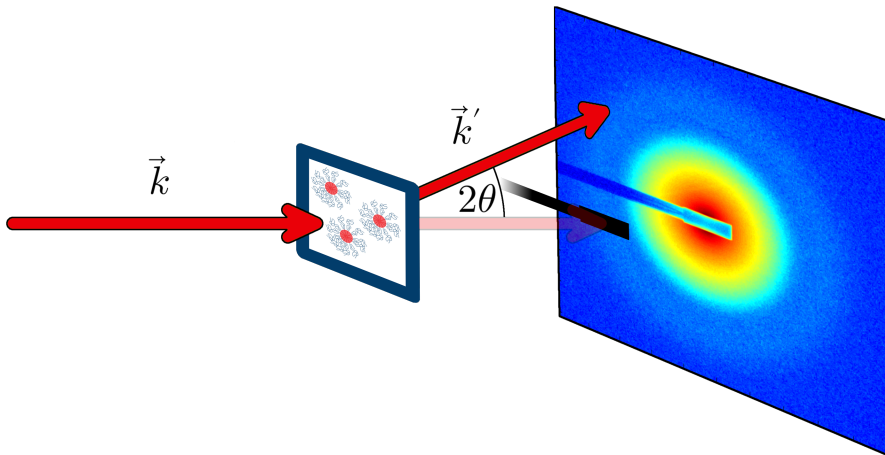
Figure 3.1: Sketch of the scattering geometry: The sample is illuminated by collimated, monochromatic radiation which is scattered by the sample. The circularly symmetric scattering pattern is recorded by a 2D detector while the direct beam is blocked by a beamstop.

by $\vec{k}'$. Here, only elastic scattering is considered where the energy is unaffected. Therefore, the modulus of the wave vector

$$k = \left|\vec{k}\right| = \left|\vec{k}'\right| = \frac{2\pi}{\lambda} \tag{3.1}$$

does not change, with λ being the wavelength, whereas the change in direction is described by the momentum transfer (or scattering vector)

$$\vec{Q} = \vec{k}' - \vec{k}. \tag{3.2}$$

For isotropic scattering like from freely tumbling particles in solution, only its modulus is of relevance, which depends solely on the scattering angle 2θ:

$$Q = \left|\vec{Q}\right| = 4\pi \sin(\theta)/\lambda. \tag{3.3}$$

The actual quantum mechanical scattering process can be described in Born approximation [220]. Here, one assumes that the interaction potential is weak so that no multiple scattering occurs and attenuation is negligible. For SANS, this is generally justified because neutron scattering cross-sections are rather small. For SAXS, the approximation still holds for most Soft Matter systems as they contain mainly light elements like hydrogen, carbon and oxygen.

The scattering pattern recorded by the detector arises from the secondary waves emitted from individual atoms within a coherently scattering volume.[1]

---

[1]The much more intense primary beam is blocked by the beamstop.
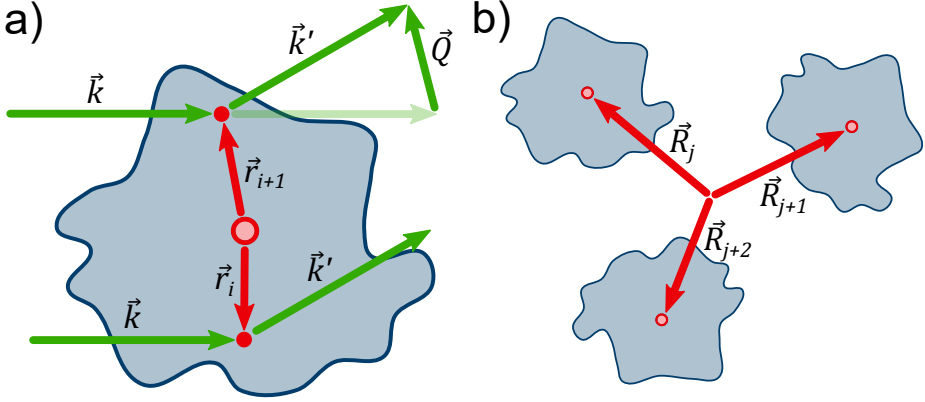
Figure 3.2: a) Scattering from a single particle: The incident radiation $\vec{k}$ is scattered into the direction $\vec{k}'$. Exemplary scatterers are located at $\vec{r}_i$ and $\vec{r}_{i+1}$. The momentum transfer $\vec{Q}$ describes the scattering direction. **b)** Multiple particles in solution: The particles are located at positions $\vec{R}_j$ and orientated randomly.

This could, for instance, be a particle in solution. Applying both Fraunhofer and Born approximation, the superpositioned amplitude of the scattered waves can be written as

$$A\!\left(\vec{Q}\right) = \sum_i b_i \, \mathrm{e}^{i\vec{Q}\vec{r}_i}, \tag{3.4}$$

where the atoms i are located at $\vec{r}_i$, as sketched in Figure 3.2a). The scattering length b_i represents the strength of the interaction potential and depends on the considered type of radiation. For X-rays, it scales with the number of electrons in the atomic shell and for neutrons it is isotope- and spin-dependent.

Unfortunately, there is no experimental access to the scattering amplitude. The detector is only able to measure the scattering intensity which is proportional to the differential scattering cross-section

$$\frac{\mathrm{d}\sigma}{\mathrm{d}\Omega}\!\left(\vec{Q}\right) = A\!\left(\vec{Q}\right) A^*\!\left(\vec{Q}\right). \tag{3.5}$$

Here, * indicates the complex conjugate. The differential scattering cross-section gives the ratio between the flux density scattered into the solid angle Ω and the incident flux density. Thus, the intensity measured by the detector is

$$I_{\mathrm{meas}}\!\left(\vec{Q}\right) = \frac{I_0}{L^2}\frac{\mathrm{d}\sigma}{\mathrm{d}\Omega}\!\left(\vec{Q}\right), \tag{3.6}$$

where I_0 is the incident intensity and L the sample-detector distance. In practice, though, the macroscopic differential scattering cross-section

$$\frac{\mathrm{d}\Sigma}{\mathrm{d}\Omega}\!\left(\vec{Q}\right) = \frac{1}{V_P}\frac{\mathrm{d}\sigma}{\mathrm{d}\Omega}\!\left(\vec{Q}\right) \tag{3.7}$$

is more common, which is normalized for the particle volume V_P.

Yet, a typical SAS sample does not consist of a single, static particle but of a multitude of particles randomly oriented in solution as depicted in Figure 3.2b). That means that the scattering pattern arises from N particles j at positions $\vec{R}_j$ which each contribute a scattering amplitude $A_j\left(\vec{Q}\right)$ so that the cross-section becomes

$$\frac{\mathrm{d}\Sigma}{\mathrm{d}\Omega}\left(\vec{Q}\right) = \left\langle \frac{1}{V_S} \left[\sum_j^N A_j\left(\vec{Q}\right) \mathrm{e}^{i\vec{Q}\vec{R}_j} \right] \left[\sum_k^N A_k^*\left(\vec{Q}\right) \mathrm{e}^{-i\vec{Q}\vec{R}_k} \right] \right\rangle_\Omega \tag{3.8a}$$

$$= \left\langle \frac{1}{V_S} \sum_{j,k}^N A_j\left(\vec{Q}\right) A_k^*\left(\vec{Q}\right) \mathrm{e}^{i\vec{Q}(\vec{R}_j - \vec{R}_k)} \right\rangle_\Omega , \tag{3.8b}$$

where $\langle . \rangle_\Omega$ denotes an average over all rotational states and V_S is the sample volume. Assuming all particles are identical, it can be split up in intraparticle ($j = k$) and interparticle ($j \neq k$) contributions, where for $j \neq k$ the rotationally averaged amplitudes are uncorrelated:

$$\frac{\mathrm{d}\Sigma}{\mathrm{d}\Omega}\left(\vec{Q}\right) = \frac{1}{V_S} \left\langle \sum_{j=k}^N A_j\left(\vec{Q}\right) A_k^*\left(\vec{Q}\right) + \sum_{j\neq k}^N A_j\left(\vec{Q}\right) A_k^*\left(\vec{Q}\right) \mathrm{e}^{i\vec{Q}(\vec{R}_j - \vec{R}_k)} \right\rangle_\Omega \tag{3.9a}$$

$$= \frac{1}{V_S} \left\langle \sum_j^N A_j\left(\vec{Q}\right) A_j^*\left(\vec{Q}\right) + \sum_{j\neq k}^N A_j\left(\vec{Q}\right) A_k^*\left(\vec{Q}\right) \mathrm{e}^{i\vec{Q}(\vec{R}_j - \vec{R}_k)} \right\rangle_\Omega \tag{3.9b}$$

$$= \frac{1}{V_S} \left(N \left\langle \left|A\left(\vec{Q}\right)\right|^2 \right\rangle_\Omega + \left|\left\langle A\left(\vec{Q}\right)\right\rangle_\Omega\right|^2 \left\langle \sum_{j\neq k}^N \mathrm{e}^{i\vec{Q}(\vec{R}_j - \vec{R}_k)} \right\rangle_\Omega \right) \tag{3.9c}$$

$$= \frac{N}{V_S} \underbrace{\left\langle \left|A\left(\vec{Q}\right)\right|^2 \right\rangle_\Omega}_{P(\vec{Q})} \underbrace{\left(1 + \frac{1}{N} \frac{\left|\left\langle A\left(\vec{Q}\right)\right\rangle_\Omega\right|^2}{\left\langle \left|A\left(\vec{Q}\right)\right|^2 \right\rangle_\Omega} \left\langle \sum_{j\neq k}^N \mathrm{e}^{i\vec{Q}(\vec{R}_j - \vec{R}_k)} \right\rangle_\Omega \right)}_{S(\vec{Q})}$$
$$\tag{3.9d}$$

The second term, $S(\vec{Q})$, is the so-called *structure factor*. It arises from spatial correlations between the particles and therefore depends on interparticle interactions. At low concentrations, there are no spatial correlations so that $S(\vec{Q}) \approx 1$. We do not discuss the structure factor in more detail here because it is not particularly relevant for the present work. In contrast, the so-called *form factor* $P(\vec{Q})$ originates solely from intraparticle correlations and thus contains information about the particle shape.

Instead of describing individual scatterers (i.e., atoms), it is common to define an average *scattering length density* (SLD)

$$\rho = \frac{\sum_i b_i}{V} \tag{3.10}$$

of all scatterers i in a certain volume V, because SAS anyhow does not provide atomic resolution. Then, the discrete sum in the scattering amplitude, Equation (3.4), over all atoms in the particle becomes a continuous integral over the local SLD $\rho(\vec{r})$ in the particle volume V_P,

$$A(\vec{Q}) = \int_{V_P} \rho(\vec{r}) \, e^{i\vec{Q}\vec{r}} \, d\vec{r}. \tag{3.11}$$

The complex-valued scattering amplitude $A(\vec{Q})$ is obviously the Fourier transform of the real-space SLD $\rho(\vec{r})$ and therefore contains all information to reconstruct the particle shape. Unfortunately, $A(\vec{Q})$ is experimentally inaccessible. The measurable quantity is the real-valued form factor

$$P(\vec{Q}) = \left| A\left(\vec{Q}\right) \right|^2 \tag{3.12}$$

which does not contain the phase information anymore. This is the so-called *phase problem* which renders direct reconstruction of the real-space $\rho(\vec{r})$ from scattering experiments impossible. In addition, particles in solution typically have no preferential orientation so the average $\langle . \rangle_\Omega$ leads to a circularly symmetric scattering pattern and the form factor merely depends on the modulus Q of the scattering vector $\vec{Q}$. In the interpretation of SAS experiments, one therefore relies on models with a handful of adjustable parameters and calculation of theoretical scattering patterns which are then compared to the experimental data.

The fact that the particles of interest are embedded in a solvent makes another consideration necessary. The incident radiation is not only scattered by the particles but also by the surrounding matrix. Because the solvent molecules are usually small compared to the particles and there are no correlated density fluctuations, the solvent can be described by a homogeneous SLD ρ_0, which results in a featureless background scattering. This constant solvent scattering background can easily be subtracted to obtain the net scattering of the solute (the particles of interest). Therefore, the actual real-space quantity from which the scattering pattern originates is the excess SLD

$$\Delta\rho(\vec{r}) = \rho(\vec{r}) - \rho_0, \tag{3.13}$$

also known as *contrast*, and the actually measured form factor is

$$P(Q) = \left\langle \left| \int_{V_P} \Delta\rho(\vec{r}) \, e^{i\vec{Q}\vec{r}} \, d\vec{r} \right|^2 \right\rangle_\Omega. \tag{3.14}$$

Form factors of many geometrical shapes can be calculated analytically and are given in relevant textbooks.[218, 219] For arbitrary shapes like, for instance, proteins, there are several computer programs available which calculate Equation (3.14) efficiently for any given $\Delta\rho(\vec{r})$. In the course of this PhD project, geometrical models for polymer micelles and peptide filaments have been developed which are described in detail in the respective publications.
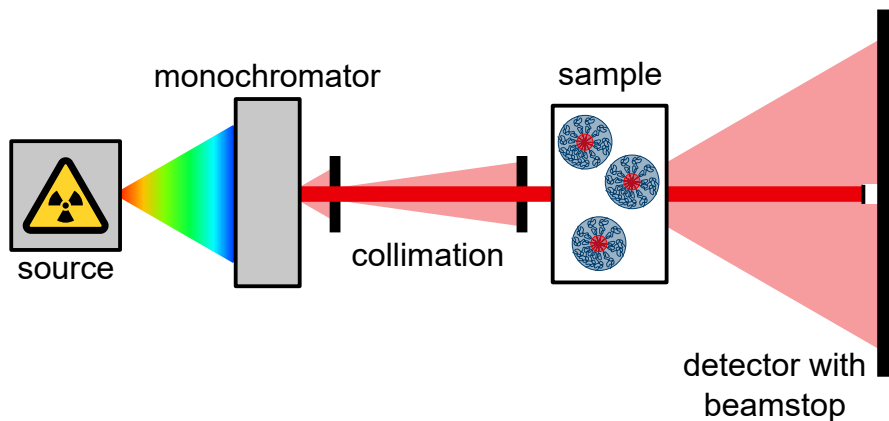
Figure 3.3: Principle setup of an SAS instrument.

3.1.2 Experimental Considerations

The principle setup of SAS instruments is depicted in Figure 3.3. Even though the exact implementation is specific to the employed kind of radiation — see Sections 3.1.3 and 3.1.4 —, the general setup is still the same for all SAS techniques. The primary radiation provided by the source is usually polychromatic ("white beam") and uncollimated. Hence, the first element is typically a monochromator which selects a certain wavelength. Thereafter, the beam is collimated and shaped to the desired size by a number of slits before it hits the sample container. Then, the primary beam as well as the scattered radiation traverse through the flight tube that contains the 2D area detector. Here, the scattering pattern is recorded with the primary beam blocked by a beamstop to avoid detector saturation/damage. Beside the immediate sample environment, all beam paths are evacuated to avoid air scattering.

The scattering recorded on the detector does not exclusively originate from the sample solution, though. There are unwanted contributions from the sample holder, parasitic scattering from the apertures, residual air scattering, electronic noise and last but not least cosmic background radiation. Therefore, the detector signal is corrected for those by a number of additional reference measurements. Then, the remaining intensity (i.e., the number of counts per second on a pixel) is converted to an absolute scale[2] by comparison with a "flat scatterer" — a material that gives a Q-independent scattering signal of known absolute intensity like water or amorphous carbon. At the end, if the scattering signal is circularly symmetric, the 2D detector image is azimuthally averaged to yield the macroscopic differential cross-section of the sample solution, $d\Sigma/d\Omega_S(Q)$. All data reduction up to this point is typically done by instrument-specific software in a standardized way. Yet, $d\Sigma/d\Omega_S(Q)$ still contains the scattering

---

[2] $\frac{d\Sigma}{d\Omega}(Q)$ is usually given in cm^{-1}.

contribution from the solvent. Therefore, the pure solvent is measured in addition and the resulting signal subtracted from $d\Sigma/d\Omega_S$ to yield only the macroscopic differential cross-section of the solute.

When comparing these experimental SAS data with calculated model scattering curves, one has to consider the experimental resolution.[221, 222] To this end, the calculated curve is convoluted with the resolution function $R(Q, \langle Q \rangle)$ that depends on the experimental parameters. The three main factors are imperfect collimation, finite detector pixel size and residual wavelength spread. They lead to an uncertainty in the experimental $\langle Q \rangle$ values that needs to be taken into account during data interpretation.

3.1.3 Small-Angle X-ray Scattering

In small-angle X-ray scattering (SAXS), incident X-ray photons interact with the electrons in the atomic shells of the sample material. Thus, the strength of the interaction potential simply scales with the atomic number Z and the scattering length of an element is given by

$$b = Z\,r_e, \tag{3.15}$$

where $r_e = 2.82 \times 10^{-15}\,\mathrm{m}$ is the classical electron radius. The consequence is that the scattering signal is dominated by heavy atoms and especially hydrogen is practically invisible.

Due to its high availability, SAXS is the most common SAS technique. On the one hand, highly intense synchrotron radiation is provided by large-scale facilities on a national and international level. These institutions offer highly specialized equipment for the worldwide research community and the immense intensity allows for high sample throughput. On the other hand, lab-based SAXS instruments with lower intensity provide local, low-level access for less demanding experiments. Even for these "low-intensity" sources, the achievable photon flux is quite high so that the beam characteristics (wavelength, collimation, size) can be defined narrowly and the resolution function is nearly negligible. Furthermore, small beam dimensions allow for reduced sample volumes which is particularly useful when only minute amounts are available, for example in the case of biological samples. On the other hand, the high flux of X-ray photons at synchrotron radiation facilities leads to the creation of hydroxyl and hydroperoxyl radicals in water. These radicals can in turn activate sample molecules which then aggregate. This form of radiation damage is negligible at lab-based sources and non-existent in neutron scattering.

Most SAXS experiments related to the present work have been performed at a lab-based Bruker Nanostar instrument at the Norwegian Centre for X-ray Diffraction, Scattering and Imaging (RECX), located at the University of Oslo.[223] Some additional data were taken at beamline BM29 at the European Synchrotron Radiation Facility (ESRF) in Grenoble, France.[224] Table 3.1 lists some key features of both instruments that exemplify the different characteristics of lab-based and synchrotron-based SAXS experiments.

	Nanostar	BM29
location	UiO	ESRF
source	Cu K_α X-ray tube	synchrotron radiation
incident flux	$\sim 10^8$ ph/s	$<10^{12}$ ph/s
monochromator	Göbel mirror	double multilayer monochromator
collimation	flight path with two sets of slits	flight path with three sets of slits and a focusing toroidal mirror
sample container	quartz capillary	quartz capillary
detector distance	$1.08\,\text{m}$	$2.87\,\text{m}$
wavelength λ	$1.54\,\text{Å}$	$0.83 - 1.77\,\text{Å}^a$
wavelength spread $\frac{\Delta\lambda}{\lambda}$	$0.1\,\%$	$1.6\,\%^b$
Q range	$0.01 - 0.3\,\text{Å}^{-1}$	$0.0025 - 0.5\,\text{Å}^{-1c}$
others	-	sample-changing robot, automated data analysis pipeline

[a] adjustable

[b] This is unusually high. For instance, the beamline ID02 at ESRF operates at $\frac{\Delta\lambda}{\lambda} = 0.015\,\%$.

[c] depending on the chosen X-ray wavelength

Table 3.1: Key features of the SAXS instruments used in the present work.

3.1.4 Small-Angle Neutron Scattering

In small-angle neutron scattering (SANS), the incident neutrons interact with the atomic nuclei in the sample. The interaction potential depends on the nuclear structure and is hence not as straightforward as the X-ray scattering length in Equation (3.15). Instead, the neutron scattering length is isotope-dependent in a more complicated fashion with values tabulated in the literature [225]. Most interestingly, the scattering length of hydrogen does not differ greatly from heavier nuclei and thus, in contrast to SAXS, hydrogen atoms contribute significantly to the SANS signal. Additionally, since the neutron carries a magnetic moment, the interaction can also depend on the spin state which allows the investigation of the sample's magnetic structure. The fact that the scattering length b does not only depend on the element, but also isotope and spin state, requires an average $\langle . \rangle$ over the scattering length b in the differential scattering cross-section, Equation (3.5) on page 39:

$$\frac{\mathrm{d}\sigma}{\mathrm{d}\Omega}\left(\vec{Q}\right) = \left\langle A\!\left(\vec{Q}\right) A^*\!\left(\vec{Q}\right) \right\rangle \tag{3.16a}$$

$$= \left\langle \sum_{i,j} b_i\, b_j\, \mathrm{e}^{i\vec{Q}(\vec{r}_i - \vec{r}_j)} \right\rangle \tag{3.16b}$$

$$= \sum_{i,j} \langle b_i\, b_j \rangle \; \mathrm{e}^{i\vec{Q}(\vec{r}_i - \vec{r}_j)}. \tag{3.16c}$$

Since the scattering lengths at positions i and j are independent,

$$\langle b_i\, b_j \rangle = \begin{cases} \langle b_i^2 \rangle = \langle b_i \rangle^2 + \langle b_i - \langle b_i \rangle \rangle & i = j \\ \langle b_i \rangle \langle b_j \rangle & i \neq j \end{cases}, \tag{3.17}$$

leading to two terms in the scattering cross-section:

$$\frac{\mathrm{d}\sigma}{\mathrm{d}\Omega}\left(\vec{Q}\right) = \underbrace{\sum_{i,j} \langle b_i \rangle \langle b_j \rangle \; \mathrm{e}^{i\vec{Q}(\vec{r}_i - \vec{r}_j)}}_{\text{coherent}} + \underbrace{\sum_{i} \langle b_i - \langle b_i \rangle \rangle}_{\text{incoherent}}. \tag{3.18}$$

While the first term, the coherent scattering contribution, embodies all spatial correlations and thus structural information, the second term, the incoherent scattering contribution, contains no phase information and represents only an additional featureless background. For isotopically pure samples and spin-independent scattering, on the other hand, $b_i = \langle b_i \rangle \; \forall i$, so that there is no incoherent scattering.

In Soft Matter science, the isotope dependence is particularly interesting, especially in the case of hydrogen. The two isotopes protium and deuterium carry very different scattering lengths: $b_{\mathrm{H}} = -3.741\,\mathrm{fm}$ and $b_{\mathrm{D}} = 6.671\,\mathrm{fm}$.[225] Thus, by blending H_2O and D_2O, the SLD of aqueous solvents can be adjusted over a wide range. That way, according to Equations (3.13) and (3.14), one can "hide" a solute by matching its SLD with the solvent SLD because the contrast vanishes. This procedure is called *contrast matching*. With multicomponent samples, contrast matching can be utilized to highlight certain components by matching out others. Furthermore, certain parts of a solute can deliberately be isotope-exchanged to match them with the solvent, without affecting the chemical nature of the solute.[3] The kinetic experiments presented in Section 3.1.5 on page 47 heavily profit from this principle.

Despite its interesting features, SANS is not as common as SAXS due to its limited availability. While high-quality X-ray beams can be produced on a lab scale, neutron beams suited for scattering experiments require large-scale facilities like nuclear reactors or spallation sources. Despite recent ambitions for neutron sources on a smaller scale [227], today's large-scale neutron sources are only available on an international level. Compared to X-ray sources, even these large-scale neutron facilities achieve only relatively low fluxes. Thus, the beam definition at SANS instruments has to be relaxed for the sake of increased intensity. For example, wavelength spreads of $5-10\,\%$ are common and the illuminated sample area is several millimeter in diameter — compared to $< 1\,\%$ polydispersities and sub-millimeter-sized beams in SAXS. Therefore, consideration of the experimental resolution is much more critical in the

---

[3]Of course, other isotope effects can occur, mostly related to the higher mass of deuterium. For instance, D_2O is more viscous than H_2O.[226] However, these effects are usually negligible.

	KWS-2	Sans2d
location	MLZ	ISIS
source	reactor	spallation
incident flux	$<10^8\,\mathrm{n/s/cm^2}$	$>10^6\,\mathrm{n/s/cm^2}$
monochromator	mechanical velocity selector	N/A
collimation	neutron guides and two sets of slits	neutron guides and two sets of slits
sample container	exchangeable quartz cuvettes	exchangeable quartz cuvettes
detector distance	$2-20\,\mathrm{m}^a$	$2-12\,\mathrm{m}^a$
wavelength λ	$4.5-20\,\text{Å}^a$	$2-14\,\text{Å}$
wavelength spread $\frac{\Delta\lambda}{\lambda}$	$2-20\,\%^a$	N/A
Q range	$0.0006-1.0\,\text{Å}^{-1\,b}$	$0.002-3.0\,\text{Å}^{-1\,b}$
others	focusing options	time-of-flight instrument

[a] adjustable
[b] depending on the detector distance and, in case of KWS-2, neutron wavelength

Table 3.2: Key features of two SANS instruments used in the present work.

evaluation of SANS data. Fortunately, scattering curves of Soft Matter systems seldom exhibit sharp features so that the relaxed resolution does not pose a critical problem. Yet, the enlarged beam diameter calls for larger sample volumes compared to SAXS experiments. This is especially problematic in the case of biological samples which are typically only available in minute quantities. On the other hand, radiation damage does not occur in neutron scattering and therefore samples can be fully recuperated.

In the works constituting the present doctoral thesis, most neutron scattering experiments were carried out at two SANS instruments: KWS-2 at the Heinz Maier-Leibnitz Zentrum (MLZ) in Garching, Germany, [228] and Sans2d at the ISIS Neutron and Muon Source in Didcot, United Kingdom [229–232]. Table 3.2 lists some of the key features of the two instruments.

Here, it is worthwhile to note that Sans2d is a time-of-flight (TOF) instrument. Being served by a pulsed spallation source, the neutrons of Sans2d come in "bursts", normally 10 bursts per second. Instead of only using a single neutron wavelength, almost all wavelengths illuminate the sample simultaneously and are later distinguished by their arrival time at the detector. By measuring the time of flight from the source to the detector, the wavelength and therewith Q value for every single counting event on a detector pixel is determined individually. Therefore, with a single measurement, a larger Q range can be covered — compared to monochromatic SANS instruments where typically measurements at multiple detector distances have to be combined. For example, at $4\,\mathrm{m}$

detector distance and $\lambda = 4.5\,\text{Å}$, KWS-2 covers roughly $Q = 0.01 - 0.2\,\text{Å}^{-1}$ whereas Sans2d provides $0.004 - 1\,\text{Å}^{-1}$ at the same detector distance, by using $\lambda = 2 - 14\,\text{Å}$ simultaneously.[4] On the one hand, the TOF design is useful in kinetic experiments because a larger Q range is covered in a single shot. On the other hand, the temporal resolution is limited by the spallation frequency (at ISIS: $10\,\text{Hz}$) and the time-averaged flux is lower in comparison to continuous experiments.

3.1.5 Kinetic Zero-Average-Contrast Experiments

As described in the previous section, neutron scattering experiments offer the unique opportunity to manipulate the contrast conditions by isotope labeling, without altering the chemical nature of the sample. One example is the *zero-average-contrast* (ZAC) scheme which allows to study the form factor of polymer chains at high concentrations.[233] To this end, deuterated and proteated but otherwise identical polymer molecules with SLDs ρ_P^d and ρ_P^h, respectively, are blended in equal molar amounts and dissolved in an isotopically blended solvent with SLDs ρ_0^d and ρ_0^h, respectively. When the solvent matches the average contrast between the two polymer species,

$$\rho_0 = \phi_0^d \, \rho_0^d + \left(1 - \phi_0^d\right) \rho_0^h = \frac{1}{2} \left(\rho_P^d + \rho_P^h\right), \tag{3.19}$$

where ϕ_0^d is the volume fraction of the deuterated solvent molecules in the solvent mixture, the partial structure factors cancel out and the scattering signal depends solely on the polymer form factor.

The ZAC condition in combination with time-resolved SANS (TR-SANS) also allows to study the molecular exchange between self-assembled entities in a very elegant way. Proposed by Willner et al. [133], *kinetic zero-average-contrast* (KZAC) experiments monitor the equilibrium exchange without any perturbations beside the H/D exchange, leading to astounding insights into the exchange kinetics of polymeric micelles — compare Section 1.5.2 on page 15. The experimental principle is illustrated in Figure 3.4: Deuterated and proteated polymers are dissolved separately in a solvent mixture according to the ZAC condition in Equation (3.19). When the two solutions are mixed, both micelle populations exhibit the same contrast but with the inverse sign,

$$\Delta\rho_P^h = \rho_P^h - \rho_0 = -\Delta\rho_P^d. \tag{3.20}$$

Since the scattering signal depends on $\Delta\rho^2$, the overall intensity is maximal at $t = 0$. But as soon as molecular exchange between the populations takes place, the micelles become isotopically mixed and the contrast decreases over time. At $t = \infty$, when all molecules have exchanged at least once, it vanishes completely:

$$\Delta\rho = \frac{\rho_P^h + \rho_P^d}{2} - \rho_0 = 0. \tag{3.21}$$

---

[4]The Q range can be extended to even higher angles by simultaneously employing a second detector closer to the sample.
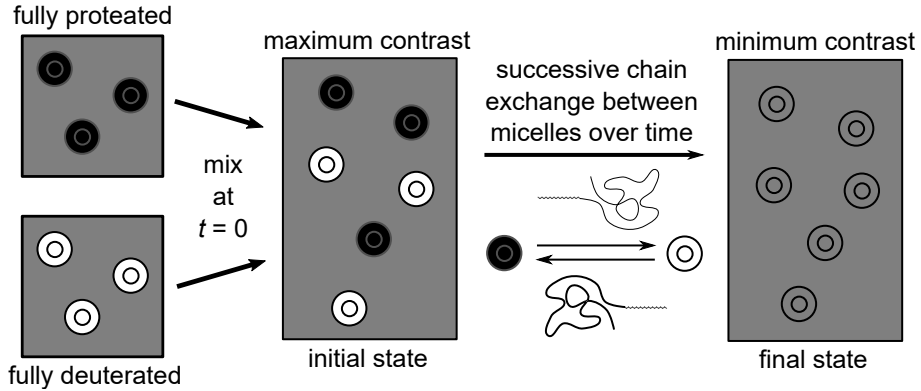
Figure 3.4: Illustration of the KZAC principle.

The molecular exchange is therefore directly observable through the decay of the scattering intensity.

Yet, the more interesting quantity, which can be compared to theoretical predictions, is the relaxation function $R(t)$ that describes the fraction of molecules that have not exchanged yet and are still part of their original micelle. In a model-independent approach, one can use the time-resolved, Q-integrated SANS signal

$$I(t) = \int \frac{d\Sigma}{d\Omega}(Q,t)\,dQ \propto \Delta\rho(t)^2 \tag{3.22}$$

to calculate the relaxation function via

$$R(t) = \sqrt{\frac{I(t) - I(\infty)}{I(0) - I(\infty)}}. \tag{3.23}$$

Alternatively, one can fit a theoretical model of the micellar form factor to the experimental data, using time-dependent contrasts

$$\Delta\rho^h(t) = f(t)\,\rho_P^h + (1 - f(t))\,\rho_P^d - \rho_0 \tag{3.24a}$$

$$\Delta\rho^d(t) = (1 - f(t))\,\rho_P^h + f(t)\,\rho_P^d - \rho_0 \tag{3.24b}$$

for the two micelle populations, where $f(t)$ is the fraction of proteated molecules in an originally fully proteated micelle. Initially, all micelles are isotopically pure, $f(0) = 1$, but after full exchange they are randomly mixed, $f(\infty) = 0.5$. Thus, the relaxation function is simply

$$R(t) = \frac{f(t) - f(\infty)}{f(0) - f(\infty)} = 2f(t) - 1. \tag{3.25}$$

These two approaches are equivalent.[105, 139]

Strictly, the considerations above are only true for fully deuterated/proteated polymer molecules. Nevertheless, the experimental scheme also works with

partially labeled molecules as long as the majority of the polymer is labeled consistently and the difference between $I(0)$ and $I(\infty)$ is sufficient. Still, for the experiments to work, a number of other requirements need to be fulfilled:

- Beside their isotopic composition, the two polymer species need to be identical and any isotope effects in both polymer and solvent behavior must be negligible.

- The exchange must occur on an experimentally accessible time scale. Typically, this would be minutes to hours, given the relatively low flux at SANS instruments. At high intensity sources and with the aid of automatic mixing devices, temporal resolutions in the sub-second regime can be achieved.

- The mixing of the two isotopically pure solutions must be homogeneous and occur within a time span much shorter than the exchange process.

- Because molecular exchange rates typically depend double-exponentially on temperature, special attention has to be paid to temperature stability. The pure solutions should be pre-thermostatted and the container of the mixed solution must be kept at constant temperature throughout the whole measurement.

- The isotopically pure solutions should be measured separately as well as a pre-equilibrated, fully exchanged blend to serve as references for $I(0)$ and $I(\infty)$, respectively.

The KZAC experiments presented in this thesis were carried out at KWS-2 and Sans2d which are described in Section 3.1.4. The experimental protocol and treatment of kinetic data from these instruments is described with the help of example data sets in the following. Figure 3.5 shows TR-SANS data from Sans2d, following the molecular exchange in micelles consisting of C_{28}-PEO5 and C_{28}-PEO10-C_{28} (C28F40) with isotope-labeled PEO blocks at $37\,°C$. The polymer volume fraction was $\phi = 1\,vol\%$ but nonetheless there is no apparent structure factor, due to the approximate ZAC condition. The isotopically pure solutions, though, exhibited a significant structure factor. Therefore, to obtain the $d\Sigma/d\Omega(Q, t = 0)$ reference, they were diluted to $0.25\,vol\%$. Then, the two SANS curves were averaged and rescaled according to the dilution factor, yielding the shown $d\Sigma/d\Omega(Q, t = 0)$ curve. For the $d\Sigma/d\Omega(Q, t = \infty)$ reference, equal volumes of the two solutions were combined and equilibrated at $60\,°C$ over night, ensuring complete randomization. Obviously, the scattering signal did not vanish completely. The residual scattering originated from the micellar alkyl cores which were not contrast-matched as well as from single-chain contributions ("blob" scattering) in the corona. In this particular case, the experimental curves were also not background-subtracted because it is unnecessary for the evaluation of kinetic data. The scattering curves with open symbols originate from a freshly mixed solution that was followed over time. Obviously, the signal decreased, starting from a shape close to $d\Sigma/d\Omega(Q, t = 0)$ and asymptotically approaching
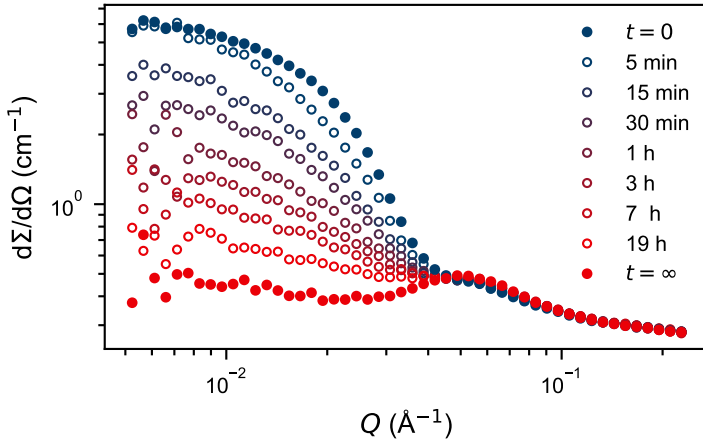
Figure 3.5: Scattering curves from an exemplary KZAC experiment at Sans2d, following the exchange of C28F40 mixed telechelic micelles. Adapted with permission from Paper IV. Copyright © 2020 American Physical Society.

$d\Sigma/d\Omega(Q, t = \infty)$. Before mixing, the separate solutions were equilibrated in the thermostatted sample holder rack at the designated temperature. Then they were quickly but thoroughly mixed in a quartz cuvette which subsequently was placed in the sample holder rack. Together with the time to close the experimental hutch, this procedure lead to a dead time of about $t_{\text{dead}} \approx 80\,\text{s}$ between mixing and commencement of the measurement. Even though the hand-mixing protocol limited the achievable t_{dead} — compared to using an automated mixing device like at KWS-2, see below —, it allowed the use of a standard sample holder rack with excellent temperature stability. Over the course of a measurement, the temperature measured with a thermocouple wire inside the cuvette was stable within $< 0.5\,\text{K}$. By using the manually noted time point when the sample was mixed, τ_{mix}, as well as the start and end of the measurement recorded in the logbook, τ_{start} and τ_{end}, the time lapsed after mixing for each measurement was calculated as

$$t = \frac{\tau_{\text{end}} - \tau_{\text{start}}}{2} - \tau_{\text{mix}}. \tag{3.26}$$

Exploiting the time-of-flight capabilities of Sans2d, some data sets were sliced in the temporal domain to increase the number of time points, particularly during the first measurement right after mixing. The data were evaluated utilizing the model-free approach presented above. To obtain $I(t)$, the scattering curves were integrated over the range $0.008\,\text{Å}^{-1} < Q < 0.04\,\text{Å}^{-1}$, in which the signal changed the most. The lowest Q points were omitted because of their large uncertainty. A preliminary $R(t)$ curve for each sample was created according to Equation (3.23), using the $I(0)$ and $I(\infty)$ values from the reference measurements.

Kinetic experiments at KWS-2 were carried out in "real time mode", measuring only the overall count rate at the detector as a function of time which corresponds to $I(t)$. In contrast to the Sans2d data shown in Figure 3.5 which covers basically the full micellar form factor with a single detector setting ($d = 4\,\mathrm{m}$) thanks to the time-of-flight capabilities, KWS-2 uses a single wavelength setting (here: $\lambda = 7\,\text{Å}$, $\Delta\lambda/\lambda = 10\,\%$) which at the chosen detector distance ($d = 8\,\mathrm{m}$) yielded a limited Q range of about $0.003-0.03\,\text{Å}^{-1}$. Therefore, a model-dependent analysis was not feasible and the model-independent approach was the natural choice, rationalizing the use of "real time mode". On the other hand, the continuous, high-intensity reactor source in combination with an automated mixing device allowed for exceptional time resolution, with measurement durations down to $t_{\mathrm{meas}} = 25\,\mathrm{ms}$ per frame. We employed a Biologic SFM 400 stopped-flow mixing device that could be controlled from outside the experimental hutch, decreasing the dead time tremendously. Solely limited by the flow rate and the volume of the tubing and cuvette, t_{dead} was only $2.5\,\mathrm{ms}$. The time point for frame $i = 1, 2, \dots$ was calculated as

$$t_i = (i - 0.5)\,t_{\mathrm{meas}} + t_{\mathrm{dead}}. \tag{3.27}$$

On the other hand, even though we employed a custom-built neutron head with improved temperature control for the stopped-flow device, variations in temperature were slightly larger, $<1\,\mathrm{K}$, than with the thermostatted Sans2d sample rack. Nevertheless, the automated mixing also ensured high reproducibility. To cover different t ranges, multiple experiments at different t_{meas} were performed. Each measurement was at least repeated once and the curves always overlapped perfectly, so they were subsequently averaged. For the lower t_{meas}, up to 12 repetitions were averaged to increase the poor counting statistics. Figure 3.6 shows $I(t)$ from a 1 vol% C_{22}-PEO5 kinetic mixture with isotope-labeled PEO chains at $9\,^\circ\mathrm{C}$. The averaged data sets from the different t_{meas} were combined and sorted into log-sized bins, where they were averaged one more time, weighted by the respective cumulated measurement duration. Similar to the procedure for the Sans2d data, these final $I(t)$ curves were translated to preliminary $R(t)$ curves according to Equation (3.23) by using reference measurements.

Unfortunately, the $I(0)$ and $I(\infty)$ values from the reference measurements did not always perfectly agree with the actual values of the individual kinetic samples. Especially when the whole exchange process of a sample was covered, like in Figure 3.6, $I(0)$ and $I(\infty)$ could be much more accurately determined directly from $I(t)$ than from the reference measurements. Deviations were expected, though, because already minute differences in concentration or mixing volume have a great effect on the ZAC conditions. Therefore, minor adjustments of $I(0)$ and $I(\infty)$ were allowed during subsequent steps of $R(t)$ analysis which are described in detail in the relevant publications, Paper III and Paper IV. In addition, it should be noted that the experimental uncertainties in $\mathrm{d}\Sigma/\mathrm{d}\Omega(Q, t)$ were propagated to $I(t)$, $I(0)$, $I(\infty)$ and $R(t)$ by Gaussian error propagation. For the integrated intensities $I(t)$, $I(0)$ and $I(\infty)$, the uncertainties in every
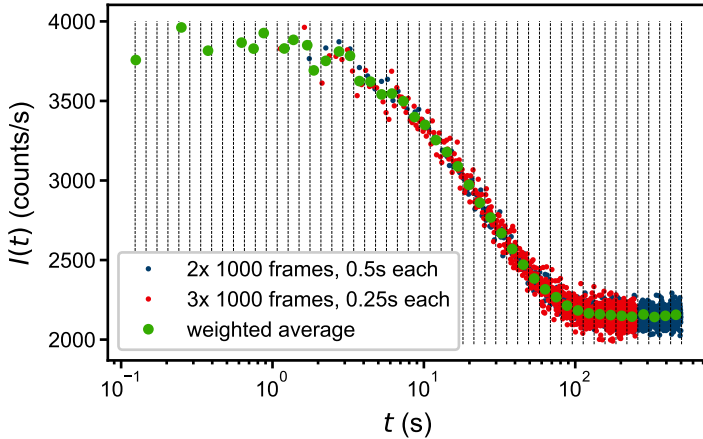
Figure 3.6: Example for the binning of kinetic KWS-2 data: Time-resolved scattering intensity of C_{22}-PEO5 followed with two different frame durations, $t_{\mathrm{meas}} = 0.25\,\mathrm{s}, 0.5\,\mathrm{s}$.

single data point $\mathrm{d}\Sigma/\mathrm{d}\Omega(Q_i, t)$ were added,

$$\mathrm{d}I(t) = \sqrt{\sum_i \left[\mathrm{d}\left(\frac{\mathrm{d}\Sigma}{\mathrm{d}\Omega}\right)(Q_i, t)\, \frac{Q_{i-1} + Q_{i+1}}{2}\right]^2},\qquad(3.28)$$

and propagated to the uncertainty in the relaxation function,

$$\mathrm{d}R(t) = \frac{\sqrt{[\mathrm{d}I(t)]^2 + [R(t)^2\mathrm{d}I(0)]^2 + [R(t)^2\mathrm{d}I(\infty)]^2}}{2\,R(t)\,[I(0) - I(\infty)]}.\qquad(3.29)$$

In total, we investigated the molecular exchange kinetics of three sample systems in the framework of this doctoral thesis. The first two are closely related: micelles consisting of C_n-PEO5 polymers (Paper III) and micelles consisting of both C_n-PEO5 and C_n-PEO10-C_n polymers (Paper IV). These samples were analyzed as described above. The third system, P-3W62, is a self-assembling peptide conjugated with PEO, which exhibited almost no molecular exchange (Paper V). None of these strictly fulfills the full-labeling criterion for KZAC experiments mentioned above. In both cases, only the PEO blocks were isotopically labeled. In the C_n-PEO systems, however, the PEO block comprises about 90 % of the molecule, whereas in P-3W62 the peptide and polymer part are of comparable size. Figure 3.7 shows calculated scattering curves, corresponding to the initial $\mathrm{d}\Sigma/\mathrm{d}\Omega(Q, t = 0)$ and final $\mathrm{d}\Sigma/\mathrm{d}\Omega(Q, t = \infty)$ state of kinetic mixtures for C_{28}-PEO5 and P-3W62 in two different contrast conditions. The curves were calculated using the models and parameters presented in Papers II
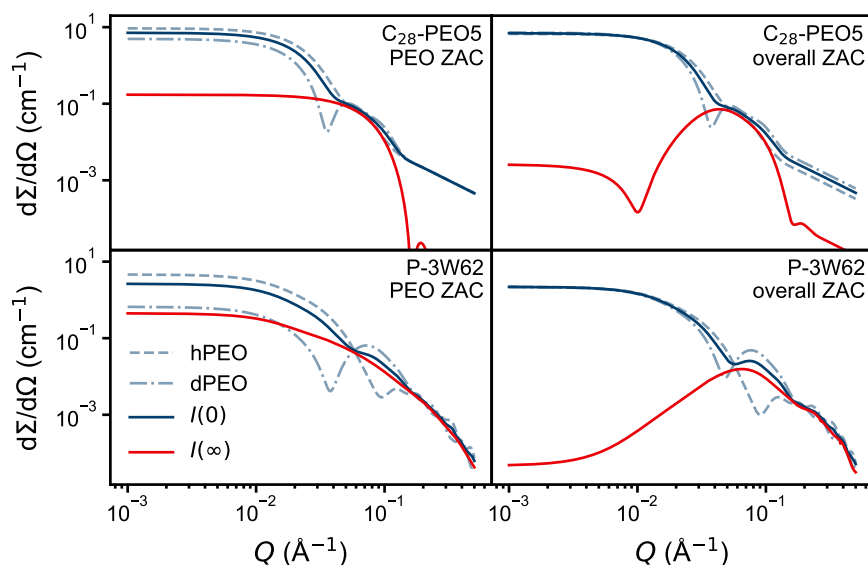
Figure 3.7: Calculated scattering curves of the start and end state of kinetic mixtures for C_{28}-PEO5 and P-3W62 in different ZAC conditions.

and V, respectively. The average contrast of hPEO and dPEO is matched by an H_2O/D_2O mixture with about $66.7\,\text{vol}\%$ D_2O ("PEO ZAC"). This solvent composition has been used in all kinetic experiments involving the C_n-PEO system (Papers III and IV). Yet, as shown in Figure 3.7, the "overall ZAC", i.e., the average scattering length between C_n-hPEO and C_n-dPEO ($59\,\text{vol}\%$ D_2O), would have been the better choice, with greater difference between $I(0)$ and $I(\infty)$. But the stringent usage of an "overall ZAC" would have required an individual ZAC solvent mixture for each C_n-PEOx sample. To simplify experiments and data analysis, we therefore decided to employ the same "PEO ZAC" solvent for all C_n-PEOx samples. In the peptide system, though, where the labeled PEO block represents only half of the molecule, the "PEO ZAC" gives little difference between $I(0)$ and $I(\infty)$. But the actual "overall ZAC" for P-3W62 is also difficult to determine because of an unknown extent of hydrogen exchange in the peptide. For the curves shown in Figure 3.7, all theoretically exchangeable protons[5] were considered as exchangeable, yielding $54.5\,\text{vol}\%$ D_2O as the average matching point. In the study reported in Paper V, we used $56\,\text{vol}\%$ D_2O, based on a slightly different calculation. In any case, though, one has to keep in mind that the curves shown in Figure 3.7 are based on geometrical $P(Q)$ models only and the true match points might be slightly different.

---

[5]Hydrogen atoms bound to oxygen or nitrogen, compare Figure 2.6 on page 35, are deemed prone to exchange with solvent hydrogen atoms.

3.2 Densitometry

Density measurements were carried out on an Anton Paar DMA 5000 density meter. This device utilizes the oscillating U-tube principle.[234, 235] The sample is filled into a U-shaped glass capillary whose eigenfrequency is directly related to the contained mass. With the known capillary volume, the sample density can be very accurately determined in this manner. The instrument was calibrated with dry air and ultrapure, degassed water according to the manufacturer's instructions.

Firstly, density measurements were employed to independently determine the melting point of the micellar core because the core density shows a discrete reduction at the melting transition. Even though the absolute value of the core density was uncertain to approximately 5 % (see below), the relative density changes with temperature were very reproducible, yielding rather accurate melting/freezing points $T_{m/f}$. Secondly, we used the measured core density to calculate the core SLD needed to fit SAS data. Yet, particularly SAXS is very sensitive to the core density, so that the measured density had to be adjusted, within the experimental uncertainty, during the fit procedure.

By measuring the density of a polymer solution d_{sol}, the solution density of the polymer d_{polym} can be determined when the solvent density d_0 and the weight fraction $w = m_{\mathrm{polym}}/(m_{\mathrm{polym}} + m_0)$ are known. The density of the solution is

$$
\begin{aligned}
d_{\mathrm{sol}} &= \frac{m_{\mathrm{polym}} + m_0}{V_{\mathrm{polym}} + V_0} \\
&= \frac{m_{\mathrm{polym}} + m_0}{\frac{m_{\mathrm{polym}}}{d_{\mathrm{polym}}} + \frac{m_0}{d_0}} \\
&= \frac{d_{\mathrm{polym}}\, d_0}{w\, d_0 + (1 - w)\, d_{\mathrm{polym}}},
\end{aligned} \tag{3.30}
$$

which can be solved for d_{polym} as

$$
d_{\mathrm{polym}} = \frac{w\, d_{\mathrm{sol}}\, d_0}{d_0 + (w - 1)\, d_{\mathrm{sol}}}. \tag{3.31}
$$

That way, we determined the apparent density of C_n-PEO5 micelles $d_{\mathrm{Cn\text{-}PEO}}$. By additionally measuring the density of PEO homopolymer in solution d_{PEO} and assuming the density of PEO was the same in the micellar corona, we determined the apparent density of the micellar core d_{Cn}. Figure 3.8 shows example data used to determine the core density of C_{28}-PEO5 micelles by the procedure described above. According to the manufacturer, the DMA 5000 measures densities with an accuracy of 10^{-6} g/mL. Repeated measurements, however, pointed rather towards 10^{-5} g/mL and the empirical uncertainty in $d_{\mathrm{Cn\text{-}PEO}}$ and d_{PEO} was even higher, around 5×10^{-3} g/mL, which can be explained by unknown uncertainties in w. This led to a cumulated uncertainty of roughly 0.04 g/mL in d_{Cn}.
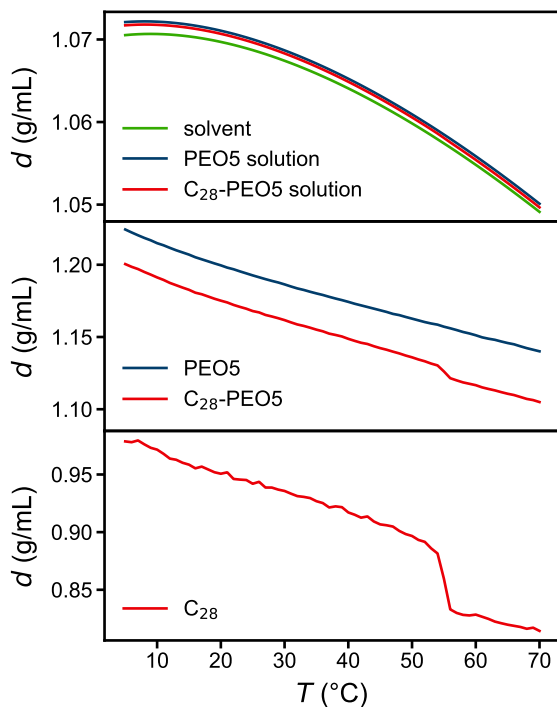
Figure 3.8: (top) Measured density of a $1.2\,\mathrm{wt\%}$ hPEO5 solution, a $1.0\,\mathrm{wt\%}$ C_{28}-hPEO5 solution and the respective solvent, water with $66.7\,\mathrm{vol\%}$ D_2O. (center) Polymer density calculated therefrom. (bottom) Density of the alkyl block in the micellar core which constitutes $7.9\,\mathrm{wt\%}$ of C_{28}-hPEO5.

3.3 Differential Scanning Calorimetry

Differential scanning calorimetry (DSC) was utilized to accurately measure melting/freezing points $T_{m/f}$ and the respective transition enthalpies $\Delta H_{m/f}$ of micellar solutions.[236] Here, the sample is heated/cooled at a constant rate β (temperature difference per unit time) and the necessary power $P(t)$ is logged. With the sample volume V, the polymer concentration c (mass per volume), the molecular weight MW and the time-temperature relation $T(t)$, $P(t)$ is converted to the differential molar heat capacity

$$C_P(T(t)) = \frac{P(t)\,\mathrm{MW}}{\beta\,V\,c}. \tag{3.32}$$

We used a TA Instruments Nano DSC which allowed to measure $C_P(T)$ of the alkyl core in dilute micellar solutions. The pure solvent hereby served as blank which was subtracted from the sample measurement. In addition, the $C_P(T)$
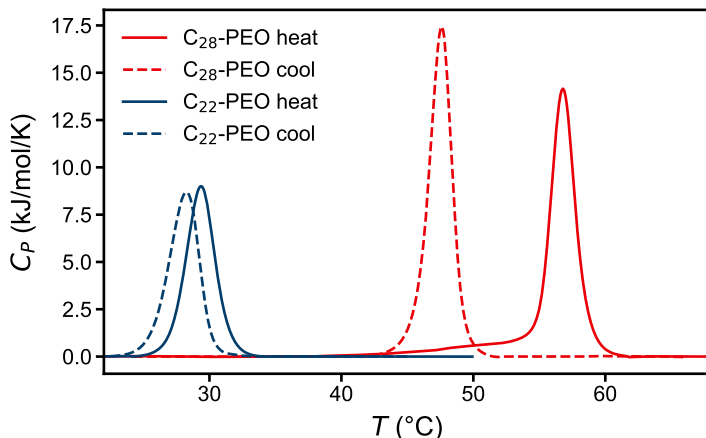
Figure 3.9: Solvent- and baseline-corrected DSC traces of $1\,\text{vol}\%$ C_{28}- and C_{22}-PEO5 micellar solution at a scan rate $\beta = \pm 2\,\text{K/min}$.

traces were baseline corrected, accounting for corona contributions etc. All data treatment up to this point was performed in the manufacturer's software suite NanoAnalyze.

Exemplary data of C_{28}- and C_{22}-PEO5 micelles are given in Figure 3.9. The peak position of $C_P(T)$ was taken as the transition temperature $T_{m/f}$ and the integral of the peak as $\Delta H_{m/f}$. Furthermore, we calculated the transition entropy as $\Delta S_{m/f} \approx \Delta H_{m/f}/T_{m/f}$, since $\Delta G = 0$ at $T = T_m$.

3.4 Nuclear Magnetic Resonance Spectroscopy

Nuclear magnetic resonance (NMR) spectroscopy allows to study the structure and dynamics of molecules in solution.[237, 238] The method exploits that the Larmor frequency ν of nuclear spins, corresponding to the transition energy $\Delta E = h\nu$ between different spin states in a homogeneous external magnetic field, is influenced by neighboring atoms, so that resonances of individual nuclei in a molecule can be identified. Therefore, resonances are conventionally not plotted against ν but against the "chemical shift" $\Delta\nu = \nu - \nu_0$ from the nucleus' native Larmor frequency ν_0. The technique obviously only works on isotopes with a finite nuclear spin, where ^{1}H proton NMR is the most prominent variety.

For Paper I, we employed ^{1}H solution NMR to qualitatively assess the mobility of the alkyl blocks in cores of C_n-PEOx micelles by analyzing the resonance line width. In chloroform, a common solvent for both blocks, the molecules tumble freely and corresponding NMR spectra exhibit very narrow alkyl signals, like in Figure 2.3 on page 32. The reason is that the nuclear interactions leading to line broadening are averaged out by rapid tumbling of molecules in solution.

In water, on the other hand, C_n-PEOx forms micelles which restricts the alkyl chain mobility; and thus nuclear interactions are not averaged out completely anymore. Above the melting point, this leads to slightly broadened resonances but below the melting point, the arrested motion broadens the alkyl signals beyond recognition.

The problem of unrecognizably broad NMR signals in solidified samples can be (partly) overcome by spinning the sample at the "magic angle" $\theta_m \approx 55°$ relative to the magnetic field.[239, 240] The spinning partially compensates the missing free tumbling so that at least some nuclear interactions are averaged out again. In Paper I, we employed magic-angle-spinning solid-state ^{13}C NMR to characterize the conformation and dynamics of the alkyl block under arrested mobility, i.e., in the micellized state and even in the solid phase below the melting temperature. We used polarization transfer experiments, cross polarization (CP) [241] and refocused insensitive nuclei enhanced by polarization transfer (refocused-INEPT) [242, 243], to qualititatively assess the alkyl block conformation and dynamics above and below the melting transition.[244] Furthermore, we determined the orientational order parameter [245, 246]

$$S_{\mathrm{CH}} = \frac{1}{2} \left\langle 3\cos^2 \theta - 1 \right\rangle \tag{3.33}$$

of the akyl chains, where θ is the angle between a ^{13}C-^{1}H internuclear vector and the magnetic field, just above the melting transition by using R-type proton detected local field (R-PDLF) experiments [247].

Chapter 4

Results and Discussion

The present doctoral thesis is part of a long-lasting research effort in our group, investigating self-assembly by means of well-defined model systems and extrapolating the resulting fundamental relations to more complex phenomena as illustrated in Figure 4.1. Starting from conventional PEP-PEO and PS-PB polymeric micelles [121, 248], the introduction of the C_n-PEOx system enabled better insight into micellar exchange kinetics [105, 106, 249]. This new system also entailed studies on its morphology [100, 108] and micellar interaction [101, 217]. In the course of these works, we discovered that the alkyl[1] cores exhibit a phase transition below a certain temperature — which we ascribed to crystallization. While we carried out first studies on how this phenomenon affects the exchange kinetics [61], a deeper understanding of the supposedly crystalline phase and the consequences of core crystallization was missing. That was the starting point for the present work. We shed light on the conformation of the alkyl chains inside the micellar core, both in the crystalline and liquid phase, and how this affects the micellar morphology (Paper I). Tuning the crystallinity by blending different alkyl chains lengths (Paper II), we revealed how crystallinity affects the molecular exchange kinetics of polymer micelles (Paper III). Also, we continued previous work on the morphology [102] and rheology [104] of telechelic C_n-PEO2x-C_n micelles by establishing a first quantitative description for the exchange mechanism of telechelic polymer micelles in solution (Paper IV). We furthermore aimed to transfer our fundamental knowledge gained from these model systems to more complex, biologically relevant systems. With our collaborator He Dong (University of Texas at Arlington), we investigated the
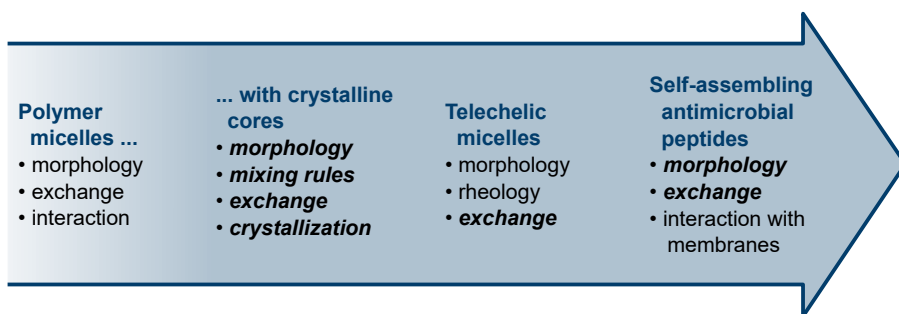
Figure 4.1: Research topics studied in our group. Aspects covered by the present thesis are highlighted in bold italics.

---

[1]As noted in Section 1.3.3 on page 11, we exclusively refer to linear n-alkanes/n-alkyl groups throughout this thesis.

self-assembled structure of 3W62 antimicrobial peptides and their molecular exchange (Paper V), while we studied the interaction of the peptide filaments with model membranes [216] in parallel.

This chapter is organized as follows: First, Papers I to V will be summarized briefly. Then, the results will be discussed across papers: Section 4.2 deals with the structure of (mixed) C_n-PEOx micelles, with special focus on core crystallization and co-assembly of length-mismatched core chains. Thereafter, Section 4.3 covers the results we obtained on the exchange kinetics of polymeric micelles, including the effect of crystallinity and the newly discovered exchange mechanism in telechelic micelles. Finally, the structure and physical integrity of (P-)3W62 filaments will be discussed in Section 4.4.

4.1 Summary of Papers

Paper I deals with the core structure in C_n-PEOx micelles. We found that the core is an oblate ellipsoid below the melting point but also retains some anisotropy above the melting point. The reason is the conformation of the alkyl chains. Below the melting point, they mostly adopt an all-trans configuration in a rotator-like phase with very slow reorientation rates. Above the melting point, the chains are almost liquid-like but their rigidity presumably hinders a spherical geometry. Furthermore, we reported a thin layer of dehydrated PEO in the immediate core vicinity, caused by the high polymer density in that region.

Paper II presents a systematic study of micelles formed from C_n-PEO5 and mixtures thereof with different alkyl chain lengths n over a wide range of temperatures. It investigates the relationship between composition, thermodynamics and structure. We found no emergent phenomena upon blending different core block lengths, the mixed micelles perfectly interpolate between "pure" C_n-PEO5 micelles, both in terms of thermodynamics
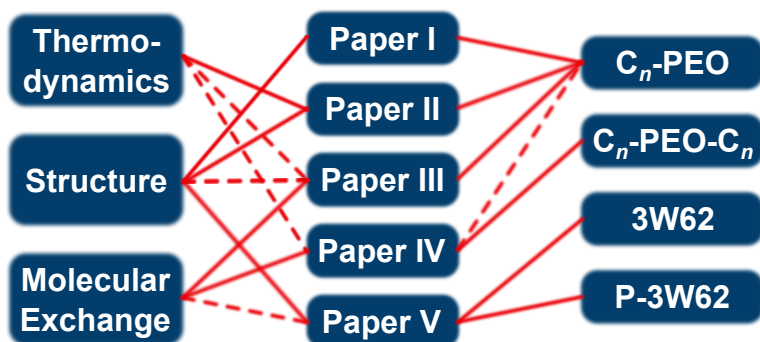
Figure 4.2: Research aspects and sample systems related to Papers I to V.

and structure. For example, the mixed micelles exhibit the same melting point depression according to a generalized Gibbs-Thomson equation as previously reported for pure micelles. In addition, we reported a novel $N_{\mathrm{agg}} \propto n^3$ scaling law for C$_n$-PEO5 micelles; but unfortunately, to this date, we lack a theoretical explanation for this behavior.

Paper III shines light on the interplay between molecular exchange and crystallization in polymeric micelles, on the example of C$_n$-PEO5 and mixtures thereof with varying n. While we found crystallization/melting to be a cooperative process between molecules, exchange of individual molecules is independent. The co-crystallization only results in an additional, cooperative free energy barrier (equal to the melting enthalpy ΔH) to the activation energy E_a of the otherwise decoupled expulsion process. But ΔH as well as the melting point T_m can conveniently be tuned by blending different alkyl block lengths. Lastly, we found that confinement enhances the miscibility of length-mismatched C$_n$ chains.

Paper IV reveals the mechanism of molecular exchange between telechelic micelles in solution. Telechelic molecules exhibit the same activation energy E_a for exchange as the respective monofunctional molecules, but their exchange rate constants k are generally lower and concentration-dependent. We explained these findings with a novel, collision-induced unimer exchange mechanism and the accompanying kinetic model concurs excellently with the experimental results.

Paper V uncovers the extraordinary physical integrity of self-assembled 3W62 filaments, withstanding strong thermal and acidic perturbations. There is virtually no thermally activated exchange of peptide molecules between filaments, it can only be triggered by intense mechanical agitation. In addition, molecular dynamics simulations revealed atomic details of the internal filament structure. In the course of data evaluation, we also developed a new geometrical scattering model for the filaments and found indication that, in the case of P-3W62, PEG forms a shell around the peptide filament.

4.2 Morphology of C$_n$-PEOx Micelles

As outlined in Section 1.4 on page 13, C$_n$-PEOx is an excellent model system that has been employed to study different phenomena in polymeric micelles. So far, C$_n$-PEOx micelles were pictured as a spherical core-shell structure, consisting of a segregated, solvent-free and homogeneous alkyl core and an extended, star-like PEO corona.[99, 100] While the corona, formed by long PEO polymer chains, adheres to classical polymer scaling theory, Zinn et al. claimed that the aggregation behavior was dictated by the relatively short alkyl blocks, leading to a surfactant-like $N_{\mathrm{agg}} \propto n^2$ scaling law.[100] Furthermore, it was discovered that the micellar cores exhibit a phase transition at a block-length-dependent temperature T_m. At this point, the core density shows a discrete step

as evidenced indirectly in SAXS curves and via direct density measurements [108] and, at the same temperature, DSC traces exhibit a clear endothermic transition.[77, 108] In addition, the alkyl NMR lines broaden beyond recognition below T_m.[107] All these experimental findings led to the conclusion that the alkyl blocks crystallize in the low-temperature phase while they are liquid-like above T_m. During the peer review of Paper III, one reviewer raised the question whether the phase transition was not actual crystallization but rather a glass transition or some other kind of solidification. However, the shape of the DSC traces clearly excludes a glass transition and alkanes under regular conditions generally do not form glasses. Even theoretically derived values for T_g are in the range of $120 - 130$ K [250], while the observed transition temperatures of C_n-PEOx are quite close to the bulk alkane crystallization temperatures [86] and the difference can be described by a simple Gibbs-Thomson behavior resulting from spatial confinement.[108] Nonetheless it is difficult to imagine the state of the alkyl blocks within the micellar core as crystalline in a classical sense because the maximum domain size is very small. It is constrained by the micellar core radius R_c. So what kind of crystalline phase do the hydrocarbon chains adopt? And how does that affect the micellar morphology?

4.2.1 Core Crystallization

The most common experimental techniques to investigate crystallinity are X-ray diffraction (XRD) and wide-angle X-ray scattering (WAXS).[2] For instance, the group of Dujin Wang employed XRD to characterize the crystalline phase of alkanes confined in micrometer-sized capsules.[81, 251] Yin et al. used the same technique to prove that the PE cores of polyethylene-poly(N,N-dimethylacrylamide) (PE-PDMA) micelles in water crystallize.[78, 252] In the case of C_n-PEOx micelles, though, diffraction experiments are difficult. The micellar cores constitute only a small fraction of the whole micelle, in the order of 10 vol%, rendering the scattering signal inevitably weak. That also implies that the cores are very small, only a few nanometer in diameter, giving rise to pronounced Scherrer broadening [73] of the Bragg reflections. The principal diffraction signal of the normal n-alkane orthorhombic crystal lattice is the (110) reflection at $Q = 1.5$ Å^{-1}.[253] With an X-ray wavelength of $\lambda = 1$ Å and typical micellar core diameters $d \lesssim 50$ Å, the Scherrer Equation (1.7) on page 10 yields $\Delta(2\theta)/(2\theta) > 0.08$. To make things worse, the alkyl core crystallizes only partially, which further reduces the chances of a fruitful WAXS/XRD experiment. As reported in Paper I, we carried out WAXS measurements regardless and exemplary data are plotted in Figure 4.3. Surprisingly, the curves reveal a relatively sharp feature at $Q = 1.5$ Å that vanishes above the melting temperature, corresponding to the aforementioned characteristic (110) reflection. Unfortunately, the second-most notable (200) reflection, which served as confirmation of crystal formation in the works of Yin et al. [78] and Fu et al. [251], was not resolvable in our experimental data. Though maybe not

---

[2] The exact distinction between these two techniques is often unclear.
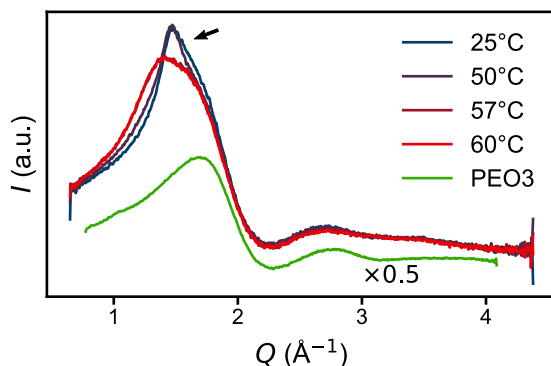
Figure 4.3: WAXS curves of C_{28}-PEO3 at $5\,\text{vol}\%$ and PEO3 homopolymer as a reference. The sharp feature at $Q = 1.5\,\text{Å}^{-1}$ vanishes above the melting temperature, $T_m = 57\,°\text{C}$. Adapted from Paper I.

ultimately convincing by itself, in the light of the other experiments discussed in the following, the WAXS experiments are still an important puzzle piece to uncover the nature of the low-temperature phase of C_n-PEOx micellar cores.

To qualitatively assess the alkyl chain dynamics, we performed ^{1}H NMR experiments (Paper I). Such experiments were employed before by Heatley et al. [107] who also investigated C_n-PEOx micelles, with $n = 12 - 21$. In samples with longer alkyl chains, namely C_{18} and C_{21}, they observed line broadening and subsequent signal loss below a certain temperature and hence deduced a liquid-solid phase transition. In our experiments, we observed the same line broadening beyond recognition as obvious in Figure 4.4. Compared to the very narrow alkyl signals in CDCl$_3$, a common solvent for both blocks, the lines are already slightly broadened in D$_2$O at elevated temperatures, because micellization restricts the alkyl mobility even though they are still liquid-like. This agrees with the findings of Ortony et al. who investigated the internal dynamics of an n-alkyl-functionalized peptide that self-assembled into nanofibers and found the alkyl blocks buried in the fiber core to have a reduced rotational diffusion rate compared to fully liquid n-alkanes in the melt.[254] But below the melting point, $T_m = 29\,°\text{C}$ in case of C_{22}-dPEO5, the characteristic alkyl signals are lost completely due to core crystallization.

Yet, to gain more quantitative insight into the alkyl dynamics, we carried out different ^{13}C magic-angle-spinning solid-state NMR experiments (Paper I). The spectra clearly revealed liquid-like PEO chains at all examined temperatures. Though, we also observed a small PEO signal that indicated some anisotropic bond reorientation which is interesting for the matter discussed in Section 4.2.3 on page 74. Below the melting temperature, the alkyl chains mostly adopt an all-trans conformation — with some disorder caused by the spatial confinement
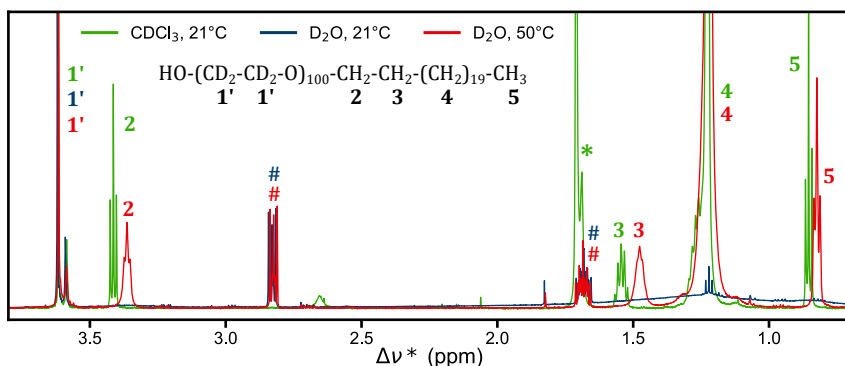
Figure 4.4: NMR spectra of C_{22}-dPEO in $CDCl_3$ and D_2O. The D_2O spectra were shifted and scaled so that the residual hPEO signals (**1'**) overlap with the $CDCl_3$ spectrum. ***** originates from residual H_2O, and **#** and **#** are unknown impurities. Adapted from Paper I.
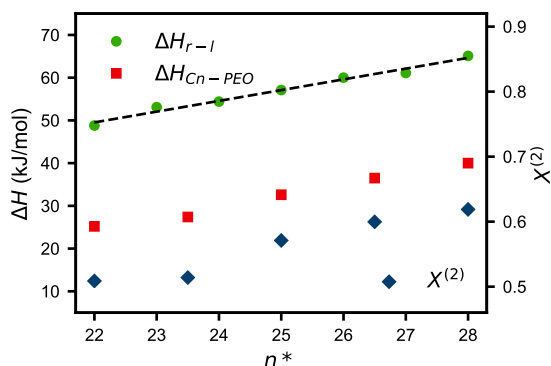
Figure 4.5: Rotator-liquid transition enthalpy of bulk alkanes [86] and C_n-PEO5 (mixed) micelles. The crystallinity of micellar cores $X^{(2)}$ was calculated as the ratio of the two enthalpies. For mixed micelles with average alkyl block length n^*, the bulk values were interpolated (black dashed line).

and tethering to the solvated PEO blocks. They also exhibit very slow relaxation and bond orientation rates, which in summary with the other results presented above points towards a rotator-like phase below the transition temperature.

That explains why there is only a single transition peak in the DSC traces of C_n-PEOx micelles (Papers II and III) while bulk alkanes typically exhibit two transitions — compare Figure 1.5 on page 12. The latter crystallize at

low temperatures, usually in an orthorhombic lattice, and with increasing temperature adopt rotator phases before they actually melt. In C$_n$-PEOx micelles, though, the alkyl blocks apparently never fully solidify. Due to spatial confinement in the micellar core and conjugation with the coronal PEO blocks, they only assume a rotator-like phase. To which degree this phase is adopted, is rather broadly distributed in the literature. Reported crystallinities of C$_n$-PEOx micelles range from 30 % [77] up to 80 % [100]. In Paper II, we reported degrees of crystallinity between $30-45$ % and $50-60$ %, depending on how they were calculated. Taking the complete transition enthalpy of bulk alkanes, from the fully crystalline phase to the liquid state, as a reference, i.e., both the transition enthalpy from crystalline to rotator phase $\Delta H_{\text{c-r}}$ and the rotator-liquid transition enthalpy $\Delta H_{\text{r-l}}$ [86],

$$X^{(1)} = \frac{\Delta H_{\text{Cn-PEO}}}{\Delta H_{\text{c-r}} + \Delta H_{\text{r-l}}}, \qquad (4.1)$$

one ends up with a degree of crystallinity $X^{(1)} = 30-45$ %. However, from the results discussed above, we know that the alkyl cores do not fully crystallize but only adopt a rotator-like phase, so the appropriate crystallinity is

$$X^{(2)} = \frac{\Delta H_{\text{Cn-PEO}}}{\Delta H_{\text{r-l}}}, \qquad (4.2)$$

which yields $X^{(2)} = 50-60$ % for mixed micelles with mean alkyl length $n^* = 22 - 28$ as shown in Figure 4.5. This is relatively high compared to values reported for PE-PDMA micelles (30 % [78]) or PE-PEO micelles (35 % [79]).

Even if the alkyl chains only partially adopt an ordered state, it remains an open question how predominantly all-trans hydrocarbons can fit in a spherical core. In principle, an "ordered hydrocarbon core" in amphiphile micelles was already predicted by Tanford.[18] A more detailed model for star-like polymer micelles with crystalline cores was later proposed by Vilgis and Halperin — compare Figure 1.4 on page 9 — and their scaling analysis produced the same scaling laws as for non-crystalline micelles.[62] A particular feature of that model is that the corona remains approximately spherical, despite the disk-like/cylindrical core shape. From an experimental point of view, though, it is not trivial to examine the shape of the micellar core. In most structural characterization techniques, the corona dominates the experimental data. For instance, we tried cryogenic transmission electron microscopy (cryoTEM), but to no avail. The contrast between alkyl core and PEO corona was too low. Yet, this is a typical example where SANS can play out its trumps. We synthesized C$_{28}$-hdPEO5 where the isotopic composition of hdPEO ensured it was matched out in D$_2$O (Paper I). Thus, the scattering signal originated predominantly from the alkyl core, enabling us to examine its shape. Although H/D isotopical substitution can alter polymer characteristics [255, 256], we never observed any significant differences between C$_n$-hPEOx and -dPEOx as shown in Paper II and References [100, 105]. Somewhat unsurprisingly, the SANS data with contrast-matched corona could not be fitted with the established spherical core-shell model
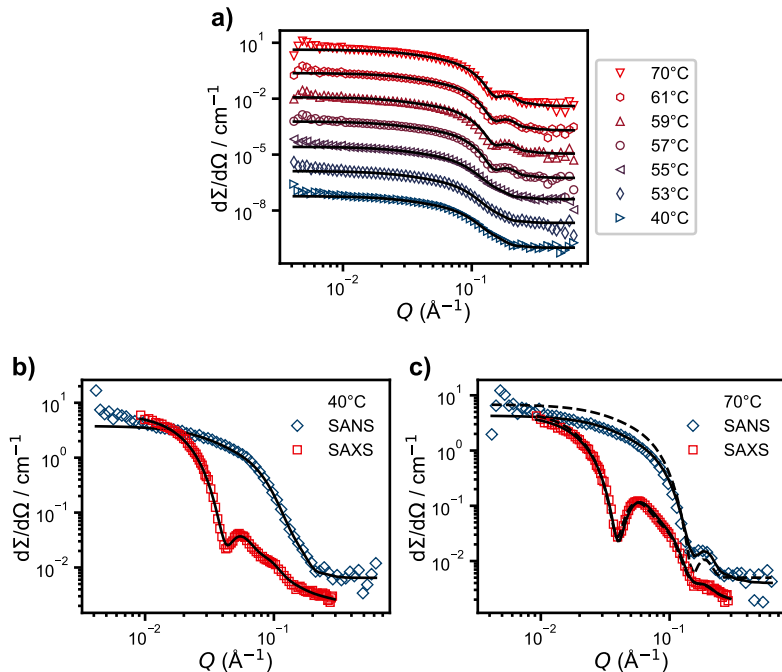
Figure 4.6: SANS and SAXS data of C_{28}-hdPEO5 in D_2O. Black lines are model fits using the elliptical core-shell model. Subplot a) shows SANS curves around the melting transition. The lowest- and highest-temperature data were fitted simultaneously with corresponding SAXS data as shown in subplots b) and c). In subplot c), a fit using the conventional spherical core-shell model is depicted as dashed black line. Adapted from Paper I.

which is described in Paper II. In a first attempt, we considered if the reason was core size polydispersity, even though we could fit all previous SAS data without applying polydispersity. To fit the core-contrast SANS data, unrealistically large variances in the aggregation number were necessary ($\Delta N_{\mathrm{agg}}/N_{\mathrm{agg}} \approx 0.5$), so we discarded that idea. Instead, we developed a new scattering model, described in Paper I, inspired by the Vilgis and Halperin model. The original scaling model assumes a disk-like shape, but considering the influence of the solvated PEO blocks, interfacial area minimization and molecular disorder evidenced by broadened ^{13}C NMR signals and reduced crystallinity, we chose an ellipsoidal core shape.[3] In the new model, the homogeneous, ellipsoidal core is surrounded by a classical star-like corona of constant thickness D. Therefore, if $D \gg R_{\mathrm{c}}$, the overall micelle still appears spherical — compare Figure I.1 in Paper I. We

---

[3]The difference between the characteristic scattering patterns of a disk and an ellipsoid is anyhow barely discernible in SAS.

also had to incorporate a thin layer of dehydrated PEO which will be discussed in Section 4.2.3. The resulting fits are shown in Figure 4.6. Obviously, the new ellipsoidal core-shell model can simultaneously fit regular contrast conditions, ensuring consistency with previous studies, as exemplarily shown in Figure 4.6b) and c). This is also reflected in the fit parameters, which excellently agree with previously reported values. In the crystalline phase, best fits were obtained with $\epsilon \approx 0.5$, which denotes the ratio between polar and equatorial core radius. Thus, the core shape is that of an oblate ellipsoid of revolution. In the center, the core thickness is about $2\epsilon R_c \approx 36$ Å. According to Tanford [18], the length of an all-trans n-alkyl chain is $l \approx (1.5 + 1.265(n - 1))$Å, which for C$_{28}$ yields 36 Å, perfectly fitting with the core thickness.

The fact that (partially) crystalline solvophobic blocks lead to anisotropic core shapes is well-documented in the literature. For instance, Zhang et al. investigated poly(ϵ-caprolactone) confined in a cross-linked poly(acrylic acid) shell.[257] By studying these nanoparticles deposited on mica surfaces with atomic force microscopy (AFM) as well as in solution with dynamic light scattering (DLS), they found spherical shapes above the melting point and an ellipsoidal or disk-like shape when the cores were crystalline. Similarly, the group around Fang-Ming Zhu characterized polyethylene-poly(ethylene oxide) (PE-PEO) and polypropylene-poly(ethylene oxide) (PP-PEO) micelles in DMF with transmission electron microscopy (TEM) and AFM and found platelet-shaped cores when the PE and PP blocks crystallized.[79, 258] Instead of using temperature to induce crystallization, Agrawal et al. chose a different approach: They synthesized polylactide-poly(ethylene oxide)-polylactide (PLA-PEO-PLA) in two versions: one with an optically "pure" poly(L-lactide) (PLLA) block and one with racemically mixed poly(L/D-lactide) (PRLA).[259] As evidenced by contrast-variation SANS, both copolymers dispersed in water assembled into micelles but the amorphous PRLA blocks formed spherical cores while the crystalline PLLA blocks formed disk-like cores. In a similar fashion, Yin et al. compared polyethylene-poly(*N*,*N*-dimethylacrylamide) (PE-PDMA) and poly(ethylene-*alt*-propylene)-poly(*N*,*N*-dimethylacrylamide) (PEP-PDMA) micelles in water.[78, 252] TEM and SANS experiments revealed spherical cores formed by the amorphous PEP blocks whereas (partially) crystalline PE chains forced the micellar core into an oblate-ellipsoidal shape.

Interestingly, all these publications report spherical core shapes above the respective melting temperature. In the case of C$_{28}$-hdPEO5, however, the SANS curves of the liquid-like phase can still not be reproduced by the conventional spherical core-shell model — see the dashed black line in Figure 4.6c). Even though less pronounced, the core apparently retains some asphericity: The SANS fits yield $\epsilon \approx 0.7$. This result concurs with NMR experiments reported in Paper I, where we found a finite order parameter $S_{CH} \approx 0.02$ in the liquid-like phase. This residual order parameter pointed towards some molecular order and/or asymmetry in the micellar core above the melting point. But why does the core not become spherical to minimize the core-corona interface area? Schmitt et al. postulate that core block polydispersity can favor aspherical shapes [260], but the C$_{28}$ chains are strictly monodisperse. Yet, they are considerably shorter than

the polymer blocks in the studies cited above.[78, 79, 252, 257–259] Therefore, we relate the retained anisotropy to the residual rigidity of the alkyl blocks in the liquid-like phase. Due to their shortness, the C_{28} chains are not as flexible as longer polymer blocks and cannot fill a spherical core volume as effectively. Concurringly, by using Brownian molecular dynamics simulations, Lin et al. found a gradual transition from spherical to disk-like micelles when the core block rigidity was increased.[261] Also the coarse-grained molecular simulations of Vuorte et al. revealed a slight anisotropy in amorphous C_{18}-PEOx micellar cores, which might become more pronounced with longer alkyl chains.[103]

On the other hand, core crystallization does not always lead to an anisotropic shape. For example, Sevgen et al. reported atomistic simulations of oligo(ethylene sulfide)-poly(ethylene glycol) (OES-PEG) micelles which maintained their spherical shape, despite partial crystallization of the OES blocks.[262] Other researchers observed the opposite effect, that the micellar morphology was completely changed to wormlike micelles upon core block crystallization [66, 252, 263, 264], which might even lead to precipitation [265]. Thus, possible effects of core crystallization on the micellar shape are manifold.

But not only does crystallization of the core block affect the micellar shape, the micelle geometry also affects the crystallization inside the core. Most notably, the spatial confinement leads to a suppression of the melting point. As the surface-to-volume ratio is greatly increased compared to bulk samples, surface effects emerge. Since the interaction between the solid core phase and the solvent/PEO phase is less favorable than the interaction between the liquid core phase and the solvent/PEO phase, the equilibrium is shifted towards the liquid core phase, so that the melting temperature decreases. The effect can be decribed by the generalized Gibbs-Thomson equation [84, 85], introduced earlier in Section 1.3.2 — compare Equation (1.8) on page 11. Both in Paper II and a previous publication [108], we found a very good agreement of the melting point depression in C_n-PEOx micellar cores with the Gibbs-Thomson law. However, in the light of the results from Paper I, the spherical geometry assumed in Paper II and Reference [108], and therefore the applied confinement radius R_c, are not strictly true. In a spherical core, the geometry factor is

$$\left.\frac{\partial S}{\partial V}\right|_{\text{sphere}} = \frac{2}{R_c}. \tag{4.3}$$

In an oblate ellipsoid with volume $V_{\text{ellipsoid}} = 4\pi/3\, \epsilon R_c^3$ and surface $S_{\text{ellipsoid}} \approx 2\pi R_c^2(1 + \epsilon^2)$, on the other hand, the geometry factor becomes

$$\left.\frac{\partial S}{\partial V}\right|_{\text{ellipsoid}} \approx \frac{1 + \epsilon^2}{\epsilon}\frac{1}{R_c}, \tag{4.4}$$

which for $\epsilon \neq 1$ is larger than $2/R_c$. Therefore, the interfacial tension γ of the core-corona interface was slightly overestimated in Paper II, where we reported $\gamma \approx 8\,\text{mN/m}$. In any case, the value is much lower than literature values for the interfacial tension between alkanes and water, which range around

50 mN/m.[97, 266, 267] Considering another finding of Paper I, though, this discrepancy makes sense. We found that there is a thin layer of dehydrated PEO in the immediate vicinity of the core, which will be discussed in Section 4.2.3. Therefore, the relevant interfacial tension might actually rather be that between alkanes and PEO. Roe measured $\gamma_{\text{PE-PEO}}$ with the pendant-drop technique, using branched PE (7 kg/mol) and linear PEO (6 kg/mol), at high temperatures (110 – 190 °C).[268] He found a linear temperature dependence,

$$\gamma_{\text{PE-PEO}}(\text{mN/m}) = 9.5 - 0.016\,[150 - T(^{\circ}\text{C})]\,, \tag{4.5}$$

which at 20 °C gives $\gamma_{\text{PE-PEO}} = 11.6$ mN/m. Gaines and Gaines later investigated the interfacial tension between n-alkanes and PEO with the same method at 20 °C, systematically varying the molecular weight.[269] They used alkanes with 7 to 16 carbons atoms and PEO molecular weights between 100 and 400 g/mol and found a $\gamma_{\text{alkane-PEO}} \propto \text{MW}^{-2/3}$ scaling law:

$$\gamma_{\text{alkane-PEO}}(\text{mN/m}) = 10.4 - 98.3\,\text{MW}_{\text{alkane}}^{-2/3} + 106.3\,\text{MW}_{\text{PEO}}^{-2/3}. \tag{4.6}$$

For example, this yields $\gamma_{\text{C28-PEO5}} = 8.9$ mN/m for C$_{28}$-PEO5 with MW$_{\text{C28}} = 394$ g/mol and MW$_{\text{PEO}} = 5000$ g/mol. These results are very close to the interfacial tension between core and corona in C$_n$-PEOx micelles determined from the Gibbs-Thomson relation. Thus, the dehydrated PEO layer, or more precisely the underlying high grafting density of PEO on the core surface, might have a significant but so far unknown impact on the micelle free energy G_{mic}, which certainly calls for a closer investigation.

4.2.2 Effect of Co-Assembly

To study the effect of core block crystallization on the molecular exchange kinetics of polymeric micelles (Section 4.3.1 on page 76 and Paper III), we wanted to tune the crystallization. To this end, it was the natural choice to vary n as both T_m and ΔH_m depend on the length of the hydrophobic block. But instead of synthesizing a range of new C$_n$-PEOx polymers, we decided to blend polymers with different n to obtain mixtures with average alkyl length n^* — in the hope that these mixtures would interpolate the properties of micelles with core block length $n = n^*$ — compare Section 1.2.3 on page 7. The first question was if mixed micelles were formed in the first place.

This is an important question because n-alkanes, which constitute the hydrophobic, core-forming block of C$_n$-PEOx, are completely miscible in the liquid phase but tend to de-mix in the crystalline phase — at least when the length mismatch is too large. As outlined in Section 1.3.3 on page 11, the corresponding mixing rules were determined by Kravchenko [86, 87]. According to his findings, crystalline alkanes with around $n \approx 20 - 30$ carbon atoms de-mix when the length mismatch is greater than $\Delta n > 4$. But in Papers II and III, we used C$_{22}$- and C$_{28}$-PEO5, because they exhibit melting points in an experimentally accessible temperature range and their exchange kinetics are on a time scale accessible with TR-SANS. That means, according to Kravchenko's mixing rules,

these alkyl groups with $\Delta n = 6$ would segregate in a crystalline bulk phase. We tried to verify this by blending n-docosane and n-octacosane and measuring melting and crystallization curves with DSC. We never obtained reproducible data, though. This was probably caused by inhomogeneous mixing which indeed signals incompatibility of the two n-alkanes in at least one of the phases.

In contrast, we obtained excellently reproducible DSC traces of C_n-PEO5 micelles. Interestingly, not only do pure micelles have just a single transition (discussed the previous section), but also the mixed micelles exhibit the same phenomenon. Density measurements yielded concurring results: As shown in Figure 2 in Paper II and Figure 1 in Paper III, there is just a single discrete step in the alkyl core density of mixed C_n-PEO5 micelles. Apparently, the alkyl groups do not segregate in the crystalline phase, despite their relatively large length mismatch. The reason is probably a confinement effect: Lamellar ordering and longitudinal diffusion, the main separation mechanisms in bulk, are suppressed under confinement. This agrees with the findings of Fu et al. who, as outlined in Section 1.3.3 on page 11, found enhanced miscibility of length-mismatched alkanes confined in micrometer-sized capsules.[251] It is noteworthy, though, that in other cases confinement can also promote de-mixing, for instance in mixtures of small molecules like methanol and water [270] or colloidal mixtures [271]. Conversely, we found not only that the blended alkyl cores remain homogeneous but also that the hydrocarbon chains crystallize and melt cooperatively.

In Section 1.2.3 on page 7, we also presented theoretical predictions for the formation of mixed micelles when polymers of different lengths are blended. Even though these works did not consider crystallization, it is still interesting to compare what they predicted for the liquid phase. According to the theory of Sens et al. [53], already a slight mismatch in core block length can prohibit formation of mixed micelles — which we can definitely exclude here because DSC and density experiments unambiguously prove mixed micelles. The theory of Borovinskii and Khokhlov [54] seems to be more applicable to C_n-PEOx micelles. They predict that with increasing overall polymer concentration, first the polymer species with longer core blocks, i.e., lower CMC, micellizes and then the short-block species is incorporated while excess molecules form separate smaller micelles. At high concentration, well above the CMC of both species, mixed micelles of equal size and composition are formed according to the theory. These predictions agree with the experiments of Renou et al. [40] who blended C_{12}- and C_{22}-PEO5. At low concentration, first C_{22}-PEO5 micelles were formed, into which C_{12}-PEO5 molecules were gradually integrated. At high concentration, they only observed mixed micelles. This is also the case in our experiments. All mixed micelle samples used for the present thesis were well above both constituents' CMC and we exclusively observed molecularly mixed micelles.

Even though mixed micelles might be the thermodynamic equilibrium structure in many cases, there are a number of reports about kinetically trapped systems. When there is no molecular exchange, the micelles are kinetically frozen, leading to non-ergodic systems where the question whether mixed micelles form depends on the sample preparation protocol. If the two species are molecularly interdispersed before micelle formation, mixed micelles are formed.
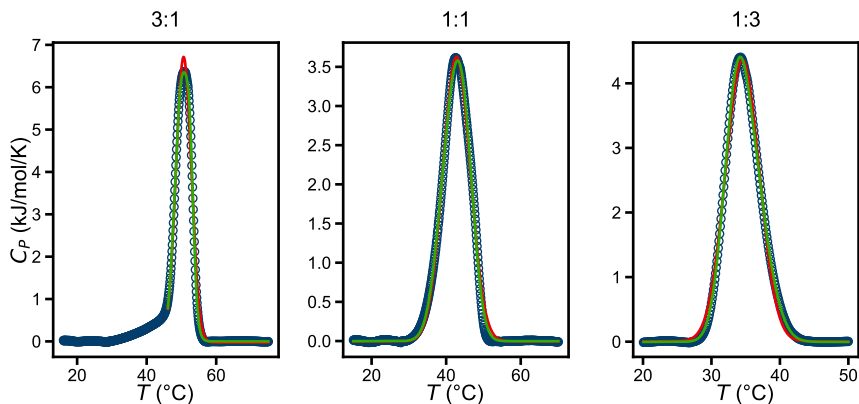
Figure 4.7: Melting curves of $C_{28/22}$-hPEO5 3:1, 1:1 and 1:3. Red lines are fits with a single Gaussian, green lines with two Gaussians (fit parameters given in Table 4.1).

	3:1	1:1	1:3
$T_{m,\text{C}28}$ (°C)	52.5	45.1	36.0
$\Delta H_{m,\text{C}28}$ (kJ/mol)	41	17	52
$T_{m,\text{C}22}$ (°C)	50.2	41.7	33.6
$\Delta H_{m,\text{C}22}$ (kJ/mol)	21	49	19

Table 4.1: Parameters of the fit with two Gaussians in Figure 4.7.

But if solutions of already micellized polymers are mixed, the populations stay separate.[153, 272, 273]

As stated above, mixed C_n-PEOx micelles exhibit a single transition peak in their DSC traces, indicating a cooperative melting/crystallization process of both constituent species. However, in Figure 2 in Paper II and Figure 1b) in Paper III, it is obvious that the transitions peaks of the mixtures are considerably broadened compared to pure micelles. Thus, one might hypothesize that the two alkyl chain species influence each other so that the individual melting points approach each other but independent melting/crystallization processes are maintained. This might be caused by partial segregation inside the micellar core. To test this hypothesis, we fitted the melting curves of $C_{28/22}$-PEO5 mixtures — shown in Figure 4.7 — with a single and a dual Gaussian function. The peaks are slightly better reproduced with the dual function, but already a single Gaussian fits the data well. The results of fitting the melting peaks with two Gaussian functions are given in Table 4.1. We assigned the Gaussian with lower T_m to C_{22}-hPEO5 and the other one to C_{28}-hPEO5. The resulting peak integrals, i.e., ΔH_m, are inconsistent, though. Therefore, the broadened peaks provide no evidence for two

71
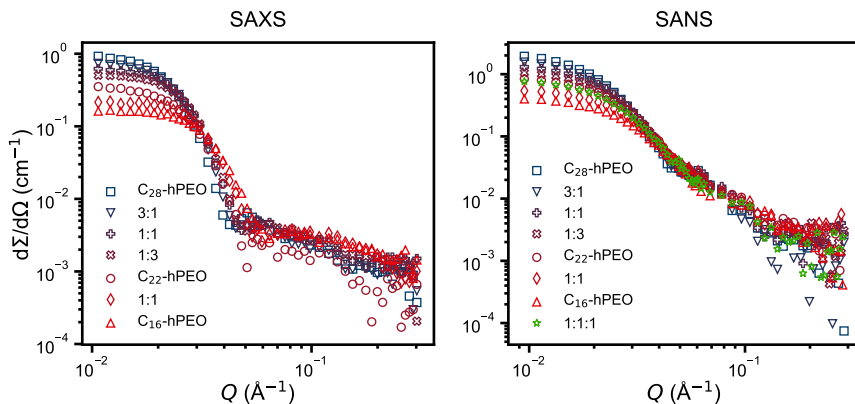
Figure 4.8: SAXS and SANS curves of C_n-hPEO5 and mixtures thereof at 25 °C.

separate melting processes. We also performed a de-mixing SANS experiment: C_{22}-hPEO5 and C_{28}-dPEO5 were blended in chloroform, a common solvent for both alkyl and PEO blocks. The homogeneously mixed polymer solution was then dried and re-dissolved in an aqueous solvent with zero-average contrast to the two PEO blocks ("PEO ZAC"). The rationale behind was that if the alkyl blocks are homogeneously mixed, also the coronal PEO chains are mixed and therefore have no scattering contrast. If the alkyl blocks in the core segregated, on the other hand, we would also expect at least a partial segregation of the isotopically labeled PEO chains and therefore an increase in scattering intensity. Yet, comparing a freshly annealed sample with a four-weeks old one revealed no difference in the scattering patterns. Taking these two results together, we conclude that the DSC peak broadening is not due to segregation inside the core but instead caused by local heterogeneities and packing restrictions.

In any case, as reported in Paper II, the melting and freezing enthalpies $\Delta H_{m/f}$ scale linearly with the mean alkyl block length n^* which is also known for neat bulk alkanes [86]. In contrast, alkane mixtures (with Δn small enough to ensure miscibility) often exhibit a lower transition enthalpy than the weighted average of the components [89, 90, 274], whereas in C_n-PEO5 the blends perfectly interpolate. Also T_m scales quasi-linearly with n^*, similar to pure alkanes of that length range [86]. In addition, the Gibbs-Thomson law reported earlier for pure micelles [108] is also valid in mixed micelles.[4] To conclude, blending C_n-PEOx polymers is a facile way to tune the crystallization of the micellar core as needed for our kinetic experiments, which are presented in Section 4.3.1 on page 76.

But how is the micellar structure affected by blending? Qualitative conclusions can already be drawn directly from the scattering curves. Figure 4.8

---

[4]We tried to separate the effects of mixing and confinement on the melting point, see the Supporting Information of Paper II, but were not successful.

shows SAXS and SANS data of C_{16}-, C_{22}- and C_{28}-hPEO5 and binary mixtures thereof, similar to Figure 1 in Paper II. The forward scattering, which depends mainly on the aggregation number N_{agg}, increases with n^*. In the SAXS curves, the principal decay shifts to lower Q with increasing n^*, indicating larger micellar radii. Obviously, the micelles become larger with increasing mean alkyl block length and the mixed micelles mimic this behavior. Notably, the mid- to high-Q scattering is similar for all n^*, so the internal structure of the micelles seems to be unaffected. The detailed analysis of these data with a geometrical scattering model (Paper II) confirms this initial assessment. Here we should note that in these analyses the core ellipticity was not taken into account. Firstly, because the core contribution in the examined contrast conditions is rather weak so that a distinction between a spherical and elliptical core shape is not possible. Secondly, the experiments of Paper II happened chronologically before those of Paper I, so during the work on the former we were not certain about the core shape yet. Anyhow, the overall corona shape is only weakly affected by the core shape and still appears approximately spherical — compare the theoretical Vilgis-Halperin model in Figure 1.4 on page 9 and the scattering model sketch in Figure I.1 in Paper I. In addition, the fit evaluation in Paper I revealed that the fit parameters of both the spherical and elliptical scattering models are commensurable. The analysis reported in Paper II yields that N_{agg}, and therewith also R_c, in mixed micelles mimics the behavior of pure micelles — though in an unexpected way which we discuss in Section 4.2.3. Also the corona of mixed micelles adheres to scaling laws expected for star-like micelles. In the SANS experiments that we did not include in Paper II, we even measured a ternary mixture of C_{16}-, C_{22}- and C_{28}-hPEO5, which is shown in Figure 4.8. While the scattering pattern coincides with that of pure C_{22}-hPEO5 as expected, the corresponding DSC melting trace was heavily broadened, more than in the binary mixtures. Nevertheless, we thus conclude that micelles consisting of mixed C_n-PEO5 polymers with mismatched alkyl chains lengths interpolate the behavior of pure micelles not only regarding their thermodynamics but also their structure. The same result was found by Renou et al. in the study cited above [40]: Micelles consisting of blended C_{12}- and C_{22}-PEO5 reproduced the behavior of pure C_n-PEO5 micelles with $n = 12 - 22$ in terms of aggregation number, hydrodynamic radius and rheological response. Also the Brownian dynamics simulations of Hafezi and Sharif yielded similar structural and dynamic properties for both mixed and pure micelles.[275] Cho et al. even reported that their branched PEO$_3$-PS copolymers with different polystyrene (PS) block lengths interpolated the packing parameter of pure polymer micelles with intermediate PS block lengths, so that a variety of micellar geometries could be reproduced by mixing two polymer species instead of using different pure polymers.[50] Another interesting example where mixed polymer micelles mimicked the behavior of pure micelles was presented by Wright et al.[276] Their core blocks were not completely hydrophobic but contained randomly distributed hydrophilic monomers. By blending two polymers with a different fraction of hydrophilic monomers in the core block, they reproduced the structure of polymers with intermediate hydrophilic fractions.

But perfect interpolation of the behavior of pure micelles is not always

the case. Newby et al. mixed Pluronics (PEO-PPO-PEO) with similar corona block lengths but different poly(propylene oxide) (PPO) lengths.[277] By using DLS, they found a larger hydrodynamic radius for the mixed micelles than for both pure micellar species. A similar effect was reported by Zhao et al. who studied poly(methyl methacrylate)-poly(n-butyl methacrylate) (PMMA-PnBMA) micelles with identical PMMA corona blocks but varying PnBMA core block lengths in an ionic liquid by DLS and SAS.[278] The mixed micelles were significantly larger than corresponding pure micelles with the same average core block length. The authors explained that finding with an optimized packing in the core, lifting the stretching penalty of the shorter block and thus allowing higher aggregation numbers. This explanation is in agreement with self-consistent field calculations of Mantha et al. which revealed that polydisperse polymers can form micelles with narrower size distributions.[51] The reason is that the different block lengths allow more effective packing in the core and thus increase the micelle stability. This phenomenon does not appear in C_n-PEOx micelles, though, because the relatively short alkyl blocks do not experience a significant stretching penalty.

4.2.3 Other

Beside answers to our primary questions about the effects of crystallization and co-assembly on the thermodynamics and structure of polymeric micelles, we also obtained interesting side results.

In the course of the study reported in Paper I, we developed a new scattering model to reproduce SANS data of C_{28}-hdPEO5 with a contrast-matched corona. To change the core shape from spherical to ellipsoidal was not sufficient to explain the data. The sample exhibited some additional scattering at intermediate scattering vectors, at higher Q than the residual characteristic contribution of the corona but lower Q than the dominant core scattering. Thus, there must have been a third scattering feature at a length scale between R_c and R_m. Already in earlier studies, Laurati et al. have not been able to fully match out the corona of PEP-PEO micelles.[279] And also in Reference [108] and Paper II, we hypothesized that the low interfacial tension obtained from the Gibbs-Thomson analysis was due to some kind of shielding of the alkyl core from the solvent by the PEO corona. Therefore, we came to the conclusion that the PEO chains partially dehydrate in the immediate vicinity of the core-corona interface, due to relatively high grafting density of PEO chains on the surface, $\sim 1.1\,\mathrm{nm}^{-2}$. And indeed, we reproduced the core-contrast SANS curves simultaneously with corresponding SAXS curves excellently by assuming a thin layer of dehydrated PEO around the core — compare Figure 4.6 on page 66. For this layer, we used the density of PEO homopolymer in the melt. In other contrast conditions, it is not visible because it is apparently very thin ($\lesssim 10\,\text{Å}$) and moreover has a low contrast against the much larger hydrated PEO corona. Only when the latter is (almost) matched out, the dehydrated layer becomes visible. The additional shell also explains the weak CP signal of PEO in the ^{13}C NMR spectra shown in Figure I.4 in Paper I, which arises from anisotropic
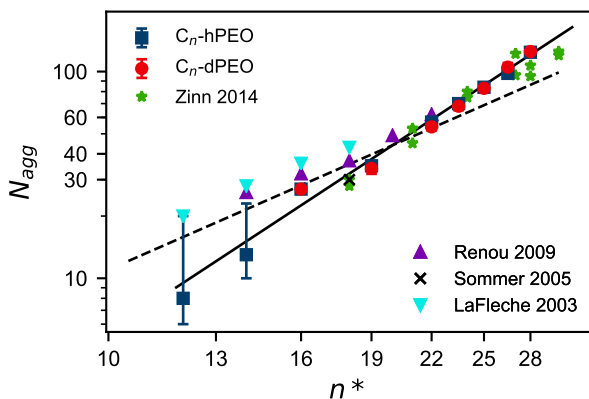
Figure 4.9: Aggregation number of C$_n$-PEO5 micelles as a function of the mean alkyl block length. Data taken from Paper II and References [40, 98–100]. The dashed line corresponds to $N_{agg} \propto n^2$, the solid line to $N_{agg} \propto n^3$. Reprinted with permission from Paper II. Copyright © 2019 The Royal Society of Chemistry.

reorientation of a small fraction of the PEO blocks. To our knowledge, this phenomenon so far has only been found in polymer-functionalized nanoparticles with very high grafting densities.[280, 281] The molecular dynamics simulations of Dahal et al. reproduced those experimental findings but also predict thin layers of dehydrated polymer at lower grafting densities.[282] Our results thus represent the first experimental evidence of this phenomenon at moderate grafting density in polymeric micelles.

Upon closer inspection of our structural data of mixed and pure C$_n$-PEO5 micelles (Paper II), we stumbled across an unexpected relation between the aggregation number N_{agg} and the alkyl block length n. In a previous work, Zinn et al. compared the aggregation numbers of C$_n$-PEOx with varying n from several publications — see Figure 3 in Reference [100]. Instead of the $N_{agg} \propto n^{4/5}$ scaling law expected for star-like micelles, the data rather agreed with a $N_{agg} \propto n^2$ relation which is known from surfactant systems. Yet, when inspecting the data more closely and also including the data from Paper II, they in fact rather adhere to a $N_{agg} \propto n^3$ scaling law as shown in Figure 4.9. The trend seems clear for $n \gtrsim 19$, but the literature data for smaller n agree more with the conventional $N_{agg} \propto n^2$ scaling law. However, also in the results of Renou et al. [40], it looks like there was a transition from $N_{agg} \propto n^2$ to $N_{agg} \propto n^3$ around $n \approx 19$. To shine more light on the issue, we also measured SAXS curves of C$_{12}$- and C$_{14}$-PEO5. At first glance, the fit results seem to support the $N_{agg} \propto n^3$ relation. But the CMC of these polymers is much higher, already in the range of the concentrations used throughout this thesis. Therefore, the fit model was amended to also account for unimeric polymer molecules but

the problem was that the fit parameters CMC and N_{agg} are strongly correlated, leading to a large uncertainty in N_{agg} as shown with the error bars in Figure 4.9. Thus, we cannot rule out a transition from $N_{\mathrm{agg}} \propto n^2$ to $N_{\mathrm{agg}} \propto n^3$ around $n \approx 19$. Interestingly, $n \approx 19$ is also the range where core crystallization emerges. But the existing scaling theory of crystalline micelles (Section 1.3 on page 9 and Reference [62]) does not predict such a scaling behavior and also our own attempts in a theoretical treatment were not fruitful (Supporting Information of Paper II). Thus the explanation of the novel $N_{\mathrm{agg}} \propto n^3$ scaling relation remains an open issue. It might be related to the elliptical core shape or the dehydrated PEO layer that affects the core-corona interaction.

4.3 Exchange Kinetics of Polymeric Micelles

Although the theory of molecular exchange in polymeric micelles (Section 1.5.1 on page 14 and Reference [115]) is already 30 years old, it took a long time before its definite experimental confirmation. As outlined in detail in Section 1.5.2 on page 15, this was mainly due to inherent polymer polydispersity and lack of suitable experimental techniques. When KZAC TR-SANS experiments were added to the picture [133], the first experiments agreed with the theory but could not be seen as definite proof because the data were still heavily obstructed by polydispersity [135, 136]. The final breakthrough came with the introduction of C_n-PEOx micelles with truly monodisperse core blocks.[105] Also in the work comprised by the present thesis, especially in Paper III, the Halperin and Alexander theory [115] was confirmed.

4.3.1 Effect of Crystallization

We aimed to investigate the effect of core crystallization on the exchange kinetics of polymeric micelles by tuning the crystallization of C_n-PEO5 alkyl blocks through co-assembly with different block lengths. As described in the previous section, C_n-PEO5 polymers form mixed micelles which mimic the behavior of their pure counterparts, both in terms of structure and thermodynamics, which offers a facile way to tune core crystallization in these micelles. So how does crystallization of the alkyl blocks affect the molecular exchange? In principle, there are two conceivable mechanisms possible: The exchange rates depend exponentially on n and thus molecules with different alkyl length exchange on very different timescales. But we showed in the previous section that crystallization in the micellar core is a cooperative process — hence, either the co-crystallization also confers a mutual exchange rate for both polymer species in mixed micelles or the exchange of the constituent species remains independent, although they crystallize cooperatively. Of course, anything in between these two extremes is possible as well. In the light of the "independent chain hypothesis" proposed by Lu et al. [146, 147], however, independent exchange is the most probable scenario.

Kastantin et al. partially shed light on the effect of crystallization on molecular exchange.[60] They investigated micelles formed from a phospholipid-

polymer conjugate, 1,2-distearoyl-*sn*-glycero-3-phosphoethanolamine-*N*-methoxy(poly(ethylene glycol)) (DSPE-PEG), a promising candidate for drug delivery applications. The lipid core of these micelles exhibits a solid-liquid phase transition at 12 °C as evidenced by DSC and the transition enthalpy accounts to about 40 kJ/mol. The authors described the solid phase as "glassy" because they observed no clear WAXS signal but, on the other hand, they did not rule out some kind of local order. They employed fluorescence quenching to monitor the molecular exchange between micelles at temperatures above and below the transition temperature and, via an Arrhenius analysis, they determined the activation energy of molecular exchange to be 160 kJ/mol in the solid phase and 80 kJ/mol in the liquid phase. The difference can partly be explained by the transition enthalpy between the two phases but that only accounts for half of it. The authors ascribed the missing energy to the fact that, in the solid phase, the reorganization of the remaining molecules after expulsion of one molecule from a micellar core is much slower than in the liquid phase, which can lead to a thermodynamically unfavorable transition state. Unfortunately, they did not address the influence of the fluorescent label on the phase transition and the molecular exchange.

Furthermore, the interplay of exchange kinetics and crystallization was treated by our group in a TR-SANS study reported in Reference [61]. In that study, the exchange kinetics of C_n-PEO5 micelles with $n = 21 - 30$ was investigated, but unfortunately only below the melting point because the exchange process became too fast in the liquid phase. By assuming a simple additivity of the activation energies,

$$E_a = E_a^0 + \Delta H, \tag{4.7}$$

where E_a is the activation energy in the solid phase and E_a^0 the activation energy in the liquid phase, interesting results on the entropic contributions to the exchange rate k were obtained. Yet, experimental proof of Equation (4.7) was missing.

With an improved experimental setup, we were now able to also measure the exchange rates of C_n-PEO5 micelles above the melting point of the hydrocarbon core (Paper III). In addition, we blended C_n-PEO5 molecules of different alkyl block lengths to tune the mutual melting temperature. In the previous section, we showed that crystallization is a cooperative process in the micellar core. So how does it affect the molecular exchange, which in the liquid phase is independent? Figure 4.10 shows experimental relaxation functions $R(t)$ of C_{28}- and C_{22}-PEO5 and a 1:1 mixture of those. Obviously, the mixed micelles exhibit two separate exchange processes, both below and above the melting point ($T_m \approx 43$ °C) — also compare Figure 2 in Paper III and Figure S3 in the accompanying Supporting Information. Thus, although the different alkyl groups form mixed micellar cores and crystallize cooperatively, their respective exchange kinetics are still decoupled and the "independent chain hypothesis" [146, 147] also holds in the crystalline phase.

Figure 4.11 shows an Arrhenius plot of the exchange rates of these three samples. Clearly, the exchange rates of C_{28}-PEO5 and C_{22}-PEO5 are identical
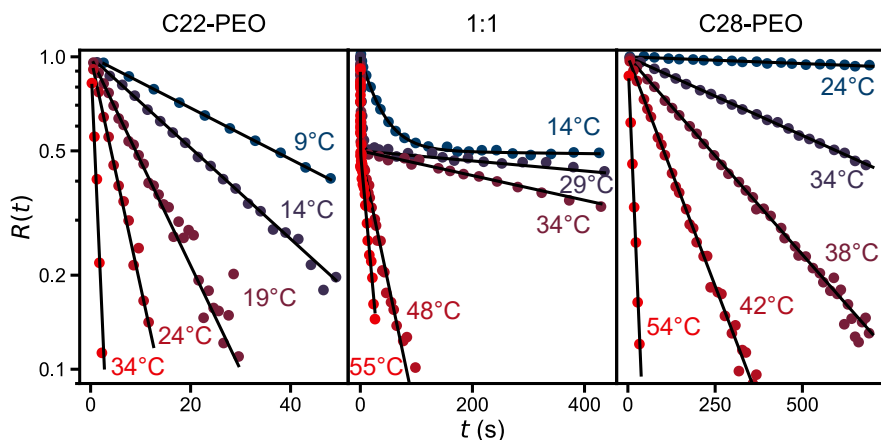
Figure 4.10: Experimental relaxation functions and exponential fits of C_{22}-PEO5, $C_{28/22}$-PEO5 1:1 and C_{28}-PEO5 at various temperatures. Adapted with permission from Paper III. Copyright © 2019 American Physical Society.
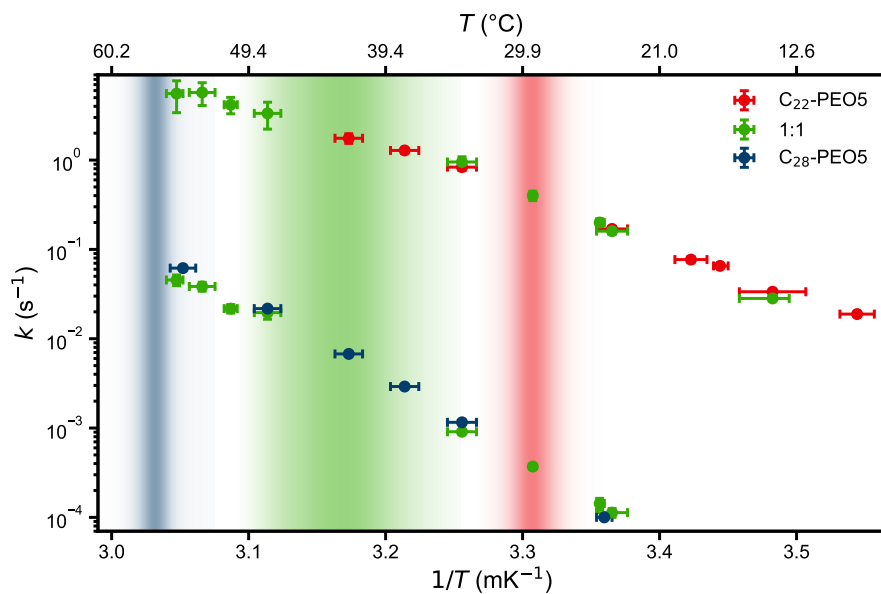

Figure 4.11: Arrhenius plot of the temperature-dependent exchange rate constants of C_{22}-PEO5, $C_{28/22}$-PEO5 1:1 and C_{28}-PEO5. The colored shades are contour plots of the respective nanoDSC melting curves and thus separate the respective liquid and crystalline regimes.
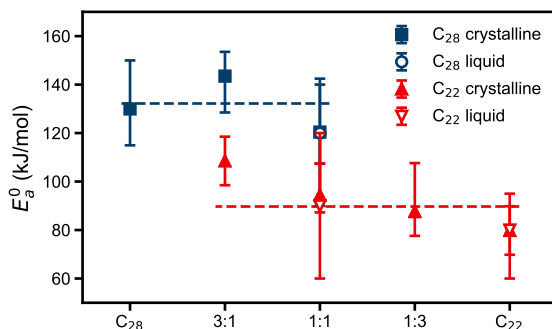
Figure 4.12: Activation energies of the chain expulsion step of C_{28}- and C_{22}-PEO5 in various mixtures. Adapted with permission from Paper III. Copyright © 2019 American Physical Society.

both in pure and mixed micelles, further confirming the "independent chain hypothesis". What becomes not as clear in Figure 4.11, though, is that the activation energy of both polymer species is different above and below the respective melting transition indicated by the colored shades. This becomes more clear in the fits shown in Figure 3 in Paper III and Figure S4 in the accompanying Supporting Information. The slope in the Arrhenius representation markedly changes at the melting temperature. For pure C_{22}-PEO5, this was straightforward to achieve because of its convenient melting point, $T_m \approx 29\,°C$. But the melting point of pure C_{28}-PEO5 is too high, $T_m \approx 57\,°C$, so we could not measure the exchange rate above the transition temperature. However, by blending both species, the mutual melting point was reduced to $T_m \approx 43\,°C$ so that the exchange kinetics of liquid-like C_{28}-PEO5 became experimentally accessible, proving the value of the blending approach. Very interestingly, the difference in activation energy between the crystalline and liquid-like phase exactly accounts to the transition enthalpy ΔH which we independently determined from DSC, confirming Equation (4.7). This is in agreement with Reference [104], where Zinn et al. measured the rheological relaxation rate k_{rheo} of C_{22}-PEO10-C_{22} telechelic hydrogels. In the crystalline phase, the activation energy determined from k_{rheo} was about $100\,\mathrm{kJ/mol}$ and, above the melting point of the C_{22} cores, is was approximately $70\,\mathrm{kJ/mol}$, which concurred well with the independently measured melting enthalpy of $26-29\,\mathrm{kJ/mol}$.

The activation energies of C_{28}- and C_{22}-PEO5 in different blending ratios are plotted in Figure 4.12. Here, the values from the crystalline regime have been corrected for the transition enthalpy from the DSC measurements, $E_a^0 = E_a - \Delta H$. With this correction, the activation energies in the crystalline and liquid-like regime clearly coincide and are independent of the blending ratio. The same picture was obtained for the respective time constants τ_0 — compare Figure S5 in the Supporting Information of Paper III. We therefore conclude that the
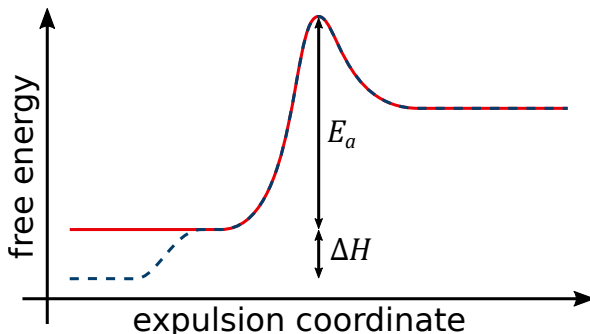
Figure 4.13: Comparison of the energy landscape of the expulsion step in molecular exchange: the conventional picture in amorphous micelles and the newly proposed picture in crystalline micelles.

cooperative crystallization infers a mutual energy penalty on the otherwise independent exchange processes and propose an amended free energy landscape of the expulsion step as sketched in Figure 4.13 — compare Figure 1.6 on page 14 for the traditional picture. Apparently, co-assembly has no effect on the activation energy E_a^0 of molecular exchange in the liquid-like phase. It solely depends on the additional hydrophobic surface created upon chain expulsion, namely the block length n and the interfacial tension γ. As the latter is similar for longer alkanes like C_{22} and C_{28}, the co-assembly has no effect. Nevertheless, we expect modified activation energies if chemically dissimilar components are blended. Still, in the crystalline regime, the individual E_a^0 is increased by the mutual ΔH, which depends on the composition and hence represents a handy tool to fine-tune the exchange kinetics of polymeric micelles for desired applications.

Admittedly, our conclusion after all relies on three points in Figure 4.12 only. For the 3:1 and 1:3 mixtures, we were not able to measure activation energies in both regimes. In addition, the data points have relatively large experimental uncertainties, due to temperature instabilities, limited temporal resolution and uncertainties in the $I(0)$ and $I(\infty)$ reference values — see Section 3.1.5 on page 47. In addition, the activation energies of C_{22}-PEO5 seem to increase when more C_{28}-PEO5 is added to the blend. Nevertheless, we do not believe that this a direct consequence of the co-assembly but rather an indirect effect of the increasing aggregation number at higher n^*. Zhao et al. prepared micelles of different sizes from the exact same polymer, by different preparation protocols.[140] They observed a decelerated exchange of molecules in the larger micelles, explained by the higher grafting density of corona chains on the core surface at higher aggregation numbers, which hinders core block expulsion. This effect also explains why the C_{22}-PEO5 activation energy increases with increasing C_{28}-PEO5 content: simply because the micelles become larger and the corona thus denser. For C_{28}-PEO5, the effect is probably concealed by the experimental uncertainty. In fact, a similar trend has already been observed by Zinn et al. in

C$_{27}$-PEOx micelles with varying PEO length.[106] With increasing MW, the aggregation number decreased and there was also a (slight) concurrent reduction in the activation energy. Hence, the grafting density on the core-corona interface might be a more relevant parameter than assumed so far — in accord with our investigation of the dehydrated PEO layer in Section 4.2.3 on page 74.

To increase confidence in the experimental E_a values, one could repeat these experiments at the actual ZAC conditions. As explained at the end of Section 3.1.5, we used the ZAC of the hPEO and dPEO blocks instead of the overall ZAC of C$_n$-hPEO and -dPEO. That way we could use the same solvent for all samples which greatly simplified experimental protocols. On the other hand, the overall ZAC would yield a larger contrast between $I(0)$ and $I(\infty)$ which potentially could yield more significant kinetic data. In addition, one could attempt a simultaneous fit of all relaxation curves at the different temperatures like in Paper IV and thereby further increase the fit reliability.

4.3.2 Telechelic Micelles

As outlined in Section 1.5.3 on page 19, the polymer architecture has tremendous effects on the behavior of polymeric micelles. Zinn et al. previously reported on the structure [102] and rheology [104] of telechelic C$_n$-PEO2x-C$_n$ micelles in aqueous solution, where they blended mono- and difunctional polymers to stabilize the micelles. The nomenclature was presented in Section 2.2 on page 33. For example, C28F40 denotes a mixture of 40 vol% C$_{28}$-PEO10-C$_{28}$ and 60 vol% C$_{28}$-PEO5. In Reference [102], Zinn et al. reported that micelles containing C$_n$-PEO10-C$_n$ polymers primarily form clusters for $n \leq 22$ but are flower-like for $n = 28$. The reason is a delicate balance the enthalpic gain ΔH_{Cn} of burying an alkyl group in the micellar core and the entropic penalty ΔS_{bend} for petal-like bending the PEO backbone. When $\Delta H_{\mathrm{Cn}} \gg \Delta S_{\mathrm{bend}}$, the alkyl groups are firmly attached to a micellar core and flower-like micelles dominate. But in the opposite case, $\Delta H_{\mathrm{Cn}} \lesssim \Delta S_{\mathrm{bend}}$, freely dangling alkyl ends can occur, allowing cluster formation.

According to the classical transient network theory by Tanaka and Edwards [181], the macroscopically observable, rheological relaxation rate k_{rheo} corresponds to the microscopic exchange rate k_{exch} of hydrophobic groups between micelles. Concurring with that theory, Zinn et al. found that the activation energy of the rheological relaxation of C22F50 hydrogels determined from linear oscillatory shear experiments was the same as the activation energy of molecular exchange in C22F00 micelles determined by the KZAC TR-SANS technique.[104] However, the molecular exchange kinetics of the difunctional C$_n$-PEO2x-C$_n$ molecules and therefore also their microscopic exchange mechanism have so far eluded experimental access.

As described in Paper IV, we considered three possible exchange mechanisms for telechelic molecules:

(i) The two hydrophobic groups are expelled simultaneously. That means the exchange rates of the individual blocks k_{Cn} with their activation energy

E_a must be multiplied. That would result in a doubled activation energy compared to the respective monofunctional polymers:

$$k_{\text{tel}} \propto k_{\text{Cn}}^2 \propto \exp(-2E_a/k_B T). \tag{4.8}$$

(ii) The two alkyl chains are expelled consecutively and diffuse freely in solution before re-inserting into a micelle. As discussed in detail in the Supporting Information of Paper IV, this leads to a rate constant approximately equal the product of the two release steps k_1 and k_2, divided by the rate constant corresponding to the re-insertion of the first block, k_{-1}:

$$k_{\text{tel}} \approx k_1 k_2 / k_{-1}. \tag{4.9}$$

In this case, the effective activation energy would differ from that of the monofunctional polymers because k_1, k_{-1} and k_2 have different temperature-dependencies. More important for the following discussion is, however, that this mechanism is concentration-independent.

(iii) Occasionally, single alkyl groups leave the micellar core, creating short-lived dangling ends. If the micelle collides with another one within this time window, a transient bridge can be formed. Then either the first alkyl group leaves the "new" micelle again, so that no exchange takes place, or the second alkyl group also leaves the original micelle, completing the exchange. This mechanism obviously requires micellar collisions and the corresponding rate would depend on the micelle concentration. A similar exchange mechanism, coined "walking diffusion", was proposed by Yokoyama and Kramer for the exchange of telechelic molecules in melt, where the chain ends form spherical aggregates on a regular lattice, surrounded by a matrix of middle blocks.[182, 183]

Experimental work on this topic is scarce. To our knowledge, only Lu et al. directly observed the molecular exchange rate between telechelic micelles in solution.[149] As outlined in Section 1.5.3 on page 19, they reported that telechelic molecules exchanged considerably slower than the corresponding monofunctional molecules, but still faster than expected for simultaneous release [scenario (i)]. Thus, a consecutive release mechanism seems plausible but no further details could be deduced. In the study reported in Paper IV, we finally uncovered the exchange mechanism between telechelic micelles in solution.

We employed the same C22F50 and C28F40 sample systems as in References [102, 104] and carried out KZAC TR-SANS experiments as described in Section 3.1.5 on page 47. Exemplary experimental relaxation functions $R(t)$ are plotted in Figure 4.14. They are clearly bimodal, indicating two separate exchange processes, similar to the binary mixtures of monofunctional C_n-PEO5 discussed in the previous section. The curves are excellently reproduced by a sum of two exponential functions,

$$R(t) = f_{\text{tel}} \cdot \exp(-k_{\text{tel}}t) + (1 - f_{\text{tel}}) \cdot \exp(-k_{\text{mon}}t), \tag{4.10}$$
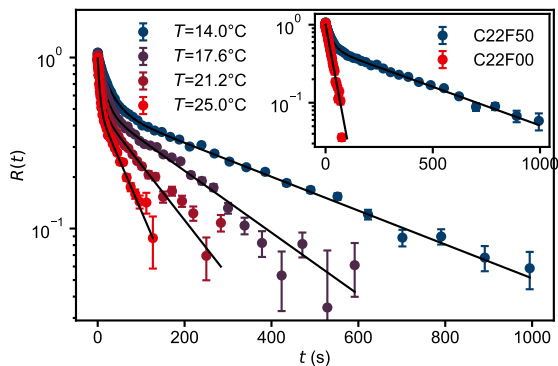
Figure 4.14: Relaxation functions of C22F50 at selected temperatures. Inset: Comparison of C22F50 and C22F00 at 14 °C. Reprinted with permission from Paper IV. Copyright © 2020 American Physical Society.

once more confirming the "independent chain hypothesis". As shown in the inset of Figure 4.14, the fast mode agrees with the exchange process of the respective monofunctional (diblock) molecules and we therefore naturally identify the slower mode with the exchange of telechelic molecules.

In a first step, we performed independent Arrhenius fits for k_{tel} and k_{mon}, similar to Paper III. The obtained activation energies $E_{a,\text{tel}}$ and $E_{a,\text{mon}}$ were almost identical. Therefore, in the second step, we performed a global Arrhenius fit of the experimental relaxation curves at all temperatures, where only the mutual activation energy $E_a = E_{a,\text{tel}} = E_{a,\text{mon}}$ and the individual time constants $\tau_{0,\text{tel}}$ and $\tau_{0,\text{mon}}$ were free fit parameters. In addition, we allowed minor adjustments of $I(0)$ and $I(\infty)$ as discussed in Section 3.1.5 on page 47. The results for the monofunctional component excellently agrees with previous results — compare Figure 3 in Paper IV. The mutual activation energy of mono- and difunctional PEO molecules instantly rules out scenario (i), simultaneous chain expulsion, as a possible exchange mechanism of telechelic molecules, in agreement with Reference [149]. Even though we enforced an equal E_a for both species in the fits, this procedure led to very good fits of the experimental data and hence the "real" activation energies can maximally be slightly different. The fact that we can describe the telechelic exchange kinetics with the same activation energy in principle also rules out scenario (ii), consecutive chain end release and free diffusion, as discussed in detail in the Supporting Information of Paper IV. However, since the covered temperature range is relatively narrow, this argument is not decisive by itself. Nevertheless, the most striking difference between scenarios (ii) and (iii) is the concentration dependence. While the former mechanism is independent of concentration like the exchange of monofunctional molecules, the latter is based on intermicellar collisions and thus clearly depends on the micellar concentration. Therefore, we conducted kinetic measurements on
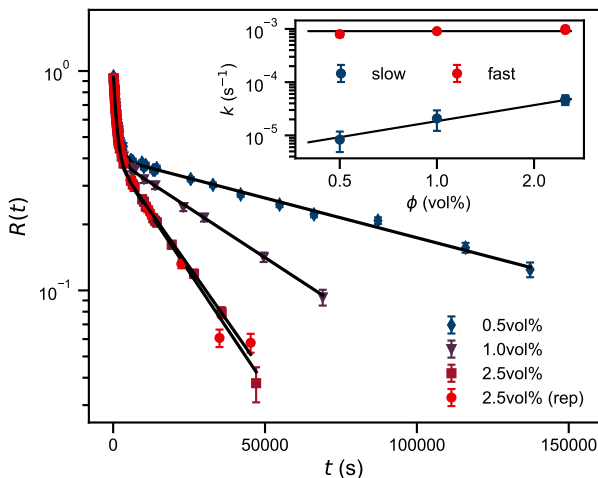
Figure 4.15: Relaxation curves of C28F40 measured at 37 °C and three different polymer volume fractions. Inset: Respective rate constants. The fast process is concentration independent while the slow process exhibits a $k \propto \phi$ dependence. Reprinted with permission from Paper IV. Copyright © 2020 American Physical Society.

C28F40 at different overall polymer volume fractions ϕ to definitely distinguish between mechanisms (ii) and (iii). Exemplary results are shown in Figure 4.15. While the exchange rate of monofunctional PEO is independent of concentration as expected, telechelic molecules exchange much faster at higher concentration and the corresponding exchange rate scales linearly with the polymer volume fraction, $k_{\text{tel}} \propto \phi$. Even though this result alone is proof enough for scenario (iii), we performed further experiments at different temperatures for a full concentration-dependent Arrhenius evaluation to rule out that the exchange mechanism changes with concentration. Indeed, we found the same activation energy at all concentrations. We would like to highlight that all experimental relaxation curves shown in the Supporting Information of Paper IV were fitted with a single set of parameters. The only free fit parameters were the mutual E_a, $\tau_{0,\text{mon}}$ and the three $\tau_{0,\text{tel}}(\phi)$ which were kept at a fixed ratio

$$1/\tau_{0,\text{tel}}(0.5 \, \text{vol\%}) : 1/\tau_{0,\text{tel}}(1.0 \, \text{vol\%}) : 1/\tau_{0,\text{tel}}(2.5 \, \text{vol\%}) = 0.5 : 1.0 : 2.5.$$

Thus we conclude that the exchange mechanism does not change over the investigated concentration range.

The sketch in Figure 4.16 illustrates the three proposed exchange scenarios, of which (i) and (ii) could be ruled out based on our experimental results. For scenario (iii), we have developed a simple kinetic model that is explained in detail in Paper IV and the accompanying Supporting Information. The key
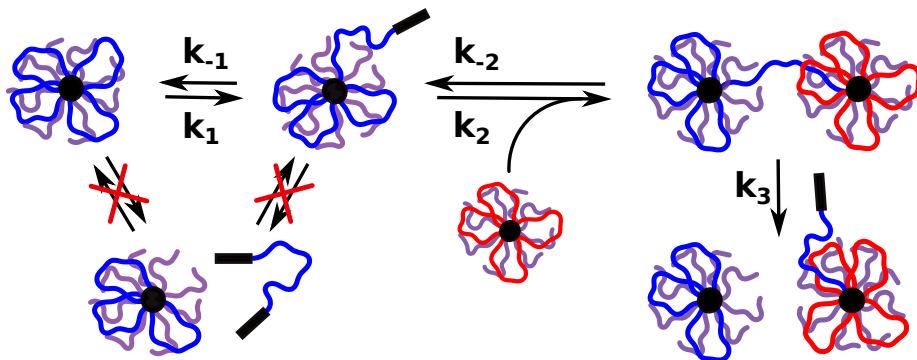
Figure 4.16: Illustration of possible exchange mechanisms between telechelic micelles in solution. Reprinted with permission from Paper IV. Copyright © 2020 American Physical Society.

result is an effective rate constant for the whole exchange process of telechelic molecules,

$$k_{\text{tel,eff}} = \frac{k_1 k_2 [M]}{2k_{-1}} + \mathcal{O}([M]^2), \qquad (4.11)$$

which is in perfect agreement with our experimental results on C28F40. The rate constants k_2 and k_{-1} have the same enthalpy difference and therefore their temperature dependence cancels out in $k_{\text{tel,eff}}$. The temperature dependence is thus solely governed by k_1, which in first approximation has the same activation energy as k_{mon}. The rate constant $k_{\text{tel,eff}}$ furthermore scales linearly with the micellar concentration $[M]$, which is directly proportional to the overall polymer concentration: $[M] = \phi/(N_A N_{\text{agg}} V_{\text{Cn-PEO-Cn}})$. And lastly, compared to k_{mon}, $k_{\text{tel,eff}}$ is reduced by the factor $k_2[M]/(2k_{-1}) < 1$, so that the telechelic exchange is generally slower than the exchange of monofunctional PEO.

Unfortunately, we were not able to perform the same concentration-dependent analysis for C22F40, because the stopped-flow device was not available at the time of the experiment. Instead, we tried to mix the isotopically labeled solutions by hand but this procedure did not yield reproducible data, probably because we did not achieve homogeneous mixing of the C22F40 clusters. In contrast, the experimental $R(t)$ curves obtained with the stopped-flow device were perfectly reproducible and did not depend on the flow rate in the mixing chamber, which points towards small, non-percolating clusters. We therefore postulate that micellar exchange between C22F50 clusters relies on the same collision-based exchange mechanism as in flower-like C28F40 micelles, while exchange within clusters might occur via the "walking diffusion" mechanism.

Interestingly, in percolating networks of telechelic polymers, the rheological relaxation rate constant $k_{\text{rheo,tel}}$ exhibits the opposite concentration dependence where the exchange rate decreases with increasing concentration, while E_a is also concentration-independent.[104, 170, 171, 179, 180] This behavior can be

explained by the re-arrangement of molecular bridges which gets slower at higher ϕ due to entanglement. Another established explanation are so-called "super bridges": At low concentration, there are only few connections between micelles, holding the network together. Thus, breaking a single of these "super bridges" can relax the network. At higher concentration, though, more bridges need to be broken up to relax the network which naturally decreases the relaxation rate. Thus for C22F40, forming small, non-percolating clusters in the dilute regime, we expect an intermediate concentration dependence.

Inspired by recent computer simulations reported by Prhashanna and Chen [151] and Peters and Lodge [150], we also attempted to measure the exchange rates of the inverted polymer architecture — an alkylene block sided by two PEO chains, PEO2.5-C_{22}-PEO2.5 — and compared it to the corresponding diblock C_{22}-PEO5. This follows the pattern of Peters and Lodge who kept the overall molecular length constant whereas Prhashanna and Chen created triblocks by fusing two diblock molecules. In the case of PEO2.5-C_{22}-PEO2.5, the different architecture creates a less extended, more crowded PEO corona compared to micelles formed by C_{22}-PEO5, which decreases the free energy gain G_{mic} of micellization. Concurringly, we observed markedly smaller triblock micelles, in agreement with the literature [149, 150]. The reduced G_{mic} also points towards very fast molecular exchange. Too fast, in fact, to be monitored with TR-SANS. In addition, core crystallization could not be exploited here to slow down the exchange kinetics because the alkylene chains in these micelles do not crystallize. Yet, as evidenced by DSC measurements, we successfully induced core crystallization by blending C_{22}-PEO5 with PEO2.5-C_{22}-PEO2.5 which might open an opportunity to observe the triblock exchange. But in the test experiments performed so far, we unfortunately only detected the diblock exchange, calling for even higher temporal resolution to observe the triblocks exchanging.

4.4 Self-Assembling Antimicrobial Peptides

As outlined in Section 1.6 on page 23, antimicrobial peptides (AMPs) pose a viable alternative to conventional small-molecule antibiotics in the quest for new therapeutics. Although their clinical application faces a number of obstacles, many of those can be mitigated via self-assembly. Such self-assembling antimicrobial peptides (SAAMPs) exhibit all characteristics of Soft Matter systems. With our experimental expertise and fundamental understanding of these systems, among others from the studies reported in Papers I to IV, we aimed to investigate the solution structure and exchange kinetics of self-assembling $K_x(QL)_yK_z$ peptides developed by the Dong group — see Section 1.6.2 on page 26. Specifically, we chose the sequences $K_3W(QL)_6K_2$ (3W62) and $WK_3(QL)_6K_2$ (W362) because they showed favorable properties in previous studies [209, 210]. In addition, PEGylated derivatives had already been studied [210] which opened up the possibility of KZAC TR-SANS experiments to investigate their exchange kinetics (Paper V).

The figure has been removed because it is part of an unpublished paper.

4.4.1 Structural Investigation

These peptides self-assemble into filaments consisting of two sandwiched beta sheets, with dimensions between $1 - 100$ nm. Therefore, small-angle scattering is excellently suited to study these assemblies in solution. In previous publications, SAXS data of peptide filaments have been analyzed by means of geometrical scattering models.[207, 209, 210] For unPEGylated peptides, a homogeneous, elongated prism has been used. This model, however, is a strong simplification of the filament structure. For example, it failed to reproduce the prominent scattering peak around $Q \approx 0.3 \, \text{Å}^{-1}$ — compare Figure S3 in the Supporting Information of Reference [209]. This peak originates from a regular structure with length scale $2\pi/0.3 \, \text{Å}^{-1} \approx 21 \, \text{Å}$ which accords with the approximate distance between the electron-rich, hydrophilic domains of the two sandwiched beta sheets and thus inherently cannot be reproduced by a homogeneous model. In addition, this model could not simultaneously fit SAXS and SANS data of 3W62 filaments. Therefore, we developed a new geometrical scattering model, taking into account the internal structure of the peptide filaments.

After extensive testing of different shapes, we decided on a rectangular core-shell geometry which is depicted in Figure 4.17. A more detailed description of the model is given in Paper V. By using this new model, we succeeded to fit absolute-scale SAXS and SANS data of 3W62 simultaneously — see Figure V.3a) in Paper V. The obtained fit parameters were in good agreement with the previous findings from both SAXS and TEM experiments.[209, 210] We should mention, though, that this includes an unusually low peptide density of 1.25 g/mL, while the consensus value for protein densities is rather around 1.35 g/mL [283].

The structural parameters obtained from model fits of scattering data were confirmed by additional molecular dynamics (MD) simulations performed in the group of our collaborator Sinan Keten at Northwestern University. Representative simulation snapshots are shown in Figure 4.18. The simulations revealed a strongly segregated, water-free hydrophobic core, consisting of Leucine and Tryptophan residues, which is surrounded by the hydrophilic Lysine

The figure has been removed because it is part of an unpublished paper.

and Glutamine residues as well as the peptide backbones. This affirms the assumptions on which the new scattering model was based. Moreover, the spatial dimensions of the simulated filaments agree well with the model fit parameters (Paper V). One obvious feature from the MD simulations is not represented in the geometrical model, though: The simulated filament is clearly twisted, with a period of about 35 strands ($\sim 165\,\text{Å}$) for a full rotation. This twisting might reduce the electrostatic repulsion between the Lysine residues. As to why this feature is not necessary in the geometrical modeling, we can only speculate. In principle, the SAS experiments are sensitive to this length scale, $2\pi/165\,\text{Å} \approx 0.04\,\text{Å}^{-1}$. It might be obscured by the rotational average.

Irrespective of these modeling details, SAXS experiments revealed an exceptional structural stability of 3W62 filaments. The scattering patterns of 3W62 solutions at pH 7.4 and pH 5.0, shown in Figure V.3b) in Paper V, are perfectly identical. The rationale behind was that intermolecular repulsion might be increased under acidic conditions, destabilizing the filament. Even though the overall shape seems unaffected as far as resolvable by SAXS, CD spectroscopy revealed minor changes in the internal order. While the CD spectrum of 3W62 at physiological pH is clearly dominated by beta sheets,

The figure has been removed because it is part of an unpublished paper.

the sheet content decreases at pH 5.0 — compare Figure V.4 in Paper V. So apparently, acidic conditions do have a disordering effect on the internal sheet structure but it is not strong enough to alter the overall shape. Comparing the CD spectra of 3W62 and W362, the internal order of the latter is much more disturbed but both peptides still form similar filaments as evidenced by SAXS and TEM.[209] Surprisingly, the X-ray scattering pattern of 3W62 does not change at 70 °C, either. Earlier, Xu et al. have reported CD melting curves of the sandwiched beta sheets in 3W62 by following the ellipticity at 205 nm wavelength and observed a clear melting transition around 67 °C — see Figure S2 in the Supporting Information of Reference [210]. One explanation for the higher temperature-stability in the SAXS experiment might be the increased concentration. While CD experiments were carried out at $100\,\mu M \approx 10 \times CAC$, the concentration in the SAXS experiment was about $4.4\,mM > 400 \times CAC$ which might have a stabilizing effect. In addition, the dissolution of the highly ordered beta sheets does not necessarily implicate the dissolution of the whole filament. They might persist with a disordered internal structure. In any case, we can conclude that 3W62 filaments exhibit a high overall stability against acidic and thermal perturbation

Interestingly, this finding also holds in case of the PEGylated P-3W62 peptide. While Xu et al. found a lightly disordering effect of PEGylation, we observe an unaltered shape and stability compared to unPEGylated 3W62 in our scattering experiments. The reason might again be that the internal order measured by CD spectroscopy and the overall shape measured by SAS are not entirely correlated. Using the core-shell-shell model presented in Paper V, we obtained a perfect fit of the SAXS curve of P-3W62, using the exact same parameters as for unPEGylated 3W62 and adding only a homogeneous, 30 Å thick layer of solvated PEG around the peptide sheet — compare Figure 4.19a). This indicates that, in contrast to previous findings [210], PEG does not adopt a Gaussian coil conformation
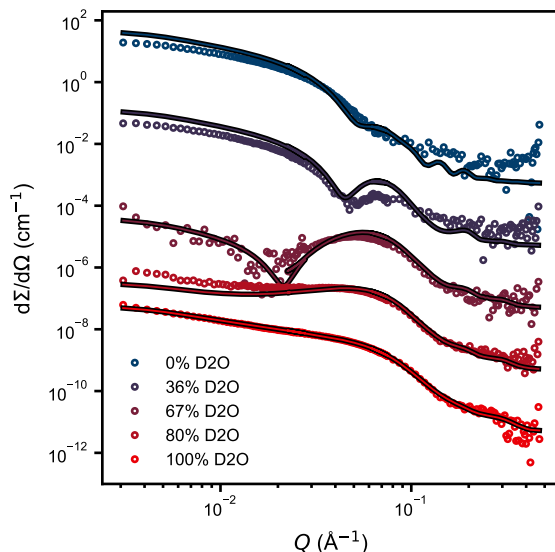
Figure 4.20: Contrast-variation SANS data of dP-3W62. Solid lines represent fits using the rectangular core-shell-shell model presented in Paper V. Curves have been shifted by factors of 100 for better visibility.

at the side of the beta sheet but instead homogeneously wraps around the peptide filament. We also performed contrast-variation SANS experiments on dP-3W62 to gain more insight into the peptide-PEG interaction. Unfortunately, we were to date not able to obtain good fits of these data using reasonable parameters, neither with the previous homogeneous peptide prism model with Gaussian polymer coils nor with the new core-shell-shell model. But since the new model improved the fits to the contrast-variation SANS data significantly as shown in Figure 4.20, we consider PEG wrapping around the peptide filament a tentative yet viable working hypothesis. In the future, we aim to perform computer simulations of PEGylated peptides to shine more light on this issue. Nonetheless, our scattering experiments clearly demonstrate that PEGylation does not negatively affect the overall filament stability shown for 3W62. In Figure 4.19b) and c), SAXS and SANS data of P-3W62 are plotted which were taken at elevated temperatures and lowered pH. All curves perfectly overlap, confirming that the overall filament structure is exceptionally stable, even at 85 °C or pH 5.7. Unfortunately, we do not have one complete set of data over all temperatures and pH from the same experiment. Instead, the data shown in Figure 4.19 are collected from different samples and SAS instruments. On the other hand, the reproducibility of the scattering curves across facilities and samples reinforces our claim that the filament structure is highly stable. We did have problems with accurately determining the peptide concentration,

though. The concentrations determined from the weighed amounts of peptide lyophilisate and solvent on the one hand and from UV absorption spectroscopy on the other hand did differ by up to a factor of 4. Although we could not definitely pinpoint the cause, we speculate that the reason are two different effects: Firstly, the peptide lyophilisates might not be completely pure and dry, so that residual salt ions (particularly TFA remnants from synthesis) and solvent contributed to the supposed peptide weight. Secondly, quenching of Tryptophan in the assembled filament could reduce the apparent peptide concentration as determined from UV spectroscopy. Due to this uncertainty, we allowed a limited adjustment of the peptide concentration during SAS fit procedures. In addition, the concentration uncertainty also prohibited a direct quantitative density measurement as described for polymer micelles in Section 3.2 on page 54, which could have confirmed that the unusually low peptide density is not an artifact.

4.4.2 Time-Resolved Experiments

At the start of the PhD project, we planned to measure the equilibrium molecular exchange kinetics of P-3W62 and P-W362, assuming that the filaments served as a molecular depot rather than having bactericidal activity themselves. That the mode of action involved the assembled filament was only confirmed recently.[211] By measuring molecular exchange rates at different temperatures via the KZAC neutron scattering scheme, we aimed to determine activation energies of P-3W62 and P-W362, comparable to the experiments reported in Papers III and IV. We expected a higher activation energy for P-3W62 because of its higher degree of internal order [210]. However, first test experiments indicated that both peptides formed filaments that were rather stable, exhibiting little to no molecular exchange, even at elevated temperatures up to 67 °C.

   In the following, we therefore focused on only one of the two peptide derivatives, P-3W62, and tested how stable the self-assembled filaments were. This study is reported in Paper V. First, we repeated the previous experiment and confirmed that at 37 °C and pH 7.4 molecular exchange was negligible over a course of 2.5 days — compare Figure 4.21a). Also at 67 °C, there was barely any thermally activated exchange. To go to the limit, we heated a freshly blended P-3W62 solution to 90 °C. As mentioned in the previous paragraph, the filament structure was still undisturbed at such high temperatures. After 30 min at 90 °C, the scattering intensity had markedly decreased — see Figure 4.21b) —, indicating some exchange of peptide molecules between filaments. Unexpectedly, though, the intensity hardly decreased further after another 90 min at 90 °C. We think the reason is that thermally activated exchange of unimers occurs only at the filament termini. While the molecules at the very ends of the beta sheets might leave and re-attach to the assembly relatively often, this process becomes exponentially slower the further a molecule is located from the sheet terminus.Although this mechanism explains the incredibly slow thermally activated exchange, we were still in doubt if the KZAC scheme worked in the established way with P-3W62 at all. It was yet an unlikely but possible

The figure has been removed because it is part of an unpublished paper.

option that the PEG conformation prohibited interchain mixing which would prevent the desired average contrast loss. Therefore, and also to further test the physical integrity of the filaments, we subjected freshly blended samples to mechanical agitation. This approach was partly motivated by a study on polymer micelles where molecular exchange was induced in kinetically trapped systems by mechanical agitation [154]. First, we used a common lab-bench vortexer which proved ineffective as obvious from Figure 4.21c). As a last resort, we turned to tip-sonication, a very disruptive mechanical treatment which is an established method to break apart stable, non-covalently bound structures like cell membranes. The data plotted in Figure 4.21d) reveal a clear decrease in scattering intensity as expected when the PEG chains become isotopically mixed. To ascertain whether the peptide-polymer conjugates were not molecularly degraded instead by the rough mechanical treatment, we carried out SAXS measurements afterwards and found no difference in the scattering curves compared to untreated sample. Therefore, we conclude that the KZAC TR-SANS technique is principally able to follow the molecular exchange in P-3W62 filaments but the latter exhibit an exceptional physical integrity, caused by the high content of hydrogen-bonded beta sheets stabilized by hydrophobic interaction. This can be quantified in a simple estimation: According to the MD simulations of the unPEGylated peptide, the whole hydrophobic-hydrophilic motif $(KW(QL)_6)$ participates in the beta sheet formation. Thus, to remove a molecule from the filament terminus, 14 hydrogen bonds need to be broken in the peptide backbone alone. Each of these contributes about $\sim 8\,\mathrm{kJ/mol}$ binding energy [284], resulting in an activation energy of $\sim 112\,\mathrm{kJ/mol}$ for removing a single peptide molecule from a filament terminus or breaking a filament in the middle. This value is comparable to the activation energies of C_n-PEOx reported in Paper III which do exhibit molecular exchange. Yet, the simple calculation for the peptide activation energy does not consider the hydrophobic interaction between Leucine residues or possible hydrogen bonds between Glutamine residues, so the actual peptide activation energy is likely much higher.

The exceptional physical integrity is good news for applications of (P-)3W62 in antimicrobial hydrogels where increased stability proved to be advantageous.[208] It is in principle also good news for applications as a systemic treatment of infections since we now know that the mode of action involves the assembled peptide in direct contact with the cell membrane [211] and physical integrity is thus a desired property. Yet, Xu et al. also found that bactericidal efficacy was higher in peptide filaments with less ordered beta sheets.[209] In fact, the disruption of bacterial membranes might involve partial fragmentation and insertion into the lipid bilayer.[216] Therefore, W362 might be a better candidate for further development. But this peptide induced eryptosis in red blood cells which, in contrast to 3W62, could not be mitigated by PEGylation.[210] Hence, more work is needed to develop $K_x(QL)_yK_z$ peptides into clinical application. Nevertheless, we gained significant insight into the stability of protein-based nanostructures which can be exploited in a range of biomedical applications.

Chapter 5

Conclusion and Outlook

The overall goal of the present doctoral thesis was to gain a deeper understanding of the principles underlying molecular self-assembly and their consequences. We shed light on the interplay between morphology, molecular interaction and exchange kinetics. Thus, we hope our work contributes to the understanding and further development of Soft Matter nanotechnology exploiting self-assembling systems.

Specifically, we investigated how molecular order inside self-assembled superstructures affects both the overall shape and the exchange kinetics between assemblies. We also looked at effects of co-assembly and molecular architecture. In these studies, our research subjects included both well-defined polymeric model systems as well as antimicrobial peptides. The characteristic length scales of these structures are on the order of $1-100$ nm, which rendered small-angle scattering the natural choice for our main experimental technique, aided by complementary methods. Furthermore, we employed theoretical modeling to rationalize our experimental results. The key findings are briefly summarized in the following:

- At low temperatures, the alkyl chains in C_n-PEO5 micellar cores adopt a rotator-like phase, resulting in an oblate ellipsoidal core shape. Above the melting temperature, the hydrocarbon blocks become more liquid-like but, nonetheless, some core anisotropy is retained. Yet, in both cases, the overall micelles still appear spherical because the PEO corona is much more extended than the alkyl core.

- Micelles created from co-assembly of length-mismatched C_n-PEO5 polymers perfectly mimic the behavior of pure micelles, both in terms of structure and thermodynamics.

- The core crystallization in these mixed micelles is cooperative whereas the molecular exchange is not. Crystallization does, however, add a mutual penalty to the individual activation energies of chain release.

- Flower-like telechelic micelles in solution exchange molecules via a collision-based mechanism, where transient molecular bridges between micellar cores mediate the transfer.

- Although we initially aimed to measure the molecular exchange between antimicrobial 3W62 peptide filaments, we ended up uncovering the exceptional physical integrity of these assemblies.

We therefore considerably extended our knowledge about self-assembling Soft Matter systems and the fundamental principles governing them. But our studies also left some unanswered questions and even opened up new ones:

We postulated that the retained core anisotropy of C_{28}-PEO5 micellar cores in the liquid-like phase is caused by the rigidity of the alkyl chains (Paper I). Here, it would be interesting to investigate if this postulate holds also for shorter alkyl groups which supposedly are more compatible with a spherical core shape. At least computer simulations of C_{18}-PEOx only revealed a slight anisotropy.[103]

During the structural analysis of mixed C_n-PEO5 micelles we discovered an unpredicted $N_{agg} \propto n^3$ scaling law (Paper II). As we to this date lack an explanation, more experimental and theoretical work is mandatory to confirm or reject this finding. Possible approaches include computer simulations or experiments on a wider n range. The phenomenon might be related to the surface curvature of the micellar core or to the dehydrated PEG layer (Paper I) caused by the high chain grafting density which might influence the micellar free energy G_{mic} to an unknown extent.

So far, our claim about the additivity of melting enthalpy and activation energy in the exchange kinetics of core-crystalline micelles is based on only a few data points (Paper III). More experiments using different block lengths and mixing ratios would strongly support our finding. In doing so, the "overall ZAC" condition might yield clearer data and a simultaneous Arrhenius fit of multiple relaxation curves could reduce the uncertainty in the determined activation energies.

While we now have a good understanding of mixed micelles with length-mismatched core blocks, we know much less about the effect of blending different corona block lengths. For example, it was shown that mixed C_{18}-PEOx micelles with two different PEO lengths segregated, when the C_{18} blocks crystallized [109], but an explanation is missing and the effect could not be reproduced in computer simulations [103]. Moreover, the effect of the corona block length on the exchange kinetics is disputed in the literature. While some works report an accelerated exchange of molecules with longer corona blocks because of a reduced G_{mic} [137, 143], others report slower exchange due to coronal crowding or slower diffusion because of the molecular size [106, 115, 118]. By mixing length-mismatched corona chains at different ratios and following their individual exchange in TR-SANS experiments, one might distinguish between the effect of diffusion and crowding.

In terms of molecular exchange between triblock copolymer micelles in solution, we uncovered the mechanism between flower-like telechelic micelles (Paper IV). It is unclear, though, how exchange works between clustered micelles like C22F50. We speculate the exchange between clusters involves the same collision-based mechanism and exchange within clusters occurs via the "walking diffusion" mechanism [182, 183]. This could be tested with a full concentration-dependent Arrhenius analysis like we performed for C28F40. Similarly interesting is the exchange kinetics of hydrophilic-hydrophobic-hydrophilic triblock copolymer micelles. Because of their accelerated molecular exchange, only computer simulations have yielded quantitative results so far [150, 151]. While the exchange of PEO2.5-C_{22}-PEO2.5 is too fast to be resolved by TR-SANS, longer alkylene blocks might exchange on accessible time scales. Unfortunately, α,ω-di-alkanols with $n > 22$ as precursor material are currently

not available.

Finally, our work on $K_x(QL)_yK_z$ antimicrobial peptides has left us with many open questions (Paper V). Despite immense modeling efforts, we could not definitely figure out the conformation of the PEG chains in P-3W62 and P-W362 peptide-polymer conjugates, but hope to gain more insight by using computer simulations. This would be a helpful puzzle piece in determining the effect of PEGylation and also help in the interpretation of the KZAC TR-SANS experiments. Still, we showed that the the the KZAC scheme works in principle and it might prove particularly useful in cases where self-assembly serves as a unimer depot so one can measure the molecular release kinetics. Having said that, we would like to investigate the physical stability of W362 filaments and other derivatives of the $K_x(QL)_yK_z$ family in the future. This work will help in the design of biomedical nanomaterials with tunable physical stability.

Bibliography

[1] J. K. G. Dhont and G. Gompper. "Introduction: Soft Matter". In: *Soft matter: from synthetic to biological materials*. Ed. by J. K. G. Dhont, G. Gompper, G. Nägele, D. Richter, and R. G. Winkler. Forschungszentrum Jülich GmbH, 2008. Chap. 1, pp. 2–13 (cited on p. 1).

[2] R. A. L. Jones. *Soft condensed matter*. Oxford University Press, 2002 (cited on p. 1).

[3] G. M. Whitesides and B. Grzybowski. "Self-Assembly at All Scales". In: *Science* vol. 295, no. 5564 (2002), pp. 2418–2421. DOI: 10.1126/science. 1070821 (cited on p. 3).

[4] B. A. Grzybowski, C. E. Wilmer, J. Kim, K. P. Browne, and K. J. M. Bishop. "Self-assembly: from crystals to cells". In: *Soft Matter* vol. 5, no. 6 (2009), pp. 1110–1128. DOI: 10.1039/B819321P (cited on p. 3).

[5] H. Cui, M. J. Webber, and S. I. Stupp. "Self-assembly of peptide amphiphiles: from molecules to nanostructures to biomaterials". In: *Biopolymers* vol. 94, no. 1 (2010), pp. 1–18. DOI: 10.1002/bip.21328 (cited on p. 4).

[6] J. Becker, L. Lu, M. B. Runge, H. Zeng, M. J. Yaszemski, and M. Dadsetan. "Nanocomposite bone scaffolds based on biodegradable polymers and hydroxyapatite". In: *Journal of Biomedical Materials Research Part A* vol. 103, no. 8 (2015), pp. 2549–2557. DOI: 10.1002/jbm.a.35391 (cited on p. 4).

[7] T. L. Doane and C. Burda. "The unique role of nanoparticles in nanomedicine: imaging, drug delivery and therapy". In: *Chemical Society Reviews* vol. 41, no. 7 (2012), pp. 2885–2911. DOI: 10.1039/C2CS15260F (cited on p. 4).

[8] M. W. Tibbitt, J. E. Dahlman, and R. Langer. "Emerging Frontiers in Drug Delivery". In: *Journal of the American Chemical Society* vol. 138, no. 3 (2016), pp. 704–717. DOI: 10.1021/jacs.5b09974 (cited on p. 4).

[9] A. Pavia-Sanders, S. Zhang, J. A. Flores, J. E. Sanders, J. E. Raymond, and K. L. Wooley. "Robust Magnetic/Polymer Hybrid Nanoparticles Designed for Crude Oil Entrapment and Recovery in Aqueous Environments". In: *ACS Nano* vol. 7, no. 9 (2013), pp. 7552–7561. DOI: 10.1021/nn401541e (cited on p. 4).

[10] P. Raffa, A. A. Broekhuis, and F. Picchioni. "Polymeric surfactants for enhanced oil recovery: A review". In: *Journal of Petroleum Science and Engineering* vol. 145 (2016), pp. 723–733. DOI: 10.1016/j.petrol.2016.07. 007 (cited on p. 4).

[11]   I. W. Hamley. "Nanostructure fabrication using block copolymers". In: *Nanotechnology* vol. 14, no. 10 (2003), R39–R54. DOI: 10.1088/0957-4484/14/10/201 (cited on p. 4).

[12]   M. Lazzari and M. A. López-Quintela. "Block Copolymers as a Tool for Nanomaterial Fabrication". In: *Advanced Materials* vol. 15, no. 19 (2003), pp. 1583–1594. DOI: 10.1002/adma.200300382 (cited on p. 4).

[13]   D. M. Vriezema, M. Comellas Aragones, J. A. A. W. Elemans, J. J. L. M. Cornelissen, A. E. Rowan, and R. J. M. Nolte. "Self-Assembled Nanoreactors". In: *Chemical Reviews* vol. 105, no. 4 (2005), pp. 1445–1490. DOI: 10.1021/cr0300688 (cited on p. 4).

[14]   V. Castelletto, I. W. Hamley, C. Whitehouse, P. J. Matts, R. Osborne, and E. S. Baker. "Self-Assembly of Palmitoyl Lipopeptides Used in Skin Care Products". In: *Langmuir* vol. 29, no. 29 (2013), pp. 9149–9155. DOI: 10.1021/la401771j (cited on p. 4).

[15]   P. Malo de Molina and M. Gradzielski. "Gels Obtained by Colloidal Self-Assembly of Amphiphilic Molecules". In: *Gels* vol. 3, no. 3 (2017), p. 30. DOI: 10.3390/gels3030030 (cited on p. 4).

[16]   A. Nasir, A. Kausar, and A. Younus. "A Review on Preparation, Properties and Applications of Polymeric Nanoparticle-Based Materials". In: *Polymer-Plastics Technology and Engineering* vol. 54, no. 4 (2015), pp. 325–341. DOI: 10.1080/03602559.2014.958780 (cited on p. 4).

[17]   U. Tritschler, S. Pearce, J. Gwyther, G. R. Whittell, and I. Manners. "50th Anniversary Perspective: Functional Nanoparticles from the Solution Self-Assembly of Block Copolymers". In: *Macromolecules* vol. 50, no. 9 (2017), pp. 3439–3463. DOI: 10.1021/acs.macromol.6b02767 (cited on p. 4).

[18]   C. Tanford. *The Hydrophobic Effect: Formation of Micelles and Biological Membranes.* Wiley, 1980 (cited on pp. 4, 9, 65, 67).

[19]   G. Riess. "Micellization of block copolymers". In: *Progress in Polymer Science* vol. 28, no. 7 (2003), pp. 1107–1170. DOI: https://doi.org/10.1016/S0079-6700(03)00015-7 (cited on pp. 5, 6).

[20]   J.-F. Gohy. "Block Copolymer Micelles". In: *Block Copolymers II*. Ed. by V. Abetz. Springer, 2005, pp. 65–136. DOI: 10.1007/12_048 (cited on pp. 5, 6).

[21]   L. Leibler, H. Orland, and J. C. Wheeler. "Theory of critical micelle concentration for solutions of block copolymers". In: *The Journal of Chemical Physics* vol. 79, no. 7 (1983), pp. 3550–3557. DOI: 10.1063/1.446209 (cited on pp. 5, 6).

[22]   R. Nagarajan and K. Ganesh. "Block copolymer self-assembly in selective solvents: Spherical micelles with segregated cores". In: *The Journal of Chemical Physics* vol. 90, no. 10 (1989), pp. 5843–5856. DOI: 10.1063/1.456390 (cited on pp. 5, 6).

[23] J. N. Israelachvili, D. J. Mitchell, and B. W. Ninham. "Theory of self-assembly of hydrocarbon amphiphiles into micelles and bilayers". In: *Journal of the Chemical Society, Faraday Transactions 2: Molecular and Chemical Physics* vol. 72 (1976), pp. 1525–1568. DOI: 10.1039/F29767201525 (cited on pp. 6, 7).

[24] I. W. Hamley. *Block copolymers in solution: fundamentals and applications.* John Wiley & Sons, 2005 (cited on p. 6).

[25] J. Noolandi and K. M. Hong. "Theory of Block Co-Polymer Micelles in Solution". In: *Macromolecules* vol. 16, no. 9 (1983), pp. 1443–1448. DOI: 10.1021/ma00243a007 (cited on p. 6).

[26] R. Nagarajan and E. Ruckenstein. "Theory of surfactant self-assembly: a predictive molecular thermodynamic approach". In: *Langmuir* vol. 7, no. 12 (1991), pp. 2934–2969. DOI: 10.1021/la00060a012 (cited on p. 6).

[27] A. Halperin and S. Alexander. "Confined Star Polymers". In: *Macromolecules* vol. 20, no. 5 (1987), pp. 1146–1152. DOI: 10.1021/ma00171a046 (cited on p. 6).

[28] A. Halperin. "Polymeric Micelles — a Star Model". In: *Macromolecules* vol. 20, no. 11 (1987), pp. 2943–2946. DOI: 10.1021/ma00177a051 (cited on p. 6).

[29] T. M. Birshtein and E. B. Zhulina. "Scaling theory of supermolecular structures in block copolymer-solvent systems: 1. Model of micellar structures". In: *Polymer* vol. 30, no. 1 (1989), pp. 170–177. DOI: 10.1016/0032-3861(89)90399-6 (cited on p. 6).

[30] D. Izzo and C. M. Marques. "Formation of micelles of diblock and triblock copolymers in a selective solvent". In: *Macromolecules* vol. 26, no. 26 (1993), pp. 7189–7194. DOI: 10.1021/ma00078a012 (cited on p. 6).

[31] M. Daoud and J. P. Cotton. "Star shaped polymers: a model for the conformation and its concentration dependence". In: *Journal de Physique* vol. 43, no. 3 (1982), pp. 531–538. DOI: 10.1051/jphys:01982004303053100 (cited on p. 6).

[32] E. B. Zhulina, M. Adam, I. LaRue, S. S. Sheiko, and M. Rubinstein. "Diblock Copolymer Micelles in a Dilute Solution". In: *Macromolecules* vol. 38, no. 12 (2005), pp. 5330–5351. DOI: 10.1021/ma048102n (cited on p. 7).

[33] E. B. Zhulina and O. V. Borisov. "Theory of Block Polymer Micelles: Recent Advances and Current Challenges". In: *Macromolecules* vol. 45, no. 11 (2012), pp. 4429–4440. DOI: 10.1021/ma300195n (cited on p. 7).

[34] M. Rubinstein and R. Colby. *Polymer Physics.* Oxford University Press, 2003 (cited on p. 7).

[35] I. A. Nyrkova, A. R. Khokhlov, and M. Doi. "Microdomains in block copolymers and multiplets in ionomers: parallels in behavior". In: *Macromolecules* vol. 26, no. 14 (1993), pp. 3601–3610. DOI: 10.1021/ma00066a019 (cited on p. 7).

[36]   S. Förster, M. Zisenis, E. Wenz, and M. Antonietti. "Micellization of strongly segregated block copolymers". In: *The Journal of Chemical Physics* vol. 104, no. 24 (1996), pp. 9956–9970. DOI: 10.1063/1.471723 (cited on p. 7).

[37]   J. Cowie and V. Arrighi. *Polymers: Chemistry and Physics of Modern Materials.* CRC Press, 2007. DOI: 10.1201/9781420009873 (cited on p. 7).

[38]   T. Liu, V. M. Nace, and B. Chu. "Self-Assembly of Mixed Amphiphilic Triblock Copolymers in Aqueous Solution". In: *Langmuir* vol. 15, no. 9 (1999), pp. 3109–3117. DOI: 10.1021/la9812525 (cited on p. 8).

[39]   C. Chaibundit, N. M. P. S. Ricardo, F. d. M. L. L. Costa, S. G. Yeates, and C. Booth. "Micellization and Gelation of Mixed Copolymers P123 and F127 in Aqueous Solution". In: *Langmuir* vol. 23, no. 18 (2007), pp. 9229–9236. DOI: 10.1021/la701157j (cited on p. 8).

[40]   F. Renou, T. Nicolai, E. Nicol, and L. Benyahia. "Structure and Viscoelasticity of Mixed Micelles Formed by Poly(ethylene oxide) End Capped with Alkyl Groups of Different Length". In: *Langmuir* vol. 25, no. 1 (2009), pp. 515–521. DOI: 10.1021/la802708m (cited on pp. 8, 13, 70, 73, 75).

[41]   M. Zhang, M. Djabourov, C. Bourgaux, and K. Bouchemal. "Nanostructured fluids from pluronic mixtures". In: *International Journal of Pharmaceutics* vol. 454, no. 2 (2013), pp. 599–610. DOI: 10.1016/j.ijpharm.2013.01.043 (cited on p. 8).

[42]   A. Einstein. "Über einen die Erzeugung und Verwandlung des Lichtes betreffenden heuristischen Gesichtspunkt". In: *Annalen der Physik* vol. 322, no. 6 (1905), pp. 132–148. DOI: 10.1002/andp.19053220607 (cited on p. 8).

[43]   A. B. Ebrahim Attia, Z. Y. Ong, J. L. Hedrick, P. P. Lee, P. L. R. Ee, P. T. Hammond, and Y.-Y. Yang. "Mixed micelles self-assembled from block copolymers for drug delivery". In: *Current Opinion in Colloid & Interface Science* vol. 16, no. 3 (2011), pp. 182–194. DOI: 10.1016/j.cocis.2010.10.003 (cited on p. 8).

[44]   C. L. Maikawa, A. Sevit, B. H. Lin, R. J. Wallstrom, J. L. Mann, A. C. Yu, R. M. Waymouth, and E. A. Appel. "Block copolymer composition drives function of self-assembled nanoparticles for delivery of small-molecule cargo". In: *Journal of Polymer Science Part A − Polymer Chemistry* vol. 57, no. 12 (2019), pp. 1322–1332. DOI: 10.1002/pola.29393 (cited on p. 8).

[45]   A. S. Manjappa, P. S. Kumbhar, A. B. Patil, J. I. Disouza, and V. B. Patravale. "Polymeric Mixed Micelles: Improving the Anticancer Efficacy of Single-Copolymer Micelles". In: *Critical Reviews in Therapeutic Drug Carrier Systems* vol. 36, no. 1 (2019), pp. 1–57. DOI: 10.1615/CritRevTherDrugCarrierSyst.2018020481 (cited on p. 8).

[46] K. Prochazka, T. J. Martin, S. E. Webber, and P. Munk. "Onion-Type Micelles in Aqueous Media". In: *Macromolecules* vol. 29, no. 20 (1996), pp. 6526–6530. DOI: 10.1021/ma9606317 (cited on p. 8).

[47] W. Zhang, L. Shi, L. Gao, Y. An, and K. Wu. "Formation of Core-Shell-Corona Micellar Complexes through Adsorption of Double Hydrophilic Diblock Copolymers into Core-Shell Micelles". In: *Macromolecular Rapid Communications* vol. 26, no. 16 (2005), pp. 1341–1345. DOI: 10.1002/marc.200500281 (cited on p. 8).

[48] G. Srinivas and J. W. Pitera. "Soft Patchy Nanoparticles from Solution-Phase Self-Assembly of Binary Diblock Copolymers". In: *Nano Letters* vol. 8, no. 2 (2008), pp. 611–618. DOI: 10.1021/nl073027q (cited on p. 8).

[49] J. Zhu, S. Zhang, K. Zhang, X. Wang, J. W. Mays, K. L. Wooley, and D. J. Pochan. "Disk-cylinder and disk-sphere nanoparticles via a block copolymer blend solution construction". In: *Nature Communications* vol. 4 (2013), p. 2297. DOI: 10.1038/ncomms3297 (cited on p. 8).

[50] A. Cho, Y. La, S. Jeoung, H. R. Moon, J.-H. Ryu, T. J. Shin, and K. T. Kim. "Mix-and-Match Assembly of Block Copolymer Blends in Solution". In: *Macromolecules* vol. 50, no. 8 (2017), pp. 3234–3243. DOI: 10.1021/acs.macromol.7b00438 (cited on pp. 8, 73).

[51] S. Mantha, S. Qi, M. Barz, and F. Schmid. "How ill-defined constituents produce well-defined nanoparticles: Effect of polymer dispersity on the uniformity of copolymeric micelles". In: *Physical Review Materials* vol. 3, no. 2 (2019), pp. 026002-1–6. DOI: 10.1103/PhysRevMaterials.3.026002 (cited on pp. 8, 74).

[52] D. F. K. Shim, C. Marques, and M. E. Cates. "Diblock copolymers: comicellization and coadsorption". In: *Macromolecules* vol. 24, no. 19 (1991), pp. 5309–5314. DOI: 10.1021/ma00019a015 (cited on p. 8).

[53] P. Sens, C. M. Marques, and J. F. Joanny. "Mixed Micelles in a Bidisperse Solution of Diblock Copolymers". In: *Macromolecules* vol. 29, no. 14 (1996), pp. 4880–4890. DOI: 10.1021/ma951553a (cited on pp. 8, 70).

[54] A. L. Borovinskii and A. R. Khokhlov. "Micelle Formation in the Dilute Solution Mixtures of Block-Copolymers". In: *Macromolecules* vol. 31, no. 22 (1998), pp. 7636–7640. DOI: 10.1021/ma980482n (cited on pp. 8, 70).

[55] A. J. Müller, M. L. Arnal, and A. T. Lorenzo. "Crystallization in Nano-Confined Polymeric Systems". In: *Handbook of Polymer Crystallization*. Ed. by E. Piorkowska and G. C. Rutledge. Wiley, 2013, pp. 347–378. DOI: 10.1002/9781118541838 (cited on pp. 9, 10).

[56] J. J. Crassous, P. Schurtenberger, M. Ballauff, and A. M. Mihut. "Design of block copolymer micelles via crystallization". In: *Polymer* vol. 62, no. Supplement C (2015), A1–A13. DOI: 10.1016/j.polymer.2015.02.030 (cited on pp. 9, 10).

[57]   S. Ganda and M. H. Stenzel. "Concepts, fabrication methods and applications of living crystallization-driven self-assembly of block copolymers". In: *Progress in Polymer Science* vol. 101 (2020), p. 101195. DOI: 10.1016/j.progpolymsci.2019.101195 (cited on pp. 9, 10).

[58]   O. R. Monaghan, P. H. H. Bomans, N. Sommerdijk, and S. J. Holder. "Controlling the melting transition of semi-crystalline self-assembled block copolymer aggregates: controlling release rates of ibuprofen". In: *Polymer Chemistry* vol. 8, no. 35 (2017), pp. 5303–5316. DOI: 10.1039/c7py01170a (cited on p. 9).

[59]   X. Zhuo et al. "Disulfiram-loaded mixed nanoparticles with high drug-loading and plasma stability by reducing the core crystallinity for intravenous delivery". In: *Journal of Colloid and Interface Science* vol. 529 (2018), pp. 34–43. DOI: 10.1016/j.jcis.2018.05.057 (cited on p. 9).

[60]   M. Kastantin, B. Ananthanarayanan, P. Karmali, E. Ruoslahti, and M. Tirrell. "Effect of the Lipid Chain Melting Transition on the Stability of DSPE-PEG (2000) Micelles". In: *Langmuir* vol. 25, no. 13 (2009), pp. 7279–7286. DOI: 10.1021/la900310k (cited on pp. 9, 18, 76).

[61]   T. Zinn, L. Willner, V. Pipich, D. Richter, and R. Lund. "Effect of Core Crystallization and Conformational Entropy on the Molecular Exchange Kinetics of Polymeric Micelles". In: *ACS Macro Letters* vol. 4, no. 6 (2015), pp. 651–655. DOI: 10.1021/acsmacrolett.5b00197 (cited on pp. 9, 13, 18, 59, 77).

[62]   T. Vilgis and A. Halperin. "Aggregation of coil-crystalline block copolymers: equilibrium crystallization". In: *Macromolecules* vol. 24, no. 8 (1991), pp. 2090–2095. DOI: 10.1021/ma00008a058 (cited on pp. 9, 65, 66, 76).

[63]   Z. M. Hudson, C. E. Boott, M. E. Robinson, P. A. Rupar, M. A. Winnik, and I. Manners. "Tailored hierarchical micelle architectures using living crystallization-driven self-assembly in two dimensions". In: *Nature Chemistry* vol. 6, no. 10 (2014), pp. 893–898. DOI: 10.1038/nchem.2038 (cited on p. 10).

[64]   H. B. Qiu, Y. Gao, C. E. Boott, O. E. C. Gould, R. L. Harniman, M. J. Miles, S. E. D. Webb, M. A. Winnik, and I. Manners. "Uniform patchy and hollow rectangular platelet micelles from crystallizable polymer blends". In: *Science* vol. 352, no. 6286 (2016), pp. 697–701. DOI: 10.1126/science.aad9521 (cited on p. 10).

[65]   X. H. Jin, M. B. Price, J. R. Finnegan, C. E. Boott, J. M. Richter, A. Rao, M. Menke, R. H. Friend, G. R. Whittell, and I. Manners. "Long-range exciton transport in conjugated polymer nanofibers prepared by seeded growth". In: *Science* vol. 360, no. 6391 (2018), pp. 897–900. DOI: 10.1126/science.aar8104 (cited on p. 10).

[66] J. R. Finnegan, X. M. He, S. T. G. Street, J. D. Garcia-Hernandez, D. W. Hayward, R. L. Harniman, R. M. Richardson, G. R. Whittell, and I. Manners. "Extending the Scope of Living Crystallization-Driven Self-Assembly: Well-Defined 1D Micelles and Block Comicelles from Crystallizable Polycarbonate Block Copolymers". In: *Journal of the American Chemical Society* vol. 140, no. 49 (2018), pp. 17127–17140. DOI: 10.1021/jacs.8b09861 (cited on pp. 10, 68).

[67] J. C. Foster, S. Varlas, B. Couturaud, Z. Coe, and R. K. O'Reilly. "Getting into Shape: Reflections on a New Generation of Cylindrical Nanostructures' Self-Assembly Using Polymer Building Blocks". In: *Journal of the American Chemical Society* vol. 141, no. 7 (2019), pp. 2742–2753. DOI: 10.1021/jacs.8b08648 (cited on p. 10).

[68] Z. Coe, A. Weems, A. P. Dove, and R. K. O'Reilly. "Synthesis of Monodisperse Cylindrical Nanoparticles via Crystallization-driven Self-assembly of Biodegradable Block Copolymers". In: *Jove − Journal of Visualized Experiments*, no. 148 (2019), p. 7. DOI: 10.3791/59772 (cited on p. 10).

[69] J. Massey, K. N. Power, I. Manners, and M. A. Winnik. "Self-Assembly of a Novel Organometallic-Inorganic Block Copolymer in Solution and the Solid State: Nonintrusive Observation of Novel Wormlike Poly(ferrocenyldimethylsilane)-b-Poly(dimethylsiloxane) Micelles". In: *Journal of the American Chemical Society* vol. 120, no. 37 (1998), pp. 9533–9540. DOI: 10.1021/ja981803d (cited on p. 10).

[70] X. Wang, G. Guerin, H. Wang, Y. Wang, I. Manners, and M. A. Winnik. "Cylindrical Block Copolymer Micelles and Co-Micelles of Controlled Length and Architecture". In: *Science* vol. 317, no. 5838 (2007), pp. 644–647. DOI: 10.1126/science.1141382 (cited on p. 10).

[71] S. Nakagawa, H. Marubayashi, and S. Nojima. "Crystallization of polymer chains confined in nanodomains". In: *European Polymer Journal* vol. 70 (2015), pp. 262–275. DOI: 10.1016/j.eurpolymj.2015.07.018 (cited on p. 10).

[72] L. Zha and W. Hu. "Molecular simulations of confined crystallization in the microdomains of diblock copolymers". In: *Progress in Polymer Science* vol. 54–55 (2016), pp. 232–258. DOI: 10.1016/j.progpolymsci.2015.10.010 (cited on p. 10).

[73] P. Scherrer. "Bestimmung der Größe und der inneren Struktur von Kolloidteilchen mittels Röntgenstrahlen". In: *Nachrichten von der Gesellschaft der Wissenschaften zu Göttingen, Mathematisch-Physikalische Klasse* (1918), pp. 98–100 (cited on pp. 10, 62).

[74] S. Nojima, Y. Ohguma, S. Namiki, T. Ishizone, and K. Yamaguchi. "Crystallization of Homopolymers Confined in Spherical or Cylindrical Nanodomains". In: *Macromolecules* vol. 41, no. 6 (2008), pp. 1915–1918. DOI: 10.1021/ma7027903 (cited on pp. 10, 11).

[75]   T. Cai, Y. Qian, Y. Ma, Y. Ren, and W. Hu. "Polymer Crystallization Confined in Hard Spherical Microdomains of Diblock Copolymers". In: *Macromolecules* vol. 42, no. 9 (2009), pp. 3381–3385. DOI: 10.1021/ma900069m (cited on p. 10).

[76]   A. Das, K. Petkau-Milroy, G. Klerks, B. van Genabeek, R. P. M. Lafleur, A. R. A. Palmans, and E. W. Meijer. "Consequences of Dispersity on the Self-Assembly of ABA-Type Amphiphilic Block Co-Oligomers". In: *ACS Macro Letters* vol. 7, no. 5 (2018), pp. 546–550. DOI: 10.1021/acsmacrolett.8b00168 (cited on p. 11).

[77]   P. R. Knowles, R. J. Barlow, F. Heatley, C. Booth, and C. Price. "A study of chain dynamics in water-swollen gels of poly(ethylene oxide) dialkyl ethers using NMR and differential scanning calorimetry". In: *Macromolecular Chemistry and Physics* vol. 195, no. 7 (1994), pp. 2547–2558. DOI: 10.1002/macp.1994.021950722 (cited on pp. 11, 13, 62, 65).

[78]   L. Yin and M. A. Hillmyer. "Disklike Micelles in Water from Polyethylene-Containing Diblock Copolymers". In: *Macromolecules* vol. 44, no. 8 (2011), pp. 3021–3028. DOI: 10.1021/ma200242b (cited on pp. 11, 62, 65, 67, 68).

[79]   Z.-Y. Li, R. Liu, B.-Y. Mai, W.-J. Wang, Q. Wu, G.-D. Liang, H.-Y. Gao, and F.-M. Zhu. "Temperature-induced and crystallization-driven self-assembly of polyethylene-b-poly(ethylene oxide) in solution". In: *Polymer* vol. 54, no. 6 (2013), pp. 1663–1670. DOI: 10.1016/j.polymer.2013.01.044 (cited on pp. 11, 65, 67, 68).

[80]   G. Reiter, G. Castelein, J.-U. Sommer, A. Röttele, and T. Thurn-Albrecht. "Direct Visualization of Random Crystallization and Melting in Arrays of Nanometer-Size Polymer Crystals". In: *Physical Review Letters* vol. 87, no. 22 (2001), p. 226101. DOI: 10.1103/PhysRevLett.87.226101 (cited on p. 11).

[81]   Y. Su, G. Liu, B. Xie, D. Fu, and D. Wang. "Crystallization Features of Normal Alkanes in Confined Geometry". In: *Accounts of Chemical Research* vol. 47, no. 1 (2014), pp. 192–201. DOI: 10.1021/ar400116c (cited on pp. 11, 12, 62).

[82]   A. Röttele, T. Thurn-Albrecht, J.-U. Sommer, and G. Reiter. "Thermodynamics of Formation, Reorganization, and Melting of Confined Nanometer-Sized Polymer Crystals". In: *Macromolecules* vol. 36, no. 4 (2003), pp. 1257–1260. DOI: 10.1021/ma021434c (cited on p. 11).

[83]   C. L. Jackson and G. B. McKenna. "The melting behavior of organic materials confined in porous solids". In: *The Journal of Chemical Physics* vol. 93, no. 12 (1990), pp. 9002–9011. DOI: 10.1063/1.459240 (cited on p. 11).

[84]   O. Petrov and I. Furo. "Curvature-dependent metastability of the solid phase and the freezing-melting hysteresis in pores". In: *Physical Review E* vol. 73, no. 1 (2006), p. 011608. DOI: 10.1103/PhysRevE.73.011608 (cited on pp. 11, 68).

[85] O. Petrov and I. Furo. "A study of freezing-melting hysteresis of water in different porous materials. Part II: surfactant-templated silicas". In: *Physical Chemistry Chemical Physics* vol. 13, no. 36 (2011), pp. 16358–65. DOI: 10.1039/c1cp21902b (cited on pp. 11, 68).

[86] M. Dirand, M. Bouroukba, V. Chevallier, D. Petitjean, E. Behar, and V. Ruffier-Meray. "Normal Alkanes, Multialkane Synthetic Model Mixtures, and Real Petroleum Waxes: Crystallographic Structures, Thermodynamic Properties, and Crystallization". In: *Journal of Chemical & Engineering Data* vol. 47, no. 2 (2002), pp. 115–143. DOI: 10.1021/je0100084 (cited on pp. 11, 12, 62, 64, 65, 69, 72).

[87] V. Kravchenko. "The eutectics and solid solutions of paraffins". In: *Acta Physicochimica URSS* vol. 21 (1946), pp. 335–344 (cited on pp. 12, 69).

[88] B. K. Annis, J. D. Londono, G. D. Wignall, and R. G. Snyder. "Study of Microphase Separation in Solid, Binary Alkane Mixtures by Small Angle Neutron and X-ray Scattering". In: *The Journal of Physical Chemistry* vol. 100, no. 5 (1996), pp. 1725–1730. DOI: 10.1021/jp9512671 (cited on p. 12).

[89] X. Guo, B. A. Pethica, J. S. Huang, and R. K. Prud'homme. "Crystallization of Long-Chain n-Paraffins from Solutions and Melts As Observed by Differential Scanning Calorimetry". In: *Macromolecules* vol. 37, no. 15 (2004), pp. 5638–5645. DOI: 10.1021/ma035848x (cited on pp. 12, 72).

[90] M. Senra, E. Panacharoensawad, K. Kraiwattanawong, P. Singh, and H. S. Fogler. "Role of n-Alkane Polydispersity on the Crystallization of n-Alkanes from Solution". In: *Energy & Fuels* vol. 22, no. 1 (2008), pp. 545–555. DOI: 10.1021/ef700490k (cited on pp. 12, 72).

[91] A. A. Date and M. S. Nagarsenker. "Design and Evaluation of Microemulsions for Improved Parenteral Delivery of Propofol". In: *AAPS PharmSciTech* vol. 9, no. 1 (2008), pp. 138–145. DOI: 10.1208/s12249-007-9023-7 (cited on p. 13).

[92] S. Filippov, M. Hruby, C. Konak, H. Mackova, M. Spirkova, and P. Stepanek. "Novel pH-Responsive Nanoparticles". In: *Langmuir* vol. 24, no. 17 (2008), pp. 9295–9301. DOI: 10.1021/la801472x (cited on p. 13).

[93] X. Dong and R. J. Mumper. "Nanomedicinal strategies to treat multidrug-resistant tumors: current progress". In: *Nanomedicine* vol. 5, no. 4 (2010), pp. 597–615. DOI: 10.2217/nnm.10.35 (cited on p. 13).

[94] M. E. N. P. Ribeiro, C. L. de Moura, M. G. S. Vieira, N. V. Gramosa, C. Chaibundit, M. C. de Mattos, D. Attwood, S. G. Yeates, S. K. Nixon, and N. M. P. S. Ricardo. "Solubilisation capacity of Brij surfactants". In: *International Journal of Pharmaceutics* vol. 436, no. 1 (2012), pp. 631–635. DOI: 10.1016/j.ijpharm.2012.07.032 (cited on p. 13).

[95]   R. P. Mandal, S. Sekh, D. Mondal, and S. De. "Multifuntional role of liposome-mimicking vesicles — Potential nanoreactors and effective storehouses for hemoglobin". In: *Colloids and Surfaces A — Physicochemical and Engineering Aspects* vol. 558 (2018), pp. 33–44. DOI: 10.1016/j.colsurfa.2018.08.048 (cited on p. 13).

[96]   L. Zhang et al. "Toltrazuril mixed nanomicelle delivery system based on sodium deoxycholate-Brij C20 polyethylene ether-triton X100: Characterization, solubility, and bioavailability study". In: *Colloids and Surfaces B — Biointerfaces* vol. 163 (2018), pp. 125–132. DOI: 10.1016/j.colsurfb.2017.12.018 (cited on p. 13).

[97]   M. Ameri, D. Attwood, J. H. Collett, and C. Booth. "Self-assembly of alcohol ethoxylate non-ionic surfactants in aqueous solution". In: *Journal of the Chemical Society, Faraday Transactions* vol. 93, no. 15 (1997), pp. 2545–2551. DOI: 10.1039/A701662J (cited on pp. 13, 69).

[98]   F. Laflèche, T. Nicolai, D. Durand, Y. Gnanou, and D. Taton. "Association of Adhesive Spheres Formed by Hydrophobically End-Capped PEO. 2. Influence of the Alkyl End-Group Length and the Chain Backbone Architecture". In: *Macromolecules* vol. 36, no. 4 (2003), pp. 1341–1348. DOI: 10.1021/ma0210776 (cited on pp. 13, 20, 75).

[99]   C. Sommer, J. S. Pedersen, and V. M. Garamus. "Structure and Interactions of Block Copolymer Micelles of Brij 700 Studied by Combining Small-Angle X-ray and Neutron Scattering". In: *Langmuir* vol. 21, no. 6 (2005), pp. 2137–2149. DOI: 10.1021/la047489k (cited on pp. 13, 61, 75).

[100] T. Zinn, L. Willner, R. Lund, V. Pipich, M. S. Appavou, and D. Richter. "Surfactant or block copolymer micelles? Structural properties of a series of well-defined n-alkyl-PEO micelles in water studied by SANS". In: *Soft Matter* vol. 10, no. 28 (2014), pp. 5212–20. DOI: 10.1039/c4sm00625a (cited on pp. 13, 32, 59, 61, 65, 75).

[101] M. Amann, L. Willner, J. Stellbrink, A. Radulescu, and D. Richter. "Studying the concentration dependence of the aggregation number of a micellar model system by SANS". In: *Soft Matter* vol. 11, no. 21 (2015), pp. 4208–17. DOI: 10.1039/c5sm00469a (cited on pp. 13, 59).

[102] T. Zinn, L. Willner, K. D. Knudsen, and R. Lund. "Self-Assembly of Mixtures of Telechelic and Monofunctional Amphiphilic Polymers in Water: From Clusters to Flowerlike Micelles". In: *Macromolecules* vol. 50, no. 18 (2017), pp. 7321–7332. DOI: 10.1021/acs.macromol.7b01501 (cited on pp. 13, 20, 21, 33, 59, 81, 82).

[103] M. Vuorte, J. Määttä, and M. Sammalkorpi. "Simulations Study of Single-Component and Mixed n-Alkyl-PEG Micelles". In: *The Journal of Physical Chemistry B* vol. 122, no. 18 (2018), pp. 4851–4860. DOI: 10.1021/acs.jpcb.8b00398 (cited on pp. 13, 68, 96).

[104]   T. Zinn, L. Willner, and R. Lund. "Telechelic Polymer Hydrogels: Relation between the Microscopic Dynamics and Macroscopic Viscoelastic Response". In: *ACS Macro Letters* vol. 5, no. 12 (2016), pp. 1353–1356. DOI: 10.1021/acsmacrolett.6b00824 (cited on pp. 13, 18, 22, 59, 79, 81, 82, 85).

[105]   T. Zinn, L. Willner, R. Lund, V. Pipich, and D. Richter. "Equilibrium exchange kinetics in n-alkyl–PEO polymeric micelles: single exponential relaxation and chain length dependence". In: *Soft Matter* vol. 8, no. 3 (2012), pp. 623–626. DOI: 10.1039/c1sm06809a (cited on pp. 13, 17, 48, 59, 65, 76).

[106]   T. Zinn, L. Willner, V. Pipich, D. Richter, and R. Lund. "Molecular Exchange Kinetics of Micelles: Corona Chain Length Dependence". In: *ACS Macro Letters* vol. 5, no. 7 (2016), pp. 884–888. DOI: 10.1021/acsmacrolett.6b00395 (cited on pp. 13, 17, 59, 80, 81, 96).

[107]   F. Heatley, H. H. Teo, and C. Booth. "Proton longitudinal and transverse magnetic relaxation in dilute aqueous solutions of poly(oxyethylene) alkyl ethers". In: *Journal of the Chemical Society, Faraday Transactions 1: Physical Chemistry in Condensed Phases* vol. 80, no. 4 (1984), pp. 981–991. DOI: 10.1039/F19848000981 (cited on pp. 13, 62, 63).

[108]   T. Zinn, L. Willner, and R. Lund. "Nanoscopic confinement through self-assembly: crystallization within micellar cores exhibits simple Gibbs-Thomson behavior". In: *Physical Review Letters* vol. 113, no. 23 (2014), p. 238305. DOI: 10.1103/PhysRevLett.113.238305 (cited on pp. 13, 59, 62, 68, 72, 74).

[109]   B. Plazzotta, J. Dai, M. A. Behrens, I. Furo, and J. S. Pedersen. "Core Freezing and Size Segregation in Surfactant Core–Shell Micelles". In: *The Journal of Physical Chemistry B* vol. 119, no. 33 (2015), pp. 10798–10806. DOI: 10.1021/acs.jpcb.5b06041 (cited on pp. 13, 96).

[110]   J. Dai, Z. Alaei, B. Plazzotta, J. S. Pedersen, and I. Furo. "Release of Solubilizate from Micelle upon Core Freezing". In: *The Journal of Physical Chemistry B* vol. 121, no. 45 (2017), pp. 10353–10363. DOI: 10.1021/acs.jpcb.7b08912 (cited on p. 13).

[111]   R. Lund, L. Willner, M. Monkenbusch, P. Panine, T. Narayanan, J. Colmenero, and D. Richter. "Structural Observation and Kinetic Pathway in the Formation of Polymeric Micelles". In: *Physical Review Letters* vol. 102, no. 18 (2009), p. 188301. DOI: 10.1103/PhysRevLett.102.188301 (cited on p. 14).

[112]   R. Zana. *Dynamics of Surfactant Self-Assemblies: Micelles, Microemulsions, Vesicles and Lyotropic Phases.* CRC Press, 2005 (cited on p. 14).

[113]   E. A. G. Aniansson, S. N. Wall, M. Almgren, H. Hoffmann, I. Kielmann, W. Ulbricht, R. Zana, J. Lang, and C. Tondre. "Theory of Kinetics of Micellar Equilibria and Quantitative Interpretation of Chemical Relaxation Studies of Micellar Solutions of Ionic Surfactants". In: *Journal of Physical Chemistry* vol. 80, no. 9 (1976), pp. 905–922. DOI: 10.1021/j100550a001 (cited on p. 14).

[114]   M. Kahlweit. "Kinetics of formation of association colloids". In: *Journal of Colloid and Interface Science* vol. 90, no. 1 (1982), pp. 92–99. DOI: 10.1016/0021-9797(82)90401-5 (cited on p. 14).

[115]   A. Halperin and S. Alexander. "Polymeric micelles: their relaxation kinetics". In: *Macromolecules* vol. 22, no. 5 (1989), pp. 2403–2412. DOI: 10.1021/ma00195a069 (cited on pp. 14, 15, 17, 18, 76, 96).

[116]   E. A. Aniansson and S. N. Wall. "Kinetics of Step-Wise Micelle Association". In: *Journal of Physical Chemistry* vol. 78, no. 10 (1974), pp. 1024–1030. DOI: 10.1021/j100603a016 (cited on p. 14).

[117]   E. A. G. Aniansson and S. N. Wall. "Correction and Improvement of on Kinetics of Step-Wise Micelle Association by Aniansson and Wall". In: *Journal of Physical Chemistry* vol. 79, no. 8 (1975), pp. 857–858. DOI: 10.1021/j100575a019 (cited on p. 14).

[118]   A. Halperin. "On Micellar Exchange: The Role of the Insertion Penalty". In: *Macromolecules* vol. 44, no. 13 (2011), pp. 5072–5074. DOI: 10.1021/ma200811x (cited on pp. 14, 17, 96).

[119]   H. A. Kramers. "Brownian motion in a field of force and the diffusion model of chemical reactions". In: *Physica* vol. 7, no. 4 (1940), pp. 284–304. DOI: https://doi.org/10.1016/S0031-8914(40)90098-2 (cited on p. 14).

[120]   S. Chandrasekhar. "Stochastic Problems in Physics and Astronomy". In: *Reviews of Modern Physics* vol. 15, no. 1 (1943), pp. 1–89. DOI: 10.1103/RevModPhys.15.1 (cited on p. 14).

[121]   R. Lund, L. Willner, and D. Richter. "Kinetics of Block Copolymer Micelles Studied by Small-Angle Scattering Methods". In: *Controlled Polymerization and Polymeric Structures: Flow Microreactor Polymerization, Micelles Kinetics, Polypeptide Ordering, Light Emitting Nanostructures*. Ed. by A. Abe, K.-S. Lee, L. Leibler, and S. Kobayashi. Springer International Publishing, 2013, pp. 51–158. DOI: 10.1007/12_2012_204 (cited on pp. 15, 59).

[122]   B. Michels, G. Waton, and R. Zana. "Dynamics of Micelles of Poly(ethylene oxide)-Poly(propylene oxide)-Poly(ethylene oxide) Block Copolymers in Aqueous Solutions". In: *Langmuir* vol. 13, no. 12 (1997), pp. 3111–3118. DOI: 10.1021/la962084o (cited on p. 15).

[123]   T. Thurn, S. Couderc-Azouani, D. M. Bloor, J. F. Holzwarth, and E. Wyn-Jones. "Ultrasonic Relaxation in Micellar Solutions of Nonionic Triblock Copolymers". In: *Langmuir* vol. 19, no. 10 (2003), pp. 4363–4370. DOI: 10.1021/la020987d (cited on p. 15).

[124] K. Prochazka, B. Bednar, E. Mukhtar, P. Svoboda, J. Trnena, and M. Almgren. "Nonradiative energy transfer in block copolymer micelles". In: *The Journal of Physical Chemistry* vol. 95, no. 11 (1991), pp. 4563–4568. DOI: 10.1021/j100164a069 (cited on p. 15).

[125] K. Prochazka, D. Kiserow, C. Ramireddy, Z. Tuzar, P. Munk, and S. E. Webber. "Time-resolved fluorescence studies of the chain dynamics of naphthalene-labeled polystyrene-block-poly(methacrylic acid) micelles in aqueous media". In: *Macromolecules* vol. 25, no. 1 (1992), pp. 454–460. DOI: 10.1021/ma00027a071 (cited on p. 15).

[126] Y. Wang, C. M. Kausch, M. Chun, R. P. Quirk, and W. L. Mattice. "Exchange of Chains between Micelles of Labeled Polystyrene-block-poly(oxyethylene) As Monitored by Nonradiative Singlet Energy Transfer". In: *Macromolecules* vol. 28, no. 4 (1995), pp. 904–911. DOI: 10.1021/ma00108a016 (cited on p. 15).

[127] C. K. Smith and G. Liu. "Determination of the Rate Constant for Chain Insertion into Poly(methyl methacrylate)-block-poly(methacrylic acid) Micelles by a Fluorescence Method". In: *Macromolecules* vol. 29, no. 6 (1996), pp. 2060–2067. DOI: 10.1021/ma951338u (cited on p. 15).

[128] R. S. Underhill, J. Ding, V. I. Birss, and G. Liu. "Chain Exchange Kinetics of Polystyrene-block-poly(2-cinnamoylethyl methacrylate) Micelles in THF/Cyclopentane Mixtures". In: *Macromolecules* vol. 30, no. 26 (1997), pp. 8298–8303. DOI: 10.1021/ma9710545 (cited on p. 15).

[129] L. Zhang, H. Shen, and A. Eisenberg. "Phase Separation Behavior and Crew-Cut Micelle Formation of Polystyrene-b-poly(acrylic acid) Copolymers in Solutions". In: *Macromolecules* vol. 30, no. 4 (1997), pp. 1001–1011. DOI: 10.1021/ma961413g (cited on p. 15).

[130] F. J. Esselink, E. E. Dormidontova, and G. Hadziioannou. "Redistribution of Block Copolymer Chains between Mixed Micelles in Solution". In: *Macromolecules* vol. 31, no. 15 (1998), pp. 4873–4878. DOI: 10.1021/ma9802069 (cited on p. 15).

[131] M. J. Kositza, C. Bohne, P. Alexandridis, T. A. Hatton, and J. F. Holzwarth. "Micellization Dynamics and Impurity Solubilization of the Block-Copolymer L64 in an Aqueous Solution". In: *Langmuir* vol. 15, no. 2 (1999), pp. 322–325. DOI: 10.1021/la9812368 (cited on p. 15).

[132] G. Waton, B. Michels, and R. Zana. "Dynamics of Block Copolymer Micelles in Aqueous Solution". In: *Macromolecules* vol. 34, no. 4 (2001), pp. 907–910. DOI: 10.1021/ma001170z (cited on p. 15).

[133] L. Willner, A. Poppe, J. Allgaier, M. Monkenbusch, and D. Richter. "Time-resolved SANS for the determination of unimer exchange kinetics in block copolymer micelles". In: *Europhysics Letters* vol. 55, no. 5 (2001), pp. 667–673. DOI: 10.1209/epl/i2001-00467-y (cited on pp. 16, 47, 76).

[134] R. Lund, L. Willner, J. Stellbrink, P. Lindner, and D. Richter. "Logarithmic chain-exchange kinetics of diblock copolymer micelles". In: *Physical Review Letters* vol. 96, no. 6 (2006), pp. 068302-1–4. DOI: 10.1103/PhysRevLett.96.068302 (cited on p. 16).

[135] S. H. Choi, T. P. Lodge, and F. S. Bates. "Mechanism of Molecular Exchange in Diblock Copolymer Micelles: Hypersensitivity to Core Chain Length". In: *Physical Review Letters* vol. 104, no. 4 (2010), pp. 047802-1–4. DOI: 10.1103/PhysRevLett.104.047802 (cited on pp. 16, 76).

[136] R. Lund, L. Willner, J. Stellbrink, P. Lindner, and D. Richter. "Correction: Logarithmic Chain-Exchange Kinetics of Diblock Copolymer Micelles (vol 96, art no 068302, 2006)". In: *Physical Review Letters* vol. 104, no. 4 (2010), pp. 049902-1–2. DOI: 10.1103/PhysRevLett.104.049902 (cited on pp. 16, 76).

[137] Z. Li and E. E. Dormidontova. "Equilibrium chain exchange kinetics in block copolymer micelle solutions by dissipative particle dynamics simulations". In: *Soft Matter* vol. 7, no. 9 (2011), pp. 4179–4188. DOI: 10.1039/C0SM01443E (cited on pp. 16, 18, 96).

[138] F. A. Garcia Daza, J. Bonet Avalos, and A. D. Mackie. "Logarithmic Exchange Kinetics in Monodisperse Copolymeric Micelles". In: *Physical Review Letters* vol. 118, no. 24 (2017), pp. 248001-1–5. DOI: 10.1103/PhysRevLett.118.248001 (cited on p. 17).

[139] R. Lund, L. Willner, V. Pipich, I. Grillo, P. Lindner, J. Colmenero, and D. Richter. "Equilibrium Chain Exchange Kinetics of Diblock Copolymer Micelles: Effect of Morphology". In: *Macromolecules* vol. 44, no. 15 (2011), pp. 6145–6154. DOI: 10.1021/ma200532r (cited on pp. 17, 18, 48).

[140] D. Zhao, Y. Ma, and T. P. Lodge. "Exchange Kinetics for a Single Block Copolymer in Micelles of Two Different Sizes". In: *Macromolecules* vol. 51, no. 6 (2018), pp. 2312–2320. DOI: 10.1021/acs.macromol.7b02550 (cited on pp. 17–19, 80).

[141] S.-H. Choi, F. S. Bates, and T. P. Lodge. "Molecular Exchange in Ordered Diblock Copolymer Micelles". In: *Macromolecules* vol. 44, no. 9 (2011), pp. 3594–3604. DOI: 10.1021/ma102788v (cited on p. 17).

[142] J. Lu, F. S. Bates, and T. P. Lodge. "Addition of Corona Block Homopolymer Retards Chain Exchange in Solutions of Block Copolymer Micelles". In: *Macromolecules* vol. 49, no. 4 (2016), pp. 1405–1413. DOI: 10.1021/acs.macromol.5b02395 (cited on p. 17).

[143] E. Wang, J. Lu, F. S. Bates, and T. P. Lodge. "Effect of Corona Block Length on the Structure and Chain Exchange Kinetics of Block Copolymer Micelles". In: *Macromolecules* vol. 51, no. 10 (2018), pp. 3563–3571. DOI: 10.1021/acs.macromol.7b02732 (cited on pp. 18, 96).

[144] Y. Ma and T. P. Lodge. "Chain Exchange Kinetics in Diblock Copolymer Micelles in Ionic Liquids: The Role of chi". In: *Macromolecules* vol. 49, no. 24 (2016), pp. 9542–9552. DOI: 10.1021/acs.macromol.6b02212 (cited on p. 18).

[145] E. Wang, J. Zhu, D. Zhao, S. Xie, F. S. Bates, and T. P. Lodge. "Effect of Solvent Selectivity on Chain Exchange Kinetics in Block Copolymer Micelles". In: *Macromolecules* vol. 53, no. 1 (2020), pp. 417–426. DOI: 10.1021/acs.macromol.9b01877 (cited on p. 18).

[146] J. Lu, S. Choi, F. S. Bates, and T. P. Lodge. "Molecular Exchange in Diblock Copolymer Micelles: Bimodal Distribution in Core-Block Molecular Weights". In: *ACS Macro Letters* vol. 1, no. 8 (2012), pp. 982–985. DOI: 10.1021/mz300285x (cited on pp. 18, 76, 77).

[147] J. Lu, F. S. Bates, and T. P. Lodge. "Chain Exchange in Binary Copolymer Micelles at Equilibrium: Confirmation of the Independent Chain Hypothesis". In: *ACS Macro Letters* vol. 2, no. 5 (2013), pp. 451–455. DOI: 10.1021/mz400167x (cited on pp. 18, 76, 77).

[148] A. Prhashanna and E. E. Dormidontova. "Micelle Self-Assembly and Chain Exchange Kinetics of Tadpole Block Copolymers with a Cyclic Corona Block". In: *Macromolecules* vol. 53, no. 3 (2020), pp. 982–991. DOI: 10.1021/acs.macromol.9b02398 (cited on p. 18).

[149] J. Lu, F. S. Bates, and T. P. Lodge. "Remarkable Effect of Molecular Architecture on Chain Exchange in Triblock Copolymer Micelles". In: *Macromolecules* vol. 48, no. 8 (2015), pp. 2667–2676. DOI: 10.1021/acs.macromol.5b00294 (cited on pp. 18–20, 22, 82, 83, 86).

[150] A. J. Peters and T. P. Lodge. "Chain Exchange Kinetics of Asymmetric B1AB2 Linear Triblock and AB1B2 Branched Triblock Copolymers". In: *Macromolecules* vol. 50, no. 16 (2017), pp. 6303–6313. DOI: 10.1021/acs.macromol.7b01046 (cited on pp. 18, 19, 86, 96).

[151] A. Prhashanna and S. B. Chen. "Chain exchange kinetics between linear ABA-type triblock copolymer micelles". In: *Polymer* vol. 118 (2017), pp. 22–29. DOI: 10.1016/j.polymer.2017.04.049 (cited on pp. 18, 19, 86, 96).

[152] L. Zhang and A. Eisenberg. "Thermodynamic vs Kinetic Aspects in the Formation and Morphological Transitions of Crew-Cut Aggregates Produced by Self-Assembly of Polystyrene-b-poly(acrylic acid) Block Copolymers in Dilute Solution". In: *Macromolecules* vol. 32, no. 7 (1999), pp. 2239–2249. DOI: 10.1021/ma981039f (cited on p. 19).

[153] S. Jain and F. S. Bates. "Consequences of Nonergodicity in Aqueous Binary PEO-PB Micellar Dispersions". In: *Macromolecules* vol. 37, no. 4 (2004), pp. 1511–1523. DOI: 10.1021/ma035467j (cited on pp. 19, 71).

[154] R. P. Murphy, E. G. Kelley, S. A. Rogers, M. O. Sullivan, and T. H. Epps. "Unlocking Chain Exchange in Highly Amphiphilic Block Polymer Micellar Systems: Influence of Agitation". In: *ACS Macro Letters* vol. 3, no. 11 (2014), pp. 1106–1111. DOI: 10.1021/mz500435d (cited on pp. 19, 93).

[155] R. Lund, L. Willner, D. Richter, H. Iatrou, N. Hadjichristidis, and P. Lindner. "Unraveling the equilibrium chain exchange kinetics of polymeric micelles using small-angle neutron scattering - architectural and topological effects". In: *Journal of Applied Crystallography* vol. 40, no. s1 (2007), s327–s331. DOI: 10.1107/S0021889807005201 (cited on p. 19).

[156] G. Moad and D. H. Solomon. "Copolymerization". In: *The Chemistry of Radical Polymerization*. Ed. by G. Moad and D. H. Solomon. Elsevier Science Ltd, 2005. Chap. 7, pp. 333–412. DOI: 10.1016/B978-008044288-4/50026-1 (cited on p. 20).

[157] T. Annable, R. Buscall, R. Ettelaie, and D. Whittlestone. "The rheology of solutions of associating polymers: Comparison of experimental behavior with transient network theory". In: *Journal of Rheology* vol. 37, no. 4 (1993), pp. 695–726. DOI: 10.1122/1.550391 (cited on pp. 20, 21).

[158] E. Alami, M. Almgren, W. Brown, and J. Francois. "Aggregation of Hydrophobically End-Capped Poly(ethylene oxide) in Aqueous Solutions. Fluorescence and Light-Scattering Studies". In: *Macromolecules* vol. 29, no. 6 (1996), pp. 2229–2243. DOI: 10.1021/ma951174h (cited on pp. 20, 21).

[159] Y. Serero, R. Aznar, G. Porte, J. F. Berret, D. Calvet, A. Collet, and M. Viguier. "Associating Polymers: From 'Flowers' to Transient Networks". In: *Physical Review Letters* vol. 81, no. 25 (1998), pp. 5584–5587. DOI: 10.1103/PhysRevLett.81.5584 (cited on pp. 20, 21).

[160] A. S. Hoffman et al. "Design of 'Smart' polymers that can direct intracellular drug delivery". In: *Polymers for Advanced Technologies* vol. 13, no. 10–12 (2002), pp. 992–999. DOI: 10.1002/pat.232 (cited on p. 20).

[161] S. V. Vinogradov, T. K. Bronich, and A. V. Kabanov. "Nanosized cationic hydrogels for drug delivery: preparation, properties and interactions with cells". In: *Advanced Drug Delivery Reviews* vol. 54, no. 1 (2002), pp. 135–147. DOI: 10.1016/S0169-409X(01)00245-9 (cited on p. 20).

[162] S. van Vlierberghe, P. Dubruel, and E. Schacht. "Biopolymer-Based Hydrogels As Scaffolds for Tissue Engineering Applications: A Review". In: *Biomacromolecules* vol. 12, no. 5 (2011), pp. 1387–1408. DOI: 10.1021/bm200083n (cited on p. 20).

[163] J. Appell, G. Porte, and M. Rawiso. "Interactions between Nonionic Surfactant Micelles Introduced by a Telechelic Polymer. A Small Angle Neutron Scattering Study". In: *Langmuir* vol. 14, no. 16 (1998), pp. 4409–4414. DOI: 10.1021/la9712395 (cited on p. 20).

[164] C. Rufier, A. Collet, M. Viguier, J. Oberdisse, and S. Mora. "Influence of Surfactants on Hydrophobically End-Capped Poly(ethylene oxide) Self-Assembled Aggregates Studied by SANS". In: *Macromolecules* vol. 44, no. 18 (2011), pp. 7451–7459. DOI: 10.1021/ma201150g (cited on p. 20).

[165] I. W. Hamley, J. P. A. Fairclough, A. J. Ryan, C. Y. Ryu, T. P. Lodge, A. J. Gleeson, and J. S. Pedersen. "Micellar Ordering in Concentrated Solutions of Di- and Triblock Copolymers in a Slightly Selective Solvent". In: *Macromolecules* vol. 31, no. 4 (1998), pp. 1188–1196. DOI: 10.1021/ma970831y (cited on pp. 20, 21).

[166] E. Beaudoin, O. Borisov, A. Lapp, L. Billon, R. C. Hiorns, and J. Francois. "Neutron Scattering of Hydrophobically Modified Poly(ethylene oxide) in Aqueous Solutions". In: *Macromolecules* vol. 35, no. 19 (2002), pp. 7436–7447. DOI: 10.1021/ma0110271 (cited on p. 20).

[167] X.-X. Meng and W. B. Russel. "Structure and Size of Spherical Micelles of Telechelic Polymers". In: *Macromolecules* vol. 38, no. 2 (2005), pp. 593–600. DOI: 10.1021/ma048968t (cited on p. 20).

[168] Q. T. Pham, W. B. Russel, J. C. Thibeault, and W. Lau. "Micellar Solutions of Associative Triblock Copolymers: Entropic Attraction and Gas-Liquid Transition". In: *Macromolecules* vol. 32, no. 9 (1999), pp. 2996–3005. DOI: 10.1021/ma982007v (cited on p. 20).

[169] W. Mingvanish, C. Chaibundit, and C. Booth. "Mixed micellisation of oxyethylene–oxybutylene diblock and triblock copolymers in water studied by light scattering". In: *Physical Chemistry Chemical Physics* vol. 4, no. 5 (2002), pp. 778–784. DOI: 10.1039/B109634F (cited on p. 20).

[170] F. Laflèche, D. Durand, and T. Nicolai. "Association of Adhesive Spheres Formed by Hydrophobically End-Capped PEO. 1. Influence of the Presence of Single End-Capped PEO". In: *Macromolecules* vol. 36, no. 4 (2003), pp. 1331–1340. DOI: 10.1021/ma021076d (cited on pp. 20, 21, 85).

[171] M. E. Seitz, W. R. Burghardt, K. T. Faber, and K. R. Shull. "Self-Assembly and Stress Relaxation in Acrylic Triblock Copolymer Gels". In: *Macromolecules* vol. 40, no. 4 (2007), pp. 1218–1226. DOI: 10.1021/ma061993+ (cited on pp. 20, 21, 85).

[172] D. G. Abebe, K.-Y. Liu, S. R. Mishra, A. H. F. Wu, R. N. Lamb, and T. Fujiwara. "Time-resolved SANS analysis of micelle chain exchange behavior: thermal crosslink driven by stereocomplexation of PLA–PEG–PLA micelles". In: *RSC Advances* vol. 5, no. 116 (2015), pp. 96019–96027. DOI: 10.1039/c5ra14921e (cited on pp. 20, 21).

[173] A. N. Semenov, J. F. Joanny, and A. R. Khokhlov. "Associating polymers: Equilibrium and linear viscoelasticity". In: *Macromolecules* vol. 28, no. 4 (1995), pp. 1066–1075. DOI: 10.1021/ma00108a038 (cited on pp. 20, 21).

[174] J. Francois, E. Beaudoin, and O. Borisov. "Association of Hydrophobically End-Capped Poly(ethylene oxide). 2. Phase Diagrams". In: *Langmuir* vol. 19, no. 24 (2003), pp. 10011–10018. DOI: 10.1021/la0208833 (cited on p. 20).

[175] A. J. de Graaf et al. "Looped Structure of Flowerlike Micelles Revealed by 1H NMR Relaxometry and Light Scattering". In: *Langmuir* vol. 27, no. 16 (2011), pp. 9843–9848. DOI: 10.1021/la2019605 (cited on p. 20).

[176] M. Ghelichi and N. T. Qazvini. "Self-organization of hydrophobic-capped triblock copolymers with a polyelectrolyte midblock: a coarse-grained molecular dynamics simulation study". In: *Soft Matter* vol. 12, no. 20 (2016), pp. 4611–4620. DOI: 10.1039/C6SM00414H (cited on p. 20).

[177] S. Maiti and P. R. Chatterji. "Transition from Normal to Flowerlike Micelles". In: *The Journal of Physical Chemistry B* vol. 104, no. 44 (2000), pp. 10253–10257. DOI: 10.1021/jp000248a (cited on pp. 20, 21).

[178] C. Chassenieux, T. Nicolai, and L. Benyahia. "Rheology of associative polymer solutions". In: *Current Opinion in Colloid & Interface Science* vol. 16, no. 1 (2011), pp. 18–26. DOI: 10.1016/j.cocis.2010.07.007 (cited on p. 21).

[179] M. Bohdan, J. Sprakel, and J. van der Gucht. "Multiple relaxation modes in associative polymer networks with varying connectivity". In: *Physical Review E* vol. 94, no. 3 (2016), p. 032507. DOI: 10.1103/PhysRevE.94.032507 (cited on pp. 21, 85).

[180] Y. N. Ye, K. Cui, T. Indei, T. Nakajima, D. Hourdet, T. Kurokawa, and J. P. Gong. "Relaxation Dynamics and Underlying Mechanism of a Thermally Reversible Gel from Symmetric Triblock Copolymer". In: *Macromolecules* vol. 52, no. 22 (2019), pp. 8651–8661. DOI: 10.1021/acs.macromol.9b01856 (cited on pp. 21, 85).

[181] F. Tanaka and S. F. Edwards. "Viscoelastic properties of physically crosslinked networks. 1. Transient network theory". In: *Macromolecules* vol. 25, no. 5 (1992), pp. 1516–1523. DOI: 10.1021/ma00031a024 (cited on pp. 21, 22, 81).

[182] H. Yokoyama and E. J. Kramer. "Diffusion of Triblock Copolymers in a Spherical Domain Structure". In: *Macromolecules* vol. 33, no. 3 (2000), pp. 954–959. DOI: 10.1021/ma991202m (cited on pp. 22, 82, 96).

[183] H. Yokoyama, E. J. Kramer, and G. H. Fredrickson. "Simulation of Diffusion of Asymmetric Diblock and Triblock Copolymers in a Spherical Domain Structure". In: *Macromolecules* vol. 33, no. 6 (2000), pp. 2249–2257. DOI: 10.1021/ma991203e (cited on pp. 23, 82, 96).

[184] R. Laxminarayan et al. "Antibiotic resistance - the need for global solutions". In: *The Lancet Infectious Diseases* vol. 13, no. 12 (2013), pp. 1057–1098. DOI: 10.1016/S1473-3099(13)70318-9 (cited on p. 23).

[185] C. Walsh. "Molecular mechanisms that confer antibacterial drug resistance". In: *Nature* vol. 406, no. 6797 (2000), pp. 775–781. DOI: 10.1038/35021219 (cited on p. 23).

[186] M. E. Falagas, S. K. Kasiakou, and L. D. Saravolatz. "Colistin: The Revival of Polymyxins for the Management of Multidrug-Resistant Gram-Negative Bacterial Infections". In: *Clinical Infectious Diseases* vol. 40, no. 9 (2005), pp. 1333–1341. DOI: 10.1086/429323 (cited on p. 23).

[187] R. E. W. Hancock and H.-G. Sahl. "Antimicrobial and host-defense peptides as new anti-infective therapeutic strategies". In: *Nature Biotechnology* vol. 24, no. 12 (2006), pp. 1551–1557. DOI: 10.1038/nbt1267 (cited on p. 24).

[188] A. Peschel and H.-G. Sahl. "The co-evolution of host cationic antimicrobial peptides and microbial resistance". In: *Nature Reviews Microbiology* vol. 4, no. 7 (2006), pp. 529–536. DOI: 10.1038/nrmicro1441 (cited on p. 24).

[189] M. Zasloff. "Antimicrobial peptides of multicellular organisms". In: *Nature* vol. 415, no. 6870 (2002), pp. 389–395. DOI: 10.1038/415389a (cited on p. 24).

[190] C. D. Fjell, J. A. Hiss, R. E. W. Hancock, and G. Schneider. "Designing antimicrobial peptides: form follows function". In: *Nature Reviews Drug Discovery* vol. 11, no. 1 (2012), pp. 37–51. DOI: 10.1038/nrd3591 (cited on p. 24).

[191] A. K. Marr, W. J. Gooderham, and R. E. W. Hancock. "Antibacterial peptides for therapeutic use: obstacles and realistic outlook". In: *Current Opinion in Pharmacology* vol. 6, no. 5 (2006), pp. 468–472. DOI: 10.1016/j.coph.2006.04.006 (cited on p. 24).

[192] X. Tian, F. Sun, X. R. Zhou, S. Z. Luo, and L. Chen. "Role of peptide self-assembly in antimicrobial peptides". In: *Journal of Peptide Science* vol. 21, no. 7 (2015), pp. 530–539. DOI: 10.1002/psc.2788 (cited on pp. 24, 25).

[193] S. Malekkhaiat Häffner and M. Malmsten. "Influence of self-assembly on the performance of antimicrobial peptides". In: *Current Opinion in Colloid & Interface Science* vol. 38 (2018), pp. 56–79. DOI: 10.1016/j.cocis.2018.09.002 (cited on pp. 24, 25).

[194] L. Lombardi, A. Falanga, V. Del Genio, and S. Galdiero. "A New Hope: Self-Assembling Peptides with Antimicrobial Activity". In: *Pharmaceutics* vol. 11, no. 4 (2019), pp. 166-1–17. DOI: 10.3390/pharmaceutics11040166 (cited on p. 24).

[195] Z. Tu, J. Hao, R. Kharidia, X. G. Meng, and J. F. Liang. "Improved stability and selectivity of lytic peptides through self-assembly". In: *Biochemical and Biophysical Research Communications* vol. 361, no. 3 (2007), pp. 712–717. DOI: 10.1016/j.bbrc.2007.06.178 (cited on pp. 24, 25).

[196] C. Chen, J. Hu, S. Zhang, P. Zhou, X. Zhao, H. Xu, X. Zhao, M. Yaseen, and J. R. Lu. "Molecular mechanisms of antibacterial and antitumor actions of designed surfactant-like peptides". In: *Biomaterials* vol. 33, no. 2 (2012), pp. 592–603. DOI: 10.1016/j.biomaterials.2011.09.059 (cited on p. 24).

[197] L. Chen and J. F. Liang. "Peptide Fibrils with Altered Stability, Activity, And Cell Selectivity". In: *Biomacromolecules* vol. 14, no. 7 (2013), pp. 2326–2331. DOI: 10.1021/bm400618m (cited on pp. 24, 25).

[198] L. Liu, K. Xu, H. Wang, P. K. Jeremy Tan, W. Fan, S. S. Venkatraman, L. Li, and Y.-Y. Yang. "Self-assembled cationic peptide nanoparticles as an efficient antimicrobial agent". In: *Nature Nanotechnology* vol. 4, no. 7 (2009), pp. 457–463. DOI: 10.1038/nnano.2009.153 (cited on pp. 24, 25).

[199] L. Schnaider et al. "Self-assembling dipeptide antibacterial nanostructures with membrane disrupting activity". In: *Nature Communications* vol. 8, no. 1 (2017), pp. 1365-1–10. DOI: 10.1038/s41467-017-01447-x (cited on pp. 24, 25).

[200] M. Hughes, S. Debnath, C. W. Knapp, and R. V. Ulijn. "Antimicrobial properties of enzymatically triggered self-assembling aromatic peptide amphiphiles". In: *Biomaterials Science* vol. 1, no. 11 (2013), pp. 1138–1142. DOI: 10.1039/C3BM60135H (cited on p. 25).

[201] D. A. Salick, D. J. Pochan, and J. P. Schneider. "Design of an Injectable beta-Hairpin Peptide Hydrogel That Kills Methicillin-Resistant Staphylococcus aureus". In: *Advanced Materials* vol. 21, no. 41 (2009), pp. 4120–4123. DOI: 10.1002/adma.200900189 (cited on p. 25).

[202] H. Chu et al. "Human alpha-Defensin 6 Promotes Mucosal Innate Immunity Through Self-Assembled Peptide Nanonets". In: *Science* vol. 337, no. 6093 (2012), pp. 477-1–6. DOI: 10.1126/science.1218831 (cited on p. 25).

[203] P. Chairatana, H. Chu, P. A. Castillo, B. Shen, C. L. Bevins, and E. M. Nolan. "Proteolysis triggers self-assembly and unmasks innate immune function of a human alpha-defensin peptide". In: *Chemical Science* vol. 7, no. 3 (2016), pp. 1738–1752. DOI: 10.1039/C5SC04194E (cited on p. 25).

[204] E. de Santis et al. "Antimicrobial peptide capsids of de novo design". In: *Nature Communications* vol. 8, no. 1 (2017), pp. 2263-1–11. DOI: 10.1038/s41467-017-02475-3 (cited on p. 25).

[205]   S. L. Porter, S. M. Coulter, S. Pentlavalli, T. P. Thompson, and G. Laverty. "Self-assembling diphenylalanine peptide nanotubes selectively eradicate bacterial biofilm infection". In: *Acta Biomaterialia* vol. 77 (2018), pp. 96–105. DOI: 10.1016/j.actbio.2018.07.033 (cited on p. 25).

[206]   H. Dong, S. E. Paramonov, L. Aulisa, E. L. Bakota, and J. D. Hartgerink. "Self-Assembly of Multidomain Peptides: Balancing Molecular Frustration Controls Conformation and Nanostructure". In: *Journal of the American Chemical Society* vol. 129, no. 41 (2007), pp. 12468–12472. DOI: 10.1021/ja072536r (cited on p. 26).

[207]   M. Yang, D. Xu, L. Jiang, L. Zhang, D. Dustin, R. Lund, L. Liu, and H. Dong. "Filamentous supramolecular peptide–drug conjugates as highly efficient drug delivery vehicles". In: *Chemical Communications* vol. 50, no. 37 (2014), pp. 4827–4830. DOI: 10.1039/C4CC01568A (cited on pp. 26, 87).

[208]   L. Jiang, D. Xu, T. J. Sellati, and H. Dong. "Self-assembly of cationic multidomain peptide hydrogels: supramolecular nanostructure and rheological properties dictate antimicrobial activity". In: *Nanoscale* vol. 7, no. 45 (2015), pp. 19160–19169. DOI: 10.1039/C5NR05233E (cited on pp. 26, 28, 93).

[209]   D. Xu, L. Jiang, A. Singh, D. Dustin, M. Yang, L. Liu, R. Lund, T. J. Sellati, and H. Dong. "Designed supramolecular filamentous peptides: balance of nanostructure, cytotoxicity and antimicrobial activity". In: *Chemical Communications* vol. 51, no. 7 (2015), pp. 1289–1292. DOI: 10.1039/C4CC08808E (cited on pp. 26, 28, 35, 86, 87, 89, 93).

[210]   D. Xu, Q. Ran, Y. Xiang, L. Jiang, B. M. Smith, F. Bou-Abdallah, R. Lund, Z. Li, and H. Dong. "Toward hemocompatible self-assembling antimicrobial nanofibers: understanding the synergistic effect of supramolecular structure and PEGylation on hemocompatibility". In: *RSC Advances* vol. 6, no. 19 (2016), pp. 15911–15919. DOI: 10.1039/C5RA24553B (cited on pp. 26, 28, 29, 35, 86, 87, 89, 91, 93).

[211]   D. Xu et al. "Fabrication and Microscopic and Spectroscopic Characterization of Cytocompatible Self-Assembling Antimicrobial Nanofibers". In: *ACS Infectious Diseases* vol. 4, no. 9 (2018), pp. 1327–1335. DOI: 10.1021/acsinfecdis.8b00069 (cited on pp. 26, 28, 29, 91, 93).

[212]   W. Chen, S. Yang, S. Li, J. C. Lang, C. Mao, P. Kroll, L. Tang, and H. Dong. "Self-Assembled Peptide Nanofibers Display Natural Antimicrobial Peptides to Selectively Kill Bacteria without Compromising Cytocompatibility". In: *ACS Applied Materials & Interfaces* vol. 11, no. 32 (2019), pp. 28681–28689. DOI: 10.1021/acsami.9b09583 (cited on p. 26).

[213]   W. Humphrey, A. Dalke, and K. Schulten. "VMD: Visual molecular dynamics". In: *Journal of Molecular Graphics* vol. 14, no. 1 (1996), pp. 33–38. DOI: 10.1016/0263-7855(96)00018-5 (cited on p. 27).

[214]   A. Abuchowski, J. R. McCoy, N. C. Palczuk, T. van Es, and F. F. Davis. "Effect of covalent attachment of polyethylene glycol on immunogenicity and circulating life of bovine liver catalase". In: *Journal of Biological Chemistry* vol. 252, no. 11 (1977), pp. 3582–3586 (cited on p. 29).

[215]   F. M. Veronese and G. Pasut. "PEGylation, successful approach to drug delivery". In: *Drug Discovery Today* vol. 10, no. 21 (2005), pp. 1451–1458. DOI: 10.1016/S1359-6446(05)03575-0 (cited on p. 29).

[216]   J. E. Nielsen, N. König, M. W. A. Skoda, A. Maestro, H. Dong, M. Cardenas, and R. Lund. *Lipid membrane interactions of self-assembling antimicrobial nanofibers: effect of PEGylation.* Manuscript in preparation (cited on pp. 29, 60, 93).

[217]   M. Amann. "Micellar Structure, Interactions and Phase Behavior of C28-PEO Polymer Micelles Studied by HR-SANS". PhD thesis. Westfälische Wilhelms-Universität Münster, 2017 (cited on pp. 32, 59).

[218]   T. Zemb and P. Lindner. *Neutrons, X-rays and Light: Scattering Methods Applied to Soft Condensed Matter.* Elsevier, 2002 (cited on pp. 37, 41).

[219]   D. I. Svergun, M. H. J. Koch, P. A. Timmins, and R. P. May. *Small Angle X-Ray and Neutron Scattering from Solutions of Biological Macromolecules.* Oxford University Press, 2013 (cited on pp. 37, 41).

[220]   M. Born. "Zur Quantenmechanik der Stoßvorgänge". In: *Zeitschrift für Physik* vol. 37, no. 12 (1926), pp. 863–867. DOI: 10.1007/BF01397477 (cited on p. 38).

[221]   J. S. Pedersen, D. Posselt, and K. Mortensen. "Analytical treatment of the resolution function for small-angle scattering". In: *Journal of Applied Crystallography* vol. 23, no. 4 (1990), pp. 321–333. DOI: 10.1107/S0021889890003946 (cited on p. 43).

[222]   J. G. Barker and J. S. Pedersen. "Instrumental Smearing Effects in Radially Symmetric Small-Angle Neutron Scattering by Numerical and Analytical Methods". In: *Journal of Applied Crystallography* vol. 28, no. 2 (1995), pp. 105–114. DOI: 10.1107/S0021889894010095 (cited on p. 43).

[223]   Norwegian Centre for X-ray Diffraction, Scattering and Imaging (RECX). *Small Angle Scattering.* Last visited on April 16, 2020. URL: http://www.recx.no/instruments/small-angle-scattering/ (cited on p. 43).

[224]   P. Pernot et al. "Upgraded ESRF BM29 beamline for SAXS on macromolecules in solution". In: *Journal of Synchrotron Radiation* vol. 20, no. 4 (2013), pp. 660–664. DOI: 10.1107/S0909049513010431 (cited on p. 43).

[225]   V. F. Sears. "Neutron scattering lengths and cross sections". In: *Neutron News* vol. 3, no. 3 (1992), pp. 26–37. DOI: 10.1080/10448639208218770 (cited on pp. 44, 45).

[226]   J. R. Rumble, ed. *CRC Handbook of Chemistry and Physics, 100th Edition (Internet Version 2019).* CRC Press/Taylor & Francis, 2019 (cited on p. 45).

[227] U. Rücker et al. "The Jülich high-brilliance neutron source project". In: *The European Physical Journal Plus* vol. 131, no. 1 (2016), pp. 19-1–14. DOI: 10.1140/epjp/i2016-16019-5 (cited on p. 45).

[228] A. Radulescu, N. K. Szekely, and M.-S. Appavou. "KWS-2: Small angle scattering diffractometer". In: *Journal of large-scale research facilities JLSRF* vol. 1 (2015), A29-1–5. DOI: 10.17815/jlsrf-1-27 (cited on p. 46).

[229] R. K. Heenan, S. E. Rogers, D. Turner, A. E. Terry, J. Treadgold, and S. M. King. "Small Angle Neutron Scattering Using Sans2d". In: *Neutron News* vol. 22, no. 2 (2011), pp. 19–21. DOI: 10.1080/10448632.2011.569531 (cited on p. 46).

[230] U. Krengel, H. Sørensen, N. Mahmoudi, R. Lund, and N. König. *Small-Angle Neutron Scattering studies of a bacterial colonization factor.* STFC ISIS Neutron and Muon Source, 2019. DOI: 10.5286/ISIS.E.RB1920565 (cited on p. 46).

[231] R. Lund, N. König, N. Mahmoudi, L. Willner, and L. Willner. *Tuning the Molecular Exchange Kinetics of Self-Assembled Antimicrobial Peptide-Polymer Conjugates.* STFC ISIS Neutron and Muon Source, 2019. DOI: 10.5286/ISIS.E.RB1910106 (cited on p. 46).

[232] R. Lund, N. König, L. Cavalcanti, L. Willner, and H. Sørensen. *Exchange kinetics of telechelic Cn-PEO-Cn micelles: effect of conformation and crystallinity.* STFC ISIS Neutron and Muon Source, 2019. DOI: 10.5286/ISIS.E.RB1920656 (cited on p. 46).

[233] J. P. Cotton. "Variations on contrast in SANS: determination of self and distinct correlation functions". In: *Advances in Colloid and Interface Science* vol. 69, no. 1 (1996), pp. 1–29. DOI: 10.1016/S0001-8686(96)00306-5 (cited on p. 47).

[234] O. Kratky, H. Leopold, and H. Stabinger. "Device for density determination". U.S. Patent 3523446A. August 11, 1970 (cited on p. 54).

[235] Anton Paar GmbH. *Density and density measurement.* Last visited on April 16, 2020. URL: https://wiki.anton-paar.com/us-en/density-and-density-measurement/ (cited on p. 54).

[236] G. Höhne, W. F. Hemminger, and H.-J. Flammersheim. *Differential Scanning Calorimetry.* Springer, 2003 (cited on p. 55).

[237] T. D. Claridge. *High-Resolution NMR Techniques in Organic Chemistry.* Elsevier, 2016. DOI: 10.1016/c2015-0-04654-8 (cited on p. 56).

[238] J. P. Hornak. *The Basics of NMR.* Last visited on April 17, 2020. URL: http://www.cis.rit.edu/htbooks/nmr/ (cited on p. 56).

[239] E. R. Andrew, A. Bradbury, and R. G. Eades. "Nuclear Magnetic Resonance Spectra from a Crystal rotated at High Speed". In: *Nature* vol. 182, no. 4650 (1958), pp. 1659–1659. DOI: 10.1038/1821659a0 (cited on p. 57).

[240] I. J. Lowe. "Free Induction Decays of Rotating Solids". In: *Physical Review Letters* vol. 2, no. 7 (1959), pp. 285–287. DOI: 10.1103/PhysRevLett.2.285 (cited on p. 57).

[241] S. R. Hartmann and E. L. Hahn. "Nuclear Double Resonance in the Rotating Frame". In: *Physical Review* vol. 128, no. 5 (1962), pp. 2042–2053. DOI: 10.1103/PhysRev.128.2042 (cited on p. 57).

[242] G. A. Morris. "Sensitivity enhancement in nitrogen-15 NMR: polarization transfer using the INEPT pulse sequence". In: *Journal of the American Chemical Society* vol. 102, no. 1 (1980), pp. 428–429. DOI: 10.1021/ja00521a097 (cited on p. 57).

[243] D. M. Thomas, M. R. Bendall, D. T. Pegg, D. M. Doddrell, and J. Field. "Two-dimensional 13C-1H polarization transfer J spectroscopy". In: *Journal of Magnetic Resonance (1969)* vol. 42, no. 2 (1981), pp. 298–306. DOI: 10.1016/0022-2364(81)90219-5 (cited on p. 57).

[244] A. Nowacka, P. C. Mohr, J. Norrman, R. W. Martin, and D. Topgaard. "Polarization transfer solid-state NMR for studying surfactant phase behavior". In: *Langmuir* vol. 26, no. 22 (2010), pp. 16848–16856. DOI: 10.1021/la102935t (cited on p. 57).

[245] T. M. Ferreira, B. Medronho, R. W. Martin, and D. Topgaard. "Segmental order parameters in a nonionic surfactant lamellar phase studied with 1H-13C solid-state NMR". In: *Physical Chemistry Chemical Physics* vol. 10, no. 39 (2008), pp. 6033–6038. DOI: 10.1039/B807693F (cited on p. 57).

[246] T. M. Ferreira, F. Coreta-Gomes, O. H. S. Ollila, M. J. Moreno, W. L. C. Vaz, and D. Topgaard. "Cholesterol and POPC segmental order parameters in lipid membranes: solid state 1H-13C NMR and MD simulation studies". In: *Physical Chemistry Chemical Physics* vol. 15, no. 6 (2013), pp. 1976–1989. DOI: 10.1039/C2CP42738A (cited on p. 57).

[247] S. V. Dvinskikh, H. Zimmermann, A. Maliniak, and D. Sandström. "Measurements of motionally averaged heteronuclear dipolar couplings in MAS NMR using R-type recoupling". In: *Journal of Magnetic Resonance* vol. 168, no. 2 (2004), pp. 194–201. DOI: 10.1016/j.jmr.2004.03.001 (cited on p. 57).

[248] R. Lund. "Chain exchange kinetics and structure of polymeric micelles". PhD thesis. Westfälische Wilhelms-Universität Münster, 2004 (cited on p. 59).

[249] T. Zinn. "Molecular Exchange Kinetics and Structure of n-Alkyl-PEO Polymeric Micelles Studied by SANS". PhD thesis. Westfälische Wilhelms-Universität Münster, 2013 (cited on p. 59).

[250] W. R. Turner. "Normal Alkanes". In: *Product R&D* vol. 10, no. 3 (1971), pp. 238–260. DOI: 10.1021/i360039a003 (cited on p. 62).

[251]   D. Fu, Y. Liu, X. Gao, Y. Su, G. Liu, and D. Wang. "Binary n-Alkane Mixtures from Total Miscibility to Phase Separation in Microcapsules: Enrichment of Shorter Component in Surface Freezing and Enhanced Stability of Rotator Phases". In: *The Journal of Physical Chemistry B* vol. 116, no. 10 (2012), pp. 3099–3105. DOI: 10.1021/jp2125119 (cited on pp. 62, 70).

[252]   L. Yin, T. P. Lodge, and M. A. Hillmyer. "A Stepwise 'Micelliza-tion–Crystallization' Route to Oblate Ellipsoidal, Cylindrical, and Bilayer Micelles with Polyethylene Cores in Water". In: *Macromolecules* vol. 45, no. 23 (2012), pp. 9460–9467. DOI: 10.1021/ma302069s (cited on pp. 62, 67, 68).

[253]   C. W. Bunn. "The crystal structure of long-chain normal paraffin hydrocarbons. The 'shape' of the CH2 group". In: *Transactions of the Faraday Society* vol. 35, no. 0 (1939), pp. 482–491. DOI: 10.1039/TF9393500482 (cited on p. 62).

[254]   J. H. Ortony, C. J. Newcomb, J. B. Matson, L. C. Palmer, P. E. Doan, B. M. Hoffman, and S. I. Stupp. "Internal dynamics of a supramolecular nanofibre". In: *Nature Materials* vol. 13, no. 8 (2014), pp. 812–816. DOI: 10.1038/nmat3979 (cited on p. 63).

[255]   C. Branca, A. Faraone, G. Maisano, S. Magazu, P. Migliardo, A. Triolo, R. Triolo, and V. Villari. "Can the isotopic H-D substitution affect the conformational properties of polymeric aqueous solutions? The poly(ethylene oxide)-water case". In: *Journal of Physics: Condensed Matter* vol. 11, no. 32 (1999), pp. 6079–6098. DOI: 10.1088/0953-8984/11/32/301 (cited on p. 65).

[256]   C. Branca, A. Faraone, S. Magazu, G. Maisano, P. Migliardo, A. Triolo, R. Triolo, and V. Villari. "Anomalous conformational properties of PEO in H2O and D2O by SANS, PCS and Raman scattering". In: *Journal of Applied Crystallography* vol. 33, no. 3-1 (2000), pp. 709–713. DOI: 10.1107/S0021889899013242 (cited on p. 65).

[257]   Q. Zhang, C. G. Clark, M. Wang, E. E. Remsen, and K. L. Wooley. "Thermally-Induced (Re)shaping of Core-Shell Nanocrystalline Particles". In: *Nano Letters* vol. 2, no. 10 (2002), pp. 1051–1054. DOI: 10.1021/nl025653n (cited on pp. 67, 68).

[258]   R. Liu, Z.-Y. Li, B.-Y. Mai, Q. Wu, G.-D. Liang, H.-Y. Gao, and F.-M. Zhu. "Crystalline-coil diblock copolymers of syndiotactic polypropylene-b-poly(ethylene oxide): synthesis, solution self-assembly, and confined crystallization in nanosized micelle cores". In: *Journal of Polymer Research* vol. 20, no. 2 (2013), pp. 64-1–11. DOI: 10.1007/s10965-012-0064-6 (cited on pp. 67, 68).

[259] S. K. Agrawal, N. Sanabria-DeLong, G. N. Tew, and S. R. Bhatia. "Structural Characterization of PLA-PEO-PLA Solutions and Hydrogels: Crystalline vs Amorphous PLA Domains". In: *Macromolecules* vol. 41, no. 5 (2008), pp. 1774–1784. DOI: 10.1021/ma070634r (cited on pp. 67, 68).

[260] A. L. Schmitt, M. H. Repollet-Pedrosa, and M. K. Mahanthappa. "Polydispersity-Driven Block Copolymer Amphiphile Self-Assembly into Prolate-Spheroid Micelles". In: *ACS Macro Letters* vol. 1, no. 2 (2012), pp. 300–304. DOI: 10.1021/mz200156s (cited on p. 67).

[261] S. Lin, X. He, Y. Li, J. Lin, and T. Nose. "Brownian Molecular Dynamics Simulation on Self-Assembly Behavior of Diblock Copolymers: Influence of Chain Conformation". In: *The Journal of Physical Chemistry B* vol. 113, no. 42 (2009), pp. 13926–13934. DOI: 10.1021/jp904707a (cited on p. 68).

[262] E. Sevgen, M. Dolejsi, P. F. Nealey, J. A. Hubbell, and J. J. de Pablo. "Nanocrystalline Oligo(ethylene sulfide)-b-poly(ethylene glycol) Micelles: Structure and Stability". In: *Macromolecules* vol. 51, no. 23 (2018), pp. 9538–9546. DOI: 10.1021/acs.macromol.8b01812 (cited on p. 68).

[263] N. Petzetakis, D. Walker, A. P. Dove, and R. K. O'Reilly. "Crystallization-driven sphere-to-rod transition of poly(lactide)-b-poly(acrylic acid) diblock copolymers: mechanism and kinetics". In: *Soft Matter* vol. 8, no. 28 (2012), pp. 7408–7414. DOI: 10.1039/C2SM25247C (cited on p. 68).

[264] S. Noack, D. Schanzenbach, J. Koetz, and H. Schlaad. "Polylactide-Based Amphiphilic Block Copolymers: Crystallization-Induced Self-Assembly and Stereocomplexation". In: *Macromolecular Rapid Communications* vol. 40, no. 1 (2019), p. 6. DOI: 10.1002/marc.201800639 (cited on p. 68).

[265] J.-T. Xu, J. P. A. Fairclough, S.-M. Mai, and A. J. Ryan. "The effect of architecture on the morphology and crystallization of oxyethylene/oxybutylene block copolymers from micelles in n-hexane". In: *Journal of Materials Chemistry* vol. 13, no. 11 (2003), pp. 2740–2748. DOI: 10.1039/b307511g (cited on p. 68).

[266] A. Goebel and K. Lunkenheimer. "Interfacial Tension of the Water/n-Alkane Interface". In: *Langmuir* vol. 13, no. 2 (1997), pp. 369–372. DOI: 10.1021/la960800g (cited on p. 69).

[267] S. Zeppieri, J. Rodriguez, and A. L. Lopez de Ramos. "Interfacial Tension of Alkane + Water Systems". In: *Journal of Chemical & Engineering Data* vol. 46, no. 5 (2001), pp. 1086–1088. DOI: 10.1021/je000245r (cited on p. 69).

[268] R.-J. Roe. "Interfacial tension between polymer liquids". In: *Journal of Colloid and Interface Science* vol. 31, no. 2 (1969), pp. 228–235. DOI: 10.1016/0021-9797(69)90330-0 (cited on p. 69).

[269] G. L. Gaines and G. L. Gaines. "The interfacial tension between n-alkanes and poly(ethylene glycols)". In: *Journal of Colloid and Interface Science* vol. 63, no. 2 (1978), pp. 394–398. DOI: 10.1016/0021-9797(78)90149-2 (cited on p. 69).

[270] Y. Liu, S. Consta, and W. A. Goddard. "Nanoimmiscibility: Selective Absorption of Liquid Methanol-Water Mixtures in Carbon Nanotubes". In: *Journal of Nanoscience and Nanotechnology* vol. 10, no. 6 (2010), pp. 3834–3843. DOI: 10.1166/jnn.2010.1999 (cited on p. 70).

[271] L. Wu, A. Malijevsky, C. Avendano, E. A. Müller, and G. Jackson. "Demixing, surface nematization, and competing adsorption in binary mixtures of hard rods and hard spheres under confinement". In: *The Journal of Chemical Physics* vol. 148, no. 16 (2018), pp. 164701-1–11. DOI: 10.1063/1.5020002 (cited on p. 70).

[272] C. Honda, K. Yamamoto, and T. Nose. "Comicellization of binary mixtures of block copolymers with different block lengths in a selective solvent". In: *Polymer* vol. 37, no. 10 (1996), pp. 1975–1984. DOI: 10.1016/0032-3861(96)87316-2 (cited on p. 71).

[273] S. I. Yoo, B.-H. Sohn, W.-C. Zin, J. C. Jung, and C. Park. "Mixtures of Diblock Copolymer Micelles by Different Mixing Protocols". In: *Macromolecules* vol. 40, no. 23 (2007), pp. 8323–8328. DOI: 10.1021/ma071534o (cited on p. 71).

[274] M. Maroncelli, H. L. Strauss, and R. G. Snyder. "Structure of the n-alkane binary solid n-C19H40/n-C21H44 by infrared spectroscopy and calorimetry". In: *The Journal of Physical Chemistry* vol. 89, no. 24 (1985), pp. 5260–5267. DOI: 10.1021/j100270a028 (cited on p. 72).

[275] M.-J. Hafezi and F. Sharif. "Brownian dynamics simulation of amphiphilic block copolymers with different tail lengths, comparison with theory and comicelles". In: *Journal of Molecular Graphics and Modelling* vol. 62 (2015), pp. 165–173. DOI: 10.1016/j.jmgm.2015.09.005 (cited on p. 73).

[276] D. B. Wright, J. P. Patterson, A. Pitto-Barry, A. Lu, N. Kirby, N. C. Gianneschi, C. Chassenieux, O. Colombani, and R. K. O'Reilly. "The Copolymer Blending Method: A New Approach for Targeted Assembly of Micellar Nanoparticles". In: *Macromolecules* vol. 48, no. 18 (2015), pp. 6516–6522. DOI: 10.1021/acs.macromol.5b01426 (cited on p. 73).

[277] G. E. Newby, I. W. Hamley, S. M. King, C. M. Martin, and N. J. Terrill. "Structure, rheology and shear alignment of Pluronic block copolymer mixtures". In: *Journal of Colloid and Interface Science* vol. 329, no. 1 (2009), pp. 54–61. DOI: 10.1016/j.jcis.2008.09.054 (cited on p. 74).

[278] D. Zhao, Y. C. Ma, E. Wang, and T. P. Lodge. "Micellization of Binary Diblock Co-polymer Mixtures in an Ionic Liquid". In: *Macromolecules* vol. 52, no. 12 (2019), pp. 4729–4738. DOI: 10.1021/acs.macromol.9b00613 (cited on p. 74).

[279] M. Laurati, J. Stellbrink, R. Lund, L. Willner, D. Richter, and E. Zaccarelli. "Starlike Micelles with Starlike Interactions: A Quantitative Evaluation of Structure Factors and Phase Diagram". In: *Physical Review Letters* vol. 94, no. 19 (2005), pp. 195504-1–4. DOI: 10.1103/PhysRevLett. 94.195504 (cited on p. 74).

[280] M. Maccarini, G. Briganti, S. Rucareanu, X.-D. Lui, R. Sinibaldi, M. Sztucki, and R. B. Lennox. "Characterization of Poly(ethylene oxide)-Capped Gold Nanoparticles in Water by Means of Transmission Electron Microscopy, Thermogravimetric Analysis, Mass Density, and Small Angle Scattering". In: *The Journal of Physical Chemistry C* vol. 114, no. 15 (2010), pp. 6937–6943. DOI: 10.1021/jp9118088 (cited on p. 75).

[281] T. A. Grünewald, A. Lassenberger, P. D. J. van Oostrum, H. Rennhofer, R. Zirbs, B. Capone, I. Vonderhaid, H. Amenitsch, H. C. Lichtenegger, and E. Reimhult. "Core-Shell Structure of Monodisperse Poly(ethylene glycol)-Grafted Iron Oxide Nanoparticles Studied by Small-Angle X-ray Scattering". In: *Chemistry of Materials* vol. 27, no. 13 (2015), pp. 4763–4771. DOI: 10.1021/acs.chemmater.5b01488 (cited on p. 75).

[282] U. Dahal, Z. Wang, and E. E. Dormidontova. "Hydration of Spherical PEO-Grafted Gold Nanoparticles: Curvature and Grafting Density Effect". In: *Macromolecules* vol. 51, no. 15 (2018), pp. 5950–5961. DOI: 10.1021/ acs.macromol.8b01114 (cited on p. 75).

[283] E. Mylonas and D. I. Svergun. "Accuracy of molecular mass determination of proteins in solution by small-angle X-ray scattering". In: *Journal of Applied Crystallography* vol. 40, no. s1 (2007), s245–s249. DOI: 10.1107/ S002188980700252X (cited on p. 87).

[284] R. Viswanathan, A. Asensio, and J. J. Dannenberg. "Cooperative Hydrogen-Bonding in Models of Antiparallel Beta-Sheets". In: *The Journal of Physical Chemistry A* vol. 108, no. 42 (2004), pp. 9205–9212. DOI: 10.1021/jp047404o (cited on p. 93).

Papers

Paper I

Spherical micelles with a non-spherical core: the effect of core crystallization

Nico König, Lutz Willner, Göran Carlström, Thomas Zinn, Kenneth D. Knudsen, Frode Rise, Daniel Topgaard and Reidar Lund

Manuscript

Spherical micelles with a non-spherical core: the effect of core crystallization

Nico König,[a,b] Lutz Willner,[b] Göran Carlström,[c] Thomas Zinn,[d]
Kenneth D. Knudsen,[e] Frode Rise,[a] Daniel Topgaard[c] and Reidar Lund[a]

[a] Department of Chemistry, University of Oslo, P.O. Box 1033, Blindern, 0315 Oslo, Norway
[b] Jülich Centre for Neutron Science (JCNS) and Institute for Complex Systems (ICS), Forschungszentrum Jülich GmbH, 52425 Jülich, Germany
[c] Division of Physical Chemistry, Department of Chemistry, Lund University, Lund, Sweden
[d] ESRF - The European Synchrotron, 38043 Grenoble, France
[e] Department for Neutron Materials Characterization, Institute for Energy Technology, P.O. Box 40, 2027 Kjeller, Norway

Introduction

The self-assembly of polymers is leading to a multitude of different nanostructures have found application in many different fields.[1–3] Generally, association is driven by a reduction in the surface energy, notably in water by the hydrophobic effect [4]. However, over recent years, other driving forces are being exploited such as crystallization-driven self-assembly (CSDA).[5–9] Crystallization, or at least packing into semi-ordered structures, is also important in more complex systems, like the cell membrane.

Yet, to better understand complex phenomena, it is customary to employ simpler, well-defined model systems. An excellent example are n-alkyl-functionalized poly(ethylene oxide) (C_n-PEOx) polymers, where the index n denotes the number of carbon atoms in the n-alkyl block and x the PEO molecular weight in kg/mol. These polymers have been used as model materials to investigate fundamental properties of non-ionic amphiphilic block copolymers. When dissolved in water, C_n-PEOx typically forms well-defined micellar entities. The highly hydrophobic, core-forming n-alkyl blocks represent the simplest hydrocarbons and are monodisperse. The hydrophilic, shell-forming PEO blocks, on the other hand, are chemically stable and can be synthesized with very low polydispersities ($Đ < 1.05$) by sophisticated living polymerization techniques. Therefore, C_n-PEOx has been employed extensively to investigate phenomena like micellar aggregation behavior[10–17], molecular exchange kinetics[18–22] or macroscopic rheology[23, 24]. A peculiar feature of C_n-PEOx with $n \gtrsim 18$ is (partial) core crystallization below a certain temperature as observed via differential scanning calorimetry (DSC), nuclear magnetic resonance spectroscopy (NMR) and density measurements [25–27] which may effect micellar structure and properties. For instance, Plazzotta et al. found that core freezing lead to size segregation in a mixture of C_{18}-PEO1 and C_{18}-PEO5, even though the core blocks were identical.[28] The same group later exploited core freezing to trigger

the release of a hydrophobic cargo from the micellar core.[29] However, the exact nature of the crystalline phase (conformational/orientational/spatial order) and how it affects the micellar shape is not yet clear.

Irrespective of unknown details about the core structure, we recently reported on the effect of core crystallization on the molecular exchange kinetics between C_n-PEOx micelles.[19, 21] Surprisingly, the effect is rather straightforward: In crystalline samples, the melting enthalpy is simply added to the thermal activation energy of the respective molten sample and the melting enthalpy can easily be tuned by co-assembling C_n-PEOx with different n-alkyl block lengths.[17] However, it is not yet clear what kind of order the n-alkyl chains adopt in the supposedly crystalline core. In bulk crystalline phases, n-alkane molecules align in parallel and adopt an all-trans conformation. In addition, there is a second solid-like phase before the actual melting transition, the so-called rotator phase. Here, the n-alkane molecules retain their parallel orientation but gain a rotational degree of freedom around the longitudinal axis.[30] Both phases are suitable candidates for the state of the C_n-PEOx n-alkyl blocks in solidified micellar cores. Nonetheless, in our previous structural studies, we assumed that the core was spherical even though it is unclear how crystallized, all-trans n-alkyl chains can arrange in a spherical domain.

In the present paper, we address these issues using scattering techniques in combination with NMR spectroscopy. We use small-angle neutron scattering (SANS) with contrast-matched PEO and sophisticated modeling of micellar form factors to determine the shape of the core. In addition, linewidth analysis of regular ^{1}H solution NMR spectra gives an idea about the general chain mobility while ^{13}C solid-state NMR (ssNMR) reveals further details. [13]C shifts indicate the n-alkyl isomerization, all-trans vs. trans-gauche. In the liquid phase, overall anisotropy and the rate of CH bond reorientation are quantified by the order parameter S_{CH}, whereas in the solid phase $R_{1\rho}$ dispersion sheds light on the correlation time τ_c. Lastly, wide-angle X-ray scattering (WAXS) yields information about the spatial order of the n-alkyl chains in both molten and crystalline condition.

Experimental Section

Synthesis

The C_n-PEOx polymers were synthesized via ring-opening living anionic polymerization of ethylene oxide (EO) in toluene. 1-Docosanol and 1-octacosanol, respectively, were used in a 80/20 mixture with their respective potassium alkanolates as initiator system. Homogeneous polymerization conditions were obtained at 95 °C and, together with a fast proton exchange, uniform polymers with desired molecular weights and narrow polydispersities were synthesized. The general chemical structure is shown in Figure I.1a). More details about the synthesis can be found in References [13] and [31]. Beside the ordinary proteated C_n-hPEOx, deuterated and partly deuterated polymers were synthesized following the same synthetic protocol. Fully deuterated C_n-dPEOx was prepared

Polymer	$N_{PEO}{}^a$	$M_n{}^a$ (g/mol)	$M_n{}^b$ (g/mol)	$M_w{}^b$ (g/mol)	$M_w/M_n{}^b$
C_{28}-hdPEO5^c	102	5240	4900	5020	1.025
C_{28}-hPEO5^d	108	5160	4800	4850	1.01
C_{28}-hPEO3^d	53	2750	2670	2780	1.04
C_{28}-hPEO5^e	108	5160	4950	5050	1.02
C_{22}-dPEO5^f	118	-	5980	6100	1.02
hPEO5^{d,g}	-	-	5000	-	-
hPEO3^{d,g}	-	-	3000	-	-

^{a} from NMR $\qquad\qquad\qquad\quad$ ^{b} from SEC
^{c} used in SAS experiments $\qquad$ ^{d} used in WAXS experiments
^{e} used in ^{13}C NMR experiments $\quad$ ^{f} used in ^{1}H NMR experiments
^{g} commercial product

Table I.1: Characteristics of the polymers used in this study.

from d-EO and partly deuterated C_{28}-hdPEOx from a 82/18 molar mixture of d- and h-EO leading to a random distribution of monomers along the PEO chains.

The polymers were characterized by size-exclusion chromatography (SEC), using a multidetector chromatographic set-up consisting of autosampler, isocratic pump (both Agilent Technologies, Series 1260 infinity), a column oven (Shimadzu CTO-20A), a refractive index (RI) detector (Optilab rEX), and an 18 angle light scattering detector (DAWN HELEOS-II), both detectors from Wyatt Technologies. The SEC instrument was equipped with three consecutive GPC columns with continuous pore size distribution (Agilent PlusPore) which ensured high resolution. To suppress interaction effects, a mixture of tetrahydrofuran, *N,N*-dimethylacetamide and acetic acid (85:14:1vol%) was used as eluent at a flux rate of $1\,\text{mL/min}$ and a temperature of $40\,°C$. Absolute molecular weight characteristics, M_w and M_n, were obtained from Zimm analysis of the RI and LS signals of the chromatograms using Astra Software from Wyatt Technologies. The polydispersities were determined as $Đ \approx 1.02$ for all polymers. As a consistency check, M_n of the proteated polymers was additionally determined by ^{1}H NMR in deuterochloroform. The *n*-alkane signals served as internal reference for the calculation of the degree of PEO polymerization. Characterization results of all polymers used in this study are summarized in Table I.1.

Sample preparation

For all samples mentioned in this work, dry polymer powder was dissolved in ultrapure H_2O/D_2O ($18.2\,\text{M}\Omega \cdot \text{cm}$) to attain the desired volume fraction. The solutions were shaken for at least one hour at $70\,°C$, well above all relevant melting points, and then over night at room temperature to ensure well-equilibrated, homogeneous samples. The following volume fractions and isotopic mixtures were used:

SANS/SAXS. C_{28}-hdPEO5 with $82\,\text{vol}\%$ dEO content was dissolved in pure

D$_2$O (Sigma-Aldrich), which is very close to the PEO match point. Samples with volume fractions $\phi = 0.25$ vol% and 4.0 vol% were prepared.

WAXS. C$_{28}$-hPEO5 and -hPEO3 were dissolved in H$_2$O to attain a polymer volume fraction of 5 vol%.

^{1}*H NMR.* C$_{22}$-dPEO5 was dissolved in pure D$_2$O (Sigma-Aldrich) at $\phi = 0.5$ vol%. Traces of 3-(trimethylsilyl)-2,2,3,3-tetradeuteropropionic acid (TMSP-d_4, Sigma-Aldrich) were added to calibrate the chemical shifts. As a reference, a second sample was prepared in CDCl$_3$ (Sigma-Aldrich) at the same volume fraction.

^{13}*C ssNMR.* C$_{28}$-hPEO5 lyophilisate was mechanically mixed with an equal volume of D$_2$O (Sigma-Aldrich). The sample was repeatedly centrifuged to obtain a homogeneous gel.

Small-Angle Neutron Scattering

Small-angle neutron scattering (SANS) experiments were performed at the time-of-flight instrument Sans2d at the STFC ISIS Neutron and Muon Source in Didcot, United Kingdom.[32] At a detector distance of 4 m, a Q range of about $0.004 - 0.7 \,\text{Å}^{-1}$ was covered and the collection time was 50 min per sample and temperature. The scattering patterns were reduced and background-corrected according to instrument standard procedures. Since the PEO corona was almost contrast-matched, the scattering signal was dominated by the contribution of the alkyl core. This allowed us to follow the structural evolution of the core during melting by increasing the temperature from below the melting point to above ($T_{\text{exp}} = 40 - 70\,^\circ\text{C}, T_m = 57\,^\circ\text{C}$). To achieve high-quality data over the whole Q-range, both a high- and low-concentration sample (0.25 vol% and 4 vol%) were measured. On the one hand, the low-concentration sample provides the pure micellar form factor without structure factor contributions at low Q but the signal-to-noise ratio at higher Q is very low. On the other hand, the high-concentration sample exhibits a strong structure factor at low Q but provides high-quality data at high Q. Therefore, both data sets were normalized by concentration — which yielded a perfect overlap at intermediate Q — and then combined to yield the pure form factor with high signal-to-noise ratio over the entire Q range. The combined data were then analyzed with a theoretical scattering model described below.

Small-Angle X-ray Scattering

Complementary small-angle X-ray scattering (SAXS) experiments were performed at our in-house Bruker NanoStar SAXS instrument at the Norwegian Centre for X-ray Diffraction, Scattering and Imaging (RECX), located at the University of Oslo, Norway. The instrument covers a Q range of $0.009 - 0.3\,\text{Å}^{-1}$ and the collection time was 60 min. The exact same samples from the SANS beamtime were measured both at 40 $^\circ$C and 70 $^\circ$C to provide reference scattering

patterns with PEO contribution, both below and above the core melting transition. Data reduction and background-correction were performed according to instrument standard procedures and the high- and low-concentration measurements were combined in the same way as the SANS measurements. The data were analyzed simultaneously with the respective SANS measurements using the scattering model described below.

Wide-Angle X-ray Scattering

Additional wide-angle X-ray scattering (WAXS) experiments were performed at beamline ID02 (ESRF, France) using an X-ray energy of 12.46 keV (wavelength $\lambda = 0.995$ Å). Typically, the WAXS detector (Rayonix LX-170HS) permits to covers the Q-range of $5 - 50$ /nm and the angular resolution determined by the point spread function of the detector is about 0.01°.

^{1}H Nuclear Magnetic Resonance Spectroscopy

Conventional solution proton nuclear magnetic resonance spectroscopy (^{1}H NMR) was performed at the University of Oslo NMR Center using a Bruker Avance I 600 MHz NMR spectrometer equipped with a TCI cryo probe. The program Topspin 2.1 (patch level 6) was used for both acquisition and processing. C_{22}-dPEO5 samples dissolved in D_2O and $CDCl_3$ at approximately 0.5 vol% were measured in standard 5 mm NMR tubes at temperatures $T = 10 - 50$ °C ($T_m = 29$ °C). In D_2O, minute amounts of TMSP-d_4 were used to calibrate the chemical shifts, whereas in deuterochloroform the residual $CHCl_3$ signal was used. After the set temperature was reached, the spectrometer was shimmed and the sample left to equilibrate for 10 min before a second round of shimming as well as tuning and matching were performed, followed by the actual measurement. To suppress the residual H_2O signal, an excitation sculpting (pulse programme: zgesgp) suppression scheme[33] was employed.

^{13}C Solid-State Nuclear Magnetic Resonance Spectroscopy

Magic angle spinning (MAS) solid-state carbon nuclear magnetic resonance spectroscopy (^{13}C ssNMR) was performed at the NMR Center of Lund University using a Bruker Avance Neo 500 MHz NMR spectrometer equipped with a Bruker 4 mm HCP E-free MAS probe. Topspin 4.0 (patch level 7) was used for both acquisition and processing. A ~ 50 wt% C_{28}-hPEO5 gel in D_2O was filled into disposable MAS inserts (Bruker) in a 4 mm rotor and spun at $4 - 6$ kHz.

Firstly, polarization transfer experiments using cross polarization (CP) [34] and refocused insensitive nuclei enhanced by polarization transfer (refocused-INEPT) [35, 36] were performed at $T = 41 - 74$ °C and a spin rate of 6 kHz to assess the CH bond reorientation of the alkyl and PEO blocks around the melting transition of the core ($T_m = 57$ °C). Prior to the measurement, the sample was heated to 76 °C for equilibration and then cooled again to 40 °C.

Afterwards, the temperature was increased step-wise with 5 min equilibration time before the start of each experiment.

Secondly, the longitudinal relaxation rate R_1 and the relaxation rate in the rotating frame $R_{1\rho}$ were determined below the melting transition, $T = 41 - 55\,°\text{C}$, revealing details about the CH bond correlation time τ_c in the solid phase. The experiments used CP polarization transfer and a MAS spin rate of 6 kHz. R_1 was measured using inversion recovery, and $R_{1\rho}$ was measured using an on-resonance spin-lock.

Thirdly, R-type proton detected local field (R-PDLF) experiments [37] were performed just above the melting transition, $T = 57 - 77\,°\text{C}$, using refocused-INEPT polarization transfer and a spin rate of 4 kHz, to determine the liquid order parameter S_{CH} of CH bonds in the alkyl block.

The following experimental set-ups were used for all experiment types: a recycle delay D1 of 5 s, ^1H and ^{13}C high power 90° pulses of 3.1 µs, corresponding to a RF-field of 80.6 kHz. ^1H decoupling during acquisition used the two pulse phase modulated (TPPM) scheme [38].

The CP polarization transfer in all CP experiments used a contact time of 1 ms, ramped ^1H nutation frequencies from 64.5 to 80.6 kHz, and a ^{13}C nutation frequency of 72.6 kHz. The INEPT polarization transfer used refocused-INEPT delays τ_1 and τ_2 of 1.79 ms and 1.19 ms, respectively.

Specific parameter set-up are listed here:

CP- and INEPT-MAS. 256 scans were recorded using a spectral width of 305.8 ppm, an acquisition time of 49.2 ms, and 68.0 kHz TPPM ^1H decoupling pulses during acquisition.

INEPT R-PDLF. 64 scans were recorded using a spectral width of 159.0 ppm, an acquisition time of 200 ms, and 39.0 kHz TPPM ^1H decoupling during acquisition. The rotor-synchronised $R18_1^7$ pulses [39] had a nutation frequency of 36.0 kHz. The t_1 increment was equal to $13.889\,\text{µs} \times 36 \times 4 = 2.0\,\text{ms}$, and 48 points in the indirect dimension were recorded.

CP R_1. 256 scans were recorded using a spectral width of 159.0 ppm, an acquisition time of 50 ms, and 68.0 kHz TPPM ^1H decoupling during acquisition. Six different relaxation delays were acquired: 0.1, 0.3, 0.6, 1, 2, and 4 s.

CP $R_{1\rho}$. 256 scans were recorded using a spectral width of 159.0 ppm, an acquisition time of 50 ms, and 68.0 kHz TPPM ^1H decoupling during acquisition. Data for seven different spin-lock nutation frequencies ν_1 were acquired, using six different spin-lock times for each spin lock field. The values were: $\nu_1 = 18.2, 20.7\,\text{kHz}$, spin lock times = 0.1, 0.25, 0.5, 0.75, 0.9, and 1.2 s; $\nu_1 = 22.5, 25.9, 32.4, 36.5\,\text{kHz}$, spin lock times = 0.1, 0.25, 0.5, 0.75, 1.5, and 3 s; $\nu_1 = 46.9\,\text{kHz}$, spin lock times = 0.1, 0.3, 0.6, 1.2, 2.5, and 5 s.
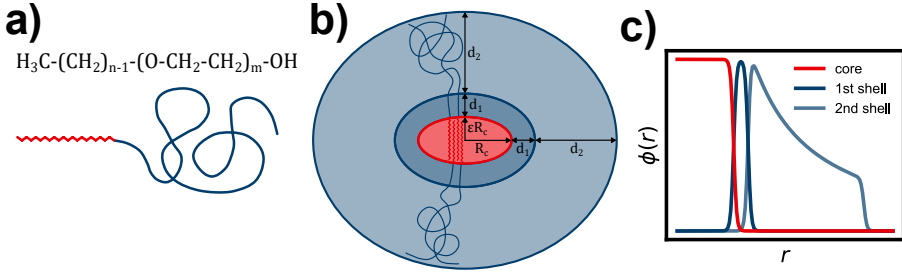
Figure I.1: a) Chemical structure of C_n-PEOx. b) Sketch to illustrate the scattering model. c) Sketch of the local polymer volume fraction assumed in the model.

Scattering Model

In previous publications, we used a spherical core-shell model to describe scattering data from C_n-PEOx micelles.[13, 17, 21, 27] This model, however, fails in describing the SANS data with dominant core scattering contribution. The data rather suggest an aspherical core shape and indeed good fits were obtained using an oblate ellipsoid of revolution. But the intensity predicted by the model around intermediate Q was slightly too low, indicating an additional scattering contribution in a size range between core and corona. Finally, we achieved a very good fit by adding a thin layer ($<1\,\mathrm{nm}$) of dehydrated PEO around the core. Details will be discussed in the Results section.

Figure I.1b) shows a sketch of the scattering model, including the important geometrical parameters. The micellar core is modeled as a homogeneous ellipsoid of revolution with an equatorial radius R_c and polar radius ϵR_c. Thus, $\epsilon < 1$ corresponds to an oblate and $\epsilon > 1$ to a prolate shape. The general scattering amplitude for such an ellipsoid of revolution is given by [40]

$$A_{\mathrm{el}}(Q, R_{\mathrm{eff}}) = 3\frac{\sin\left(QR_{\mathrm{eff}}\right) - QR_{\mathrm{eff}}\cos\left(QR_{\mathrm{eff}}\right)}{\left(QR_{\mathrm{eff}}\right)^3}, \tag{I.1}$$

where R_{eff} is an effective radius depending on the equatorial radius R as well as the angle α between the axis of the ellipsoid and the scattering vector $\vec{Q}$:

$$R_{\mathrm{eff}}(R, \alpha) = R\sqrt{\sin^2\alpha + \epsilon^2\cos^2\alpha}. \tag{I.2}$$

Thus, with the effective core radius $R_{c,\mathrm{eff}} = R_{\mathrm{eff}}(R_c, \alpha)$, the core scattering amplitude is

$$A_{\mathrm{c}}(Q, \alpha) = A_{\mathrm{el}}(Q, R_{c,\mathrm{eff}})\, \mathrm{e}^{-\frac{Q^2\sigma_{\mathrm{int1}}^2}{2}}. \tag{I.3}$$

It contains a Debye-Waller factor accounting for an interface roughness σ_{int1} between core and first shell. The first shell of dehydrated polymer is assumed to be homogeneous and of constant thickness d_1 around the ellipsoidal core, so

that the scattering amplitude is

$$A_{s1}(Q,\alpha) = \frac{1}{V_{s1}} \left\{ [V_c + V_{s1}] A_{el}(Q, R_{s1,eff}) - V_c A_c(Q,\alpha) \right\} \, e^{-\frac{Q^2 \sigma_{int2}^2}{2}}, \qquad \text{(I.4)}$$

with the effective inner and outer radii $R_{c,eff}$ and $R_{s1,eff} = R_{c,eff} + d_1$, another Debye-Waller factor with interface roughness σ_{int2} between the shells as well as the respective volumes of core and first shell:

$$V_c = \frac{4\pi}{3} \epsilon R_c^3, \qquad \text{(I.5)}$$

$$V_{s1} = \frac{4\pi}{3} (R_c + d_1)^2 (\epsilon R_c + d_1) - V_c. \qquad \text{(I.6)}$$

The second shell of hydrated polymer has a constant thickness d_2 and is modeled with a density profile $\propto r^{-4/3}$ according to the Halperin theory [41, 42] for star-like micelles,

$$A_{s2}(Q,\alpha) = \frac{1}{C} \, e^{-\frac{Q^2 \sigma_{int2}^2}{2}} \int_{R_{s1,eff}}^{\infty} 4\pi r^2 \frac{r^{-4/3}}{1 + \exp \frac{r - R_{s2,eff}}{\sigma_{out} R_{s2,eff}}} \frac{\sin Qr}{Qr} \, dr. \qquad \text{(I.7)}$$

A Fermi-like cut-off function at the effective micellar radius $R_{s2,eff} = R_{s1,eff} + d_2$ with width σ_{out} was introduced to account for the finite length of the polymer blocks and C is a normalization constant:

$$C = \int_{R_{s1,eff}}^{\infty} 4\pi r^2 \frac{r^{-4/3}}{1 + \exp \frac{r - R_{s2,eff}}{\sigma_{out} R_{s2,eff}}} \, dr. \qquad \text{(I.8)}$$

The density profiles assumed in this model, including rough interfaces, are sketched in Figure I.1c). Finally, the model considers the so-called "blob" scattering [43], a scattering contribution arising from the internal polymer structure in the second shell:

$$B(Q) = \frac{P_{Beau}(Q)}{1 + \nu \, P_{Beau}(Q)}, \qquad \text{(I.9)}$$

where ν is an effective surface coverage and $P_{Beau}(Q)$ is the Beaucage form factor.[44]

The actual fit parameters of the model are the aggregation number N_{agg}, the thicknesses d_1 and d_2 of the shells, the asphericity ϵ, the interface roughnesses σ_{int1} and σ_{int2}, the radius of gyration R_g in the Beaucage form factor as well as the surface coverage ν. The relative width of the outer surface was fixed at $\sigma_{out} = 0.1$, based on previous studies.[13, 17] All other model parameters are calculated in the following way: The molecular volume of an n-alkyl chain is calculated from its molecular weight and density, $V_{M,Cn} = M_{Cn}/d_{Cn}$, which determines the core radius via

$$N_{agg} V_{M,Cn} = \frac{4\pi}{3} \epsilon R_c^3. \qquad \text{(I.10)}$$

The partial molecular volume of a single PEO chain in the dehydrated layer is $V_{\mathrm{M,PEO,s1}} = V_{\mathrm{s1}}/N_{\mathrm{agg}}$ and therefore the mass fraction of PEO in the first shell

$$X_{\mathrm{s1}} = \frac{d_{\mathrm{PEO,s1}}V_{\mathrm{M,PEO,s1}}}{M_{\mathrm{PEO}}}. \tag{I.11}$$

This leaves the remaining partial PEO molecular volume in the hydrated second shell to be

$$V_{\mathrm{M,PEO,s2}} = (1 - X_{\mathrm{s1}})M_{\mathrm{PEO}}/d_{\mathrm{PEO,s2}}, \tag{I.12}$$

so that the overall micellar volume becomes

$$V_{\mathrm{mic}} = N_{\mathrm{agg}}\left(V_{\mathrm{M,Cn}} + V_{\mathrm{M,PEO,s1}} + V_{\mathrm{M,PEO,s2}}\right). \tag{I.13}$$

Lastly, the molecular volume of a solvent molecule is $V_{\mathrm{M,solv}} = M_{\mathrm{solv}}/d_{\mathrm{solv}}$. With these quantities and the respective scattering lengths b_x, the scattering length densities are calculated as

$$\rho_{\mathrm{c}} = b_{\mathrm{Cn}}/V_{\mathrm{M,Cn}}, \tag{I.14a}$$

$$\rho_{\mathrm{s1}} = X_{\mathrm{s1}}b_{\mathrm{PEO}}/V_{\mathrm{M,PEO,s1}}, \tag{I.14b}$$

$$\rho_{\mathrm{s2}} = (1 - X_{\mathrm{s1}})b_{\mathrm{PEO}}/V_{\mathrm{M,PEO,s2}}, \tag{I.14c}$$

$$\rho_{\mathrm{solv}} = b_{\mathrm{solv}}/V_{\mathrm{M,solv}} \tag{I.14d}$$

and the contrasts are

$$\Delta\rho_{\mathrm{c/s1/s2}} = \rho_{\mathrm{c/s1/s2}} - \rho_{\mathrm{solv}}. \tag{I.15}$$

Finally, the scattering cross-section of the micelle is[1]

$$\left(\frac{d\sigma}{d\Omega}\right)_{\mathrm{mic}}(Q) = \int_0^{\pi/2} \left[V_{\mathrm{c}}^2\Delta\rho_{\mathrm{c}}^2 A_{\mathrm{c}}^2(Q,\alpha) + V_{\mathrm{s1}}^2\Delta\rho_{\mathrm{s1}}^2 A_{\mathrm{s1}}^2(Q,\alpha) + \right.$$
$$+ N_{\mathrm{agg}}\left(N_{\mathrm{agg}} - \frac{1}{1+\nu}\right)V_{\mathrm{M,PEO,s2}}^2\Delta\rho_{\mathrm{s2}}^2 A_{\mathrm{s2}}^2(Q,\alpha) +$$
$$+ 2V_{\mathrm{c}}V_{\mathrm{s1}}\Delta\rho_{\mathrm{c}}\Delta\rho_{\mathrm{s1}}A_{\mathrm{c}}(Q,\alpha)A_{\mathrm{s1}}(Q,\alpha) +$$
$$+ 2V_{\mathrm{c}}N_{\mathrm{agg}}V_{\mathrm{M,PEO,s2}}\Delta\rho_{\mathrm{c}}\Delta\rho_{\mathrm{s2}}A_{\mathrm{c}}(Q,\alpha)A_{\mathrm{s2}}(Q,\alpha) +$$
$$\left. + 2V_{\mathrm{s1}}N_{\mathrm{agg}}V_{\mathrm{M,PEO,s2}}\Delta\rho_{\mathrm{s1}}\Delta\rho_{\mathrm{s2}}A_{\mathrm{s1}}(Q,\alpha)A_{\mathrm{s2}}(Q,\alpha)\right]\sin\alpha\,d\alpha \tag{I.16}$$

and, with the blob scattering added incoherently, the overall macroscopic scattering cross-section is

$$\frac{d\Sigma}{d\Omega}(Q) = \frac{\phi}{V_{\mathrm{mic}}}\left[\left(\frac{d\sigma}{d\Omega}\right)_{\mathrm{mic}}(Q) + N_{\mathrm{agg}}V_{\mathrm{M,PEO,s2}}^2\Delta\rho_{\mathrm{s2}}^2 B(Q)\right]. \tag{I.17}$$
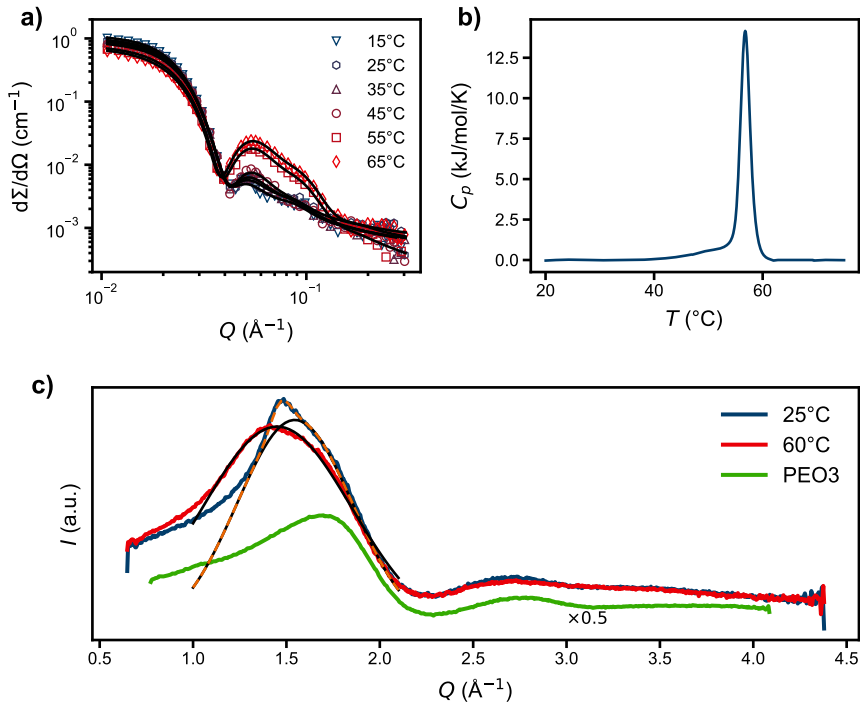
Figure I.2: a) Temperature-dependent SAXS curves of C_{28}-hPEO5 in H_2O, taken from Ref. [17]. Note the increased core scattering contribution at intermediate Q for $T \geq 55\,°C$. b) NanoDSC trace of C_{28}-hPEO5 in H_2O, also taken from Ref. [17]. The melting point is at $T_m \approx 57\,°C$. c) WAXS curves of C_{28}-PEO3 at $5\,vol\%$ above and below the melting transition. The black lines are guides to the eye, illustrating the dominant peaks in both curves whereas the orange dashed line represents an additional spike that vanishes below the melting transition. Moreover, a scaled WAXS curve of PEO3 homopolymer is shown as reference.

Results and Discussion

Previously, we have postulated that the n-alkyl core in C_n-PEOx micelles crystallizes.[17, 19, 21, 27] Without microscopic insight about the molecular order, this hypothesis was based on small-angle X-ray scattering (SAXS) experiments in combination with density measurements and differential scanning calorimetry (DSC). At the melting temperature T_m, there is a distinct decrease in n-alkyl core density. This was both observed via direct density measurements but also indirectly in the respective SAXS curves, where a significant increase in the core scattering contribution is caused by the lowered n-alkyl density and therefore increased core contrast, see Figure I.2a) for an example data set of C_{28}-PEO5. In addition, DSC revealed a clear endothermic phase transition at T_m, see Figure I.2b). These findings led us to the conclusion that the n-alkyl blocks (partially) crystallize below T_m. In the following, we address the microscopic order inside the supposedly crystalline micellar core.

n-Alkyl Block Conformation

One might raise the question whether the n-alkyl blocks assume a similar conformation as crystalline bulk n-alkanes or if some other form of solidification takes place, e.g. a glass transition. Normal n-alkanes do not show a glass transition under regular conditions. Theoretically derived T_g-values are in the range of $120-130\,\text{K}$ [45], far below our measured transition and bulk crystallization temperatures [30]. We successfully related the difference between transition temperatures in micellar cores and bulk to the small core size and described it excellently by a simple Gibbs-Thomson behaviour.[21, 27]

Nonetheless one cannot describe the state of the n-alkyl blocks within the core as crystalline in a classical sense because the maximum domain size is very small as it is constrained by the micellar core radius R_c. Moreover, comparing the melting enthalpy obtained from DSC with the melting enthalpy of the corresponding bulk n-alkanes yields a degree of crystallinity around $30-50\,\%$.[17, 26]

In order to further elucidate the conformation of the n-alkyl chains in the core, we performed wide-angle X-ray scattering (WAXS) experiments. The crystallites inside the micellar cores are very small ($\leq R_c$) and thus any Bragg peaks are heavily affected by Scherrer broadening.[46] Therefore, to increase the chances of observing Bragg scattering, we used a shorter PEO block, C_{28}-PEO3, as this molecule forms larger micelles.[13] WAXS data above and below the melting point are shown in Figure I.2c), together with data from PEO3 homopolymer in solution. As evidenced by the PEO3 reference data, the main features of the C_{28}-PEO3 WAXS curves originate from the PEO3 corona. Only the large peak around $1-2\,\text{Å}^{-1}$, highlighted with the solid black lines, seems to stem from the n-alkyl core. Interestingly, there is a pronounced spike on top of it (dashed orange

---

[1]The correction factor $1/(1+\nu)$ in the outer shell scattering results from the blob scattering.[43]
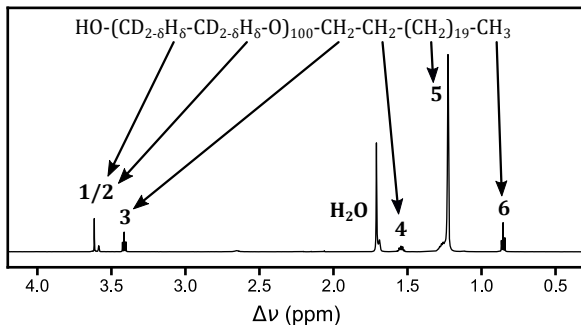
Figure I.3: ^{1}H NMR spectrum of C_{22}-dPEO5 in $CDCl_3$ at $21\,°C$ with assignment of the alkyl signals as well as residual H_2O and hEO signals.

line) that vanishes above the melting transition. The exact same effect, only less pronounced, was also observed in C_{28}-PEO5 micelles, compare Figure S1 in the Supporting Information. We identify this feature at $Q = 1.5\,Å^{-1}$ as the dominant (110) reflection of the normal n-alkane orthorhombic crystal lattice [47], which was also found by Yin and Hillmyer [48] in crystalline polyethylene micellar cores as well as by Fu et al. [49] in n-alkanes confined in microcapsules. Both groups, however, also observed the second-most dominant (200) reflection but since it is much weaker than the (110) reflection, it is not discernible in our data. Nonetheless, we conclude that the crystalline n-alkyl chains in C_n-PEOx micellar cores adopt a conformation similar to that in bulk.

To further shed light on the conformation of the n-alkyl block, we employed nuclear magnetic resonance (NMR) spectroscopy. First, we performed conventional ^{1}H solution NMR of C_{22}-dPEO micelles in D_2O to observe the change of the characteristic n-alkyl peaks with temperature. Figure I.3 shows a reference spectrum in $CDCl_3$ that assigns the proton signals. However, in aqueous solution above the melting point ($T_m = 29\,°C$), i.e., in the micellized state with liquid-like core, the n-alkyl peaks are slightly broadened, indicating a minor reduction in mobility due to micellization. This agrees with the findings of Ortony et al. who investigated the internal dynamics of an n-alkyl-functionalized, self-assembling peptide using electron paramagnetic resonance spectroscopy [50] and found the alkyl blocks buried in the fiber core to have a reduced rotational diffusion rate compared to fully liquid n-alkanes in the melt. When the temperature of C_{22}-dPEO is reduced below the melting point, though, the NMR peaks become undetectably broad which means that the n-alkyl chain mobility is strongly restricted. To investigate the peak broadening more quantitatively, we fitted the individual signals with Lorentzian curves and the determined peak widths (full width at half maximum, FWHM) are plotted in Figure I.7a), while the fits are shown in Figure S2 in the Supporting Information, together with a more detailed description of the fit procedure.

The width of the two residual hPEO peaks (**1** and **2**) is unaltered over the entire temperature range while the *n*-alkyl peaks (**3**–**6**) are broadened very quickly below the melting point. Interestingly, the inner carbons (**4** and **5**) are broadened immediately below the melting transition: Already at 25 °C they cannot be distinguished from the background anymore whereas the PEO grafting site (**3**) and the terminal methyl group (**6**) can be distinguished at least down to 21 °C. This can be rationalized by the fact that the CH_2 group next to the PEO block is most effected by the free polymer and methyl groups generally are rather mobile, while the inner methylenes are more prone to order, which has also been revealed in the computer simulations of Sevgen et al. [51].

To investigate the internal dynamics of the *n*-alkyl blocks further, we employed magic-angle-spinning ^{13}C solid-state NMR spectroscopy (ssNMR). To this end, we produced a high-concentration C_{28}-hPEO gel in D_2O. First, we conducted INEPT and CP experiments at various temperatures around the melting transition, where CP signals arise from restricted, solid-like phases and INEPT signals originate from liquid-like CH bonds with a fast, isotropic reorientation. The spectra are shown in Figure I.4 and there is a clear phase transition around $T_m = 57$ °C. The peaks were assigned based on the results of Ferreira et al. [52] who investigated a similar C_{12}-oligo(ethylene oxide) system. The most dominant peak, at 70 ppm, (**1**) is the main PEO signal and the resonance at 61 ppm (**2**) stems from the terminal PEO carbon next to the OH group. The PEO block is clearly liquid-like but there is also a CP signal at 70 ppm (**1**) which probably originates from PEO in the immediate vicinity of the core which undergoes anisotropic reorientation on account of being anchored to the core surface. The peaks at 24 ppm (**5**) and 14 ppm (**6**) are the penultimate CH_2 and terminal CH_3 group, respectively. They show a clear liquid-like behavior above the melting transition but their relaxation times become undetectably slow ($\tau_c > 10$ ns) below the melting point. Yet, no significant CP signal arises which is in agreement with our conclusion from the ^1H NMR spectra that the hydrocarbon tail as well as the PEO grafting site remain relatively mobile below the melting transition. Furthermore, there is a strong signal at 31 ppm (**4**) from the liquid *n*-alkyl chain above the melting point which interestingly also exhibits a weak CP signal (**2***). This points towards a certain degree of anisotropy in the system. Finally, there is also an INEPT signal at 33 ppm (**3**) from the penultimate CH_2 group in the C_{28} chain. Below the melting point, there is a strong CP signal at the same chemical shift (**2**) which is characteristic for *n*-alkyl chains in all-trans conformation. The increased width of that signal indicates irregular packing which is reasonable given the spatial constraints within the micellar core.
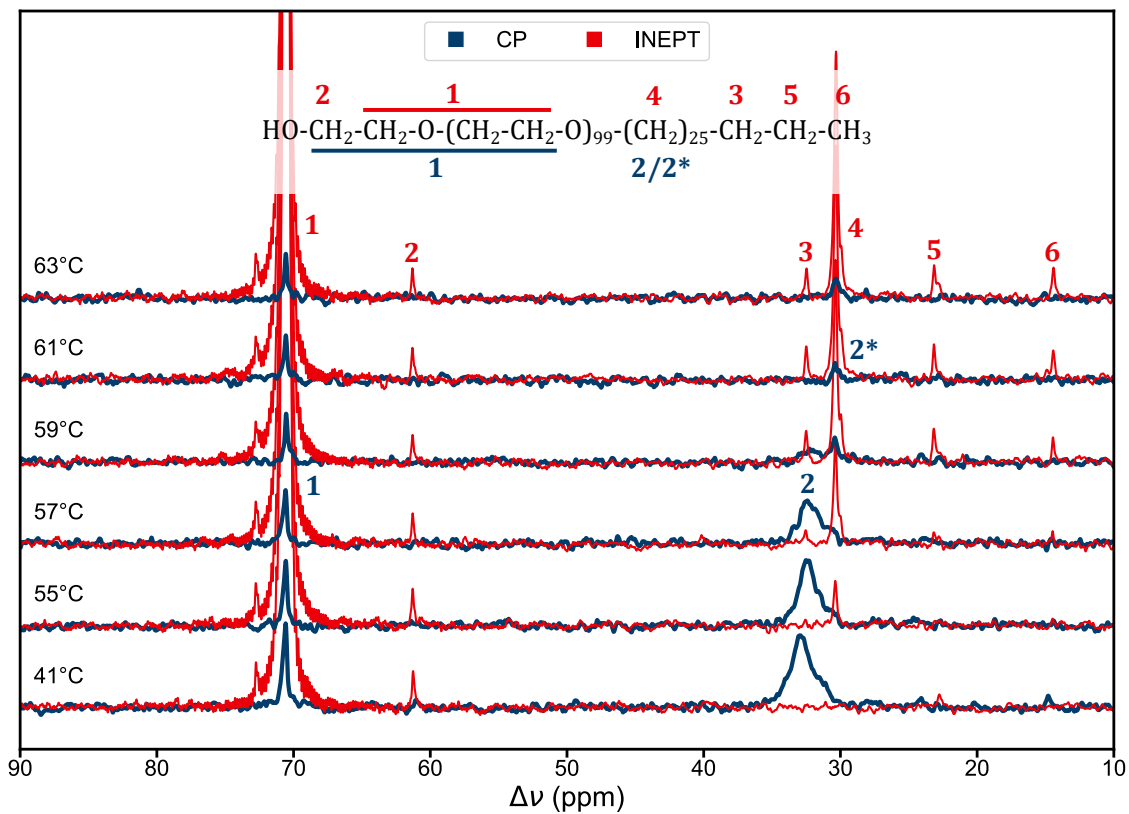
Figure I.4: CP and INEPT ^{13}C ssNMR spectra of a C_{28}-hPEO gel in D_2O. Clear phase transition visible around $T_m = 57\,°C$.
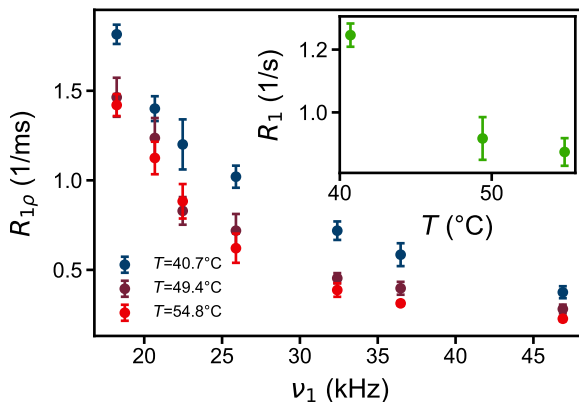
Figure I.5: CH bond relaxation rate of all-trans n-alkyl blocks (**2** in Figure I.4) in the rotating frame $R_{1\rho}$ and in the laboratory frame R_1 as a function of temperature and spin lock pulse nutation frequency ν_1.

However, we wanted to further characterize the state of the hydrocarbon chains in the solid phase and therefore conducted CP $R_{1\rho}$ and R_1 experiments. To determine the n-alkyl CH bond relaxation rate in the rotating frame $R_{1\rho}$, the integrated intensity of the CP peak **2** was measured as a function of the delay time t at different spin lock pulse nutation frequencies ν_1. These data were fitted with a relaxation function $I(t) = I_0 \exp\left(-R_{1\rho} t\right)$, shown in Figures S3–S5 in the Supporting Information. In the same way, the relaxation rate in the laboratory frame, R_1, was obtained. This is shown in Figures S6–S8 and all results are plotted together in Figure I.5. The obtained relaxation rates are surprisingly high and the huge difference between $R_{1\rho}$ and R_1 indicates relaxation processes on the time scale of microseconds. It should be noted, though, that the R_1 relaxation rates agree fairly well with values reported for C_{21}-PEO10-C_{21} hydrogels.[26] In summary, these results point towards a rotator-like phase with mostly all-trans conformation of the C_{28} blocks. Nonetheless, the molecular packing is perturbed due to the strong spatial confinement in the micellar core and the bond reorientation is unusually slow, on the milli- to microsecond scale.

Finally, we performed INEPT-RPDLF experiments to analyze the anisotropy in the micellar core still present above the melting transition by calculating the orientational order parameter S_{CH}. To this end, we measured the integrated intensity of the INEPT signals (**1–6** in Figure I.4) as a function of the delay time t_1, shown in Figure S9 in the Supporting Information. For the strongest signal at 31 ppm (**4**), there is a clear minimum at $t_{1,\text{min}} \approx (16 \pm 1)$ ms which corresponds to a frequency splitting of $\Delta\nu_{\text{CH}} = \frac{2}{t_{1,\text{min}}} \approx (125 \pm 8)$ Hz. With an effective scaling factor 0.315 [53] this gives a dipolar coupling $d_{\text{CH}} = \Delta\nu_{\text{CH}}/0.315 \approx (400 \pm 25)$ Hz. Estimating the maximum splitting for a static CH bond to be ~ 21 kHz [54],

145

we obtain an order parameter of $S_{CH} \approx 0.02$ which agrees with the small but detectable CP signal **2***. At 57 °C, directly at the melting point, the minimum is slightly shifted to shorter delay times which indicates an increased S_{CH}. This seems reasonable given the system is on the brink of the solid phase. Even though the other alkyl signals **3**, **5** and **6** exhibit a much lower signal-to-noise ratio, they all follow the same trend. Albeit small, the orientational order parameter in the C_{28} block is finite and thus suggests some molecular order and/or asymmetry in the micellar core above the melting point.

The calculated S_{CH} of the n-alkyl is in fair agreement with the work of Ferreira et al. who investigated (penta(ethylene glycol))-mono-n-dodecyl ether (i.e., C_{12}-PEO0.25) in D_2O at a similar temperature range ($27-62$ °C), where the system exhibits a liquid-crystalline L_α lamellar phase.[52, 55] For the n-alkyl tail, they found orientational order parameters between 0.01 and 0.08, using the same experimental technique. Yet, the higher S_{CH} values belonged to the carbon atoms close to the hydrophilic-hydrophobic junction. These signals could not be resolved in the present experiment and thus their lower $t_{1,min}$ are obscured by the majority of signals with $t_{1,min} \approx 16$ ms. The other n-alkyl resonances in the study of Ferreira et al. exhibited S_{CH} between 0.02 and 0.05, close to the value found here. Interestingly, they found $S_{CH} \approx 0.01$ for the terminal methyl group. The order parameter of the methyl group cannot be accurately determined here because of the poor signal-to-noise ratio, but it agrees with the increased mobility of this group found in the ^{1}H NMR experiments — compare Figure I.7b). Ferreira et al. also reported non-zero order parameters for the eight CH bonds in the PEO block closest to the hydrophilic-hydrophobic junction. These are probably obscured by the majority of disordered EO groups in the same fashion. In general, Ferreira et al. found the highest orientational order around the n-alkyl-PEO junction which we do not observe in our significantly longer molecules since the NMR peaks overlap indistinguishably and the majority of CH bonds exhibits a lower orientational order. In addition, the geometry of the hydrophilic-hydrophobic interface is different in these studies: While Ferreira et al. studied a lamellar phase, C_{28}-PEO5 forms spheroidal micelles. This might lead to a different kind of order in the interfacial region.

Core shape

In all our previous works on the C_n-PEOx system, we used a spherical core-shell model for star-like micelles which yielded very good agreement with the experimental small-angle scattering data, see for instance Figure I.2a).[13, 14, 17, 18, 21, 27] Though, in the light of the results presented above, it is not obvious how (partially) crystalline n-alkyl chains could be arranged in a spherical core. This question is particularly relevant as micellar assemblies with crystalline cores have attracted significant research activity in recent years.[5, 9] Yet, in most cases the (partially crystalline) micellar core is surrounded by a voluminous corona of swollen polymer which dominates in the usual characterization techniques like small-angle scattering (SAS) and transmission electron microscopy (TEM), rendering a thorough characterization of the core difficult. Therefore, we set
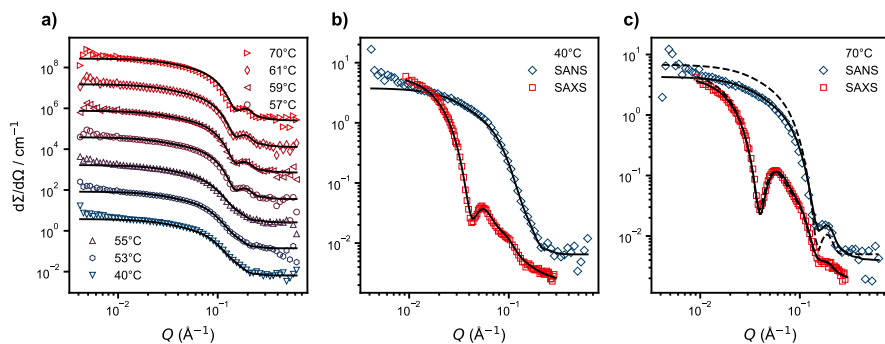
Figure I.6: a) SANS curves of C_{28}-hdPEO5 in D_2O at increasing temperatures around the melting transition. The data have been shifted by factors of 20 for the sake of clarity. Black lines represent model fits which are discussed in more detail in the main text. b) Simultaneous fit of SAXS and SANS data at 40 °C. c) Simultaneous fit of SAXS and SANS data at 70 °C. The black dashed line is a simultaneous fit using our conventional, spherical core-corona model.

out to have a closer look on the actual core shape. Using small-angle neutron scattering (SANS) on C_{28}-hdPEO5 with a contrast-matched PEO corona, we obtained high-quality scattering curves dominated by the n-alkyl core.

In his definitive book *The Hydrophobic Effect* [4], Charles Tanford already stated that amphiphiles would form an ordered hydrocarbon core in micelles. Later, Vilgis and Halperin predicted that diblock copolymers with rodlike or crystallizing solvophobic blocks would form disk-like cores, where the core chains align along their axis and the solvophilic chains stick out from the basal planes.[56, 57] These micelles are only stable in the star-like limit, though, when the corona chains are much longer than the core chains. Interestingly, in this case the corona would still be approximately spherical, rendering it hard to discriminate them from regular spherical star-like micelles. Neutron scattering offers an opportunity to still investigate the core selectively, due to the unique dependence of the scattering signal on the isotopic composition of the sample. Therefore, we prepared C_{28}-hdPEO5 with 82 % deuterated PEO which has almost no contrast to D_2O, enhancing the scattering signal of the core. Even though it is known that H/D exchange can have an effect on the PEO conformation[58, 59], we never observed any significant isotope effect in our experiments.

	SAXS 40 °C	SANS 40 °C	SANS 53 °C	SANS 55 °C	SANS 57 °C	SANS 59 °C	SANS 61 °C	SAXS 70 °C	SANS 70 °C
N_{agg}	140 ± 10	[a]	131 ± 15	125 ± 10	135 ± 10	130 ± 10	135 ± 10	130 ± 10	[a]
d_1 (Å)	6 ± 2	[a]	10 ± 4	12 ± 5	7 ± 3	9 ± 5	6 ± 3	7 ± 2	[a]
d_2 (Å)	76 ± 5	[a]	75 ± 25	85 ± 25	90 ± 25	80 ± 25	75 ± 25	67 ± 5	[a]
ϵ	0.48 ± 0.05	[a]	0.50 ± 0.05	0.51 ± 0.05	0.73 ± 0.05	0.72 ± 0.04	0.72 ± 0.04	0.72 ± 0.05	[a]
σ_{int1} (Å)	4.3 ± 1.2	[a]	4.0 ± 2.0	3.5 ± 1.0	2.5 ± 1.0	2.0 ± 1.0	2.0 ± 1.0	2.0 ± 1.0	[a]
σ_{int2} (Å)	10.8 ± 4.0	[a]	7.0 ± 7.0	9.2 ± 5.0	5.0 ± 5.0	5.0 ± 5.0	5.0 ± 4.0	9.0 ± 4.0	[a]
R_g (Å)	52 ± 10	[a]	50 ± 50	50 ± 50	50 ± 50	50 ± 50	50 ± 50	50 ± 8	[a]
ν	2 ± 2	[a]	2 ± 2	2 ± 2	2 ± 2	2 ± 2	2 ± 2	2 ± 2	[a]
R_{c}[b] (Å)	37	[a]	36	36	33	33	33	33	[a]
b_{Cn} (10^{-12} cm)	63.4	-2.71	-2.71	-2.71	-2.71	-2.71	-2.71	63.4	-2.71
b_{PEO} (10^{-10} cm)	6.92	3.87	3.87	3.87	3.87	3.87	3.87	6.92	3.87
b_{solv} (10^{-12} cm)	2.82	1.91	1.91	1.91	1.91	1.91	1.91	2.82	1.91
d_{Cn} (g/mL)	0.88 ± 0.01	[a]	0.85^c	0.84^c	0.80^c	0.79^c	0.79^c	0.78 ± 0.01	[a]
$d_{\mathrm{PEO,s1}}$ (g/mL)	1.10 ± 0.02	[a]	1.10^d	1.095^d	1.09^d	1.09^d	1.09^d	1.08 ± 0.02	[a]
$d_{\mathrm{PEO,s2}}$ (g/mL)	1.176 ± 0.010	[a]	1.16^e	1.16^e	1.15^e	1.15^e	1.15^e	1.155 ± 0.010	[a]
d_{solv} (g/mL)	1.100^f	[a]	1.094^f	1.093^f	1.092^f	1.091^f	1.090^f	1.085^f	[a]
M_{Cn} (g/mol)					394				
M_{PEO} (g/mol)					4510^g				
M_{solv} (g/mol)					20				
$\Delta\rho_{\mathrm{c}}$ (10^{10} cm^{-2})	-0.80	-6.68	-6.63	-6.61	-6.60	-6.59	-6.59	-1.64	-6.55
$\Delta\rho_{\mathrm{s1}}$ (10^{10} cm^{-2})	0.84	-0.63	-0.60	-0.62	-0.64	-0.63	-0.63	0.78	-0.65
$\Delta\rho_{\mathrm{s2}}$ (10^{10} cm^{-2})	1.54	-0.24	-0.29	-0.28	-0.33	-0.32	-0.32	1.47	-0.26

[a] SANS and SAXS fitted simultaneously; [b] calculated via Equation (I.10); [c] fixed, based on previous results in Reference [17]; [d] value for bulk hPEO, taken from Reference [60]; [e] value for hPEO, fixed, based on previous results in Reference [17]; [f] taken from Reference [61]; [g] corresponding value for hPEO

**Table I.2:** Model parameters used for the fits shown in Figure I.6.

Figure I.6a) shows neutron scattering curves of the aforementioned C_{28}-hdPEO5 in D_2O with contrast-matched corona, stitched together from a low and high concentration sample as described in the Experimental Section. The temperature was increased step-wise from $40\,°C$ to $70\,°C$ to reveal changes during the melting transition. Indeed, there is a very distinct change in the scattering pattern between $55\,°C$ and $57\,°C$. In addition, the same samples were measured with SAXS at $40\,°C$ and $70\,°C$ which serves as comparison with dominant corona scattering, see Figure I.6b) and c). These SAXS curves can be fitted very well with our established spherical core-shell model for star-like micelles but we were not able to reproduce the SANS data with reasonable parameters. Inspired by the works of Halperin and Vilgis [56, 57], we hypothesized about an anisotropic core shape. But since the alkyl cores in C_n-PEOx micelles are only partially crystalline, we deemed it rather unlikely that a proper disk shape is adopted. Instead, we created an ellipsoidal core-shell model which resulted in much better fits than the spherical model. Still, there were systematic deviations from the experimental data in the intermediate Q range, indicating that there was an additional scattering contribution from a structure on a length scale between core and shell. We finally were able to reproduce all scattering curves satisfactorily (black lines in Figure I.6) by assuming a thin layer of dehydrated PEO just around the core, where the polymer volume fraction is highest. Such a layer can occur when the grafting density on the core surface is very high, so that the PEO dehydrates simply due to spatial constraints, and has been reported for densely polymer-grafted nanoparticles.[62, 63] These two new features, aspherical core and dehydrated PEO layer, have not been detected before because the star-like PEO corona dominates the scattering signal under usual full-contrast conditions and, since $d_1 + d_2 \gg R_c$, the overall micelle appears approximately spherical despite an ellipsoidal core, compare Figure I.1b).

The data were fitted with the theoretical model presented in the Experimental Section, with SAXS and SANS data fitted simultaneously at $40\,°C$ and $70\,°C$ to ensure consistency between contrast conditions. The resulting parameters are shown in Table I.2. Fit parameters were the aggregation number N_{agg}, the thicknesses d_1 and d_2 of the shells, the asphericity ϵ, the interface roughnesses σ_{int1} and σ_{int2}, the radius of gyration R_g in the Beaucage form factor as well as the surface coverage ν. The scattering lengths b_x were calculated based on the polymer characterization (Table I.1) and tabulated atomic scattering lengths [64]. To facilitate calculations, PEO parameters other than b_{PEO} were calculated as if the polymer was fully proteated. The density of the C_{28} core and hydrated PEO shell are based on previous results [17] and the density of the dehydrated PEO shell was assumed to equal the bulk PEO density [60]. Densities needed to be slightly adjusted to fit the SAXS data, see Table I.2. The density of D_2O was taken from Reference [61]. Since the contrast of the hydrated PEO is very low in the SANS experiments, the latter are insensitive to R_g and ν and also d_2 and σ_{int2} are rather ill-defined. The overall micellar radius $R_m = R_c + d_1 + d_2 \approx 105 - 120\,Å$ as well as the $R_g \approx 50\,Å$, determined mostly from the SAXS data, though, are in perfect agreement with previous findings.[17] Also the temperature-independent N_{agg} has been reported in the same article.

Furthermore, the interface roughness between n-alkyl core and dehydrated PEO shell decreases slightly above the melting transition. Supposedly, the partially crystalline C_{28} chains are incommensurable with a smooth interface while the molten state allows a more effective packing. In the crystalline phase, the core thickness is about $2\epsilon R_c \approx 36\,\text{Å}$. Tanford [4] calculates the length of a fully stretched n-alkyl tail as $l \approx (1.5 + 1.265(n-1))\text{Å}$, which for C_{28} gives about $36\,\text{Å}$. Therefore, at least in the middle of the ellipsoidal core, the C_{28} chains can adopt an all-trans conformation, while the spatial constraints towards the rim lead to some molecular disorder, in agreement with the ssNMR results.

The most striking finding, however, is that the asphericity ϵ changes abruptly from ~ 0.5 to ~ 0.7 at the melting transition ($T_m = 57\,^{\circ}\text{C}$), which causes the very distinct change in the shape of the scattering curves in Figure I.6a). The evolution of ϵ is also plotted in Figure I.7c). This means the micellar core is a rather flat oblate ellipsoid below the melting transition, almost disk-like as proposed by Halperin and Vilgis, since n-alkyl chains crystallize parallel to each other. Nevertheless, the shape is not exactly disk-like but more smeared out into an ellipsoidal shape — probably because the C_{28} blocks do not crystallize completely, caused by the disordering effect of the grafted PEO chains and spatial confinement which is also reflected in the decreased melting enthalpy [17, 27] as well as the broadened ssNMR signal **2** in Figure I.4. Yet, it should be noted that the scattering patterns of oblate ellipsoid and disk are very similar so that an actual disk-like shape cannot be definitely excluded. Surprisingly, though, the core does not become completely spherical above the melting transition but instead maintains a somewhat oblate shape, in agreement with the finite S_{CH} observed in the ssNMR experiments. Such an asymmetry can be caused by block length polydispersity [65] but the n-alkyl blocks in C_n-PEOx polymers are strictly monodisperse. Therefore, the effect might instead be explained by the fact that the n-alkyl chains still preferably align in parallel, only the driving force for alignment is weaker above the melting temperature. The Kuhn length of polyethylene, in principle a very long linear alkane, is approximately $14\,\text{Å}$ [66], corresponding to about 11 CH_2 repeat units. Thus, the C_{28} block has on average only 1-2 kinks in the liquid state which means that it is still rather rigid, explaining the persistent core anisotropy. This explanation is supported by computer simulations of Lin et al. who found a gradual transition from disk to sphere with decreasing core block rigidity.[67] Furthermore, Vuorte et al. simulated C_{18}-PEO micelles with non-crystalline cores. They also found a slight anisotropy which might become more pronounced with longer n-alkyl chains.[16]

Even though to our knowledge the data set presented here is the most extensive experimental study on core shape change around the melting transition, similar disk-sphere transitions have been reported in the literature. Zhang et al. investigated poly(ϵ-caprolactone) (PCL) confined in a crosslinked acrylic acid/acrylamide shell both on a mica substrate using atomic force microscopy (AFM) and in solution using dynamic light scattering (DLS).[68] They also found the nanoparticles to be ellipsoidal/disk-like below the PCL melting point and spherical above. Using AFM and TEM, Zhu and coworkers saw a similar sphere-platelet transition in polyethylene-poly(ethylene oxide) (PE-PEO) and
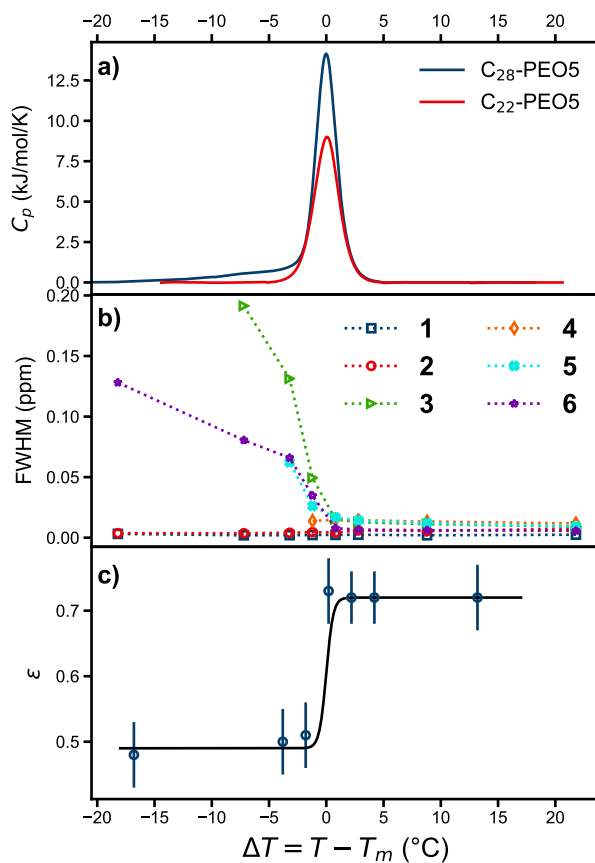
Figure I.7: a) Melting curves of C_{28}- and C_{22}-PEO5 determined by Nano DSC, taken from Reference [17]. b) FWHM of the characteristic C_{22}-dPEO5 ^{1}H NMR signals as assigned in Figure I.3. c) Asphericity ϵ of the C_{28}-hdPEO5 micellar core, determined from the fits in Figure I.6a). The black line is a guide to the eye.

syndiotactic polypropylene-poly(ethylene oxide) (PP-PEO) micelles in DMF when the solutions were cooled below the respective melting points.[69, 70] A different interesting approach was employed by Agrawal et al. who investigated micelles with polylactide cores in solution using (contrast-variation) SANS.[71] They compared optically pure L-lactide which crystallizes with racemic L/D-lactide which remains amorphous and also found "lamellar micelles" in the former polymer and spherical micelles in the latter. Yin and Hillmyer presented a similar study, comparing poly(N,N-dimethylacrylamide)-polyethylene (PDMA-PE) and poly(N,N-dimethylacrylamide)-poly(ethylene-alt- propylene) (PDMA-PEP) in water with TEM and SANS.[48, 72] At 120 °C, both polymers formed spherical micelles with a PDMA corona surrounding the hydrophobic core. When cooled to room temperature, however, the PE block crystallized and forced the core into an oblate ellipsoidal shape while the PEP core remained amorphous and spherical. We would like to highlight that the PDMA-PE system is kinetically frozen so there is no molecular exchange between micelles and the system cannot attain the thermodynamically most favourable state.[48] In contrast, C_{28}-PEO5 exhibits active chain exchange. Even at the lowest experimental temperature, 40 °C, molecular exchange takes place within minutes.[21] Interestingly, the aggregation number still remains unchanged above the melting temperature and only the core shape changes.

But crystallization does not always imply an anisotropic core shape. For instance, the simulations of oligo(ethylene sulfide)-poly(ethylene glycol) (OES-PEG) by Sevgen et al. revealed a spherical core shape, even though the OES chains partially crystallized.[51] In other cases, crystallization leads to aggregation into micellar worms [72–75], which is often exploited in CDSA, or it even leads to precipitation [76]. Thus, the effect of core crystallization on the micellar shape cannot be universally predicted but instead highly depends on the individual polymer architecture.

The other new feature of C_n-PEOx micelles that has been found in the present study is the existence of a thin layer of dehydrated PEO around the C_{28} core. It has not been discovered before because the densities of melt and solution PEO are not very different (compare Table I.2) and the hydrated PEO corona has a much greater volume compared to the dehydrated shell. Only when the outer corona is nearly matched out, the contrast conditions are shifted so that the inner layer becomes visible. Apparently, PEO dehydrates in the immediate vicinity of the core simply because of spatial constraints, imposed by the rather high grafting density of approximately $1.1 \, \text{nm}^{-2}$. The phenomenon has been experimentally found on densely polymer-grafted nanoparticles [62, 63] using SAS. Maccarini et al. observed a $\sim 17 \, \text{Å}$ dehydrated PEO layer on gold nanoparticles with a grafting density of almost $6 \, \text{nm}^{-2}$ and Grünewald et al. reported a $\sim 25 \, \text{Å}$ dehydrated PEO layer on iron oxide nanoparticles with a grafting density of $3.5 \, \text{nm}^{-2}$. Recently, Dahal et al. employed computer simulations to investigate the phenomenon more systematically.[77] They simulated gold nanoparticles of various sizes and PEO grafting densities and found a distinct dehydration layer of up to $15 \, \text{Å}$ when the grafting density was higher than $1.5 \, \text{nm}^{-2}$. However, also for lower grafting densities, they observed a thin dehydration layer of $\sim 5 \, \text{Å}$

which coincides with our findings.

Conclusion and Outlook

In summary, we performed an extensive study on the nature of the n-alkyl core in partially crystalline C_n-PEOx micelles, both below and above the melting transition. Employing SANS and SAXS, we found the core to be elliptical below the melting transition, in agreement with theoretical predictions and other experimental findings. In addition, we observed a less pronounced but still significantly aspherical core above the melting point and relate this to the relative rigidity of the C_{28} block, even in the liquid-like state. In the future, we aim to investigate the core shape of shorter n-alkyl blocks to see if the asphericity persists. We furthermore reported a thin layer of dehydrated PEO in the immediate vicinity of the n-alkyl core. To our knowledge, such a phenomenon has so far only been reported for metallic nanoparticles with extremely high grafting densities but here we also observe it in polymeric micelles with moderate grafting density. In addition, we characterized the n-alkyl core using NMR. Above the melting transition, the core blocks are liquid-like, with low but finite orientational order in agreement with the persistent asphericity of the core. But below the melting transition, the system exhibits unusually high relaxation rates which point towards a rotator-like phase with mostly all-trans chain conformation and milli- to microsecond reorientation. This is further supported by the WAXS results where we observe a Bragg signal equivalent to normal n-alkane crystalline phases with orthorhombic chain packing. As C_n-PEOx is an excellent model for core-crystalline micelles which have attracted significant attention recently, our findings have implications for a wider field of ongoing research. We hope that this work inspires similar studies on other relevant systems with partially ordered cores.

Acknowledgment

References

[1] P. Alexandridis and B. Lindman. *Amphiphilic block copolymers: self-assembly and applications.* Elsevier, 2000 (cited on p. 131).

[2] I. W. Hamley. *Block copolymers in solution: fundamentals and applications.* John Wiley & Sons, 2005 (cited on p. 131).

[3] U. Tritschler, S. Pearce, J. Gwyther, G. R. Whittell, and I. Manners. "50th Anniversary Perspective: Functional Nanoparticles from the Solution Self-Assembly of Block Copolymers". In: *Macromolecules* vol. 50, no. 9 (2017), pp. 3439–3463. DOI: 10.1021/acs.macromol.6b02767 (cited on p. 131).

[4] C. Tanford. *The Hydrophobic Effect: Formation of Micelles and Biological Membranes.* Wiley, 1980 (cited on pp. 131, 147, 150).

[5] J. J. Crassous, P. Schurtenberger, M. Ballauff, and A. M. Mihut. "Design of block copolymer micelles via crystallization". In: *Polymer* vol. 62, no. Supplement C (2015), A1–A13. DOI: 10.1016/j.polymer.2015.02.030 (cited on pp. 131, 146).

[6] X. H. Jin, M. B. Price, J. R. Finnegan, C. E. Boott, J. M. Richter, A. Rao, M. Menke, R. H. Friend, G. R. Whittell, and I. Manners. "Long-range exciton transport in conjugated polymer nanofibers prepared by seeded growth". In: *Science* vol. 360, no. 6391 (2018), pp. 897–900. DOI: 10.1126/science.aar8104 (cited on p. 131).

[7] Z. Coe, A. Weems, A. P. Dove, and R. K. O'Reilly. "Synthesis of Monodisperse Cylindrical Nanoparticles via Crystallization-driven Self-assembly of Biodegradable Block Copolymers". In: *Jove − Journal of Visualized Experiments*, no. 148 (2019), p. 7. DOI: 10.3791/59772 (cited on p. 131).

[8] J. C. Foster, S. Varlas, B. Couturaud, Z. Coe, and R. K. O'Reilly. "Getting into Shape: Reflections on a New Generation of Cylindrical Nanostructures' Self-Assembly Using Polymer Building Blocks". In: *Journal of the American Chemical Society* vol. 141, no. 7 (2019), pp. 2742–2753. DOI: 10.1021/jacs.8b08648 (cited on p. 131).

[9] S. Ganda and M. H. Stenzel. "Concepts, fabrication methods and applications of living crystallization-driven self-assembly of block copolymers". In: *Progress in Polymer Science* vol. 101 (2020), p. 101195. DOI: 10.1016/j.progpolymsci.2019.101195 (cited on pp. 131, 146).

[10] M. Ameri, D. Attwood, J. H. Collett, and C. Booth. "Self-assembly of alcohol ethoxylate non-ionic surfactants in aqueous solution". In: *Journal of the Chemical Society, Faraday Transactions* vol. 93, no. 15 (1997), pp. 2545–2551. DOI: 10.1039/A701662J (cited on p. 131).

[11]   F. Laflèche, T. Nicolai, D. Durand, Y. Gnanou, and D. Taton. "Association of Adhesive Spheres Formed by Hydrophobically End-Capped PEO. 2. Influence of the Alkyl End-Group Length and the Chain Backbone Architecture". In: *Macromolecules* vol. 36, no. 4 (2003), pp. 1341–1348. DOI: 10.1021/ma0210776 (cited on p. 131).

[12]   C. Sommer, J. S. Pedersen, and V. M. Garamus. "Structure and Interactions of Block Copolymer Micelles of Brij 700 Studied by Combining Small-Angle X-ray and Neutron Scattering". In: *Langmuir* vol. 21, no. 6 (2005), pp. 2137–2149. DOI: 10.1021/la047489k (cited on p. 131).

[13]   T. Zinn, L. Willner, R. Lund, V. Pipich, M. S. Appavou, and D. Richter. "Surfactant or block copolymer micelles? Structural properties of a series of well-defined n-alkyl-PEO micelles in water studied by SANS". In: *Soft Matter* vol. 10, no. 28 (2014), pp. 5212–20. DOI: 10.1039/c4sm00625a (cited on pp. 131, 132, 137, 138, 141, 146).

[14]   M. Amann, L. Willner, J. Stellbrink, A. Radulescu, and D. Richter. "Studying the concentration dependence of the aggregation number of a micellar model system by SANS". In: *Soft Matter* vol. 11, no. 21 (2015), pp. 4208–17. DOI: 10.1039/c5sm00469a (cited on pp. 131, 146).

[15]   T. Zinn, L. Willner, K. D. Knudsen, and R. Lund. "Self-Assembly of Mixtures of Telechelic and Monofunctional Amphiphilic Polymers in Water: From Clusters to Flowerlike Micelles". In: *Macromolecules* vol. 50, no. 18 (2017), pp. 7321–7332. DOI: 10.1021/acs.macromol.7b01501 (cited on p. 131).

[16]   M. Vuorte, J. Määttä, and M. Sammalkorpi. "Simulations Study of Single-Component and Mixed n-Alkyl-PEG Micelles". In: *The Journal of Physical Chemistry B* vol. 122, no. 18 (2018), pp. 4851–4860. DOI: 10.1021/acs.jpcb.8b00398 (cited on pp. 131, 150).

[17]   N. König, L. Willner, and R. Lund. "Structure and thermodynamics of mixed polymeric micelles with crystalline cores: tuning properties via co-assembly". In: *Soft Matter* vol. 15, no. 39 (2019), pp. 7777–7786. DOI: 10.1039/C9SM01452G (cited on pp. 131, 132, 137, 138, 140, 141, 146, 148–151).

[18]   T. Zinn, L. Willner, R. Lund, V. Pipich, and D. Richter. "Equilibrium exchange kinetics in n-alkyl–PEO polymeric micelles: single exponential relaxation and chain length dependence". In: *Soft Matter* vol. 8, no. 3 (2012), pp. 623–626. DOI: 10.1039/c1sm06809a (cited on pp. 131, 146).

[19]   T. Zinn, L. Willner, V. Pipich, D. Richter, and R. Lund. "Effect of Core Crystallization and Conformational Entropy on the Molecular Exchange Kinetics of Polymeric Micelles". In: *ACS Macro Letters* vol. 4, no. 6 (2015), pp. 651–655. DOI: 10.1021/acsmacrolett.5b00197 (cited on pp. 131, 132, 141).

[20] T. Zinn, L. Willner, V. Pipich, D. Richter, and R. Lund. "Molecular Exchange Kinetics of Micelles: Corona Chain Length Dependence". In: *ACS Macro Letters* vol. 5, no. 7 (2016), pp. 884–888. DOI: 10.1021/acsmacrolett.6b00395 (cited on p. 131).

[21] N. König, L. Willner, V. Pipich, T. Zinn, and R. Lund. "Cooperativity during Melting and Molecular Exchange in Micelles with Crystalline Cores". In: *Physical Review Letters* vol. 122, no. 7 (2019), pp. 078001-1–6. DOI: 10.1103/PhysRevLett.122.078001 (cited on pp. 131, 132, 137, 141, 146, 152).

[22] N. König, L. Willner, V. Pipich, N. Mahmoudi, and R. Lund. "Tale of Two Tails: Molecular Exchange Kinetics of Telechelic Polymer Micelles". In: *Physical Review Letters* vol. 124, no. 19 (2020), pp. 197801-1–6. DOI: 10.1103/PhysRevLett.124.197801 (cited on p. 131).

[23] F. Renou, T. Nicolai, E. Nicol, and L. Benyahia. "Structure and Viscoelasticity of Mixed Micelles Formed by Poly(ethylene oxide) End Capped with Alkyl Groups of Different Length". In: *Langmuir* vol. 25, no. 1 (2009), pp. 515–521. DOI: 10.1021/la802708m (cited on p. 131).

[24] T. Zinn, L. Willner, and R. Lund. "Telechelic Polymer Hydrogels: Relation between the Microscopic Dynamics and Macroscopic Viscoelastic Response". In: *ACS Macro Letters* vol. 5, no. 12 (2016), pp. 1353–1356. DOI: 10.1021/acsmacrolett.6b00824 (cited on p. 131).

[25] F. Heatley, H. H. Teo, and C. Booth. "Proton longitudinal and transverse magnetic relaxation in dilute aqueous solutions of poly(oxyethylene) alkyl ethers". In: *Journal of the Chemical Society, Faraday Transactions 1: Physical Chemistry in Condensed Phases* vol. 80, no. 4 (1984), pp. 981–991. DOI: 10.1039/F19848000981 (cited on p. 131).

[26] P. R. Knowles, R. J. Barlow, F. Heatley, C. Booth, and C. Price. "A study of chain dynamics in water-swollen gels of poly(ethylene oxide) dialkyl ethers using NMR and differential scanning calorimetry". In: *Macromolecular Chemistry and Physics* vol. 195, no. 7 (1994), pp. 2547–2558. DOI: 10.1002/macp.1994.021950722 (cited on pp. 131, 141, 145).

[27] T. Zinn, L. Willner, and R. Lund. "Nanoscopic confinement through self-assembly: crystallization within micellar cores exhibits simple Gibbs-Thomson behavior". In: *Physical Review Letters* vol. 113, no. 23 (2014), p. 238305. DOI: 10.1103/PhysRevLett.113.238305 (cited on pp. 131, 137, 141, 146, 150).

[28] B. Plazzotta, J. Dai, M. A. Behrens, I. Furo, and J. S. Pedersen. "Core Freezing and Size Segregation in Surfactant Core–Shell Micelles". In: *The Journal of Physical Chemistry B* vol. 119, no. 33 (2015), pp. 10798–10806. DOI: 10.1021/acs.jpcb.5b06041 (cited on p. 131).

[29]   J. Dai, Z. Alaei, B. Plazzotta, J. S. Pedersen, and I. Furo. "Release of Solubilizate from Micelle upon Core Freezing". In: *The Journal of Physical Chemistry B* vol. 121, no. 45 (2017), pp. 10353–10363. DOI: 10.1021/acs.jpcb.7b08912 (cited on p. 132).

[30]   M. Dirand, M. Bouroukba, V. Chevallier, D. Petitjean, E. Behar, and V. Ruffier-Meray. "Normal Alkanes, Multialkane Synthetic Model Mixtures, and Real Petroleum Waxes: Crystallographic Structures, Thermodynamic Properties, and Crystallization". In: *Journal of Chemical & Engineering Data* vol. 47, no. 2 (2002), pp. 115–143. DOI: 10.1021/je0100084 (cited on pp. 132, 141).

[31]   M. Amann. "Micellar Structure, Interactions and Phase Behavior of C28-PEO Polymer Micelles Studied by HR-SANS". PhD thesis. Westfälische Wilhelms-Universität Münster, 2017 (cited on p. 132).

[32]   U. Krengel, H. Sørensen, N. Mahmoudi, R. Lund, and N. König. *Small-Angle Neutron Scattering studies of a bacterial colonization factor*. STFC ISIS Neutron and Muon Source, 2019. DOI: 10.5286/ISIS.E.RB1920565 (cited on pp. 134, 153).

[33]   T. Hwang and A. Shaka. "Water Suppression That Works. Excitation Sculpting Using Arbitrary Wave-Forms and Pulsed-Field Gradients". In: *Journal of Magnetic Resonance, Series A* vol. 112, no. 2 (1995), pp. 275–279. DOI: 10.1006/jmra.1995.1047 (cited on p. 135).

[34]   S. R. Hartmann and E. L. Hahn. "Nuclear Double Resonance in the Rotating Frame". In: *Physical Review* vol. 128, no. 5 (1962), pp. 2042–2053. DOI: 10.1103/PhysRev.128.2042 (cited on p. 135).

[35]   G. A. Morris. "Sensitivity enhancement in nitrogen-15 NMR: polarization transfer using the INEPT pulse sequence". In: *Journal of the American Chemical Society* vol. 102, no. 1 (1980), pp. 428–429. DOI: 10.1021/ja00521a097 (cited on p. 135).

[36]   D. M. Thomas, M. R. Bendall, D. T. Pegg, D. M. Doddrell, and J. Field. "Two-dimensional 13C-1H polarization transfer J spectroscopy". In: *Journal of Magnetic Resonance (1969)* vol. 42, no. 2 (1981), pp. 298–306. DOI: 10.1016/0022-2364(81)90219-5 (cited on p. 135).

[37]   S. V. Dvinskikh, H. Zimmermann, A. Maliniak, and D. Sandström. "Measurements of motionally averaged heteronuclear dipolar couplings in MAS NMR using R-type recoupling". In: *Journal of Magnetic Resonance* vol. 168, no. 2 (2004), pp. 194–201. DOI: 10.1016/j.jmr.2004.03.001 (cited on p. 136).

[38]   A. E. Bennett, C. M. Rienstra, M. Auger, K. V. Lakshmi, and R. G. Griffin. "Heteronuclear decoupling in rotating solids". In: *The Journal of Chemical Physics* vol. 103, no. 16 (1995), pp. 6951–6958. DOI: 10.1063/1.470372 (cited on p. 136).

[39]   X. Zhao, M. Eden, and M. H. Levitt. "Recoupling of heteronuclear dipolar interactions in solid-state NMR using symmetry-based pulse sequences". In: *Chemical Physics Letters* vol. 342, no. 3 (2001), pp. 353–361. DOI: 10.1016/S0009-2614(01)00593-0 (cited on p. 136).

[40]   J. S. Pedersen. "Modelling of Small-Angle Scattering Data from Colloids and Polymer Systems". In: *Neutrons, X-Rays and Light.* Ed. by P. Lindner and T. Zemb. Elsevier, 2002. Chap. 16, pp. 391–420 (cited on p. 137).

[41]   A. Halperin and S. Alexander. "Confined Star Polymers". In: *Macromolecules* vol. 20, no. 5 (1987), pp. 1146–1152. DOI: 10.1021/ma00171a046 (cited on p. 138).

[42]   A. Halperin. "Polymeric Micelles — a Star Model". In: *Macromolecules* vol. 20, no. 11 (1987), pp. 2943–2946. DOI: 10.1021/ma00177a051 (cited on p. 138).

[43]   J. S. Pedersen and C. Svaneborg. "Scattering from block copolymer micelles". In: *Current Opinion in Colloid & Interface Science* vol. 7, no. 3–4 (2002), pp. 158–166. DOI: 10.1016/S1359-0294(02)00044-4 (cited on pp. 138, 141).

[44]   G. Beaucage. "Approximations Leading to a Unified Exponential/Power-Law Approach to Small-Angle Scattering". In: *Journal of Applied Crystallography* vol. 28, no. 6 (1995), pp. 717–728. DOI: 10.1107/S0021889895005292 (cited on p. 138).

[45]   W. R. Turner. "Normal Alkanes". In: *Product R&D* vol. 10, no. 3 (1971), pp. 238–260. DOI: 10.1021/i360039a003 (cited on p. 141).

[46]   P. Scherrer. "Bestimmung der Größe und der inneren Struktur von Kolloidteilchen mittels Röntgenstrahlen". In: *Nachrichten von der Gesellschaft der Wissenschaften zu Göttingen, Mathematisch-Physikalische Klasse* (1918), pp. 98–100 (cited on p. 141).

[47]   C. W. Bunn. "The crystal structure of long-chain normal paraffin hydrocarbons. The 'shape' of the CH2 group". In: *Transactions of the Faraday Society* vol. 35, no. 0 (1939), pp. 482–491. DOI: 10.1039/TF9393500482 (cited on p. 142).

[48]   L. Yin and M. A. Hillmyer. "Disklike Micelles in Water from Polyethylene-Containing Diblock Copolymers". In: *Macromolecules* vol. 44, no. 8 (2011), pp. 3021–3028. DOI: 10.1021/ma200242b (cited on pp. 142, 152).

[49]   D. Fu, Y. Liu, X. Gao, Y. Su, G. Liu, and D. Wang. "Binary n-Alkane Mixtures from Total Miscibility to Phase Separation in Microcapsules: Enrichment of Shorter Component in Surface Freezing and Enhanced Stability of Rotator Phases". In: *The Journal of Physical Chemistry B* vol. 116, no. 10 (2012), pp. 3099–3105. DOI: 10.1021/jp2125119 (cited on p. 142).

[50] J. H. Ortony, C. J. Newcomb, J. B. Matson, L. C. Palmer, P. E. Doan, B. M. Hoffman, and S. I. Stupp. "Internal dynamics of a supramolecular nanofibre". In: *Nature Materials* vol. 13, no. 8 (2014), pp. 812–816. DOI: 10.1038/nmat3979 (cited on p. 142).

[51] E. Sevgen, M. Dolejsi, P. F. Nealey, J. A. Hubbell, and J. J. de Pablo. "Nanocrystalline Oligo(ethylene sulfide)-b-poly(ethylene glycol) Micelles: Structure and Stability". In: *Macromolecules* vol. 51, no. 23 (2018), pp. 9538–9546. DOI: 10.1021/acs.macromol.8b01812 (cited on pp. 143, 152).

[52] T. M. Ferreira, B. Medronho, R. W. Martin, and D. Topgaard. "Segmental order parameters in a nonionic surfactant lamellar phase studied with 1H-13C solid-state NMR". In: *Physical Chemistry Chemical Physics* vol. 10, no. 39 (2008), pp. 6033–6038. DOI: 10.1039/B807693F (cited on pp. 143, 146).

[53] T. M. Ferreira, F. Coreta-Gomes, O. H. S. Ollila, M. J. Moreno, W. L. C. Vaz, and D. Topgaard. "Cholesterol and POPC segmental order parameters in lipid membranes: solid state 1H-13C NMR and MD simulation studies". In: *Physical Chemistry Chemical Physics* vol. 15, no. 6 (2013), pp. 1976–1989. DOI: 10.1039/C2CP42738A (cited on p. 145).

[54] S. V. Dvinskikh, V. Castro, and D. Sandström. "Probing segmental order in lipid bilayers at variable hydration levels by amplitude- and phase-modulated cross-polarization NMR". In: *Physical Chemistry Chemical Physics* vol. 7, no. 18 (2005), pp. 3255–3257. DOI: 10.1039/B508190D (cited on p. 145).

[55] T. M. Ferreira, D. Topgaard, and O. H. S. Ollila. "Molecular Conformation and Bilayer Pores in a Nonionic Surfactant Lamellar Phase Studied with 1H-13C Solid-State NMR and Molecular Dynamics Simulations". In: *Langmuir* vol. 30, no. 2 (2014), pp. 461–469. DOI: 10.1021/la404684r (cited on p. 146).

[56] A. Halperin. "Rod-coil copolymers: their aggregation behavior". In: *Macromolecules* vol. 23, no. 10 (1990), pp. 2724–2731. DOI: 10.1021/ma00212a023 (cited on pp. 147, 149).

[57] T. Vilgis and A. Halperin. "Aggregation of coil-crystalline block copolymers: equilibrium crystallization". In: *Macromolecules* vol. 24, no. 8 (1991), pp. 2090–2095. DOI: 10.1021/ma00008a058 (cited on pp. 147, 149).

[58] C. Branca, A. Faraone, G. Maisano, S. Magazu, P. Migliardo, A. Triolo, R. Triolo, and V. Villari. "Can the isotopic H-D substitution affect the conformational properties of polymeric aqueous solutions? The poly(ethylene oxide)-water case". In: *Journal of Physics: Condensed Matter* vol. 11, no. 32 (1999), pp. 6079–6098. DOI: 10.1088/0953-8984/11/32/301 (cited on p. 147).

[59] C. Branca, A. Faraone, S. Magazu, G. Maisano, P. Migliardo, A. Triolo, R. Triolo, and V. Villari. "Anomalous conformational properties of PEO in H2O and D2O by SANS, PCS and Raman scattering". In: *Journal of Applied Crystallography* vol. 33, no. 3-1 (2000), pp. 709–713. DOI: 10.1107/S0021889899013242 (cited on p. 147).

[60] M. A. I. Shao-Min, C. Booth, and V. M. Nace. "Specific Volumes of Poly(Oxybutylene) and Poly(Oxyethylene) Dimethyl Ethers in the Liquid State". In: *European Polymer Journal* vol. 33, no. 7 (1997), pp. 991–996. DOI: 10.1016/s0014-3057(96)00304-7 (cited on pp. 148, 149).

[61] E. W. Lemmon, M. O. McLinden, and D. G. Friend. "Thermophysical Properties of Fluid Systems". In: *NIST Chemistry WebBook, NIST Standard Reference Database Number 69.* Ed. by P. Linstrom and W. Mallard. National Institute of Standards and Technology, 2020. DOI: 10.18434/T4D303 (cited on pp. 148, 149).

[62] M. Maccarini, G. Briganti, S. Rucareanu, X.-D. Lui, R. Sinibaldi, M. Sztucki, and R. B. Lennox. "Characterization of Poly(ethylene oxide)-Capped Gold Nanoparticles in Water by Means of Transmission Electron Microscopy, Thermogravimetric Analysis, Mass Density, and Small Angle Scattering". In: *The Journal of Physical Chemistry C* vol. 114, no. 15 (2010), pp. 6937–6943. DOI: 10.1021/jp9118088 (cited on pp. 149, 152).

[63] T. A. Grünewald, A. Lassenberger, P. D. J. van Oostrum, H. Rennhofer, R. Zirbs, B. Capone, I. Vonderhaid, H. Amenitsch, H. C. Lichtenegger, and E. Reimhult. "Core-Shell Structure of Monodisperse Poly(ethylene glycol)-Grafted Iron Oxide Nanoparticles Studied by Small-Angle X-ray Scattering". In: *Chemistry of Materials* vol. 27, no. 13 (2015), pp. 4763–4771. DOI: 10.1021/acs.chemmater.5b01488 (cited on pp. 149, 152).

[64] V. F. Sears. "Neutron scattering lengths and cross sections". In: *Neutron News* vol. 3, no. 3 (1992), pp. 26–37. DOI: 10.1080/10448639208218770 (cited on p. 149).

[65] A. L. Schmitt, M. H. Repollet-Pedrosa, and M. K. Mahanthappa. "Polydispersity-Driven Block Copolymer Amphiphile Self-Assembly into Prolate-Spheroid Micelles". In: *ACS Macro Letters* vol. 1, no. 2 (2012), pp. 300–304. DOI: 10.1021/mz200156s (cited on p. 150).

[66] R. H. Colby and M. Rubinstein. *Polymer physics.* Oxford University Press, 2007 (cited on p. 150).

[67] S. Lin, X. He, Y. Li, J. Lin, and T. Nose. "Brownian Molecular Dynamics Simulation on Self-Assembly Behavior of Diblock Copolymers: Influence of Chain Conformation". In: *The Journal of Physical Chemistry B* vol. 113, no. 42 (2009), pp. 13926–13934. DOI: 10.1021/jp904707a (cited on p. 150).

[68] Q. Zhang, C. G. Clark, M. Wang, E. E. Remsen, and K. L. Wooley. "Thermally-Induced (Re)shaping of Core-Shell Nanocrystalline Particles". In: *Nano Letters* vol. 2, no. 10 (2002), pp. 1051–1054. DOI: 10.1021/nl025653n (cited on p. 150).

[69] Z.-Y. Li, R. Liu, B.-Y. Mai, W.-J. Wang, Q. Wu, G.-D. Liang, H.-Y. Gao, and F.-M. Zhu. "Temperature-induced and crystallization-driven self-assembly of polyethylene-b-poly(ethylene oxide) in solution". In: *Polymer* vol. 54, no. 6 (2013), pp. 1663–1670. DOI: 10.1016/j.polymer.2013.01.044 (cited on p. 152).

[70] R. Liu, Z.-Y. Li, B.-Y. Mai, Q. Wu, G.-D. Liang, H.-Y. Gao, and F.-M. Zhu. "Crystalline-coil diblock copolymers of syndiotactic polypropylene-b-poly(ethylene oxide): synthesis, solution self-assembly, and confined crystallization in nanosized micelle cores". In: *Journal of Polymer Research* vol. 20, no. 2 (2013), pp. 64-1–11. DOI: 10.1007/s10965-012-0064-6 (cited on p. 152).

[71] S. K. Agrawal, N. Sanabria-DeLong, G. N. Tew, and S. R. Bhatia. "Structural Characterization of PLA-PEO-PLA Solutions and Hydrogels: Crystalline vs Amorphous PLA Domains". In: *Macromolecules* vol. 41, no. 5 (2008), pp. 1774–1784. DOI: 10.1021/ma070634r (cited on p. 152).

[72] L. Yin, T. P. Lodge, and M. A. Hillmyer. "A Stepwise 'Micellization–Crystallization' Route to Oblate Ellipsoidal, Cylindrical, and Bilayer Micelles with Polyethylene Cores in Water". In: *Macromolecules* vol. 45, no. 23 (2012), pp. 9460–9467. DOI: 10.1021/ma302069s (cited on p. 152).

[73] N. Petzetakis, D. Walker, A. P. Dove, and R. K. O'Reilly. "Crystallization-driven sphere-to-rod transition of poly(lactide)-b-poly(acrylic acid) diblock copolymers: mechanism and kinetics". In: *Soft Matter* vol. 8, no. 28 (2012), pp. 7408–7414. DOI: 10.1039/C2SM25247C (cited on p. 152).

[74] J. R. Finnegan, X. M. He, S. T. G. Street, J. D. Garcia-Hernandez, D. W. Hayward, R. L. Harniman, R. M. Richardson, G. R. Whittell, and I. Manners. "Extending the Scope of Living Crystallization-Driven Self-Assembly: Well-Defined 1D Micelles and Block Comicelles from Crystallizable Polycarbonate Block Copolymers". In: *Journal of the American Chemical Society* vol. 140, no. 49 (2018), pp. 17127–17140. DOI: 10.1021/jacs.8b09861 (cited on p. 152).

[75] S. Noack, D. Schanzenbach, J. Koetz, and H. Schlaad. "Polylactide-Based Amphiphilic Block Copolymers: Crystallization-Induced Self-Assembly and Stereocomplexation". In: *Macromolecular Rapid Communications* vol. 40, no. 1 (2019), p. 6. DOI: 10.1002/marc.201800639 (cited on p. 152).

[76] J.-T. Xu, J. P. A. Fairclough, S.-M. Mai, and A. J. Ryan. "The effect of architecture on the morphology and crystallization of oxyethylene/oxybutylene block copolymers from micelles in n-hexane". In: *Journal of Materials Chemistry* vol. 13, no. 11 (2003), pp. 2740–2748. DOI: 10.1039/b307511g (cited on p. 152).

[77] U. Dahal, Z. Wang, and E. E. Dormidontova. "Hydration of Spherical PEO-Grafted Gold Nanoparticles: Curvature and Grafting Density Effect". In: *Macromolecules* vol. 51, no. 15 (2018), pp. 5950–5961. DOI: 10.1021/acs.macromol.8b01114 (cited on p. 152).

Supporting Information

for

Spherical micelles with a non-spherical core: the effect of core crystallization

Nico König,[†,‡] Lutz Willner,[∗,‡] Göran Carlström,[¶] Thomas Zinn,[§] Kenneth D. Knudsen,[‖] Frode Rise,[†] Daniel Topgaard,[¶] and Reidar Lund[∗,†]

†*Department of Chemistry, University of Oslo, P.O. Box 1033, Blindern, 0315 Oslo, Norway*

‡*Jülich Centre for Neutron Science (JCNS) and Institute for Complex Systems (ICS), Forschungszentrum Jülich GmbH, 52425 Jülich, Germany*

¶*Division of Physical Chemistry, Department of Chemistry, Lund University, Lund, Sweden*

§*ESRF - The European Synchrotron, 38043 Grenoble, France*

‖*Department for Neutron Materials Characterization, Institute for Energy Technology, P.O. Box 40, 2027 Kjeller, Norway*

E-mail: l.willner@fz-juelich.de; reidar.lund@kjemi.uio.no

1

Additional WAXS Data
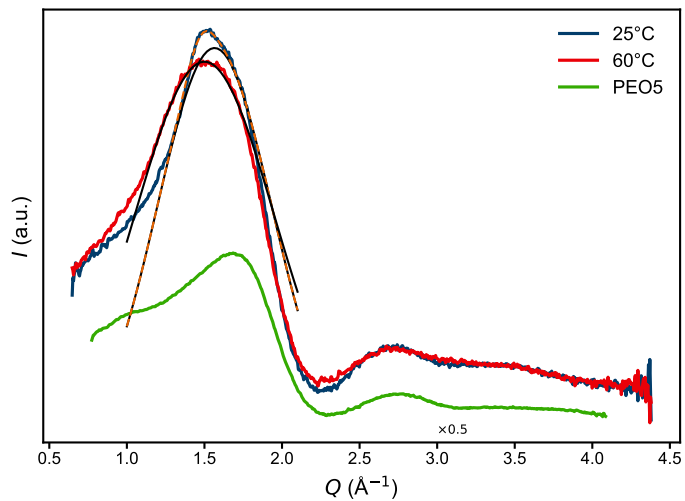
Figure S1: WAXS curves of C_{28}-PEO5 at 5 vol% and PEO5 homopolymer as a reference. The sharp feature at $Q = 1.5\,\mathrm{\AA}^{-1}$ (orange dashed line) vanishes above the melting temperature, $T_m = 57\,°\mathrm{C}$.

2

^{1}H NMR Linewidth

To determine the temperature-dependent linewidth of the ^{1}H NMR signals of C_{22}-dPEO5 in D_2O, the peaks were fitted with Lorentzian curves of the type

$$f\left(\nu, A_0, \nu_0, \sigma_0\right) = \frac{A_0}{(\nu^2 - \nu_0^2)^2 + \sigma_0^2\,\nu_0^2}, \tag{1}$$

where the amplitude A_0, the peak position ν_0 and the peak width σ_0 are fit parameters. The full width at half maximum is

$$\text{FWHM} = \sqrt{\nu_0^2 + \sigma_0\,\nu_0} - \sqrt{\nu_0^2 - \sigma_0\,\nu_0}. \tag{2}$$

The triplets of the first methylene (**3**) and the terminal methyl (**6**) signal were fitted with

$$f_{\text{trip}}\left(\nu, A_0, \nu_0, \sigma_0, \Delta\nu_0\right) =$$
$$= f\left(\nu, A_0, \nu_0 + \Delta\nu_0, \sigma_0\right) + f\left(\nu, 2A_0, \nu_0, \sigma_0\right) + f\left(\nu, A_0, \nu_0 - \Delta\nu_0, \sigma_0\right), \tag{3}$$

where the line splitting $\Delta\nu_0$ is another fit parameter. Similarly, the methylene (**4**) quintet was fitted with

$$f_{\text{quin}}\left(\nu, A_0, \nu_0, \sigma_0, \Delta\nu_0\right) =$$
$$= f\left(\nu, A_0, \nu_0 + 2\Delta\nu_0, \sigma_0\right) + f\left(\nu, 4A_0, \nu_0 + \Delta\nu_0, \sigma_0\right) + f\left(\nu, 6A_0, \nu_0, \sigma_0\right) +$$
$$+ f\left(\nu, 4A_0, \nu_0 - \Delta\nu_0, \sigma_0\right) + f\left(\nu, A_0, \nu_0 - 2\Delta\nu_0, \sigma_0\right). \tag{4}$$

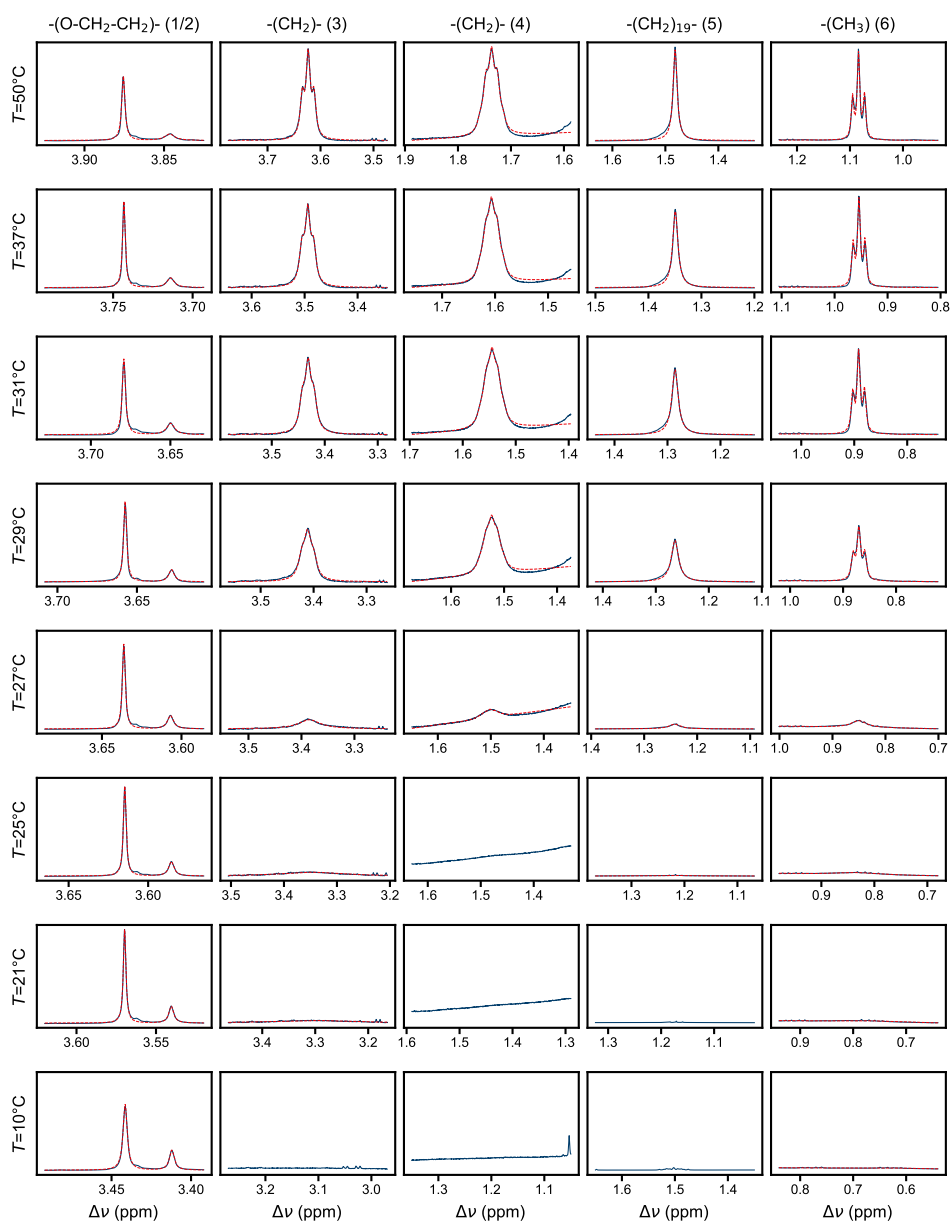Constant or linear backgrounds were added where necessary. The resulting fits are shown in Figure S2.

3

Figure S2: ^{1}H NMR signals of C_{22}-dPEO5 in D_2O fitted with Lorentzian curves.
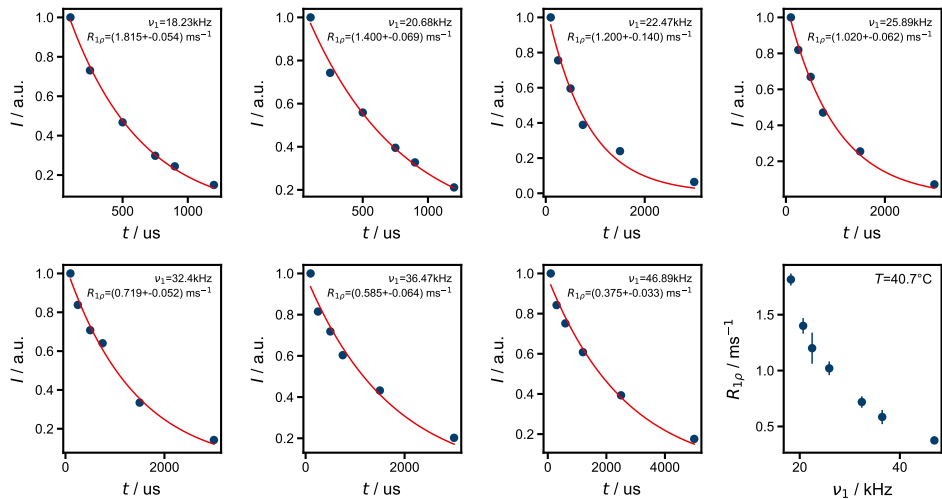
4

Determination of R_1 and $R_{1\rho}$

Figure S3: Determination of $R_{1\rho}$ at 41 °C.

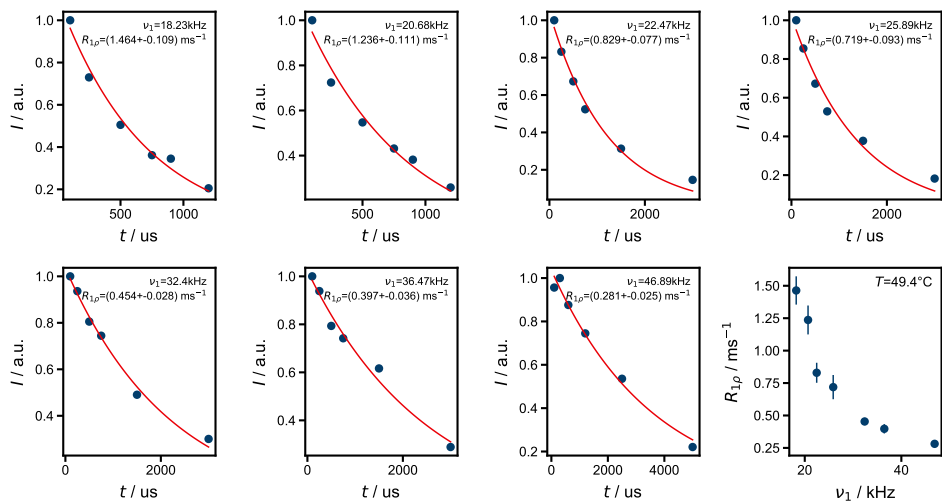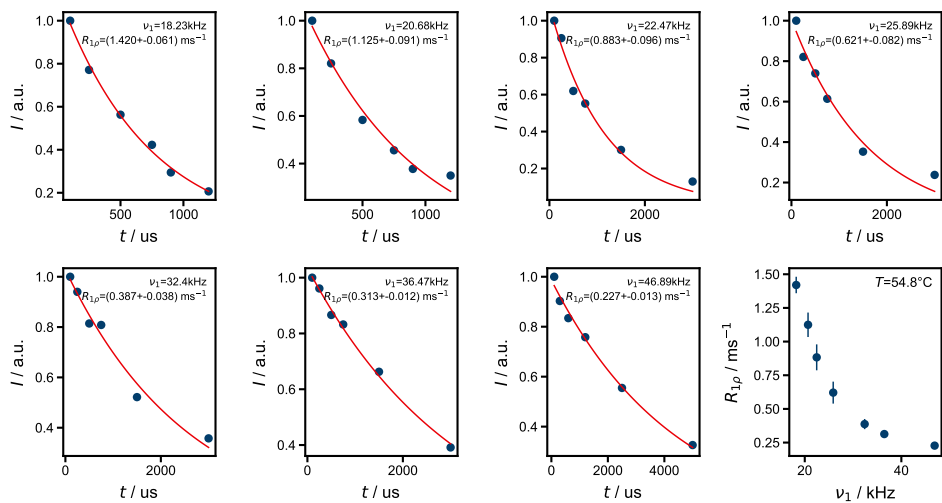Figure S4: Determination of $R_{1\rho}$ at 49 °C.

Figure S5: Determination of $R_{1\rho}$ at 55 °C.

6
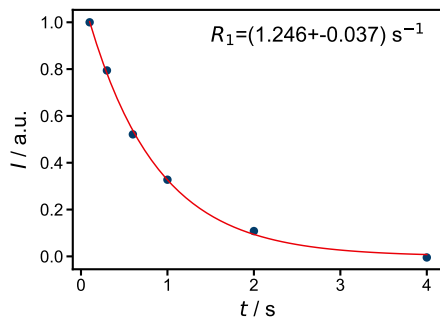
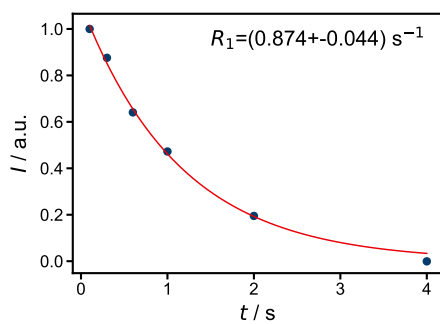Figure S6: Determination of R_1 at 41 °C.
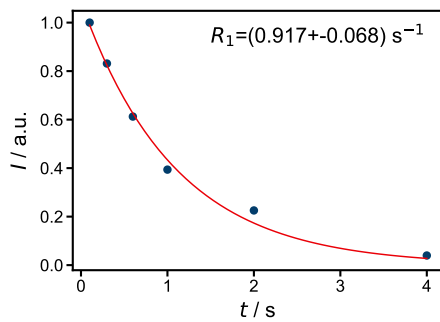
Figure S7: Determination of R_1 at 49 °C.

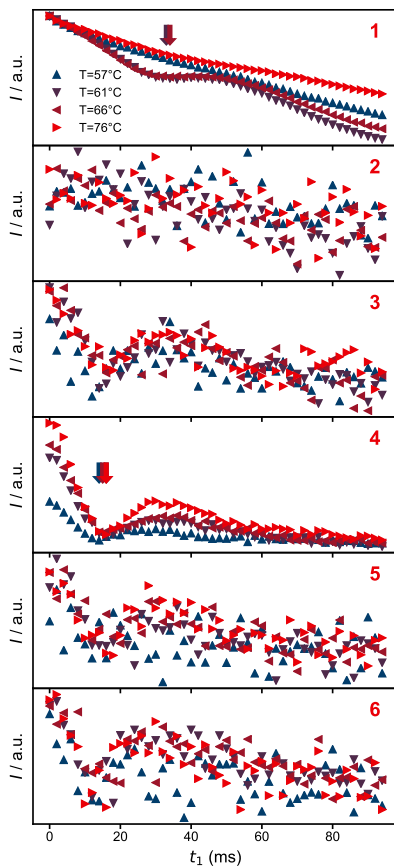Figure S8: Determination of R_1 at 55 °C.

7

INEPT-RPDLF Experiments

Figure S9: Integrated intensity of the INEPT signals **1–6** in Fig. 4 in the main manuscript as a function of the delay time t_1. The clear minima in the traces of **1** and **4** are marked with arrows.

8

Paper II

Structure and thermodynamics of mixed polymeric micelles with crystalline cores: tuning properties via co-assembly

Nico König, Lutz Willner and Reidar Lund

II

Check for updates

Structure and thermodynamics of mixed polymeric micelles with crystalline cores: tuning properties *via* co-assembly†

Nico König, [ab] Lutz Willner [*b] and Reidar Lund [*a]

We investigate micelles formed by mixtures of *n*-alkyl-poly(ethylene oxide) block copolymers, C_n-PEO, with different alkyl block lengths in aqueous solution. This model system has previously been used to shed light on the interplay between exchange kinetics and crystallinity in self-assembling systems [König *et al.*, *Phys. Rev. Lett.*, 2019, **122**, 078001]. Now we report on the structure and thermodynamics of these micelles by combining results from small-angle X-ray scattering, differential scanning calorimetry and volumetric measurements. We show that mixed micelles are formed despite the fact that length-mismatched *n*-alkanes of similar weights in bulk tend to demix below the crystallization temperature. Instead, the system exhibits similar properties as single-component micelles but with a modulated melting region. Interestingly, the melting point depression due to self-confinement within the micellar core can be approximately described by a generalized Gibbs–Thomson equation, similar to single-component micelles [Zinn *et al. Phys. Rev. Lett.*, 2014, **113**, 238305]. Furthermore, we find a novel scaling law for these micelles where, at least for larger *n*, the aggregation number scales with the third power of the length of the hydrophobic block, $N_{agg} \propto n^3$. Possibly, there might be a cross-over from the conventional $N_{agg} \propto n^2$ behaviour around $n \approx 19$. However, the reason for such a transition as well as the strong *n* dependence remains a challenge and requires more theoretical work.

1 Introduction

Micelles comprising amphiphilic block copolymers are a paramount example of self-assembly and have found application in various fields, among others personal care products, biotechnology, and drug delivery.[1–6] In the latter case, the hydrophobic micellar core is used as a nano-carrier for hydrophobic active ingredients, solubilized by the hydrophilic corona.[7] Beside the hydrophobic effect, crystallization can also be a driving force for self-assembly, enabling novel morphologies.[8] For example, Manners and coworkers[9–11] and O'Reilly and coworkers[12,13] have utilized crystallization to achieve impressive control of the morphology and composition of polymeric micelles.

One relatively simple but important class of amphiphilic copolymers are *n*-alkyl-poly(ethylene oxide)s, C_n-PEO, that form well-defined micelles upon self-assembly in water. This system, that comes in various molecular weights, is sold under the trade name "Brij" and has found widespread applications.[14–17]

As is well-known, the core forming blocks of C_n-PEO, *n*-alkanes, tend to crystallize in bulk. In recent works by Zinn *et al.* on well-defined C_n-PEO[18] and Plazzotta *et al.* on Brij polymers,[19] it was found that crystallization also occurs in the micellar state, although at significantly lower temperatures. In the former work, it was shown that this melting point depression nicely follows the well-known Gibbs–Thomson law showing that the Laplace pressure plays a significant role, in analogy with hard confined systems. For instance, the active ingredient Nifedipine exhibits the typical depression of both glass transition and melting point when confined in nanoporous glass.[20] It is yet not fully clear how crystallization of the *n*-alkyl groups takes place in nano-confined entities like the micellar core.

Core crystallization also opens up new questions regarding the loading capacity for drug delivery applications.[21] For instance, it has been found that crystalline cores retard drug release[22] but decrease the micellar loading capacity.[23] Here, also the exchange kinetics of the micelles is of particular interest. On the one hand, the micelles need to be stable enough to contain the load; on the other hand, there must be an appropriate release mechanism. We recently reported how core crystallization influences the exchange kinetics of polymeric micelles:[24,25] Somehow surprisingly, it was found that the crystallization affects the kinetics in the simplest conceivable way; the melting enthalpy ΔH_m is added to the activation energy E_a of the chain expulsion process of the non-crystalline phase.

a Department of Chemistry, University of Oslo, Postboks 1033 Blindern, 0315 Oslo, Norway. E-mail: reidar.lund@kjemi.uio.no

b Jülich Centre for Neutron Science JCNS and Institute for Complex Systems ICS, Forschungszentrum Jülich GmbH, 52425 Jülich, Germany. E-mail: l.willner@fz-juelich.de

Thus the classical chain expulsion step[26] is preceded by the local melting of an individual core block. In that study, we used mixtures of well-defined model polymers, n-alkyl-poly(ethylene oxide), C$_n$-PEO, with different lengths of the hydrophobic alkyl block to tune the crystallization behavior within the micellar core. This disclosed new questions regarding how the micellar morphology and thermodynamics were affected by the presence of multiple components but those were beyond the scope of that study.[25] This topic is all the more interesting as blending has become a handy tool to optimize micellar properties for drug-delivery applications[27–29] and also allows for designing completely new morphologies and exotic structures.[30,31] In the present manuscript, we specifically address the relationship between the micellar structure and thermodynamics by systematically blending various C$_n$-PEO polymers with different alkyl block lengths n = 16, 22, 28 in various ratios. The blends were dissolved in water where they form mixed micelles. Thereupon, the micellar solutions were investigated using small-angle X-ray scattering (SAXS), differential scanning calorimetry (DSC) and densiometry to shed light on how mixing affects both the micelle morphology and the melting transition of the alkyl core. Because we needed both hydrogenated and deuterated PEO blocks for our simultaneous kinetic neutron scattering experiments,[25] both C$_n$-hPEO and C$_n$-dPEO are used in the present work. Here they serve as an additional verification of internal consistency.

This study has important implications for the various applications of polymeric micelles, where typically many different components are blended and even the copolymers themselves usually exhibit a significant degree of polydispersity, making them effectively a mixture of different block lengths. The results might even be extrapolated to more biologically relevant examples like the cell membrane, which is a self-assembled structure of a mixture of different amphiphilic lipids. Our results show that there are no emergent phenomena related to mixing different block lengths. Instead, the mixture of different polymers with mean hydrophobic block length n* essentially behaves like a single-component system with block length n = n*. For example, the confined alkyl blocks in the micellar core exhibit a significant melting point depression compared to their bulk alkane counterparts which can be rationalized by a generalized Gibbs–Thomson equation, similar to single-component micelles.[18] Unexpectedly, our analysis shows that, at least for larger n, the micellar aggregation number scales with the length of the hydrophobic block to the power of 3, $N_{agg} \propto n^3$, with a possible cross-over from the conventional surfactant scaling $N_{agg} \propto n^2$ around n ≈ 19. To the best of our knowledge, such a scaling law has never been experimentally observed or theoretically predicted before.

2 Experimental

2.1 Synthesis and characterization

Poly(ethylene oxide)-mono-n-alkylethers, C$_n$-PEO, with a target molecular weight of 5 kg mol^{-1} were prepared by ring opening living anionic polymerisation of h- and d-ethylene oxide (hEO, dEO), respectively, in toluene at 95 °C. Details of the synthesis have been extensively reported in previous publications.[32,33] In brief, the n-alkanols 1-dodecanol (C$_{12}$-OH), 1-tetradecanol (C$_{14}$-OH), 1-hexadecanol (C$_{16}$-OH), 1-docosanol (C$_{22}$-OH), and 1-octacosanol (C$_{28}$-OH) were used in an 80:20 mixture with their respective potassium alkanolates as initiator. Fast proton exchange between alcohols and alcoholates and complete solubility at the polymerization temperature ensured homogeneous initiation/propagation conditions during the course of the poly-merisation. After complete consumption of EO monomer, the living polymers were terminated with acetic acid resulting in a hydroxy group at their chain ends. For density measurements, a dPEO homopolymer (5 kg mol^{-1}) was prepared as reference sample. In this case, the initiator was a mixture of methoxyethanol/potassium methoxyethanolate (80:20) leading to a methyl group at the initial position. In contrast to potassium methanolate, potassium methoxyethanolate is soluble in toluene at room temperature and was therefore taken as initiator. A similar proteated hPEO was purchased from Sigma-Aldrich.

The polymers were characterised by ^{1}H NMR and size exclusion chromatography (SEC). The NMR spectra were recorded in deuterochloroform with a Bruker Avance III 600 MHz spectrometer equipped with CryoProbe Prodigy. The degree of polymerization, N(PEO), and the number average molar mass, M_n, were quantitatively calculated by end-group analysis relating the integral intensity of PEO protons to those of the n-alkyl groups.

SEC data were recorded with a chromatographic set-up consisting of autosampler, isocratic pump (Agilent Technologies, Series 1260 infinity), column oven (Shimadzu CTO-20A), refractive index detector, 18 angle light scattering detector (Wyatt Technologies, Optilab T-rEX and DAWN HELEOS-II) and three Agilent PlusPore GPC columns with a continuous pore size distribution. A mixture of tetrahydrofuran, N,N-dimethylacetamide, and acetic acid (84:15:1) was taken as eluent. The measurements were conducted at 50 °C at a flux rate of 1 mL min^{-1}. The combination of RI and light scattering detector allows for absolute molar mass characterisation. The chromatograms were quantitatively analyzed using ASTRA Software from Wyatt Technologies. The polymer characteristics obtained from NMR and SEC are summarized in Table 1.

2.2 Sample preparation

For pure reference samples, dry C$_n$-PEO powder was dissolved in water. The solutions were heated up and shaken at 60 °C for

Table 1 Molar masses and dispersities of C$_n$-PEO polymers obtained from NMR and SEC

Polymer	M_n^a (g mol^{-1})	M_n^b (g mol^{-1})	M_w^b (g mol^{-1})	M_w/M_n^b
C$_{12}$-hPEO	5040	5020	5090	1.01
C$_{14}$-hPEO	4970	4900	4970	1.01
C$_{16}$-hPEO	4730	4900	4980	1.02
C$_{16}$-dPEO	—	5260	5320	1.01
C$_{22}$-hPEO	4810	4660	4730	1.02
C$_{22}$-dPEO	—	5460	5570	1.02
C$_{28}$-hPEO	5160	5260	5310	1.01
C$_{28}$-dPEO	—	5210	5290	1.02

^{a} From NMR. ^{b} From SEC.

at least one hour to ensure equilibration. Under constant shaking, they were then left to cool down for at least four hours. This procedure leads to homogeneous, clear micellar solutions. Throughout this work, a mixture of H_2O and D_2O with $\phi_{D_2O} = 66.7$ vol% was used in order to keep consistency with the zero-average-contrast solvent composition used for our previously published kinetic experiments.[25] H_2O was taken from a water purification device (18.2 MΩ cm), D_2O was bought from Sigma-Aldrich.

For mixed samples, dry C_n-PEO powders were weighed in the desired ratios. The blended powder was then dissolved in chloroform, a common solvent for both copolymer blocks, to achieve homogeneous mixing. The chloroform was removed under vacuum, yielding a homogeneous dry polymer blend. This was then dissolved in water and equilibrated as described above for the pure micellar solutions.

To calculate the density of the n-alkyl block in the micellar core, the density of pure PEO in solution is needed. Commercially available hPEO (Sigma-Aldrich) and dPEO (synthesis described above) were thus prepared like the block copolymer samples and used as density references.

2.3 Density measurements

Polymer densities in solution were measured using an Anton Paar DMA 5000 density meter. The device was calibrated using degassed, ultrapure H_2O (18.2 MΩ cm) on a temperature range 5 to 70 °C. The densities of water ($\phi_{D_2O} = 66.7$ vol%), PEO solutions and micellar solutions were measured on the same temperature range. All samples were degassed before measurement.

The average density of the copolymer in solution d_{polym} was then calculated using the water density d_{water} and the density of the sample solution d_{sol}:

$$d_{polym} = \frac{\chi_{polym} d_{sol} d_{water}}{d_{water} + (\chi_{polym} - 1) d_{sol}}, \quad (1)$$

where $\chi_{polym} = m_{polym}/(m_{polym} + m_{water})$ is the mass fraction of the polymer. Under the assumption that the PEO block in the corona has the same density as the PEO homopolymer in solution d_{PEO}, the density of the alkane core d_{Cn} can be calculated in a similar manner:

$$d_{Cn} = \frac{\chi_{Cn} d_{PEO} d_{polym}}{d_{PEO} + (\chi_{Cn} - 1) d_{polym}}, \quad (2)$$

where $\chi_{Cn} = m_{Cn}/(m_{Cn} + m_{PEO})$ is the mass fraction of the alkane block in the diblock copolymer. Using 1 vol% polymer solutions, the density of the alkane core can thus be determined with an accuracy of about 5%.

2.4 Calorimetry

Differential scanning calorimetry (DSC) was used to determine the melting point T_m and the melting enthalpy ΔH_m of the alkane block in the micellar core. The heat capacity of 1 vol% micellar solutions was measured with a Nano DSC device (TA Instruments). Consequently, three heating and two cooling runs were performed on each sample on a temperature range of 15 to 75 °C and at a scanning speed of 2 K min^{-1}. The first

heating run was discarded as equilibration run but the other two heating runs and the two cooling runs usually showed perfect agreement. The solvent contribution was subtracted and the data baseline-corrected, using the manufacturer's software suite NanoAnalyze. The maximum position of the melting/freezing peak represents the melting/freezing point $T_{m/f}$ and the integral over the transition peak determines the melting/freezing enthalpy $\Delta H_{m/f} = \int C_P dT$.

2.5 Small-angle scattering experiments

Small-angle X-ray scattering (SAXS) experiments were performed at our in-house Bruker NanoStar instrument (RECX, University of Oslo, Norway). The scattering intensity was recorded as a function of the wave vector $Q = \frac{4\pi}{\lambda} \sin\theta$, with the wavelength of the incident radiation λ and the scattering angle 2θ. The instrument uses Cu K_α radiation ($\lambda = 1.54$ Å) and yields scattering data in the Q range 0.01–0.3 Å^{-1}. According to instrument standard procedures, the scattering intensity was corrected for detector sensitivity, electronic noise and empty cell scattering and calibrated to absolute units using water scattering, yielding the macroscopic differential scattering cross-section dΣ/dΩ. Then, the scattering contribution from the solvent was subtracted.

The data were analyzed by fitting a model for star-like micelles.[32] Here, the alkyl core is considered as a homogeneous sphere of radius R_c with the scattering amplitude

$$A_c(Q) = 3\frac{\sin QR_c - QR_c \cos QR_c}{(QR_c)^3}. \quad (3)$$

According to theoretical predictions,[34,35] the corona of star-like micelles exhibits a density profile $\propto r^{-4/3}$. Therefore, the scattering amplitude of the PEO shell is taken as

$$A_s(Q) = \frac{1}{C}\int_{R_c}^\infty 4\pi r^2 \frac{r^{-4/3}}{1 + \exp\frac{r - R_m}{\sigma_{out}R_m}} \frac{\sin Qr}{Qr} dr, \quad (4)$$

the rotationally averaged Fourier transform of the star density profile. A Fermi-like cut-off function at the micellar radius R_m with relative width σ_{out} was introduced to account for the finite length of the corona blocks and C is a normalization constant:

$$C = \int_{R_c}^\infty 4\pi r^2 \frac{r^{-4/3}}{1 + \exp\frac{r - R_m}{\sigma_{out}R_m}} dr. \quad (5)$$

There is an additional scattering contribution from the corona, originating from the internal polymer structure, the so-called blob scattering[36]

$$B(Q) = \frac{P_{Beau}(Q)}{1 + \nu P_{Beau}(Q)}, \quad (6)$$

where ν is an effective surface coverage and $P_{Beau}(Q)$ is the Beaucage form factor.[37] Weighted by the appropriate contrast factors, the individual scattering contributions are

$$I_c(Q) = (\rho_c - \rho_0)^2 N_{agg}{}^2 V_c{}^2 A_c(Q)^2 e^{-Q^2\sigma_{int}{}^2}, \quad (7)$$

$$I_s(Q) = (\rho_s - \rho_0)^2 N_{agg}\left(N_{agg} - \frac{1}{1-\nu}\right)V_s^2 A_s(Q)^2 e^{-Q^2\sigma_{int}^2}, \quad (8)$$

$$I_{cross}(Q) = 2(\rho_s - \rho_0)(\rho_c - \rho_0)N_{agg}^2 V_s V_c A_s(Q)A_c(Q)e^{-Q^2\sigma_{int}^2}, \quad (9)$$

and

$$I_{blob}(Q) = (\rho_s - \rho_0)^2 N_{agg} V_s^2 B(Q). \quad (10)$$

Here, N_{agg} is the micellar aggregation number, $V_{c/s}$ the molecular volume of the core/corona block and $\rho_{c/s/0}$ the scattering length density (SLD) of core, corona and solvent, respectively. The SLD is the sum of the scattering lengths of all atoms constituting a particular molecule, divided by the molecular volume of the molecule. In addition, the amplitudes of core and corona are multiplied with a Debye–Waller factor to account for a finite roughness σ_{int} of the core–corona interface. The macroscopic differential scattering cross section is then

$$\frac{d\Sigma}{d\Omega}(Q) = \frac{\phi}{N_{agg}(V_c + V_s)}[(I_c(Q) + I_s(Q) + I_{cross}(Q))S(Q) + I_{blob}(Q)], \quad (11)$$

where ϕ is the volume fraction and $S(Q)$ is a hard-sphere structure factor,[38] which is accurate enough for dilute solutions–compare ref. 39 and references therein. The model contains a number of parameters, of which most are determined by independent methods so only a few free fit parameters remain.

The free fit parameters were the aggregation number N_{agg}, the overall micellar radius R_m, the interface roughness σ_{int}, the blob size R_g in the Beaucage form factor, the effective surface coverage ν and the effective hard-sphere radius R_{HS} of the structure factor. The relative roughness of the outer corona surface was fixed to $\sigma_{out} = 0.1$ which has been shown in previous works[32,33] to give a reasonable description of the scattering data. The molecular volumes were calculated from the molecular weight and the density. As the SAXS curves are quite sensitive to the core density, the latter was slightly adjusted ($<5\%$) from the density measurements during the fit process. The SLDs were calculated from molecular volume and atomic composition, using atomic scattering lengths $b = Zr_e$ where Z is the atomic number and $r_e = 2.82$ fm the classical electron radius. Assuming dense packing in the core, the core radius is $R_c = \left(\frac{3N_{agg}V_c}{4\pi}\right)^{1/3}$. The volume fraction ϕ was calculated from the weighed in masses of polymer and water using the respective densities. Finally, the second parameter of the hard-sphere structure factor, the effective volume fraction η_{HS}, was calculated as $\eta_{HS} = c\frac{4\pi R_{HS}^3}{3}$ where $c = \frac{\phi}{N_{agg}(V_c + V_s)}$ is the micelle number density.

3 Results and discussion

3.1 SAXS data analysis

Fig. 1(a) shows representative SAXS data of mixed and pure micelles measured at 25 °C, polymer volume fraction $\phi = 1$ vol%. For mixtures, we use the following nomenclature: $C_{28/22}$-hPEO 3:1 is a mixture of C_{28}- and C_{22}-hPEO in the ratio 3:1, $C_{22/16}$-hPEO 1:1 is a 1:1 mixture of C_{22}- and C_{16}-hPEO, etc. The scattering curves show typical features of micelles: a high intensity at low Q, a steep intensity decay at intermediate Q, and at high Q a slowly decaying weak intensity reflecting details of the internal structure of the micelles. By comparing the different scattering curves, one observes a significant decrease of intensity at low Q and a shift of the principal intensity decay to larger Q with decreasing mean alkyl block length. Since the forward scattering mainly depends on the aggregation number and the onset of the intensity decay on the overall micellar radius, one can qualitatively deduce that the micelles become smaller both in N_{agg} and R_m as $n^\star$ decreases. At intermediate to high Q, on the other hand, the curves are essentially the same, indicating that the internal structure of

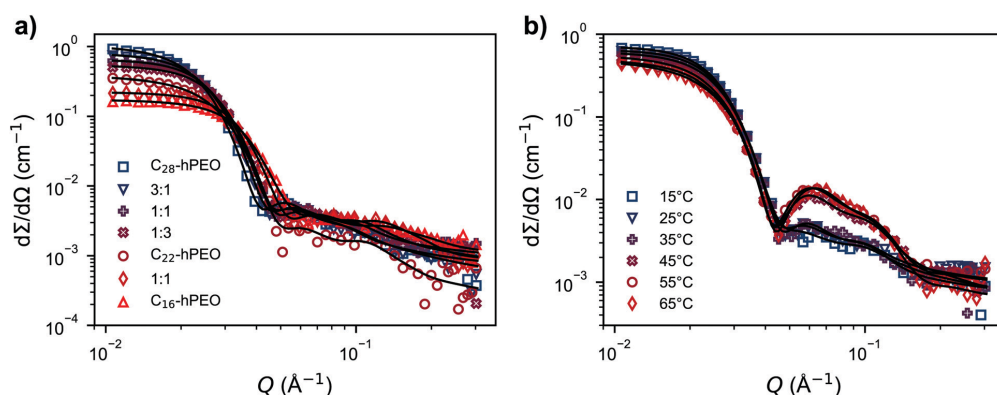**Fig. 1** Representative SAXS data of C_n-hPEO mixtures at $\phi = 1$ vol%, black lines are model fits. (a) Different mixtures at 25 °C; the key fit parameters are given in Table 3. (b) $C_{28/22}$-hPEO 1:1 at different temperatures. Temperature-dependent scattering curves of the other samples can be found in Fig. S3 and S4 in the ESI,† together with a compilation of the respective fit parameters in Tables S2–S15.

the micelles does not change significantly with $n^\star$. For a quantitative evaluation, the SAXS data were fitted by the model introduced in Section 2.5. Excellent fits are obtained by using the same procedure as specified in detail earlier by Zinn *et al.*[32] Fits are shown as solid lines in Fig. 1(a), important structural parameters summarized in Table 3. SAXS measurements were additionally conducted at different temperatures in the range $T = 15–65\ ^\circ\text{C}$. Corresponding scattering curves of the $C_{28/22}$-hPEO 1 : 1 mixture are exemplarily shown in Fig. 1(b). With temperature one observes a slight decrease of the low-Q scattering which is mainly due to thermal expansion and thus loss in contrast. There are, however, significant changes at intermediate to high Q, where we observe a 'jump' in intensity between 35 and 45 $^\circ\text{C}$. As stated above, SAXS is very sensitive to the core density. The 'intensity jump' can hence be attributed to a discrete change in core density, similar to what we described in a previous publication.[18] This effect will be treated in more detail in the next Section 3.2. The complete set of SAXS data from both C_n-hPEO and -dPEO mixtures are shown in Fig. S3 and S4 in the ESI.† Corresponding model fit parameters are given in Tables S2–S15 (ESI†). Noteworthily, there is no systematic difference between C_n-hPEO and -dPEO samples. The structural parameters obtained from the model fits will be thoroughly discussed in Section 3.3.

3.2 Thermodynamics

The SAXS data of $C_{28/22}$-hPEO 1 : 1 in Fig. 1(b) exhibit a discrete intensity jump between 35 and 45 $^\circ\text{C}$, which is attributed to a sudden decrease of the alkyl core density. The same effect is also visible in the temperature-dependent SAXS data of the other samples in Fig. S3 and S4 in the ESI.† Within experimental uncertainty, the core densities obtained from SAXS are in quantitative agreement with the direct measurement using a density meter, as shown in the top of Fig. 2. We and others have reported earlier that the density decrease originates from a melting transition within the micellar core.[18,19,40] This transition is also visible in the DSC curves shown in the bottom of Fig. 2. Melting and freezing temperatures as well as the respective enthalpies are given in Table 2. Comparing the obtained melting/freezing enthalpies with the respective enthalpies of bulk alkanes[41] yields crystallinities between 30 and 45%. However, bulk n-alkanes are known to exhibit two exothermic transitions from the crystalline to the liquid phase. There is a so-called rotator phase in between, where the molecules obtain a rotational degree of freedom but remain longitudinally aligned. The literature values reported in Table 2 are the total melting enthalpy of both melting processes. If we only take the actual melting transition from the rotator to the liquid phase as a reference, we obtain core crystallinities between 50 and 60%. However, one should keep in mind that the estimate is based on the assumption that the amorphous phase in the confined state is similar to that in bulk.

The micellar cores only exhibit a single transition from a frozen to the liquid phase. Here it is noteworthy that also in the mixed cores with different block lengths there is only a single transition. The transition temperature shifts monotonously with the mixing ratio, in agreement with a study on n-alkane
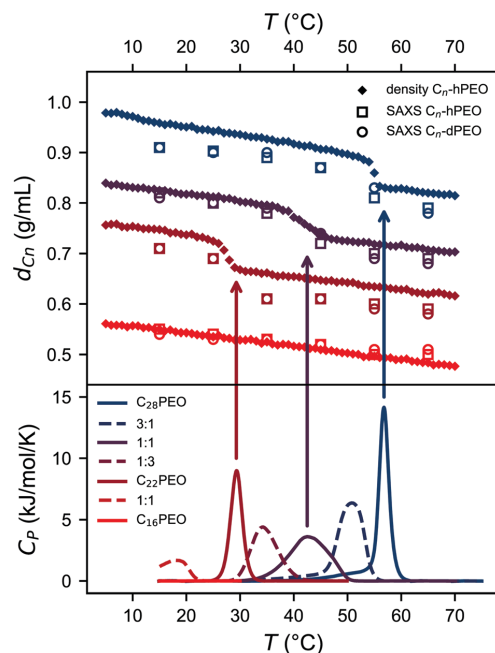

Fig. 2 (top) Density of the alkyl blocks of C_{28}- and C_{22}-PEO, a 1 : 1 mixture thereof and C_{16}-PEO – shifted by -0.1, -0.2 and -0.3 g mL^{-1}, respectively. Shown are values measured with the density meter as well as the refined values from SAXS. (bottom) DSC heating runs of 1 vol% solutions of C_n-hPEO and mixtures thereof. C_{16}-hPEO exhibits no transition peak on the accessible temperature range.

mixtures.[42] As we have reported before,[25] this proves that the different alkyl blocks in fact mix within the micellar cores and do not form two separate populations of micelles. This is surprising since n-alkane mixtures with such a large length mismatch, $\Delta n = 6$, are known to demix in the solid phase.[42–44] The effect has long been known under the name of Kravchenko's rules,[41,45] according to which only n-alkanes with a length mismatch $\Delta n \leq 4$ cocrystallize. But it has been shown that microconfinement enhances the miscibility of n-alkanes.[46] This is due to the fact that the main demixing mechanism, lamellar ordering and longitudinal diffusion,[43,46] is suppressed under confinement. This explains why in the present study, under nanoconfinement, even alkyl blocks with $\Delta n = 6$ do not phase separate. Furthermore, it should be noted that the concentrations used for mixed samples are well above the critical micellar concentrations of the individual components and thus the contribution from unimers can be ignored.

However, the melting transitions of the mixed samples are significantly broadened compared to the pure samples, see Fig. 2. This might be due to local inhomogeneities and packing restrictions within the small micellar core.‡ Unfortunately, the

---

‡ It should be mentioned that the broadened peaks of the mixtures cannot be consistently fitted with two peaks, indicating that it is not just a simple overlay of two transition peaks.

Table 2 Thermodynamic parameters of (mixed) C_n-PEO micelles together with literature values of the respective bulk n-alkanes. The uncertainty intervals of the melting/freezing points represent the HWHM of the melting peak. The intervals around the enthalpies are an estimated uncertainty. Bulk alkanes typically exhibit two phase transitions, from the crystalline to the so-called rotator phase and then to the liquid phase.[41] The given bulk melting point is the rotator-liquid transition while the given bulk enthalpy is the total melting enthalpy from crystalline to liquid. For mixtures, the literature values were interpolated between the constituents

	$n^{\star}$	$T_m{}^a$ (°C)	$T_m{}^b$ (°C)	$T_f{}^b$ (°C)	$\Delta H_m{}^b$ (kJ mol^{-1})	$\Delta H_f{}^b$ (kJ mol^{-1})	$T_{m,lit}^0{}^c$ (°C)	$\Delta H_{m,lit}^0{}^c$ (kJ mol^{-1})
C$_{28}$-hPEO	28	55 ± 1	56.8 ± 1.0	47.6 ± 1.0	40 ± 3	40 ± 1	61.0	100.3
C$_{28}$-dPEO	28	56 ± 1	57.2 ± 1.1	47.5 ± 1.0	45 ± 3	47 ± 1	61.0	100.3
C$_{28/22}$-hPEO 3:1	26.5	—	50.9 ± 2.7	44.4 ± 1.5	39 ± 3	37 ± 1	56.7^d	94.7^d
C$_{28/22}$-hPEO 1:1	25	42 ± 2	42.5 ± 4.5	41.2 ± 2.5	33 ± 2	33 ± 1	52.3^d	89.1^d
C$_{28/22}$-dPEO 1:1	25	—	44.1 ± 6.4	42.0 ± 2.2	36 ± 2	36 ± 1	52.3^d	89.1^d
C$_{28/22}$-hPEO 1:3	23.5	—	34.2 ± 2.9	33.2 ± 2.5	27 ± 1	27 ± 1	48.0^d	83.5^d
C$_{22}$-hPEO	22	28 ± 1	29.3 ± 1.3	28.2 ± 1.4	25 ± 1	25 ± 1	43.6	77.8
C$_{22}$-dPEO	22	27 ± 1	28.6 ± 1.4	27.4 ± 1.5	23 ± 1	22 ± 1	43.6	77.8
C$_{22/16}$-hPEO 1:1	19	—	18.3 ± 2.3	16.4 ± 2.1	—	—	30.8^d	65.6^d
C$_{16}$-hPEO	16	—	—	—	—	—	18.0	53.3

^{a} From density measurement. ^{b} From DSC. ^{c} Taken from ref. 41. ^{d} Interpolated.

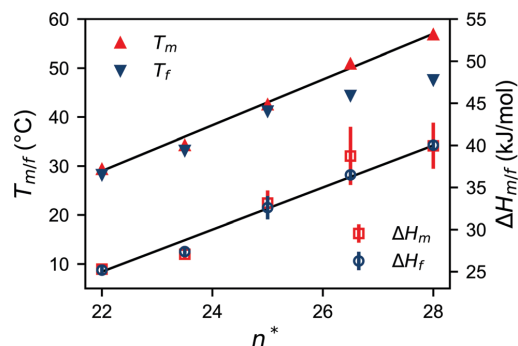**Table 3** Key model parameters, obtained from SAXS experiments at T = 25 °C

	N_{agg}	R_m (Å)	R_{HS} (Å)	d_{Cn} (g mL^{-1})	$R_c{}^a$ (Å)	η_{HS} (vol%)
C$_{28}$-hPEO	124	122	118	0.90	27.8	7.3
C$_{28}$-dPEO	125	115	112	0.90	27.9	6.3
C$_{28/22}$-hPEO 3:1	98	116	111	0.91	25.2	8.4
C$_{28/22}$-dPEO 3:1	105	116	112	0.91	25.7	8.4
C$_{28/22}$-hPEO 1:1	84	112	107	0.90	23.5	9.1
C$_{28/22}$-dPEO 1:1	83	112	107	0.90	23.4	9.4
C$_{28/22}$-hPEO 1:3	70	108	100	0.89	21.8	9.2
C$_{28/22}$-dPEO 1:3	68	111	103	0.90	21.5	9.9
C$_{22}$-hPEO	57	106	95	0.89	19.9	7.4
C$_{22}$-dPEO	54	109	101	0.89	19.6	8.1
C$_{22/16}$-hPEO 1:1	35	94	84	0.84	16.4	11.1
C$_{22/16}$-dPEO 1:1	34	97	86	0.83	16.3	11.2
C$_{16}$-hPEO	27	90	78	0.84	14.2	10.9
C$_{16}$-dPEO	27	90	79	0.83	14.3	11.2
C$_{14}$-hPEO^b	13	79	—	0.76^c	11.0	—
C$_{12}$-hPEO^b	8	70	—	0.75^c	8.9	—

^{a} Derived from N_{agg} and d_{Cn}. ^{b} Data shown in the ESI. ^{c} Taken from ref. 53.

Fig. 3 Melting/freezing points and respective enthalpies determined from DSC as a function of the mean alkyl block length of the C_n-hPEO samples.

melting transition of C$_{22/16}$-hPEO 1:1 stretches down to experimentally inaccessible temperatures and therefore no integration could be performed to calculate the transition enthalpy, whereas C$_{16}$-hPEO shows no sign of a transition at all on the accessible temperature range.

The thermodynamic parameters obtained from DSC are plotted in Fig. 3. The experimental melting and freezing enthalpies agree within uncertainty and increase linearly with the mean alkyl block length, similar to bulk n-alkanes.[41] Also the data of the mixtures fit perfectly in the trend. For bulk n-alkane mixtures a lowered melting/freezing enthalpy compared to the weighted average of the pure components was found[42,44,47] which is attributed to a preferred cocrystallization of the shorter n-alkane.[44] § This phenomenon is not found here. Furthermore, the melting and freezing points of bulk n-alkanes are known to increase with the number of carbon atoms which for small n shows the typical odd–even effect. This effect levels off for large n and is quasi-linear in the

§ The cited studies use n-alkane mixtures with $\Delta n \leq 4$, where the bulk alkanes (partially) cocrystallize.

range between n = 20–30,[41] in agreement with what we extracted from our DSC data.

Interestingly, the difference between T_m and T_f, i.e., the undercooling necessary to induce the phase transition, increases with the block length. This might be related to the fact that it becomes more and more difficult to arrange in an ordered manner the longer the blocks get. But once the order is established, it is also more stable – reflected in a higher transition enthalpy. Again, the mixtures show no deviation from the behavior of the pure micelles.

We previously reported on the effect of self-confinement on the melting point of the alkyl blocks.[18] Due to unfavourable interaction between the swollen corona and the ordered core phase, compared to the disordered core phase, the melting point is reduced as[48]

$$\Delta T_m = T_m^0 - T_m = \frac{\alpha \gamma V_{Cn} T_m^0}{R_c \Delta H_m}. \qquad (12)$$

In this generalized Gibbs–Thomson equation, T_m^0 is the melting point of the unconfined n-alkane, V_{C_n} the molecular volume, γ the surface tension and α a prefactor depending on the confinement geometry. Fig. 4 shows the normalized melting
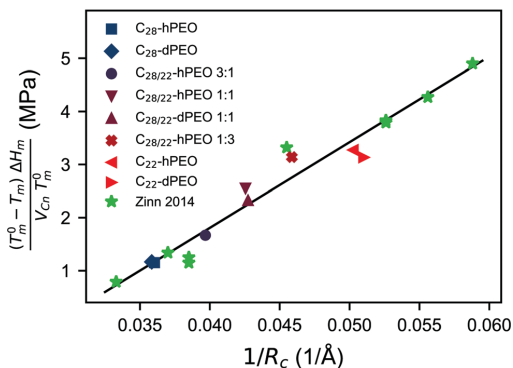
Fig. 4 Melting point depression of the alkyl blocks as a result of self-confinement in the micellar core as a function of the inverse core radius. Previously reported data[18] have been added for comparison. The black line is a fit to all data points shown. R_c and V_{C_n} were obtained from SAXS experiments at 25 °C, data for all temperatures are shown in Fig. S5 in the ESI.†

point depression in mixed micelles as a function of the inverse core radius, with parameters obtained from DSC (T_m and ΔH_m), SAXS and densiometry (R_c and V_m), as well as literature (T_m^0).[41] For mixed micelles, the bulk melting point was interpolated between the constituent block lengths. The data from mixed micelles show very good agreement with our previously reported results from single-component micelles[18] and exhibit a linear dependency as expected from the generalized Gibbs–Thomson equation (12). According to this equation, the slope $m = 16$ mN m^{-1} indicated by the black line should equal $\alpha\gamma$. For a spherical shape $\alpha = 2$,[48] so we obtain an interfacial tension between core and corona of $\gamma = 8$ mN m^{-1}.¶ This value is much lower than typical interfacial tensions between n-alkanes and water $\gamma_{lit} \approx 50$ mN m^{-1}.[49–51] This can be rationalized by the fact that the swollen PEO chains somehow shield the core from direct interaction with the solvent.

It is interesting that the melting point depression mainly depends on the confinement size, R_c. However, in addition, the melting point is also affected by the presence of the other component which might explain the slight deviations from the Gibbs–Thomson law. For a more detailed discussion of this issue we refer to the ESI.†

Summarizing this section, it can be concluded that from a macroscopic thermodynamic point of view, mixed micelles approximately behave like pure ones comprised of the mean alkyl block length – only the melting/freezing transition is broadened. A similar result was obtained by Renou et al.[52] where they found that the rheology of mixed C_n-PEO micelles does not differ from single-component micelles with block length $n = n^\star$.

¶ In the literature, both $\alpha = 2$ and $\alpha = 3$ have been used for spherical domains.[48,66] In the previous publication[18] we used $\alpha = 3$, but following ref. 48, $\alpha = 2$ should be more appropriate. The chosen value will only affect the value of γ.

3.3 Scaling laws of star-like micelles

There are a number of theoretical treatments of polymeric and surfactant micelles which predict the scaling behavior of various structural parameters.[34,35,54,55] We have shown before that the n-alkyl-PEO system exhibits features of both polymeric and surfactant micelles.[32] Now it is interesting if these scaling laws also hold for mixtures of different alkyl block lengths or if new phenomena emerge. The most interesting micellar property is likely the aggregation number N_{agg} which describes the number of molecules constituting one micellar entity. In the limit of very long polymer blocks, a free energy minimization predicts that the aggregation number scales with the length of the solvo-phobic block n as $N_{agg} \propto n^{4/5}$.[34,35,55] For short core-forming blocks like in surfactants, on the other hand, a simple packing argument yields $N_{agg} \propto n^2$.[54] In our previous publication[32] we plotted N_{agg} of a series of C_n-PEO micelles together with data from literature, normalized for the PEO block length dependence suggested by Nagarayan and Ganesh[56] (compare Fig. 3 in ref. 32). The data, covering a broad range of alkyl chain lengths but also PEO molecular weights, suggested a surfactant-like scaling $N_{agg} \propto n^2$.

In Fig. 5 we have now replotted our previous and new data from pure and mixed micelles constituted by C_n-PEO with $M_{PEO} \approx 5$ kg mol^{-1}, together with data from the literature where C_n-PEO with a similar PEO molecular weight was used. Surprisingly, we find that our data, both from mixtures and pure micelles, are better described by a slope of 3 rather than 2. This is even clearer when we only consider our data (Fig. S6 in the ESI†). The data of Renou et al.[52] and LaFleche et al.,[57] however, rather suggest the conventional $N_{agg} \propto n^2$ surfactant scaling.

To determine whether there is a cross-over from a slope of 2 to a slope of 3 at longer alkyl block lengths or if the slope of 3 is a general feature of our model system, we expanded our polymer series to shorter alkyl blocks, namely C_{12}-PEO and C_{14}-PEO, and performed SAXS experiments on these which are documented in the ESI.† Firstly, these additional data points
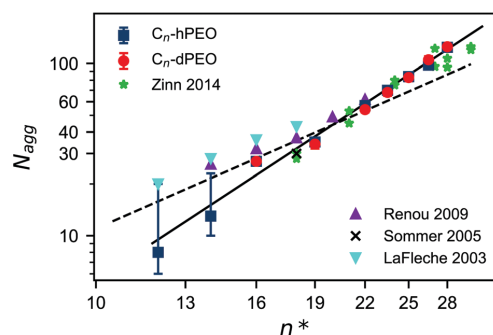

Fig. 5 Aggregation number as a function of the mean alkyl block length, obtained from model fits of SAXS data measured at 25 °C. Previously published results[32] as well as literature data on C_n-PEO with PEO blocks of similar molecular weight[52,57,61] were added for comparison. The dashed line corresponds to $N_{agg} \propto n^2$, the solid line to $N_{agg} \propto n^3$.

seem to support that the $N_{agg} \propto n^3$ behaviour is a universal feature and valid over the whole n range (compare Fig. 5 and Fig. S6, ESI†). Yet, for micelles with such small aggregation numbers, polydispersity becomes more pronounced as $\Delta N_{agg}/N_{agg} \propto N_{agg}^{-3/2}$.[58] We therefore also included a certain degree of polydispersity in our model fits but that had only little effect so we did not use it in the reported fit curves. Furthermore, for these polymers with shorter alkyl blocks, the critical micellar concentration (CMC) is already in the range of the experimental concentrations. This means there is a non-negligible amount of unimers present in the samples which has to be considered in the fit procedure (see the ESI† for details). We obtain the best fits with $N_{agg,C12-PEO} = 8$ and $CMC_{C12-PEO} = 6.2$ mg mL^{-1} or $N_{agg,C14-PEO} = 13$ and $CMC_{C14-PEO} = 0.4$ mg mL^{-1}, respectively. Unfortunately, CMC and N_{agg} are strongly correlated fit parameters which was also reported by LaFleche et al.[57] for their light scattering data. That means we can force a higher aggregation number by using a higher critical concentration. With $N_{agg,C12-PEO} = 18$ and $CMC_{C12-PEO} = 7.2$ mg mL^{-1} or $N_{agg,C14-PEO} = 25$ and $CMC_{C14-PEO} = 0.6$ mg mL^{-1}, respectively, we still obtained a reasonable fit to the experimental data. This is indicated by the error bars in the plots which render the data points of C$_{12}$-PEO and C$_{14}$-PEO less precise. However, for all other samples with $n \geq 16$, the effect of CMC is negligible.

In light of these considerations we cannot unambiguously conclude from our data whether the novel $N_{agg} \propto n^3$ behaviour holds over the entire range of studied alkyl chain lengths or there is a cross-over from the well-reported, surfactant-like scaling $N_{agg} \propto n^2$ to the novel $N_{agg} \propto n^3$. This cross-over, which seems to occur around $n \approx 19$, would indeed be in agreement with the literature data of similar polymers shown in Fig. 5. In fact, when closer examining the data reported by Renou et al.,[52] they seem to indicate a cross-over to a higher exponent as well. To the best of our knowledge, a cross-over to a scaling law of $N_{agg} \propto n^3$ or a $N_{agg} \propto n^3$ scaling law in general have neither been experimentally found nor theoretically predicted before.

In order to explain this unexpected behavior, we first took into account that for starlike micelles the aggregation number also depends on the interfacial tension $N_{agg} \propto \gamma^{6/5}$.[35] In Fig. 5 we have assumed a constant γ for all alkyl chain lengths. Interfacial tension measurements of short n-alkanes, however, show a moderate but clear increase of γ with n.[49–51] Unfortunately, values for chain lengths $n > 16$ are unknown. Therefore we have estimated γ-values by extrapolating data of Goebel and Lunkenheimer[50] as well as Zeppieri et al.[51] for our longer chain lengths ($n = 16–28$), assuming that γ does not approach a limiting value. In order to see whether the increase of the interfacial tension has an effect on the scaling behavior, our data were rescaled by $\gamma^{6/5}$, see Fig. S7 in the ESI.† Yet, the effect is insignificant.

We then proceeded to consider the crystalline nature of the core-forming blocks (which are also relatively stiff) because the cross-over seems to be around $n \approx 19$ which interestingly is also the n range in which the crystallization phenomenon sets in (compare Fig. 2). There have been theoretical treatments of

micelles where the core-forming blocks are either rod-like[59] or crystalline,[60] but none of them predicts a $N_{agg} \propto n^3$ scaling law. Also our own attempts in a theoretical treatment, reported in the ESI,† could not yield a scaling law in accord with the experimental data. Even though the unusual scaling behavior $N_{agg} \propto n^3$ remains unexplained, it is worth noting that the data points obtained from mixed micelles perfectly fit to the data from pure micelles. Furthermore, the temperature dependence of the aggregation number has been debated in the literature: While Renou et al.[52] state they found no effect of temperature, the aggregation numbers reported by Amari et al.[49] increase significantly at higher temperatures. In this study we found no influence of the temperature on N_{agg} which can be seen in Fig. S6 (ESI†) where the symbols from all temperatures overlap.

Even though the aggregation number exhibits a novel scaling behavior, the corona behaves as predicted for starlike micelles. With constant corona block length, the micellar radius is expected to scale $R_m \propto N_{agg}^{1/5}$.[35] This is perfectly reflected in our data, compare Fig. 6. In addition, Fig. S8 in the ESI† shows the overall micellar radius R_m as a function of the mean alkyl length $n^\star$. In the original theory of Halperin and Alexander, the micellar radius scales as $R_m \propto N_{agg}^{1/5} \propto n^{4/25}$.[35] This is depicted as a dashed black line in Fig. S8 (ESI†) and poorly describes the data. With $N_{agg} \propto n^3$, however, the scaling becomes $R_m \propto n^{3/5}$ (solid line) which correlates well with the data. Thus, considering the stronger n-dependence the PEO corona behaves as expected. And, once again, there is no difference between the mixed micelles and their pure counterparts – in agreement with the findings of Renou et al.[52] where they compared the hydrodynamic radii of pure and mixed micelles. Furthermore it is obvious in Fig. 6 and Fig. S8 (ESI†) that the micellar radius decreases with temperature. This is due to the fact that with increasing temperature, water becomes a poorer solvent for PEO and hence the corona shrinks.[63,64] The coronal structure also affects the interaction between micelles. With increasing aggregation number, the effective hard-sphere radius increases from $\sim 0.85 R_m$ to $\sim 0.95 R_m$, see Fig. S9 in the ESI.† That means the corona effectively becomes 'harder' and more repellent, due to a higher grafting density of PEO chains.
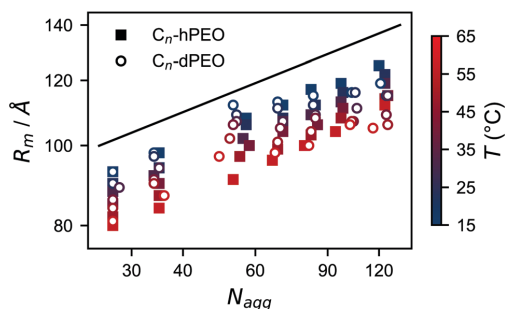

Fig. 6 Micellar radius as a function of the aggregation number, obtained from model fits of SAXS data measured between 15 and 65 °C. The solid line corresponds to $R_m \propto N_{agg}^{1/5}$.
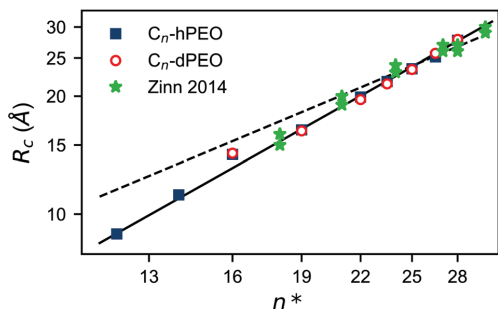
Fig. 7 Core radius as a function of the alkyl block length with previously reported data[32] for comparison. The solid line corresponds to $R_c \propto n^{4/3}$, the dashed line represents the end-to-end distance of a flexible n-alkane according to Tanford.[62]

Finally we investigated how the core radius scales with the length of the alkyl block which is shown in Fig. 7. Assuming dense packing inside the core, a scaling relation $R_c^3 \propto N_{agg}V_{Cn}$ is expected. Given our finding $N_{agg} \propto n^3$ as well as $V_{Cn} \propto n$, this leads to $R_c \propto n^{4/3}$ which is nicely reflected in our data. Regarding the chain conformation inside the core, Tanford[62] proposes $L_{Cn,flex} = 0.75 \times (1.5 + 1.265n)$ as the end-to-end distance of a flexible alkane molecule. This calculation agrees fairly with our experimentally determined core radii, indicating that the alkyl blocks inside the micellar core adopt a flexible conformation. The shorter alkyl blocks, $n = 12, 14$, might even assume a slightly collapsed conformation. Zhao et al. very recently presented a study on binary mixtures of block copolymers with different core block lengths as well.[65] They surprisingly found that mixed micelles with average block length n^* are significantly larger than single-component micelles with block length $n = n^*$. The explanation is that the presence of two block lengths facilitates packing inside the core and thus the chains experience a lower entropic penalty due to chain stretching which results in larger equilibrium micelles. In our case, however, the alkyl blocks are relatively stiff and thus the core block stretching is negligible anyway. This explains why we do not find a similar effect.

4 Conclusion

In the present work we systematically investigated mixtures of the diblock copolymer n-alkyl-poly(ethylene oxide) C_n-PEO with different alkyl block lengths but constant PEO molecular weight in water. An extensive thermodynamic and structural study combining densiometry, DSC, and SAXS revealed that the alkyl-length mismatched polymers form mixed micelles with properties that perfectly interpolate the behavior of single-component micelles. For example, the mixed alkyl blocks experience a melting point depression due to the self-confinement which can well be modeled by a generalized Gibbs–Thomson equation.

Interestingly, a careful analysis of our data reveals a novel $N_{agg} \propto n^3$ scaling behaviour that is not unique to the mixed micelles but is also found for pure C_n-PEO micelles. From our

data it is not unambiguously clear, though, if this holds over the entire range of alkyl lengths under investigation or if there is a cross-over from the traditional surfactant-like scaling law $N_{agg} \propto n^2$ to the novel $N_{agg} \propto n^3$ behaviour around $n \approx 19$. Unfortunately, we have no explanation for this unexpected power law yet.

It should be noted that throughout this and previous works on C_n-PEO micelles we assumed a spherical shape of the alkyl core. It is difficult, however, to picture how the relatively short and stiff alkyl blocks can efficiently pack into a spherical shape, particularly in the ordered phase. The nature of the core shape as well as whether the micellar cores are in a crystalline or rather liquid-crystalline/rotator-like phase still need to be clarified. The issue is currently under investigation and will be the topic of a future publication.

Conflicts of interest

There are no conflicts to declare.

References

1 P. Alexandridis and B. Lindman, *Amphiphilic block copolymers: self-assembly and applications*, Elsevier, 2000.
2 J. D. Hartgerink, E. Beniash and S. I. Stupp, *Science*, 2001, **294**, 1684.
3 I. W. Hamley, *Block copolymers in solution: fundamentals and applications*, John Wiley & Sons, 2005.
4 A.-V. Ruzette and L. Leibler, *Nat. Mater.*, 2005, **4**, 19–31.
5 Z. L. Tyrrell, Y. Shen and M. Radosz, *Prog. Polym. Sci.*, 2010, **35**, 1128–1143.
6 U. Tritschler, S. Pearce, J. Gwyther, G. R. Whittell and I. Manners, *Macromolecules*, 2017, **50**, 3439–3463.
7 A. M. Bodratti and P. Alexandridis, *Expert Opin. Drug Delivery*, 2018, **15**, 1085–1104.
8 J. J. Crassous, P. Schurtenberger, M. Ballauff and A. M. Mihut, *Polymer*, 2015, **62**, A1–A13.
9 Z. M. Hudson, C. E. Boott, M. E. Robinson, P. A. Rupar, M. A. Winnik and I. Manners, *Nat. Chem.*, 2014, **6**, 893–898.
10 H. B. Qiu, Y. Gao, C. E. Boott, O. E. C. Gould, R. L. Harniman, M. J. Miles, S. E. D. Webb, M. A. Winnik and I. Manners, *Science*, 2016, **352**, 697–701.
11 X. H. Jin, M. B. Price, J. R. Finnegan, C. E. Boott, J. M. Richter, A. Rao, M. Menke, R. H. Friend, G. R. Whittell and I. Manners, *Science*, 2018, **360**, 897–900.
12 Z. Coe, A. Weems, A. P. Dove and R. K. O'Reilly, *J. Visualized Exp.*, 2019, 7(148), e59772.

181

13 J. C. Foster, S. Varlas, B. Couturaud, Z. Coe and R. K. O'Reilly, *J. Am. Chem. Soc.*, 2019, **141**, 2742–2753.

14 S. Filippov, M. Hruby, C. Konak, H. Mackova, M. Spirkova and P. Stepanek, *Langmuir*, 2008, **24**, 9295–9301.

15 X. Dong and R. J. Mumper, *Nanomedicine*, 2010, **5**, 597–615.

16 R. P. Mandal, S. Sekh, D. Mondal and S. De, *Colloids Surf., A*, 2018, **558**, 33–44.

17 L. Zhang, D. D. Ren, J. Y. Zhou, G. N. Peng, G. Shu, Z. X. Yuan, F. Shi, L. Zhao, L. Z. Yin, G. Q. Fan, C. Liu and H. L. Fu, *Colloids Surf., B*, 2018, **163**, 125–132.

18 T. Zinn, L. Willner and R. Lund, *Phys. Rev. Lett.*, 2014, **113**, 238305.

19 B. Plazzotta, J. Dai, M. A. Behrens, I. Furó and J. S. Pedersen, *J. Phys. Chem. B*, 2015, **119**, 10798–10806.

20 S. Cheng and G. B. McKenna, *Mol. Pharmaceutics*, 2019, 856–866.

21 E. Elmowafy, H. Gad, F. Biondo, L. Casettari and M. E. Soliman, *Int. J. Pharm.*, 2019, **566**, 573–584.

22 O. R. Monaghan, P. H. H. Bomans, N. Sommerdijk and S. J. Holder, *Polym. Chem.*, 2017, **8**, 5303–5316.

23 X. Zhuo, T. Lei, L. Miao, W. Chu, X. Li, L. Luo, J. Gou, Y. Zhang, T. Yin, H. He and X. Tang, *J. Colloid Interface Sci.*, 2018, **529**, 34–43.

24 T. Zinn, L. Willner, V. Pipich, D. Richter and R. Lund, *ACS Macro Lett.*, 2015, **4**, 651–655.

25 N. König, L. Willner, V. Pipich, T. Zinn and R. Lund, *Phys. Rev. Lett.*, 2019, **122**, 078001.

26 R. Lund, L. Willner and D. Richter, in *Kinetics of Block Copolymer Micelles Studied by Small-Angle Scattering Methods*, ed. A. Abe, K.-S. Lee, L. Leibler and S. Kobayashi, Springer International Publishing, Cham, 2013, pp. 51–158.

27 A. B. Ebrahim Attia, Z. Y. Ong, J. L. Hedrick, P. P. Lee, P. L. R. Ee, P. T. Hammond and Y.-Y. Yang, *Curr. Opin. Colloid Interface Sci.*, 2011, **16**, 182–194.

28 C. L. Maikawa, A. Sevit, B. H. Lin, R. J. Wallstrom, J. L. Mann, A. C. Yu, R. M. Waymouth and E. A. Appel, *J. Polym. Sci., Part A: Polym. Chem.*, 2019, **57**, 1322–1332.

29 A. S. Manjappa, P. S. Kumbhar, A. B. Patil, J. I. Disouza and V. B. Patravale, *Crit. Rev. Ther. Drug Carrier Syst.*, 2019, **36**, 1–57.

30 J. Zhu, S. Zhang, K. Zhang, X. Wang, J. W. Mays, K. L. Wooley and D. J. Pochan, *Nat. Commun.*, 2013, **4**, 2297.

31 A. Cho, Y. La, S. Jeoung, H. R. Moon, J.-H. Ryu, T. J. Shin and K. T. Kim, *Macromolecules*, 2017, **50**, 3234–3243.

32 T. Zinn, L. Willner, R. Lund, V. Pipich, M. S. Appavou and D. Richter, *Soft Matter*, 2014, **10**, 5212–5220.

33 M. Amann, L. Willner, J. Stellbrink, A. Radulescu and D. Richter, *Soft Matter*, 2015, **11**, 4208–4217.

34 M. Daoud and J. P. Cotton, *J. Phys.*, 1982, **43**, 531–538.

35 A. Halperin, *Macromolecules*, 1987, **20**, 2943–2946.

36 C. Svaneborg and J. S. Pedersen, *Macromolecules*, 2002, **35**, 1028–1037.

37 G. Beaucage, *J. Appl. Crystallogr.*, 1995, **28**, 717–728.

38 D. J. Kinning and E. L. Thomas, *Macromolecules*, 1984, **17**, 1712–1718.

39 J. S. Pedersen, C. Svaneborg, K. Almdal, I. W. Hamley and R. N. Young, *Macromolecules*, 2003, **36**, 416–433.

40 F. Heatley, H. H. Teo and C. Booth, *J. Chem. Soc., Faraday Trans. 1*, 1984, **80**, 981–991.

41 M. Dirand, M. Bouroukba, V. Chevallier, D. Petitjean, E. Behar and V. Ruffier-Meray, *J. Chem. Eng. Data*, 2002, **47**, 115–143.

42 X. Guo, B. A. Pethica, J. S. Huang and R. K. Prud'homme, *Macromolecules*, 2004, **37**, 5638–5645.

43 B. K. Annis, J. D. Londono, G. D. Wignall and R. G. Snyder, *J. Phys. Chem.*, 1996, **100**, 1725–1730.

44 M. Senra, E. Panacharoensawad, K. Kraiwattanawong, P. Singh and H. S. Fogler, *Energy Fuels*, 2008, **22**, 545–555.

45 V. Kravchenko, *Acta Physicochim. URSS*, 1946, **21**, 335–344.

46 Y. Su, G. Liu, B. Xie, D. Fu and D. Wang, *Acc. Chem. Res.*, 2014, **47**, 192–201.

47 M. Maroncelli, H. L. Strauss and R. G. Snyder, *J. Phys. Chem.*, 1985, **89**, 5260–5267.

48 O. Petrov and I. Furo, *Phys. Rev. E: Stat., Nonlinear, Soft Matter Phys.*, 2006, **73**, 011608.

49 M. Ameri, D. Attwood, J. H. Collett and C. Booth, *J. Chem. Soc., Faraday Trans.*, 1997, **93**, 2545–2551.

50 A. Goebel and K. Lunkenheimer, *Langmuir*, 1997, **13**, 369–372.

51 S. Zeppieri, J. Rodríguez and A. L. López de Ramos, *J. Chem. Eng. Data*, 2001, **46**, 1086–1088.

52 F. Renou, T. Nicolai, E. Nicol and L. Benyahia, *Langmuir*, 2009, **25**, 515–521.

53 *CRC Handbook of Chemistry and Physics (Internet Version 2019)*, ed. J. R. Rumble, CRC Press/Taylor & Francis, Boca Raton, FL, 100th edn, 2019.

54 S. Förster, M. Zisenis, E. Wenz and M. Antonietti, *J. Chem. Phys.*, 1996, **104**, 9956–9970.

55 E. B. Zhulina, M. Adam, I. LaRue, S. S. Sheiko and M. Rubinstein, *Macromolecules*, 2005, **38**, 5330–5351.

56 R. Nagarajan and K. Ganesh, *J. Chem. Phys.*, 1989, **90**, 5843–5856.

57 F. Laflèche, T. Nicolai, D. Durand, Y. Gnanou and D. Taton, *Macromolecules*, 2003, **36**, 1341–1348.

58 L. Leibler, H. Orland and J. C. Wheeler, *J. Chem. Phys.*, 1983, **79**, 3550–3557.

59 A. Halperin, *Macromolecules*, 1990, **23**, 2724–2731.

60 T. Vilgis and A. Halperin, *Macromolecules*, 1991, **24**, 2090–2095.

61 C. Sommer, J. S. Pedersen and V. M. Garamus, *Langmuir*, 2005, **21**, 2137–2149.

62 C. Tanford, *The hydrophobic effect: formation of micelles and biological membranes*, Wiley, 1980.

63 R. Kjellander and E. Florin, *J. Chem. Soc., Faraday Trans. 1*, 1981, **77**, 2053–2077.

64 M. J. Hey, S. M. Ilett and G. Davidson, *J. Chem. Soc., Faraday Trans.*, 1995, **91**, 3897–3900.

65 D. Zhao, Y. C. Ma, E. Wang and T. P. Lodge, *Macromolecules*, 2019, **52**, 4729–4738.

66 O. Petrov and I. Furo, *Phys. Chem. Chem. Phys.*, 2011, **13**, 16358–16365.

Supplementary Information

for

Structure and Thermodynamics of Mixed Polymeric Micelles with Crystalline Cores: Tuning Properties via Co-Assembly

Nico König,[1, 2] Lutz Willner,[2, *] and Reidar Lund[1, †]

[1] *Department of Chemistry, University of Oslo, Postboks 1033 Blindern, 0315 Oslo, Norway*
[2] *Jülich Centre for Neutron Science JCNS and Institute for Complex Systems ICS, Forschungszentrum Jülich GmbH, 52425 Jülich, Germany*

FITS OF C_{12}- AND C_{14}-PEO SAXS DATA

The scattering data of C_{12}- and C_{14}-PEO are shown separately here because they require special treatment since the critical micellar concentration (CMC) of these polymers is close to the experimental concentrations. Thus for these samples concentration-dependent measurements were performed at only one temperature, $T = 25\,°C$. In the scattering data in figure S1 it is eminent that micellar scattering only emerges above a certain concentration threshold. Thus, the model was amended by unimer scattering in the form of an additional Beaucage form factor, see reference [1] for details. The fit parameters are given in table S1. Unfortunately, the CMC and the aggration number are highly correlated fit parameters. Therefore, even though the fits shown in figure S1 are the best fits, there is a large uncertainty in N_{agg} and acceptable fits can still be obtained with aggregation numbers which are more in line with a $N_{agg} \propto n^2$ scaling for small n. See the main manuscript for details.
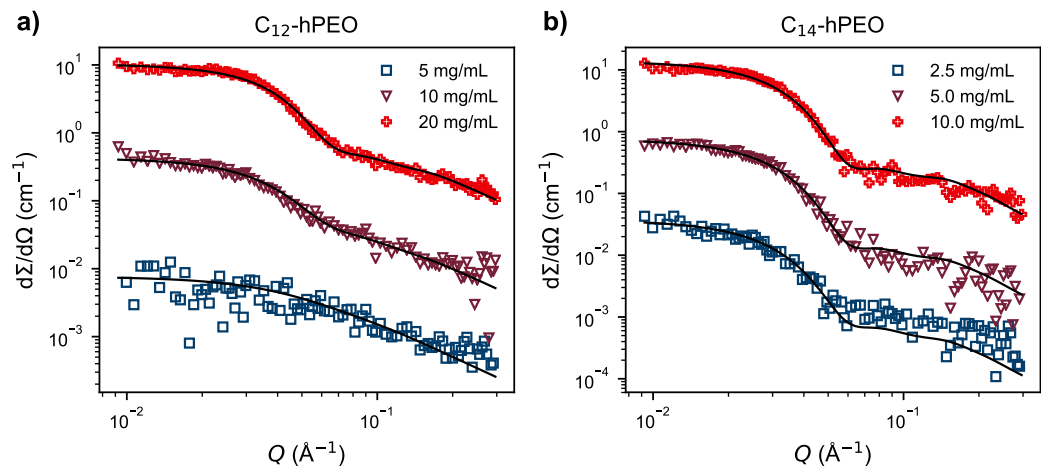

FIG. S1: Scattering data of a) C_{12}- and b) C_{14}-hPEO at various concentrations around the CAC at 25 °C. Solid lines represent a simultaneous fit of all concentrations according to the model presented in reference [1] and fit parameters are given in table S1.

TABLE S1: SAXS model parameters of C_{12}- and C_{14}-hPEO shown in figure S1

	C_{12}-hPEO	C_{14}-hPEO
$N_{agg}{}^{a}$	8^{+10}_{-3}	13^{+12}_{-2}
$R_m{}^{a}$ (Å)	70 ± 10	79 ± 6
$d_{Cn}{}^{b}$ (g/mL)	0.75	0.76
$R_c{}^{c}$ (Å)	$8.9^{+4.2}_{-1.3}$	$11.0^{+2.7}_{-0.9}$
d_{PEO} (g/mL)	1.20	1.20
$R_{g,chain}{}^{a}$ (Å)	36 ± 1	39 ± 1
CMC^{a} (mg/mL)	6.2 ± 1.5	0.4 ± 0.2
ρ_c ($10^{10}\,cm^{-2}$)	7.30	7.40
ρ_s ($10^{11}\,cm^{-2}$)	1.11	1.11
ρ_0 ($10^{10}\,cm^{-2}$)	9.43	9.43

^{a} free fit parameter ^{b} taken from reference [2]
^{c} derived from N_{agg} and d_{Cn}

SCALING ANALYSIS OF MICELLES WITH CRYSTALLINE CORES

As mentioned in the main manuscript, there has been a theoretical treatment of micelles with crystalline cores[3] already. However, this work dealt with long solvophobic blocks that repeatedly fold to form the micellar core. Also, there is a treatment of micelles with rod-like solvophobic blocks[4] which does not consider the enthalpic gain upon crystallization. The polymeric model system under investigation in the present manuscript, C_n-PEO, unites both characteristics. On the one hand, the alkyl blocks crystallize partially within the micellar core. On the other hand, the blocks are relatively short, with a contour length of $L = (15\text{-}27) \times \cos\frac{109.5°}{2} \times 1.54\,\text{Å} = 13.3\text{-}24.0\,\text{Å}$. Comparing the Kuhn length of poly(ethylene), $l_K = 14\,\text{Å}$,[5] it is clear that the alkyl blocks can be considered rod-like. Thus it is hard to conceive a packing order for the partially crystallizing, rod-like alkyl blocks to form a spherical core. Indeed, we have experimental evidence that the micellar cores are aspherical and the effect of crystallisation on the core geometry will be topic of a forthcoming paper. A straightforward way to form the core is by aligning the alkyl block longitudinally into a cylindrical shape, with the PEO corona chains attached to the basal planes. With sufficiently long PEO blocks coiling around the core, the overall shape of the micelle would still appear spherical, in agreement with the reported scattering data. This has also been suggested by Halperin and Vilgis.[3, 4] In line with their argumentation, the total free energy of the micelle comprises three terms:

$$F_{\text{mic}} = F_{\text{core}} + F_{\text{corona}} + F_{\text{interface}}, \tag{1}$$

the contributions from the core, the corona and the interface in between. Traditionally, F_{core} considers stretching penalties of the core block but here it will reflect the enthalpic gain of crystallization. F_{corona}, however, reflects the conventional stretching entropy of the corona blocks which are grafted to the core surface and $F_{\text{interface}}$ contains the surface energy between the solvophobic core and the solvent-swollen corona.

Each alkyl block consists of n CH_2 units with diameter a so that the contour length is $L = na$. We assume the core has a cylindrical shape with radius R_c and thickness L and comprises N_{agg} molecules. Consequently, the area of one of the two basal interfaces is $S_b = N_{\text{agg}}a^2 = \pi R_c^2$ and thus $R_c = \left(N_{\text{agg}}a^2/\pi\right)^{1/2}$. Then the lateral interface is $S_l = 2\pi R_c L = 2na^2 \left(\pi N_{\text{agg}}\right)^{1/2}$. This results in the interfacial energy per molecule

$$F_{\text{interface}} = \frac{2\gamma_b S_b}{N_{\text{agg}}} + \frac{\gamma_l S_l}{N_{\text{agg}}} = 2\gamma_b a^2 + 2\gamma_l na^2 \left(\frac{\pi}{N_{\text{agg}}}\right)^{1/2}, \tag{2}$$

with the interfacial tensions γ_b and γ_l of the basal and lateral interfaces, respectively.

For the coronal free energy, we follow the arguments of Halperin[6] for star-like micelles which will not be recapitulated here. In the leading order, the free energy per molecule resulting from stretching of the corona blocks scales as

$$F_{\text{corona}} \propto N_{\text{agg}}^{1/2} k_B T. \tag{3}$$

We assume each CH_2 unit immersed in the crystalline core gains a hypothetical enthalpy amount H_c so that every alkyl block fully buried in the core gains nH_c. For molecules located at the lateral interface of the cylindrical core, we assume an enthalpy gain of $nH_c/2$ from crystalline interaction. We can calculate the number of molecules at the lateral interface as

$$N_l = \frac{2\pi R_c}{a} = 2 \left(\pi N_{\text{agg}}\right)^{1/2}. \tag{4}$$

Therefore, the core contribution to the free energy per molecule is

$$F_{\text{core}} = -\frac{N_l nH_c}{2N_{\text{agg}}} - \frac{(N_{\text{agg}} - N_l)nH_c}{N_{\text{agg}}} = nH_c \left[\left(\frac{\pi}{N_{\text{agg}}}\right)^{1/2} - 1\right]. \tag{5}$$

As we are only interested in the scaling behavior with respect to the aggregation number, we will now drop all irrelevant prefactors as well as terms independent of N_{agg}:

$$F_{\text{mic}} \propto \frac{\gamma_l na^2}{N_{\text{agg}}^{1/2}} + N_{\text{agg}}^{1/2} k_B T + \frac{nH_c}{N_{\text{agg}}^{1/2}}. \tag{6}$$

Minimization with respect to N_{agg} yields

$$N_{\text{agg}} \propto \frac{\gamma_l na^2 + nH_c}{k_B T}. \tag{7}$$

Thus our considerations lead to a linear dependency of N_{agg} on n, similar to the apporaches of Halperin and Vilgis[3, 4]. Unfortunately, they fail to explain the $N_{\text{agg}} \propto n^3$ behavior found experimentally which must originate from circumstances not reflected in our calculations.

INDIVIDUAL INSPECTION OF THE MELTING POINTS OF C_{28}- AND C_{22}-PEO

As described in the main manuscript, the melting point of the alkyl block within the micellar core is affected by two phenomena simultaneously: on the one hand, the melting point is influenced by the other component's presence and, on the other hand, it is suppressed because of the self-confinement in the core. We tried to separate these two effects under the assumption of simple additivity. Due to the presence of the other respective component, the melting point is altered to

$$T_m^{0\dagger} = T_m^0 + x\Delta T_m, \tag{8}$$

where T_m^0 is the bulk melting point of C_{22} or C_{28}, respectively, x the fraction of the other respective component and ΔT_m the melting point difference between both components. This altered melting point is furthermore reduced due to the Gibbs-Thomson effect as explained in the main manuscript,

$$T_m = T_m^{0\dagger} - \frac{\alpha\gamma V_{\text{Cn}} T_m^0}{\Delta H_m}. \tag{9}$$

Here, V_{Cn} is the molar volume of C_{22} or C_{28}, respectively, and ΔH_m is the melting enthalpy of the mixture. Figure S2 shows the data for C_{22} and C_{28} individually. Only data at 15 and 65 °C are shown because at those temperatures all mixtures are either frozen or molten, respectively. It is not obvious, though, if $T_m^{0\dagger}$ or T_m^0 should serve as reference point in the numerator of eq. (9). Furthermore, the nature of ΔT_m is not straightforward. For figure S2, the bulk melting point difference $|\Delta T_m| = |T_{m,C28}^0 - T_{m,C22}^0| = 17.4\,\text{K}$ has been chosen. But the micellar melting point difference $|\Delta T_m| = |T_{m,C28} - T_{m,C22}| = 27.5\,\text{K}$ is similarly valid. The problem is that ΔT_m is simultaneously affected by the confinement. Thus, no consistent conclusion on the individual effects on C_{22} and C_{28} can be drawn.
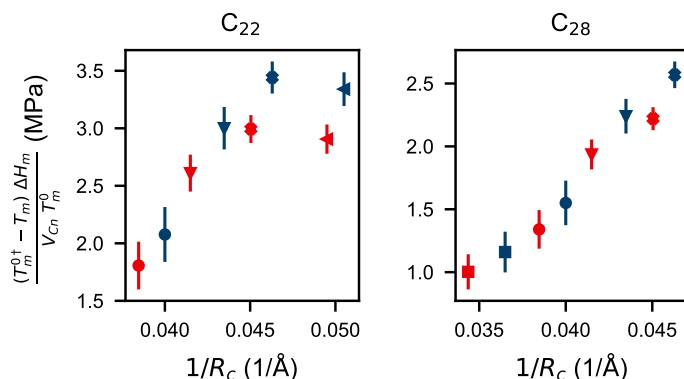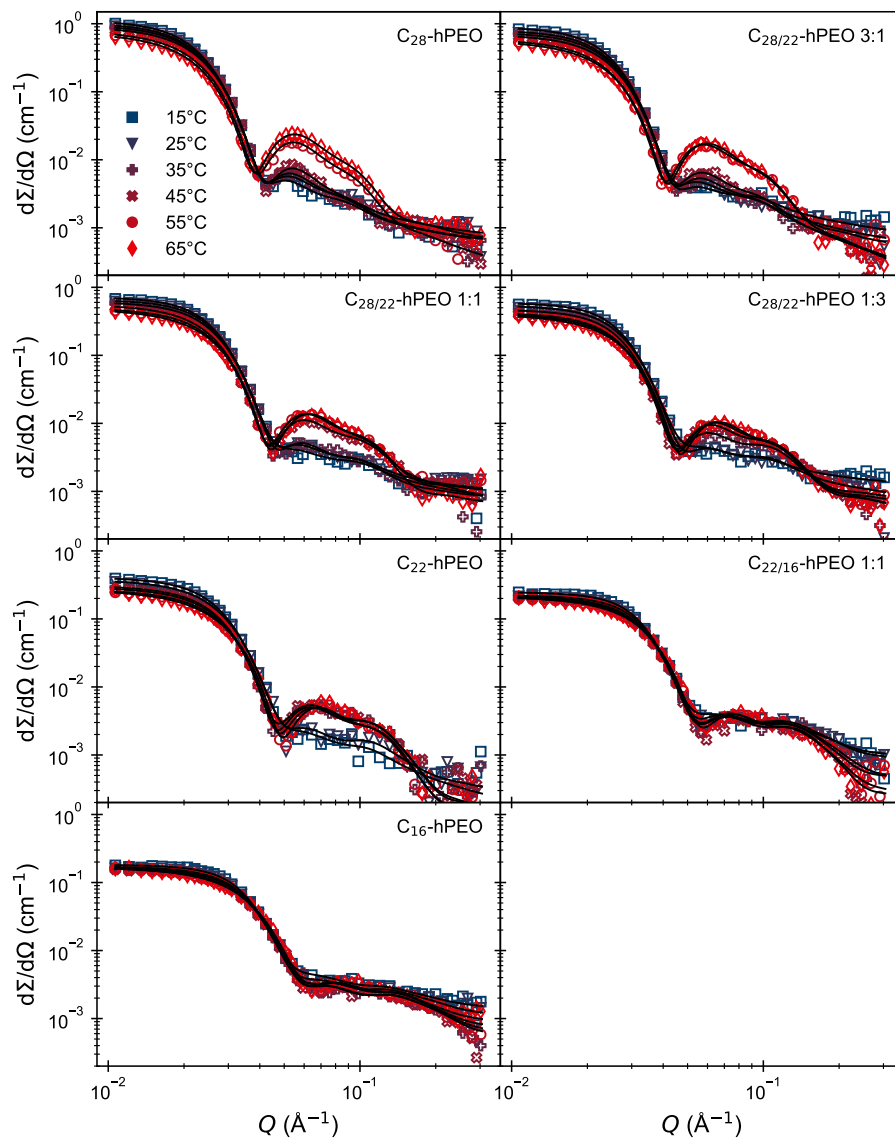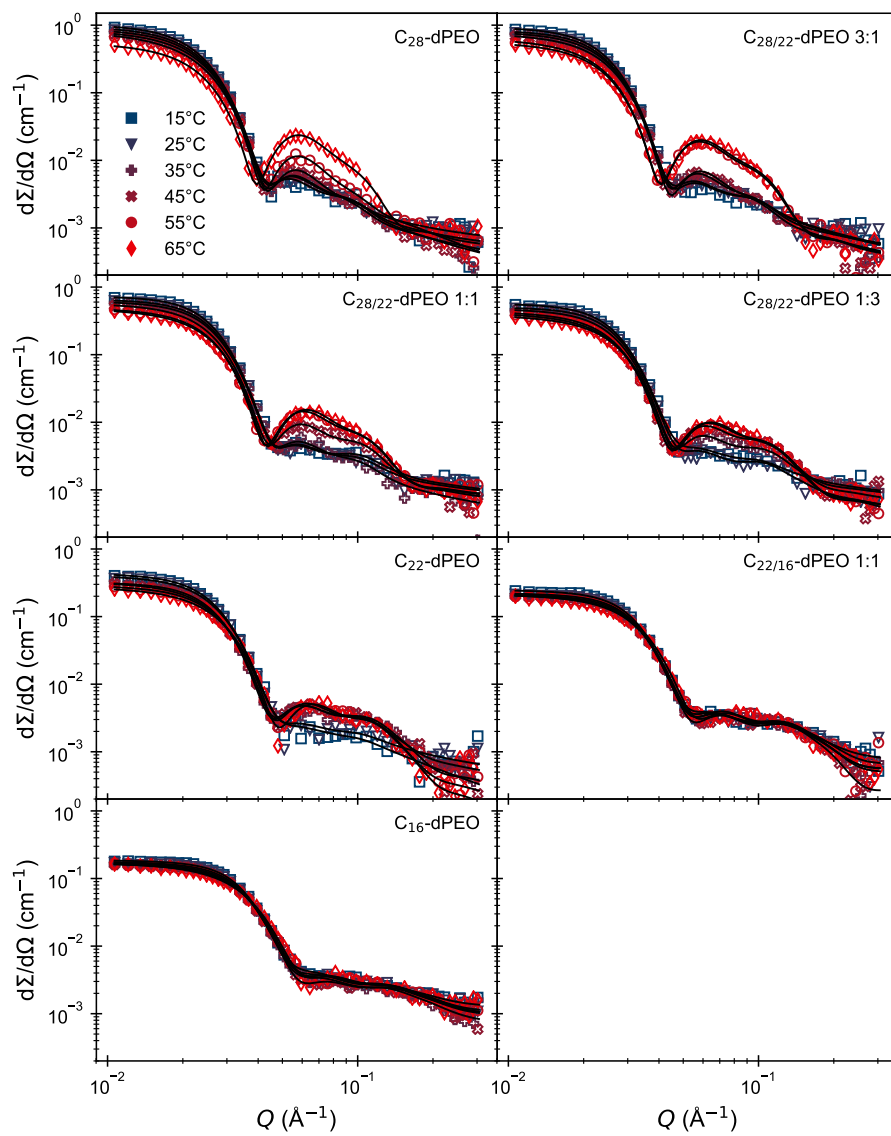

FIG. S2: Individual inspection of the Gibbs-Thomson effect on C_{22} and C_{28} at 15 °C (blue) and 65 °C (red). See text for further explanation.

SUPPLEMENTARY FIGURES

FIG. S3: SAXS data of C_n-hPEO

FIG. S4: SAXS data of C$_n$-dPEO
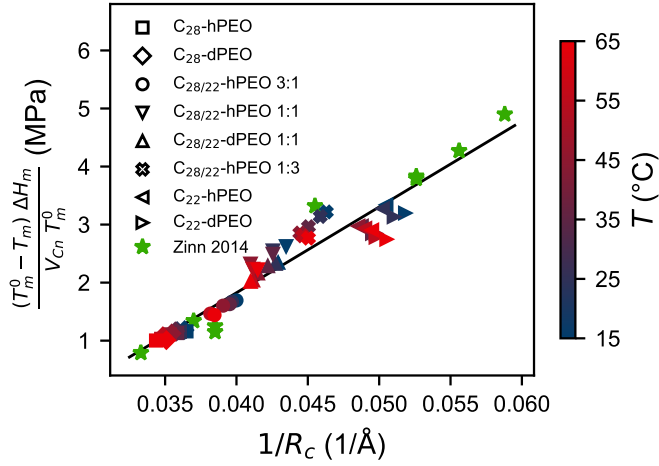
FIG. S5: Reproduction of figure 4 in the main manuscript, containing data from all temperatures: Melting point depression of the alkyl blocks as a result of self-confinement in the micellar core as a function of the inverse core radius. Previously reported data[7] have been added for comparison. The black line is a fit to all data points shown and yields $\gamma = 7.4\,\mathrm{mN/m}$, similar to the value reported in the main manuscript.

FIG. S6: Aggregation number as a function of the mean alkyl block length, obtained from model fits of SAXS data measured between 15 and 65 °C. Obviously, as the points obtained at different temperatures T overlap, N_{agg} does not depend on T. Previously reported results[8] obtained from the same n-alkyl-PEO system were added for comparison. The dashed line corresponds to $N_{\mathrm{agg}} \propto n^2$, the solid line to $N_{\mathrm{agg}} \propto n^3$.
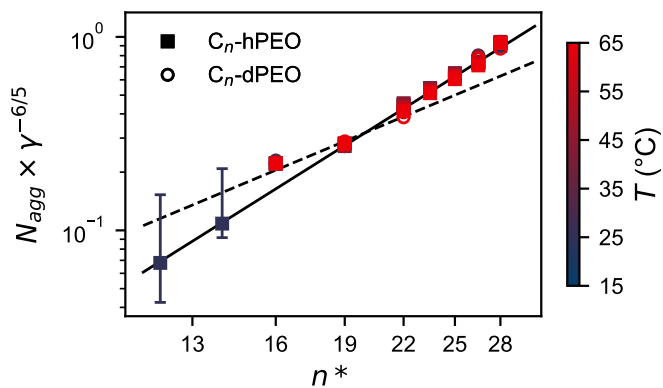
FIG. S7: Aggregation number scaled with the interfacial tension as a function of the mean alkyl block length, obtained from model fits of SAXS data measured between 15 and 65 °C. The dashed line corresponds to $N_{\mathrm{agg}} \propto n^2$, the solid line to $N_{\mathrm{agg}} \propto n^3$.
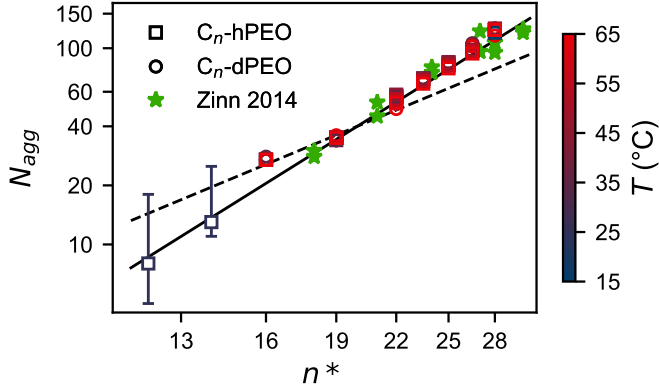

FIG. S8: Micellar radius as a function of the mean alkyl block length, obtained from model fits of SAXS data measured between 15 and 65 °C. The dashed line corresponds to $R_m \propto n^{4/25}$, the solid line to $R_m \propto n^{3/5}$.

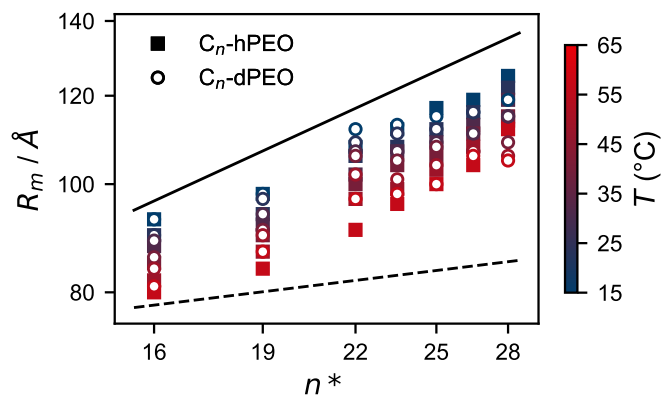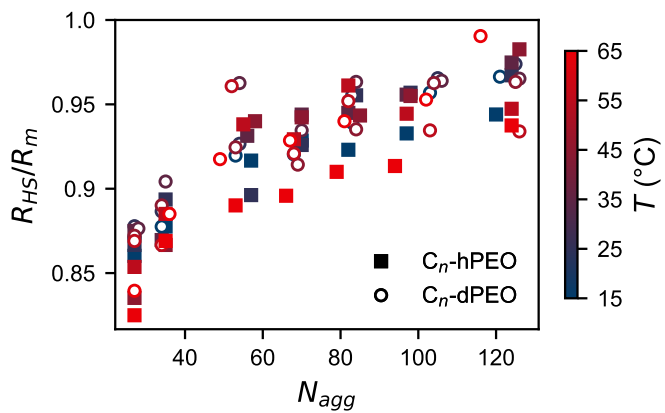FIG. S9: The hard-sphere interaction radius divided by the micellar radius as a function of the aggregation number. With increasing N_{agg} the corona becomes denser and hence more repellent.

SUPPLEMENTARY TABLES

TABLE S2: SAXS model parameters of C_{28}-hPEO

T (°C)	15	25	35	45	55	65
$N_{agg}{}^{a}$	120	124	124	126	124	124
$R_{m}{}^{a}$ (Å)	125	122	119	115	114	112
$R_{HS}{}^{a}$ (Å)	118	118	116	113	108	105
$d_{Cn}{}^{a}$ (g/mL)	0.91	0.90	0.89	0.87	0.81	0.79
R_{c} (Å)	27.4	27.8	27.9	28.3	28.8	29.1
d_{PEO} (g/mL)	1.21	1.20	1.19	1.17	1.16	1.15
ρ_{c} (10^{10} cm^{-2})	8.84	8.77	8.62	8.45	7.86	7.65
ρ_{s} (10^{11} cm^{-2})	1.12	1.11	1.10	1.09	1.08	1.07
ρ_{0} (10^{10} cm^{-2})	9.42	9.41	9.38	9.35	9.30	9.26

^{a} free fit parameter

TABLE S3: SAXS model parameters of C_{28}-dPEO

T (°C)	15	25	35	45	55	65
$N_{agg}{}^{a}$	121	125	126	125	126	116
$R_{m}{}^{a}$ (Å)	119	115	115	109	106	105
$R_{HS}{}^{a}$ (Å)	115	112	111	105	99	104
$d_{Cn}{}^{a}$ (g/mL)	0.91	0.90	0.90	0.87	0.83	0.78
R_{c} (Å)	27.5	27.9	28.0	28.2	28.7	28.5
d_{PEO} (g/mL)	1.32	1.30	1.29	1.28	1.27	1.25
ρ_{c} (10^{10} cm^{-2})	8.89	8.77	8.72	8.46	8.10	7.58
ρ_{s} (10^{11} cm^{-2})	1.12	1.11	1.10	1.09	1.08	1.07
ρ_{0} (10^{10} cm^{-2})	9.42	9.41	9.38	9.35	9.30	9.26

^{a} free fit parameter

TABLE S4: SAXS model parameters of $C_{28/22}$-hPEO 3:1

T (°C)	15	25	35	45	55	65
$N_{agg}{}^{a}$	97	98	97	98	97	94
$R_{m}{}^{a}$ (Å)	119	116	113	111	108	104
$R_{HS}{}^{a}$ (Å)	111	111	108	106	102	95
$d_{Cn}{}^{a}$ (g/mL)	0.92	0.91	0.89	0.87	0.80	0.78
R_{c} (Å)	25.0	25.2	25.3	25.6	26.2	26.0
d_{PEO} (g/mL)	1.21	1.20	1.19	1.17	1.16	1.15
ρ_{c} (10^{10} cm^{-2})	8.94	8.82	8.61	8.47	7.74	7.61
ρ_{s} (10^{11} cm^{-2})	1.12	1.11	1.10	1.09	1.08	1.07
ρ_{0} (10^{10} cm^{-2})	9.42	9.41	9.38	9.35	9.30	9.26

^{a} free fit parameter

TABLE S5: SAXS model parameters of $C_{28/22}$-dPEO 3:1

T (°C)	15	25	35	45	55	65
$N_{\mathrm{agg}}{}^{a}$	103	105	106	104	103	102
$R_{\mathrm{m}}{}^{a}$ (Å)	116	116	111	107	107	106
$R_{\mathrm{HS}}{}^{a}$ (Å)	111	112	107	103	100	101
$d_{\mathrm{Cn}}{}^{a}$ (g/mL)	0.91	0.91	0.88	0.86	0.79	0.79
R_c (Å)	25.5	25.7	26.1	26.2	26.8	26.8
d_{PEO} (g/mL)	1.32	1.30	1.29	1.28	1.27	1.25
ρ_c ($10^{10}\,\mathrm{cm}^{-2}$)	8.84	8.84	8.55	8.36	7.71	7.63
ρ_s ($10^{11}\,\mathrm{cm}^{-2}$)	1.12	1.11	1.10	1.09	1.08	1.07
ρ_0 ($10^{10}\,\mathrm{cm}^{-2}$)	9.42	9.41	9.38	9.35	9.30	9.26

^{a} free fit parameter

TABLE S6: SAXS model parameters of $C_{28/22}$-hPEO 1:1

T (°C)	15	25	35	45	55	65
$N_{\mathrm{agg}}{}^{a}$	82	84	82	85	82	79
$R_{\mathrm{m}}{}^{a}$ (Å)	117	112	109	106	103	100
$R_{\mathrm{HS}}{}^{a}$ (Å)	108	107	103	100	99	91
$d_{\mathrm{Cn}}{}^{a}$ (g/mL)	0.92	0.90	0.88	0.82	0.80	0.79
R_c (Å)	23.0	23.5	23.5	24.4	24.3	24.1
d_{PEO} (g/mL)	1.21	1.20	1.19	1.17	1.16	1.15
ρ_c ($10^{10}\,\mathrm{cm}^{-2}$)	9.03	8.77	8.57	8.00	7.76	7.65
ρ_s ($10^{11}\,\mathrm{cm}^{-2}$)	1.12	1.11	1.10	1.09	1.08	1.07
ρ_0 ($10^{10}\,\mathrm{cm}^{-2}$)	9.42	9.41	9.38	9.35	9.30	9.26

^{a} free fit parameter

TABLE S7: SAXS model parameters of $C_{28/22}$-dPEO 1:1

T (°C)	15	25	35	45	55	65
$N_{\mathrm{agg}}{}^{a}$	83	83	84	84	82	81
$R_{\mathrm{m}}{}^{a}$ (Å)	115	112	109	108	104	100
$R_{\mathrm{HS}}{}^{a}$ (Å)	108	107	105	101	99	94
$d_{\mathrm{Cn}}{}^{a}$ (g/mL)	0.91	0.90	0.89	0.84	0.79	0.78
R_c (Å)	23.3	23.4	23.7	24.1	24.3	24.4
d_{PEO} (g/mL)	1.32	1.30	1.29	1.28	1.27	1.25
ρ_c ($10^{10}\,\mathrm{cm}^{-2}$)	8.84	8.78	8.61	8.14	7.69	7.61
ρ_s ($10^{11}\,\mathrm{cm}^{-2}$)	1.12	1.11	1.10	1.09	1.08	1.07
ρ_0 ($10^{10}\,\mathrm{cm}^{-2}$)	9.42	9.41	9.38	9.35	9.30	9.26

^{a} free fit parameter

TABLE S8: SAXS model parameters of $C_{28/22}$-hPEO 1:3

T (°C)	15	25	35	45	55	65
$N_{\mathrm{agg}}{}^{a}$	70	70	70	70	68	66
$R_{\mathrm{m}}{}^{a}$ (Å)	112	108	107	104	88	96
$R_{\mathrm{HS}}{}^{a}$ (Å)	104	100	101	98	92	86
$d_{\mathrm{Cn}}{}^{a}$ (g/mL)	0.92	0.89	0.84	0.81	0.80	0.79
R_c (Å)	21.6	21.8	22.2	22.5	22.4	22.2
d_{PEO} (g/mL)	1.21	1.20	1.19	1.17	1.16	1.15
ρ_c ($10^{10}\,\mathrm{cm}^{-2}$)	8.91	8.69	8.21	7.90	7.76	7.66
ρ_s ($10^{11}\,\mathrm{cm}^{-2}$)	1.12	1.11	1.10	1.09	1.08	1.07
ρ_0 ($10^{10}\,\mathrm{cm}^{-2}$)	9.42	9.41	9.38	9.35	9.30	9.26

^{a} free fit parameter

TABLE S9: SAXS model parameters of $C_{28/22}$-dPEO 1:3

T (°C)	15	25	35	45	55	65
$N_{\mathrm{agg}}{}^{a}$	68	68	70	69	68	67
$R_{\mathrm{m}}{}^{a}$ (Å)	113	111	107	105	101	98
$R_{\mathrm{HS}}{}^{a}$ (Å)	104	103	100	96	93	91
$d_{\mathrm{Cn}}{}^{a}$ (g/mL)	0.91	0.90	0.85	0.81	0.80	0.79
R_c (Å)	21.4	21.5	22.1	22.3	22.4	22.3
d_{PEO} (g/mL)	1.32	1.30	1.29	1.28	1.27	1.25
ρ_c (10^{10} cm^{-2})	8.88	8.77	8.27	7.91	7.76	7.70
ρ_s (10^{11} cm^{-2})	1.12	1.11	1.10	1.09	1.08	1.07
ρ_0 (10^{10} cm^{-2})	9.42	9.41	9.38	9.35	9.30	9.26

^{a} free fit parameter

TABLE S10: SAXS model parameters of C_{22}-hPEO

T (°C)	15	25	35	45	55	65
$N_{\mathrm{agg}}{}^{a}$	57	57	56	58	55	53
$R_{\mathrm{m}}{}^{a}$ (Å)	108	106	102	100	97	91
$R_{\mathrm{HS}}{}^{a}$ (Å)	99	95	95	94	91	81
$d_{\mathrm{Cn}}{}^{a}$ (g/mL)	0.91	0.89	0.81	0.81	0.80	0.79
R_c (Å)	19.8	19.9	20.5	20.6	20.4	20.2
d_{PEO} (g/mL)	1.21	1.20	1.19	1.17	1.16	1.15
ρ_c (10^{10} cm^{-2})	8.84	8.64	7.87	7.87	7.77	7.67
ρ_s (10^{11} cm^{-2})	1.12	1.11	1.10	1.09	1.08	1.07
ρ_0 (10^{10} cm^{-2})	9.42	9.41	9.38	9.35	9.30	9.26

^{a} free fit parameter

TABLE S11: SAXS model parameters of C_{22}-dPEO

T (°C)	15	25	35	45	55	65
$N_{\mathrm{agg}}{}^{a}$	53	54	54	53	52	49
$R_{\mathrm{m}}{}^{a}$ (Å)	112	109	107	106	102	97
$R_{\mathrm{HS}}{}^{a}$ (Å)	103	101	103	87	98	89
$d_{\mathrm{Cn}}{}^{a}$ (g/mL)	0.91	0.89	0.81	0.81	0.79	0.78
R_c (Å)	19.3	19.6	20.2	20.1	20.1	19.8
d_{PEO} (g/mL)	1.32	1.30	1.29	1.28	1.27	1.25
ρ_c (10^{10} cm^{-2})	8.88	8.77	8.27	7.91	7.76	7.70
ρ_s (10^{11} cm^{-2})	1.12	1.11	1.10	1.09	1.08	1.07
ρ_0 (10^{10} cm^{-2})	9.42	9.41	9.38	9.35	9.30	9.26

^{a} free fit parameter

TABLE S12: SAXS model parameters of $C_{22/16}$-hPEO

T (°C)	15	25	35	45	55	65
$N_{\mathrm{agg}}{}^{a}$	35	35	34	35	35	35
$R_{\mathrm{m}}{}^{a}$ (Å)	98	94	92	90	87	84
$R_{\mathrm{HS}}{}^{a}$ (Å)	86	84	80	78	77	73
$d_{\mathrm{Cn}}{}^{a}$ (g/mL)	0.85	0.84	0.83	0.82	0.81	0.80
R_c (Å)	16.3	16.4	16.4	16.6	16.7	16.7
d_{PEO} (g/mL)	1.21	1.20	1.19	1.17	1.16	1.15
ρ_c (10^{10} cm^{-2})	8.30	8.12	8.03	7.96	7.83	7.73
ρ_s (10^{11} cm^{-2})	1.12	1.11	1.10	1.09	1.08	1.07
ρ_0 (10^{10} cm^{-2})	9.42	9.41	9.38	9.35	9.30	9.26

^{a} free fit parameter

TABLE S13: SAXS model parameters of $C_{22/16}$-dPEO

T (°C)	15	25	35	45	55	65
$N_{\mathrm{agg}}{}^{a}$	34	34	35	34	34	36
$R_{\mathrm{m}}{}^{a}$ (Å)	98	97	94	91	90	87
$R_{\mathrm{HS}}{}^{a}$ (Å)	86	86	85	81	78	77
$d_{\mathrm{Cn}}{}^{a}$ (g/mL)	0.85	0.83	0.82	0.81	0.81	0.81
R_{c} (Å)	16.2	16.3	16.5	16.5	16.5	16.7
d_{PEO} (g/mL)	1.32	1.30	1.29	1.28	1.27	1.25
ρ_{c} (10^{10} cm^{-2})	8.21	8.10	8.00	7.88	7.84	7.91
ρ_{s} (10^{11} cm^{-2})	1.12	1.11	1.10	1.09	1.08	1.07
ρ_{0} (10^{10} cm^{-2})	9.42	9.41	9.38	9.35	9.30	9.26

[a] free fit parameter

TABLE S14: SAXS model parameters of C_{16}-hPEO

T (°C)	15	25	35	45	55	65
$N_{\mathrm{agg}}{}^{a}$	27	27	27	27	27	27
$R_{\mathrm{m}}{}^{a}$ (Å)	93	90	88	85	82	80
$R_{\mathrm{HS}}{}^{a}$ (Å)	80	78	77	71	70	66
$d_{\mathrm{Cn}}{}^{a}$ (g/mL)	0.85	0.84	0.83	0.82	0.80	0.80
R_{c} (Å)	14.1	14.2	14.2	14.3	14.4	14.4
d_{PEO} (g/mL)	1.21	1.20	1.19	1.17	1.16	1.15
ρ_{c} (10^{10} cm^{-2})	8.25	8.14	8.07	7.99	7.79	7.80
ρ_{s} (10^{11} cm^{-2})	1.12	1.11	1.10	1.09	1.08	1.07
ρ_{0} (10^{10} cm^{-2})	9.42	9.41	9.38	9.35	9.30	9.26

[a] free fit parameter

TABLE S15: SAXS model parameters of C_{16}-dPEO

T (°C)	15	25	35	45	55	65
$N_{\mathrm{agg}}{}^{a}$	27	27	28	27	27	27
$R_{\mathrm{m}}{}^{a}$ (Å)	93	90	89	86	84	81
$R_{\mathrm{HS}}{}^{a}$ (Å)	81	79	78	75	73	68
$d_{\mathrm{Cn}}{}^{a}$ (g/mL)	0.84	0.83	0.83	0.82	0.81	0.81
R_{c} (Å)	14.1	14.3	14.4	14.4	14.5	14.4
d_{PEO} (g/mL)	1.32	1.30	1.29	1.28	1.27	1.25
ρ_{c} (10^{10} cm^{-2})	8.18	8.06	8.08	7.99	7.88	7.85
ρ_{s} (10^{11} cm^{-2})	1.12	1.11	1.10	1.09	1.08	1.07
ρ_{0} (10^{10} cm^{-2})	9.42	9.41	9.38	9.35	9.30	9.26

[a] free fit parameter

REFERENCES

———————

* l.willner@fz-juelich.de

† reidar.lund@kjemi.uio.no

[1] V. A. Bjørnestad, *Liposomes as a model system for the study of surface active peptides*, Master thesis, Department of Chemistry - University of Oslo (2018).

[2] J. R. Rumble (ed.), *CRC Handbook of Chemistry and Physics, 100th Edition (Internet Version 2019)*, edited by J. R. Rumble (CRC Press/Taylor & Francis, Boca Raton, FL, 2019).

[3] T. Vilgis and A. Halperin, Macromolecules **24**, 2090 (1991).

[4] A. Halperin, Macromolecules **23**, 2724 (1990).

[5] M. Rubinstein and R. Colby, *Polymer Physics* (Oxford University Press, 2003).

[6] A. Halperin, Macromolecules **20**, 2943 (1987).

[7] T. Zinn, L. Willner, and R. Lund, Physical Review Letters **113**, 238305 (2014).

[8] T. Zinn, L. Willner, R. Lund, V. Pipich, M. S. Appavou, and D. Richter, Soft Matter **10**, 5212 (2014).

Paper III

Cooperativity during Melting and Molecular Exchange in Micelles with Crystalline Cores

Nico König, Lutz Willner, Vitaliy Pipich, Thomas Zinn and Reidar Lund

III

Cooperativity during Melting and Molecular Exchange in Micelles with Crystalline Cores

Nico König,[1,2,§] Lutz Willner,[1,*] Vitaliy Pipich,[3,¶] Thomas Zinn,[2,†] and Reidar Lund[2,‡]

[1]*Jülich Centre for Neutron Science (JCNS) and Institute for Complex Systems (ICS),*
Forschungszentrum Jülich GmbH, 52425 Jülich, Germany
[2]*Department of Chemistry, University of Oslo, P.O. Box 1033, Blindern, 0315 Oslo, Norway*
[3]*Jülich Centre for Neutron Science (JCNS) at Heinz Maier-Leibnitz Zentrum (MLZ),*
Forschungszentrum Jülich GmbH, 85747 Garching, Germany

Molecular exchange processes are important equilibration and transport mechanisms in both synthetic and biological self-assembled systems such as micelles, vesicles, and membranes. Still, these processes are not entirely understood, in particular the effect of crystallinity and the interplay between cooperative melting processes and chain exchange. Here we focus on a set of simple polymer micelles formed by binary mixtures of poly(ethylene oxide)-mono-n-alkyl-ethers (C_n-PEO5) which allows the melting point to be tuned over a wide range. We show that the melting transition is cooperative in the confined 4–5 nm micellar core, whereas the exchange process is widely decoupled and unimeric in nature. As confirmed by differential scanning calorimetry, the total activation energy for ejecting a molecule out of the micellar core below the melting point is the sum of the enthalpy of fusion and the corresponding activation energy in the melt state. This suggests that a "local, single-chain melting process" preludes the molecular diffusion out of the micelle during chain exchange.

Partially crystalline, self-assembling systems with multiple components are omnipresent in nature with living cells as a prominent example. Their structural integrity is maintained by a membrane consisting of various lipids that can be in a liquid, gel, or crystalline state. For other self-assembling systems like block copolymers with crystallizable blocks, crystallization may even be the driving force behind self-assembly and can yield a whole range of remarkable nanostructural morphologies [1]. In the resulting micellar systems with crystalline cores of typically a few nanometers in diameter, interesting questions relate to the role of confinement. For example, it was recently discovered that the melting points of n-alkanes under soft nanoscopic confinement in micellar cores exhibit a simple Gibbs-Thomson behavior [2], typical for hard-confined liquids. In this context, it is also interesting how the dynamics of self-assembling systems, like molecular exchange kinetics, are affected by confinement and crystallinity, as these processes control the equilibration and sometimes even the resulting morphology.

So far, the existing theories for micelle kinetics have been devoted to amorphous micelles. For instance, the general theory developed by Halperin and Alexander [3] considers starlike micelles with molten cores where the chain expulsion is the rate-determining step. The expulsion is pictured as a process in which the chain diffuses over a free energy barrier with an activation energy E_a, which stems from the additional solvophobic surface created upon chain expulsion. This is a first-order kinetic process where the fraction of exchanged chains is described by an exponential relaxation function $R(t) = \exp(-t/\tau)$. Here the characteristic timescale is given by $\tau = \tau_0 \exp[E_a/(k_B T)]$, where k_B is Boltzmann's constant, T the absolute temperature, and τ_0 a prefactor that is associated with the attempt time, i.e., the time between two consecutive attempts of a molecule to leave the micellar core. In a previous study of C_n-PEO5 micelles [4], we could show that in molten cores the activation energy E_a scales linearly with the length of the solvophobic block n because the relatively short alkyl block does not fully collapse into a spherical shape—in contrast to the $E_a \propto n^{2/3}$ scaling of fully collapsed solvophobic blocks predicted by Halperin and Alexander [3]. Since $R(t)$ is an exponential function of τ and the exchange time τ in turn depends exponentially on $E_a \propto n$, the relaxation function shows an extremely strong sensitivity to the solvophobic block length. For block copolymers with even a narrow distribution of n (dispersity M_w/M_n close to unity), there is thus a relatively broad distribution of exchange rates which results in a close-to-logarithmic decay instead of a single exponential [5–7]. This renders an exact determination of τ and E_a impossible for block copolymers with finite dispersity. The effect is even more drastic in binary block copolymer mixtures of different molecular weight, so only qualitative conclusions can be drawn [8,9]. In this work, our goal is twofold: (i) understand the role of crystallinity and possible effects of cooperativity quantitatively and (ii) understand the mutual

influence on the dynamics in systems with multiple components.

Until now, it has been found that in micellar systems crystallinity yields an additional energy barrier upon chain expulsion [4,10], but the interplay between the cooperative melting processes and chain exchange is still unknown. An interesting approach to shed light on these processes is coassembling different amphiphiles which allows the melting point to be tuned. Here we use binary mixtures of amphiphilic, micelle-forming copolymers as a model system, namely, two poly(ethylene oxide)-mono-n-alkyl-ethers (C_n-PEO5 with different alkyl lengths $n = 22, 28$ and a PEO molecular weight of 5 kg/mol) in aqueous solution. The polymers are prepared by well-established living anionic polymerization techniques leading to materials with desired PEO molar mass and narrow molar mass distributions of $M_w/M_n < 1.04$ [11]. The n-alkanes, on the other hand, are monodisperse, $M_w/M_n = 1$, which assures a single expulsion time, and do not exhibit the strong broadening inherent in polydisperse systems. Calorimetry and densiometry data show that the hydrophobic blocks mix within the micellar cores, and the melting point can be tuned continuously from 29 to 57 °C. In contrast, neutron scattering measurements reveal that the molecular exchange kinetics is governed by two unique expulsion rates corresponding to each component, both in the molten and crystalline state. That means, while the individual diffusion processes are decoupled, the two components are still subject to the same cooperative melting process which, below the melting point, imposes an additional activation energy term equal to the enthalpy of fusion ΔH_{fus}.

The micelles were structurally characterized by small-angle neutron and x-ray scattering (SANS, SAXS). Figure 1(a) shows representative SANS data of neat C_{28}- and C_{22}-PEO5 solutions and of a solution of a premixed 1:1 blend. A fit analysis of the scattering data using a
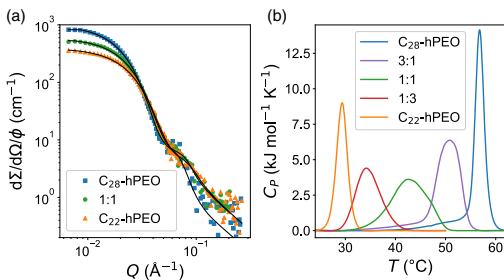
previously reported model [11] shows that the micelles exhibit a typical core-shell structure consisting of a fully segregated, solvent-free core of constant density and an extended starlike PEO corona. The structural key parameters are given in Table I. Complementary SAXS data are shown in Fig. S1 in the Supplementary Material [12], together with the resulting fit parameters and a brief outline of the fit model. Evidently, the size of the 1:1 mixed micelles is in between those of the neat ones, indicating that both species mix on a molecular level. This is further supported by differential scanning calorimetry (nanoDSC) shown in Fig. 1(b). For mixed micelles, only a single exothermic peak is observed which is attributed to a cooperative melting process in the micellar core. The individual melting transitions widely disappear and therefore strongly suggest mixing of C_{28} and C_{22} blocks, even though the broadening of the transition indicates some local heterogeneities and a distribution of mobility caused by the small number of molecules present in the core and their tethering to the core-corona interface. The melting points and fusion enthalpies are also given in Table I. Noteworthily, the observed melting transitions are in quantitative agreement with density measurements performed on the same samples (see Fig. S2 in the Supplemental Material [12]). It is interesting that we observe miscibility of the C_{28} and C_{22} blocks ($\Delta n = 6$) in the core, even though bulk alkanes with $\Delta n > 4$ are not miscible according to Kravchenko's rules [13,14]. This is consistent with studies reviewed by Su et al. [15] which show that micrometer confinement enhances the miscibility of n-alkanes. The enhanced miscibility is attributed to a suppressed lamellar ordering and longitudinal diffusion under confinement, which are processes involved in the phase separation of length-mismatching n-alkanes in bulk.

The kinetic experiments were performed by time-resolved SANS using a kinetic zero-average-contrast experiment [16]. Briefly, the method works by mixing two populations of micelles, one with a deuterated and the other with a proteated PEO block, both in a zero average contrast H_2O/D_2O mixture ($\phi_{D_2O} = 66.7$ vol%), which matches exactly the average scattering length density of

FIG. 1. (a) SANS data of pure C_{28}- and C_{22}-hPEO5 micellar solutions and of a premixed 1:1 blend (volume fraction $\phi = 0.25$ vol%). Solid lines represent fits according to a quantitative core-shell model reported in Ref. [11] and outlined in the Supplementary Material [12]. The key fit parameters are shown in Table I. (b) nanoDSC traces of the same samples and two additional mixtures measured at a scan speed of 2 K/min.

TABLE I. Structural and calorimetric data of the investigated micelles obtained from fitting SANS curves and analyzing DSC traces, respectively: N_{agg}, aggregation number; R_m, micellar radius; R_c, core radius; T_m, melting point; ΔH_{fus}, enthalpy of fusion.

	N_{agg}	R_m	R_c	T_m	ΔH_{fus}
		(Å)	(Å)	(°C)	(kJ/mol)
C_{28}-hPEO5	130 ± 5	135 ± 5	28 ± 1	57 ± 1	40 ± 3
3:1	108 ± 5	127 ± 4	26 ± 1	51 ± 1	39 ± 3
1:1	84 ± 4	121 ± 4	24 ± 1	43 ± 1	33 ± 2
1:3	72 ± 3	116 ± 3	22 ± 1	34 ± 1	27 ± 1
C_{22}-hPEO5	57 ± 2	107 ± 3	20 ± 1	29 ± 1	25 ± 1

200

the two PEO blocks. We note that the deuterated polymers have almost the same PEO length as their proteated counterparts and that the deuteration has no significant effect on the micellar structure (as shown in the Supplemental Material of Ref. [4]). Upon mixing equal volumes of the oppositely labeled micellar solutions, initially at $t = 0$, the two micelle populations scatter with maximum contrast. But as soon as molecules are exchanging, the contrast decreases to a minimum at $t = \infty$, where the h- and dPEO chains are fully randomized and matched out by the solvent on larger length scales. Rapid mixing in the millisecond range was accomplished with a stopped-flow apparatus equipped with a separately temperature-controlled neutron probe head which ensures a high thermal stability in the range between 5 and 55 °C. From the integrated detector intensity $I(t) = \int I(Q, t) dQ$ the relaxation function $R(t) = \{[I(t) - I(\infty)]/[I(0) - I(\infty)]\}^{1/2}$ can be calculated [7], with the initial intensity immediately after mixing $I(0)$ and the intensity from randomly mixed micelles $I(\infty)$. This procedure allows for a much better time resolution (down to 25 ms) compared to tracking the full scattering pattern $I(Q, t)$.

Example curves of C_{22}-PEO5, C_{28}-PEO5, and the 1:1 mixture at various temperatures are shown in Fig. 2. The neat micelles exhibit an exponential relaxation function, as predicted by the theory of Halperin and Alexander [3]. Surprisingly, the mixture shows two distinct exchange processes which can be modeled simply by a sum of two exponentials without any broadening. We intuitively attribute the faster process to C_{22}- and the slower process to C_{28}-PEO5 molecules exchanging. That suggests that even though the different alkyl blocks mix inside the micellar core and crystallize cooperatively, the exchange processes are still decoupled, in agreement with previous reports on amorphous micelles [8,9]. This is shown more quantitatively in Fig. 3 which displays an Arrhenius plot for the
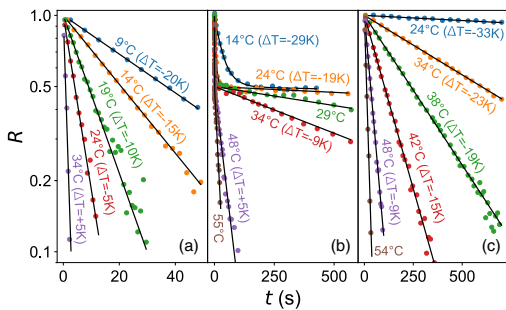
exchange times in the 1:1 mixture compared to those in the neat C_n-PEO5 micelles. For an accurate comparison, a contour plot of the corresponding DSC traces, which shows the melting transition, has been included.

Evidently, two distinct regimes with different slopes emerge which reflect the molten and crystalline state as determined by nanoDSC. Moreover, the difference in slope in the Arrhenius plot, and hence, activation energy, exactly matches the enthalpy of fusion as determined from the nanoDSC experiments. For example, for neat C_{22}-PEO5 we obtain $E_a = 105$ kJ/mol below melting and $E_a = 80$ kJ/mol above melting, which corresponds very nicely with $\Delta H_{fus} = 25$ kJ/mol. Unfortunately, we could not compose a similar plot for neat C_{28}-PEO5 because temperature stability in the stopped-flow setup was not achievable above the melting point $T_m = 57$ °C. Thus, the respective plot only exhibits a uniform slope below T_m corresponding to the activation energy of C_{28}-PEO5 in the crystalline regime (170 kJ/mol). However, via reducing the melting point by mixing C_{28}- and C_{22}-PEO5, we were able to obtain similar results for C_{28}-PEO. Analogous to neat C_{22}-PEO5, the reduced melting point in the 1:1 mixture allows for an Arrhenius plot which is separated into the molten and crystalline regimes. Likewise, the activation energies of both regimes differ by the enthalpy of fusion. Additionally,
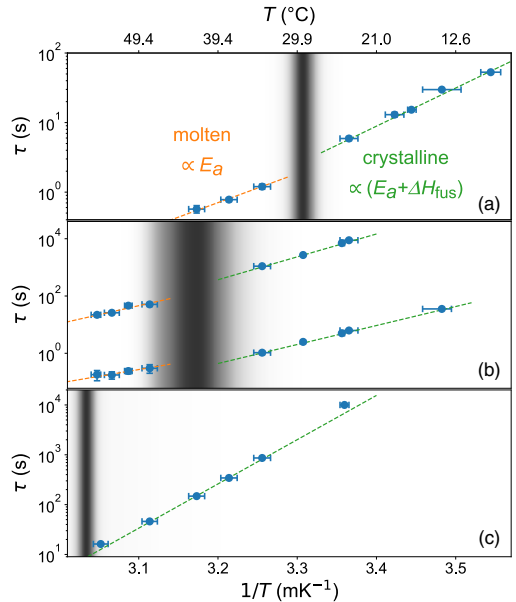

FIG. 2. Experimental relaxation functions and exponential fits at various temperatures. (a) C_{22}-PEO5, (b) $C_{28/22}$-PEO5 1:1, (c) C_{28}-PEO5. The temperature difference $\Delta T = T_{exp} - T_m$ to the melting point is given in brackets. Some curves have been left out for reasons of clarity.

FIG. 3. Arrhenius plot of the temperature-dependent characteristic exchange times of (a) C_{22}-PEO5, (b) the $C_{28/22}$-PEO5 1:1 mixture, and (c) C_{28}-PEO5. The gray shade is a contour plot of the respective nanoDSC melting curve and thus separates the molten and crystalline regimes.

201

we performed a similar analysis of 1:3 and 3:1 mixtures (see Figs. S3 and S4 in the Supplemental Material [12]).

Based on these findings, activation energies obtained below T_m have been corrected for the enthalpy of fusion, as measured by nanoDSC, via $E_a \rightarrow E_a - \Delta H_{fus}$. The thus obtained individual net activation energies E_a of C_{22}- and C_{28}-PEO5 in the different compositions are shown in Fig. 4(a). The plot clearly reveals that within experimental uncertainty, E_a remains virtually unchanged for both alkane lengths in mixed micelles. Apparently, the individual expulsion of the alkane block is almost independent of the core composition, thus, confirming the "independent chain hypothesis" [9]. This is straightforwardly explained by the fact that—in the molten regime—the core blocks only "feel" an alkane environment, and the specific length of the neighboring chains does not significantly influence the energy barrier imposed by the additional hydrophobic surface upon chain expulsion. Nevertheless, when inspecting the C_{22}-PEO5 activation energies more closely, there is a trend of increasing E_a with increasing C_{28}-PEO5 content. We attribute this to the influence of core-corona-interface area per chain as described by Zhao *et al.* [17]. As the average alkyl chain length in the mixture increases, so does the aggregation number and core radius (compare Table I), but the interface area per chain decreases $\propto 1/R_c$. The "orifice" through which the alkyl block leaves the core thus becomes smaller and the corona denser, both effects hindering chain expulsion and increasing the apparent activation energy.

FIG. 4. (a) Activation energies of the chain expulsion step of C_{28}- and C_{22}-PEO5 in various mixtures. Values obtained from the crystalline regime were corrected for the enthalpy of fusion determined from nanoDSC. The (dashed-)dotted lines are guides to the eye. (b) Tentative free energy landscape of the expulsion step where y is the reaction coordinate.

We should note that the experimental uncertainty of the C_{28}-PEO5 activation energies is generally larger than those of C_{22}-PEO5, and hence prevent similar deductions for C_{28}-PEO5. This is basically due to the necessary long collection times (several hours) to get the full relaxation profile and to determine accurately the final intensity, $I(\infty)$.

Inspecting the corresponding attempt times τ_0 yields a similar picture (see Fig. S5 in the Supplemental Material [12]): When correcting for the entropy of fusion $\Delta S_{fus} \approx \Delta H_{fus}/T_m$ [$\tau_0 \rightarrow \tau_0 \exp(\Delta S_{fus}/R)$, where R is the universal gas constant] [4], the attempt times in the molten and crystalline regimes agree [18]. We thus propose that the cocrystallization gives an additional, cooperative energy barrier to the otherwise decoupled expulsion processes in mixed micelles as is depicted in Fig. 4(b).

To summarize, employing this well-defined model system, we show that cooperative solid-liquid phase transitions in nanocrystalline self-assembled micellar systems not necessarily imply cooperativity in intermicellar exchange processes. That implicates that the segmental diffusion (i.e., local conformational transitions and segmental motion) is essentially decoupled from the center-of-mass diffusion (i.e., molecular exchange). However, it should be noted that this does not translate to an effective friction coefficient but rather a modification of the activation energy of the expulsion step. Even though the expulsion process includes a partial premediating melting process as the chain escapes the crystalline core [19], we still find two unique release processes corresponding to each component in the binary mixtures. Furthermore, the data show that the activation energy of the expulsion step governing the diffusion process out of the core undergoes an abrupt reduction at the melting point that exactly amounts to the enthalpy of fusion. Very interestingly, the transition temperature can be accurately tuned by coassembling polymers with different n-alkyl length. Above the melting transition, this occurs without affecting the activation energies of the individual compounds, which only depend on the hydrophobic surface created upon chain expulsion. However, below the melting transition, an additional term ΔH_{fus} is added to the total activation energy, a quantity which depends on the mixing ratio and the nature of the n-alkane. Hence, cocrystallization, although less effective than varying the core block length [5,7], corona block length [20,21], and molecular architecture [22–24], represents a handy tool to fine-tune the temperature response of the timescale on which the molecular exchange takes place. This is important insight for the accurate design of multicomponent self-assembling systems, although in the case of mixing chemically dissimilar components, additional modification of the dynamics may be expected, e.g., a change in the local segmental motion. We also shed light on the thermodynamics and kinetics of low-molecular-weight molecules in nanoconfined systems. It has been reported that confinement may induce demixing of small molecules like, for
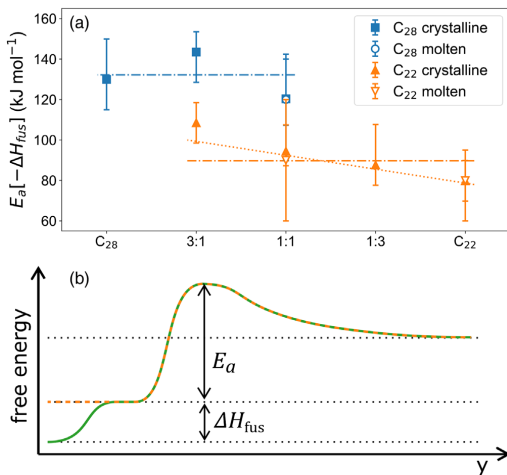
202

instance, water and methanol [25] or colloidal mixtures [26]. In our case, however, the data demonstrate that the spherical nanoconfinement greatly enhances the miscibility of crystalline long n-alkanes which are incompatible on a macroscopic scale—in agreement with previous studies on microconfinement [15]. Moreover, we show that the dynamics in crystalline self-assembled materials can be rather straightforwardly predicted from their amorphous state based on quantities easily measurable using standard techniques such as DSC. Similar ideas and experimental approaches can be applied within biophysics to understand the properties of membranes that consist of a range of lipids with similar chemical compositions but varying melting points.

[*]l.willner@fz-juelich.de
ORCID ID:0000-0001-6482-7937
[†]Present address: ESRF—The European Synchrotron, 38043 Grenoble Cedex 9, France.
[‡]reidar.lund@kjemi.uio.no
ORCID ID:0000-0001-8017-6396
[§]ORCID ID:0000-0003-3319-5708
[¶]ORCID ID:0000-0002-3930-3602

[1] J. J. Crassous, P. Schurtenberger, M. Ballauff, and A. M. Mihut, Design of block copolymer micelles via crystallization, Polymer **62**, A1 (2015).

[2] T. Zinn, L. Willner, and R. Lund, Nanoscopic Confinement through Self-Assembly: Crystallization within Micellar Cores Exhibits Simple Gibbs-Thomson Behavior, Phys. Rev. Lett. **113**, 238305 (2014).

[3] A. Halperin and S. Alexander, Polymeric micelles: their relaxation kinetics, Macromolecules **22**, 2403 (1989).

[4] T. Zinn, L. Willner, V. Pipich, D. Richter, and R. Lund, Effect of core crystallization and conformational entropy on the molecular exchange kinetics of polymeric micelles, ACS Macro Lett. **4**, 651 (2015).

[5] S. H. Choi, T. P. Lodge, and F. S. Bates, Mechanism of Molecular Exchange in Diblock Copolymer Micelles: Hypersensitivity to Core Chain Length, Phys. Rev. Lett. **104**, 047802 (2010).

[6] R. Lund, L. Willner, J. Stellbrink, P. Lindner, and D. Richter, Erratum: Logarithmic Chain-Exchange Kinetics of Diblock Copolymer Micelles, Phys. Rev. Lett. **104**, 049902 (2010).

[7] R. Lund, L. Willner, V. Pipich, I. Grillo, P. Lindner, J. Colmenero, and D. Richter, Equilibrium chain exchange kinetics of diblock copolymer micelles: effect of morphology, Macromolecules **44**, 6145 (2011).

[8] J. Lu, S. Choi, F. S. Bates, and T. P. Lodge, Molecular exchange in diblock copolymer micelles: bimodal distribution in core-block molecular weights, ACS Macro Lett. **1**, 982 (2012).

[9] J. Lu, F. S. Bates, and T. P. Lodge, Chain exchange in binary copolymer micelles at equilibrium: confirmation of the independent chain hypothesis, ACS Macro Lett. **2**, 451 (2013).

[10] M. Kastantin, B. Ananthanarayanan, P. Karmali, E. Ruoslahti, and M. Tirrell, Effect of the lipid chain melting transition on the stability of DSPE-PEG(2000) micelles, Langmuir **25**, 7279 (2009).

[11] T. Zinn, L. Willner, R. Lund, V. Pipich, M. S. Appavou, and D. Richter, Surfactant or block copolymer micelles? Structural properties of a series of well-defined n-alkyl–PEO micelles in water studied by SANS, Soft Matter **10**, 5212 (2014).

[12] See Supplemental Material at http://link.aps.org/supplemental/10.1103/PhysRevLett.122.078001 for additional experimental data and an outline of the treatment of scattering data.

[13] V. Kravchenko, The eutectics and solid solutions of paraffins, Acta Physicochim. URSS **21**, 335 (1946).

[14] M. Dirand, M. Bouroukba, V. Chevallier, D. Petitjean, E. Behar, and V. Ruffier-Meray, Normal alkanes, multialkane synthetic model mixtures, and real petroleum waxes: Crystallographic structures, thermodynamic properties, and crystallization, J. Chem. Eng. Data **47**, 115 (2002).

[15] Y. Su, G. Liu, B. Xie, D. Fu, and D. Wang, Crystallization features of normal alkanes in confined geometry, Acc. Chem. Res. **47**, 192 (2014).

[16] L. Willner, A. Poppe, J. Allgaier, M. Monkenbusch, and D. Richter, Time-resolved SANS for the determination of unimer exchange kinetics in block copolymer micelles, Europhys. Lett. **55**, 667 (2001).

[17] D. Zhao, Y. Ma, and T. P. Lodge, Exchange kinetics for a single block copolymer in micelles of two different sizes, Macromolecules **51**, 2312 (2018).

[18] The different attempt times of C_{22}- and C_{28}-PEO can be understood from the different gain in conformational entropy of the n-alkanes upon chain expulsion. This depends on the chain length n as elaborated in Ref. [4].

[19] The hypothesis of crystallization inside the micellar core is based on the presented DSC and density measurements as well as wide-angle x-ray scattering. However, a local (short-range) order, which probably is indistinguishable from a crystalline order with very small correlation length, cannot be entirely excluded.

[20] T. Zinn, L. Willner, V. Pipich, D. Richter, and R. Lund, Molecular exchange kinetics of micelles: corona chain length dependence, ACS Macro Lett. **5**, 884 (2016).

[21] Z. Li and E. E. Dormidontova, Equilibrium chain exchange kinetics in block copolymer micelle solutions by dissipative particle dynamics simulations, Soft Matter **7**, 4179 (2011).

[22] A. Prhashanna and S. B. Chen, Chain exchange kinetics between linear ABA-type triblock copolymer micelles, Polymer **118**, 22 (2017).

[23] J. Lu, F. S. Bates, and T. P. Lodge, Remarkable Effect of Molecular Architecture on Chain Exchange in Triblock Copolymer Micelles, Macromolecules **48**, 2667 (2015).

[24] A. J. Peters and T. P. Lodge, Chain exchange kinetics of asymmetric B_1AB_2 linear triblock and AB_1B_2 branched triblock copolymers, Macromolecules **50**, 6303 (2017).

[25] Y. Liu, S. Consta, and W. A. Goddard, Nanoimmiscibility: Selective absorption of liquid methanol–water mixtures in carbon nanotubes, J. Nanosci. Nanotechnol. **10**, 3834 (2010).

[26] L. Wu, A. Malijevský, C. Avendaño, E. A. Müller, and G. Jackson, Demixing, surface nematization, and competing adsorption in binary mixtures of hard rods and hard spheres under confinement, J. Chem. Phys. **148**, 164701 (2018).

[27] A. Radulescu, N. K. Szekely, and M.-S. Appavou, KWS-2: Small angle scattering diffractometer, J. Large-Scale Res. Facil. **1**, A29 (2015).

204

Supplemental Material
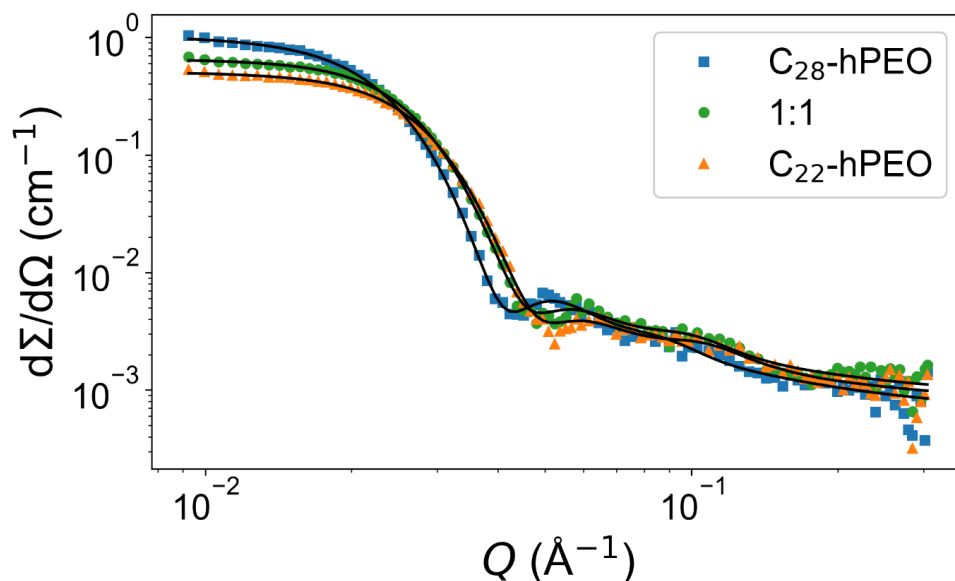
FIG. S1. SAXS data of pure C28- and C22-hPEO5 micellar solutions and of a premixed 1:1 blend (volume fraction 1vol%). Solid lines represent fits according to a quantitative core-shell model as outlined below in the Supplemental Material. Fit parameters shown in Table SI.

TABLE SI. Key fit parameters of the SAXS data shown in Figure S1, in agreement with the data shown in Figure 1(a) and Table I.

|	N_{agg}	R_m (Å)	R_c (Å)
C28-hPEO	125 ± 8	122 ± 10	27 ± 1
3:1	98 ± 7	116 ± 8	25 ± 1
1:1	84 ± 7	112 ± 8	24 ± 1
1:3	70 ± 6	108 ± 8	22 ± 1
C22-hPEO	69 ± 6	107 ± 8	21 ± 1
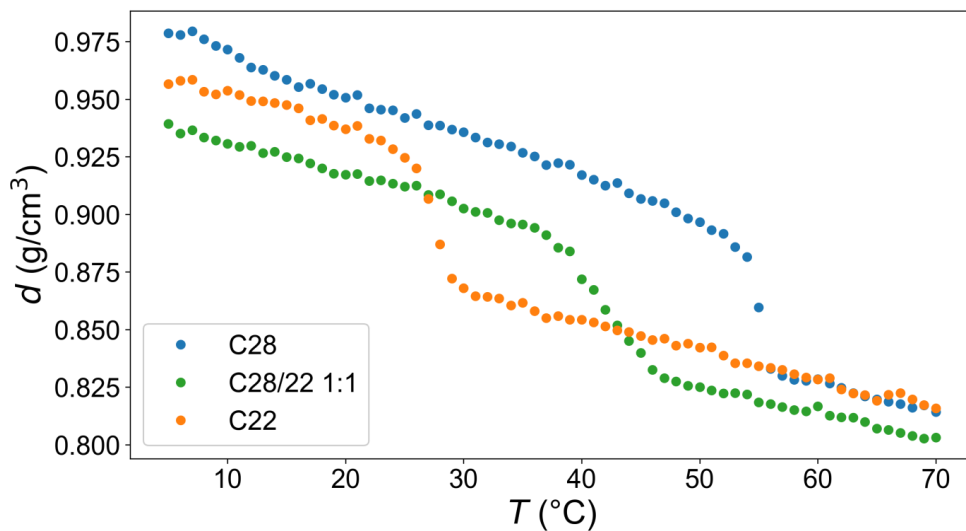
FIG. S2. Apparent density of the micellar core determined from 1vol% micellar solutions of C_{28}-hPEO, C_{22}-hPEO and the 1:1 mixture. Only a single melting transition is visible for the mixture. The melting temperatures agree with the nanoDSC traces (Figure 1(b)).
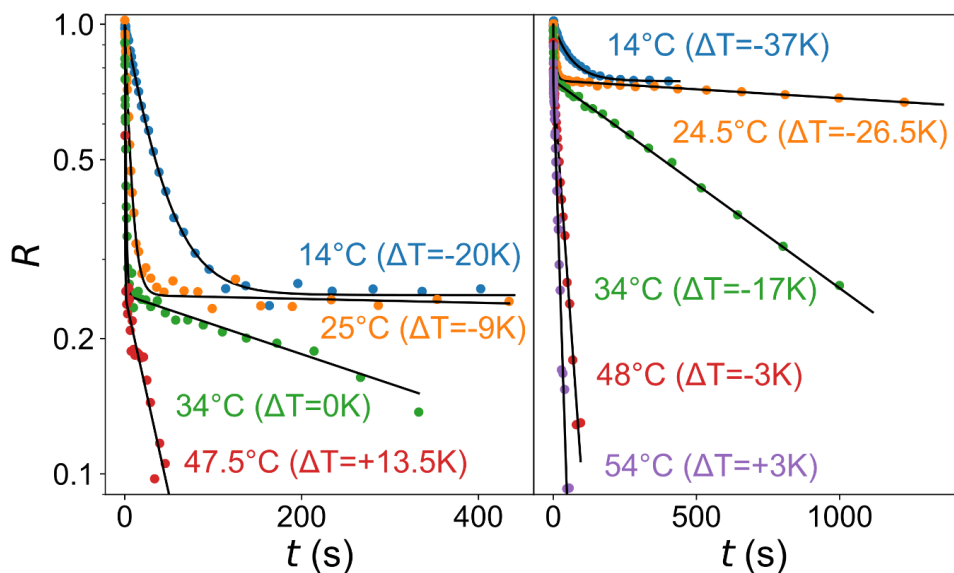
FIG. S3. Experimental relaxation functions and exponential fits of the C28/22-PEO 1:3 (left) and 3:1 (right) mixtures.
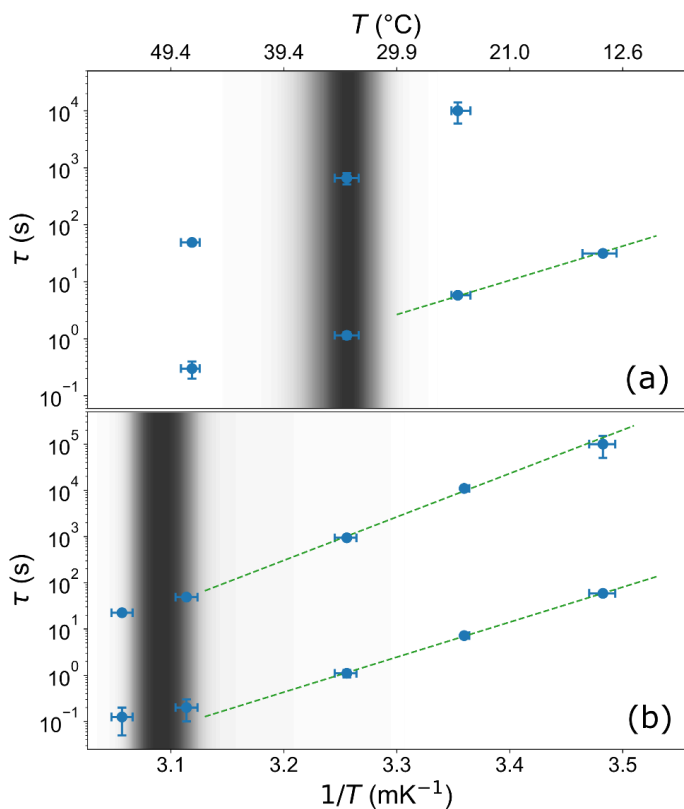
FIG. S4. Arrhenius plot of the temperature-dependent characteristic exchange times of C28/22-PEO 1:3 (a) and 3:1 (b) mixtures. The grey shade represents the respective nanoDSC melting curve and thus divides the molten and crystalline regime, similar to Figure 3.
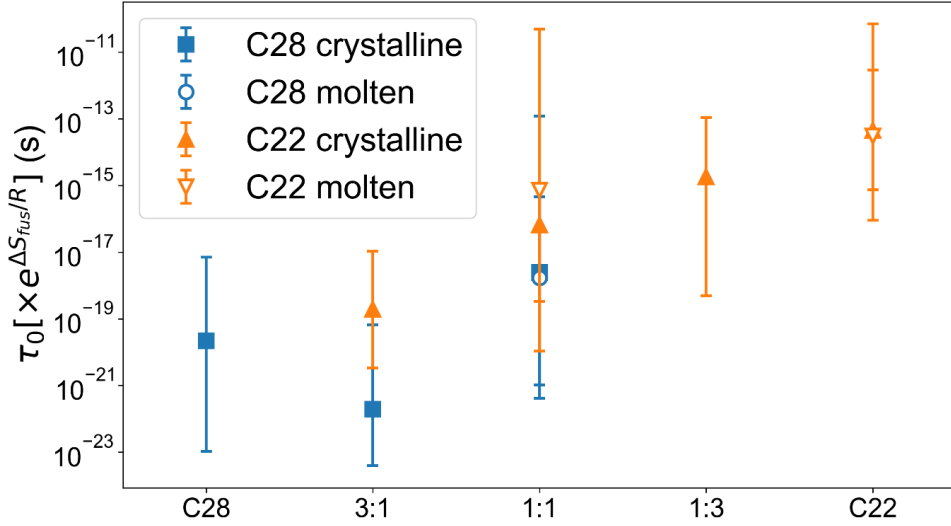
FIG. S5. Attempt times of C_{28}- and C_{22}-PEO. Values obtained from the crystalline regime were corrected for the entropy of fusion determined from nanoDSC.

Data Treatment and Analytical Fit Model

SANS scattering data were collected at the KWS-2 instrument operated by the Jülich Center for Neutron Science at Heinz Maier-Leibnitz Zentrum in Garching, Germany. At 7Å wavelength and detector distances 2m and 8m, a Q-range of 0.008-0.3Å^{-1} was covered. SAXS scattering data were collected using a Bruker NanoStar instrument located at the Resource Center for X-rays at the University of Oslo, Norway. The instrument covers a Q-range of 0.009-0.3Å^{-1}. Both SAXS and SANS data have been reduced according to instrument standard protocols.

The data were fitted on an absolute scale using a core-shell model previously reported in reference [11]. It is only briefly outlined here. The differential scattering cross-section is calculated as

$$\frac{d\Sigma}{d\Omega}(Q) = \phi[P(Q) \cdot S(Q) + P_{blob}(Q)] + bgr. \tag{1}$$

Here, ϕ is the volume fraction, $P(Q)$ is a core-shell form factor, $P_{blob}(Q)$ is scattering resulting from internal structure within the corona and bgr is a residual background resulting from insufficient background subtraction. $S(Q)$ was set to 1 for the SANS measurements ($\phi = 0.25\%$, dilute regime). For the SAXS measurements ($\phi = 1\%$, semi-dilute regime), a simple hard-sphere structure factor proved to be sufficient to model the data [D. J. Kinning and E. L. Thomas, Macromolecules **17**, 1712 (1984)]. The so-called blob scattering

$$P_{blob}(Q) = \frac{1}{N_{agg}(V_c + V_s)} (\rho_s - \rho_0)^2 N_{agg} V_s^2 B(Q) \tag{2}$$

is based on the ideas of Svaneborg and Pedersen [Macromolecules **35**, 1028 (2002)]. N_{agg} is the aggregation number, V_s the molecular volume of the corona block, V_c the molecular volume of the core block, ρ_s the scattering length density of the corona block and ρ_0 the scattering length density of the solvent. $B(Q)$ is calculated as

208

$$B(Q) = \frac{P_{beau}(Q)}{1 + \nu \, P_{beau}(Q)} \tag{3}$$

in a random phase approximation, where ν is an effective surface concentration and $P_{beau}(Q)$ is a Beaucage form factor. The micellar form factor

$$P(Q) = \frac{1}{N_{agg}(V_c + V_s)} \left[I_c(Q) + I_s(Q) + I_{cross}(Q) \right] \tag{4}$$

with

$$I_c(Q) = (\rho_c - \rho_0)^2 \, N_{agg}^2 \, V_c^2 \, A_c^2(Q), \tag{5.1}$$

$$I_s(Q) = (\rho_s - \rho_0)^2 \, N_{agg} \left(N_{agg} - \frac{1}{1+\nu} \right) V_s^2 \, A_s^2(Q), \tag{5.2}$$

and

$$I_{cross}(Q) = 2(\rho_c - \rho_0)(\rho_s - \rho_0) \, N_{agg}^2 \, V_c \, V_s \, A_c(Q) \, A_s(Q), \tag{5.3}$$

is based on the scattering amplitudes $A_c(Q)$ of the core and $A_s(Q)$ of the shell. The core scattering is modelled by the scattering of a uniform sphere, damped exponentially because of a finite roughness σ_{int} of the core-corona interface:

$$A_c(Q) = 3 \frac{\sin QR_c - QR_c \cos QR_c}{(QR_c)^3} \exp\left(-\frac{\sigma_{int}^2 Q^2}{2} \right). \tag{6}$$

According to the predictions of Daoud and Cotton [Journal de Physique **43**, 531 (1982)] for star-like micelles, our shell model follows a density profile

$$d(r) \propto \frac{r^{-4/3}}{1 + \exp\left(\frac{r - R_m}{\sigma_{out} R_m} \right)}, \tag{7}$$

which is cut off at the micellar radius R_m by a smooth Fermi function with width σ_{out}, to account for the finite length of the corona blocks. The shell scattering amplitude is thus

$$A_s(Q) = \frac{\int 4\pi r^2 \, d(r) \, \frac{\sin Qr}{Qr} \, dr}{\int 4\pi r^2 \, d(r) \, dr} \exp\left(-\frac{\sigma_{int}^2 Q^2}{2} \right), \tag{8}$$

also damped due to the finite roughness of the core-shell interface.

Paper IV

Tale of Two Tails: Molecular Exchange Kinetics of Telechelic Polymer Micelles

Nico König, Lutz Willner, Vitaliy Pipich, Najet Mahmoudi and Reidar Lund

IV

Tale of Two Tails: Molecular Exchange Kinetics of Telechelic Polymer Micelles

Nico König[1,2] Lutz Willner[2,*] Vitaliy Pipich[3] Najet Mahmoudi[4] and Reidar Lund[1,†]

[1]*Department of Chemistry, University of Oslo, P.O. Box 1033, Blindern, 0315 Oslo, Norway*
[2]*Jülich Centre for Neutron Science (JCNS) and Institute for Complex Systems (ICS),
Forschungszentrum Jülich GmbH, 52425 Jülich, Germany*
[3]*Jülich Centre for Neutron Science (JCNS) at Heinz Maier-Leibnitz Zentrum (MLZ),
Forschungszentrum Jülich GmbH, 85747 Garching, Germany*
[4]*ISIS-STFC, Rutherford Appleton Laboratory, Chilton, Oxon OX11 0QX, United Kingdom*

Telechelic polymers contain two chain ends that are able to promote self-assembly into "flowerlike" or interconnected micellar structures. Here, we investigate the molecular exchange kinetics of such micelles using time-resolved small-angle neutron scattering. We show that the activation energies of monofunctional and telechelic chain exchange are identical. This demonstrates that the two chain ends are not simultaneously released in a single event. Instead, the results show that, contrary to regular micelles, the kinetics occurs in a multistep process involving a collision-induced single-molecule exchange mechanism where the exchange rate is directly proportional to the polymer concentration. We show that this novel mechanism can be quantitatively explained by a simple kinetic model.

Hydrophobically end-capped polymers, e.g., telechelic polymers bearing two hydrophobic stickers in terminal positions of a water-soluble backbone, are well-studied model systems for self-assembly. Telechelic polymers have attracted a lot of interest because their properties encompass many interesting aspects in soft matter physics, including hierarchical self-assembly, non-Newtonian flow behavior, and colloidal interactions [1–11]. Aside from a purely academic point of view, telechelic polymers are very important as associative thickeners in daily life products, e.g., paints and cosmetics. In water, telechelic polymers spontaneously self-assemble into a variety of different nanostructures. These are, depending on concentration and hydrophobic chain end ("sticker") length, flowerlike micelles, clusters of micelles, and nanostructured hydrogels, where telechelic chains interconnect individual micelles.

All these structures commonly show a continuous exchange of chains to reach and maintain their thermal equilibrium. In recent years, the exchange kinetics of diblock copolymer micelles has been thoroughly studied experimentally and by computer simulation. In particular, time-resolved small-angle neutron scattering (TR-SANS) employing contrast variation proved to be the method of choice to explore the mechanisms of chain exchange under (quasi)equilibrium conditions [12]. TR-SANS applied to different diblock copolymer micellar systems has shown that single-chain expulsion and insertion is the prevailing mechanism for chain exchange with the expulsion as the rate determining step [13–16]—in line with computer simulation [17,18] and scaling theory [19,20]. The expulsion is a thermally activated first-order kinetic process,

which is characterized by a single exponential relaxation $R(t) = \exp(-kt)$, with t as the time and k as the exchange rate constant. The temperature dependence is expressed in terms of an Arrhenius equation

$$k = \frac{1}{\tau_0} \exp(-E_a/k_B T), \qquad (1)$$

with E_a as the activation barrier, τ_0 as the hypothetical attempt time of the core block to escape from the micelle, and $k_B T$ as the thermal energy. E_a is essentially determined by the extra interface created by the insoluble block exposed to the solvent. It has been found that E_a depends linearly on the length of the insoluble block, which suggests contact between all monomers and solvent rather than collapse into a spherical globule [14,21].

In contrast to amphiphilic diblock copolymers, the exchange mechanism of telechelic micelles in aqueous solution has not yet been determined experimentally. Here, we show experimental evidence of a novel kind of exchange mechanism that consists of a collision-induced multistep process that is fundamentally different from the exchange in regular micelles. Furthermore, we provide a simple kinetic model that describes all experimental data over a range of concentrations and temperatures with a single set of parameters. We believe that the proposed mechanism is relevant to understanding diffusion in other systems where multivalency plays a role, e.g., in supramolecular networks, lipids, and proteins.

In principle, there are three possible scenarios for molecular exchange between telechelic micelles:

213

(i) The expulsion of the two core blocks occurs simultaneously. In this case, the exchange rate is expected to be proportional to the product of the two individual rates leading to a process with doubled activation energy compared to diblock exchange.

(ii) The expulsion of the two core blocks proceeds in two consecutive steps with free telechelic chains diffusing in solution. That means the exchange rate exhibits a more complicated temperature dependence and is independent of concentration (see Supplemental Material [22] for a more detailed discussion).

(iii) The expulsion of the two core blocks proceeds in two consecutive steps but with the first block reinserted into another micelle, forming a bridge before the second block escapes. The exchange thus depends on the collision of micelles and the rate would exhibit a clear concentration dependence. Such a mechanism is related to the "walking" diffusion suggested by Yokoyama *et al.* [23,24] for triblock copolymer melts forming mesocrystal domains.

According to classical transient network theory, the microscopic exchange dynamics in telechelic polymer gels plays a key role for the macroscopic rheological properties [25]. This was recently confirmed by Zinn *et al.* [10] who found the same E_a for the macroscopic relaxation time of a telechelic network determined by linear oscillatory shear experiments and the molecular exchange time for the monofunctional polymers determined by TR-SANS. Lu *et al.* [26] found that the characteristic exchange time of the triblock copolymer PS-PEP-PS in squalane increases massively compared to a PS-PEP diblock with the same PS block and half the PEP length. The exchange rate was significantly faster than expected for simultaneous release, pointing toward a sequential activation. However, a clear picture for the mechanism is not apparent from that publication.

In this Letter, we present a quantitative description of the exchange kinetics of telechelic polymers in dilute solution based on TR-SANS experiments. They were performed on mixtures of mono- and difunctionalized (telechelic) poly(ethylene oxide) n-alkyl ethers: C_n-PEO5 and C_n-PEO10-C_n, with $n = 22, 28$ the alkane chain lengths and 5 and 10 the approximate PEO molecular weights in kg/mol. It has been shown by Laflèche *et al.* [27] that phase separation, usually occurring in aqueous solutions of telechelic polymers, is avoided by blending telechelic and monofunctionalized PEO chains. We utilized this approach in the present study and employed mixtures with volume fractions of the telechelic chains of $f_{tel} = 0.5$ for C_{22} (C22F50) and $f_{tel} = 0.4$ for C_{28} (C28F40). Solutions did not show any sign of demixing in a temperature range between 5 and 60 °C, where the TR-SANS experiments have been performed. The structural details of aqueous solutions of the mixtures have been published earlier [28]. In brief, for solutions of C_{28} mixtures, flowerlike micelles with looped telechelic chains are favored over cluster
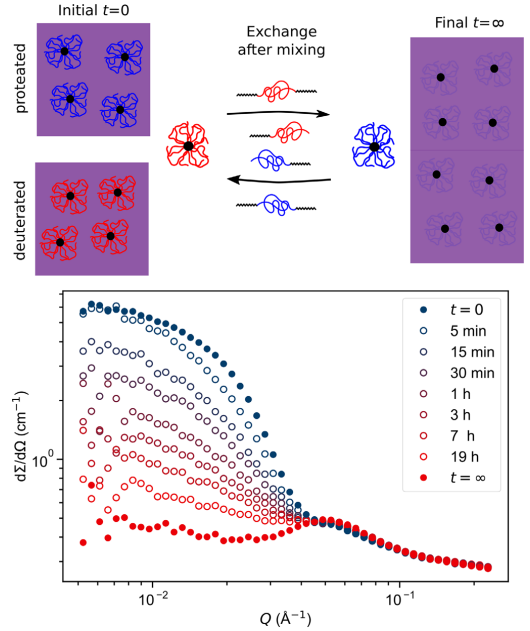

FIG. 1. (Top) Illustration of the kinetic zero average contrast technique to monitor chain exchange in diblock and triblock mixed micelles. (Bottom) Corresponding TR-SANS data of C_{28}-PEO5/C_{28}-PEO10-C_{28} micelles obtained at 37 °C and 1.0 vol% polymer volume fraction after mixing equal amounts of the deuterated and proteated reservoirs.

formation, which is the principal structure of the C_{22} samples. An inherent property of this system is partial crystallization of the n-alkane chains inside the micellar cores, which leads to a larger activation barrier for exchange amounting to the enthalpy of fusion [21,29]. Accordingly, Eq. (1) needs to be rewritten as

$$k = \frac{1}{\tau_0} \exp\left(\frac{\Delta S_m}{k_B}\right) \exp\left(-\frac{E_a + \Delta H_m}{k_B T}\right), \qquad (2)$$

with ΔH_m and $\Delta S_m \approx \Delta H_m / T_m$ as the melting enthalpy and entropy, respectively, and T_m as the melting temperature.

The exchange of chains was monitored by TR-SANS employing the kinetic zero average contrast (KZAC) technique [30], described in detail in Ref. [12]. The principles of the KZAC technique are schematically illustrated in Fig. 1 (top) for exemplary flowerlike micelles. Two reservoirs, containing proteated and deuterated micelles in an H_2O/D_2O solvent mixture with zero contrast to the average of h-PEO/d-PEO, are mixed. Initially, the contrast and, correspondingly, the scattered intensity, is maximal, but then decreases as a function of time due to the exchange of mono- and difunctional chains. At $t = \infty$, the

contrast in the mixture is minimal as the corona chains are matched out by the solvent mixture.

As an example, time-resolved scattering curves are shown in Fig. 1 (bottom) for a 1:1 mixture of d and h C_{28}-PEO5 and C_{28}-PEO10-C_{28} micelles at 37 °C and polymer volume fraction $\phi = 1.0$ vol%. At low scattering vectors Q, the plot reveals a continuous decrease of the scattered intensity with time, indicating a decrease of contrast of the PEO corona due to chain exchange. At high Q, the intensity is time independent and predominantly results from the proteated n-alkane cores and from small contributions of segmental correlations of the PEO polymer [31]. Importantly, the scattered intensity after 19 h reaches almost the intensity of a preequilibrated sample reflecting the final state. This indicates that both types of chains, monofunctional and telechelic, are exchanging within the experimentally accessible time window.

To simplify data analysis, only the integrated scattering intensity

$$I(t) = \int \frac{d\Sigma}{d\Omega}(Q,t)dQ \qquad (3)$$

was used, with $d\Sigma/d\Omega(Q,t)$ as the time-dependent macroscopic scattering cross section, i.e., the scattering intensity. This procedure is equivalent to analyzing the full scattering curve [15]. The integrated intensities were then analyzed in terms of a dimensionless relaxation function $R(t)$ defined as

$$R(t) = \sqrt{\frac{I(t) - I(\infty)}{I(0) - I(\infty)}}, \qquad (4)$$

where $I(0)$ denotes the intensity at $t = 0$ and $I(\infty)$ is the intensity of a preequilibrated sample. Figure 2 depicts typical relaxation curves of C22F50 at different temperatures.
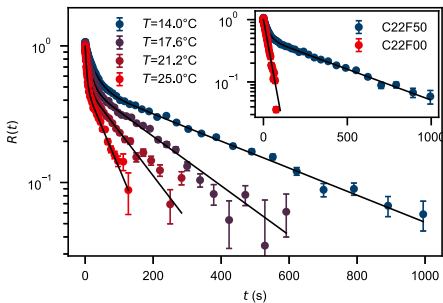

FIG. 2. Relaxation functions $R(t)$ of C22F50 at selected temperatures. Black lines represent fits according to Eq. (5). (Inset) Comparison of $R(t)$ of C22F50 and C22F00 (pure monofunctional) at 14 °C. The data were obtained using a stopped-flow mixing device.

The plot clearly reveals two well-separated processes, which we intuitively assign to the exchange of monofunctional C_{22}-PEO5 and difunctional C_{22}-PEO10-C_{22} copolymers, respectively. The assignment is further supported by comparing $R(t)$ of C22F50 with that of pure C22-PEO5 micelles (C22F00) at $T = 14$ °C, as depicted in the inset of Fig. 2. The plot shows that $R(t)$ of C22F00 coincides with the fast process of the mixture. Based on this, we have fitted the relaxation curves by a sum of two exponential functions, with prefactors corresponding to the volume fraction f_{tel} of the mixture

$$R(t) = f_{\text{tel}} \exp(-k_{\text{tel}}t) + (1 - f_{\text{tel}}) \cdot \exp(-k_{\text{mon}}t). \quad (5)$$

Excellent fits were obtained as shown with solid lines in Fig. 2, yielding the rate constants for monofunctional k_{mon} and telechelic k_{tel} chain exchange at each temperature. A preliminary Arrhenius evaluation of the fitted rate constants has shown that the E_a for chain escape is identical for both mono- and difunctional polymers. Subsequently, the data could be reanalyzed to further stabilize the fit using $E_a = E_{a,\text{mon}} = E_{a,\text{tel}}$ and perform simultaneous fits at all temperatures. Thus, only E_a, $\tau_{0,\text{mon}}$, and $\tau_{0,\text{tel}}$ were free fit parameters. T_m and ΔH_m have been determined independently by calorimetry as described recently [31]; the data are shown in Fig. S3 in the Supplemental Material [22], together with experimental relaxation curves and fits for each individual temperature for both polymers (Figs. S1 and S2). Fit values and thermodynamic parameters are summarized in Table I.

Arrhenius plots of the fitted parameters of mono- and difunctional chain exchange are presented for C_{22} and C_{28} in Fig. 3, together with rate constants obtained from an earlier study [29] of pure C_n-PEO5 polymers for comparison. The Arrhenius representations display two parallel lines, as E_a was found to be identical for monofunctional and telechelic chain exchange. The numerical values of E_a

TABLE I. Parameters of simultaneous fits at $\phi = 1$ vol% and different temperatures as well as important thermodynamic parameters of C_{28} and C_{22} polymer mixtures. Values for monofunctional polymer micelles are taken from a previous study [29] and added for comparison.

	C22F50	C22F00[a]	C28F40	C28F00[a]
$-\log_{10}[\tau_{0,\text{mon}}(\text{s})]$	15.5 ± 1.2	13.5 ± 3.0	18.7 ± 1.5	19.7 ± 2.5
$-\log_{10}[\tau_{0,\text{tel}}(\text{s})]$	14.3 ± 1.3		17.1 ± 1.6	
E_a (kJ/mol)	92 ± 7	80 ± 15	125 ± 10	130 ± 15
T_m (°C)	29 ± 1	29 ± 1	57 ± 1	57 ± 1
ΔH_m (kJ/mol)	24 ± 1	25 ± 1	40 ± 3	40 ± 3
ΔS_m (J/mol/K)	79 ± 2	84 ± 2	121 ± 8	121 ± 8
$\tau_{1/2,\text{mon}}$ (s)[b]	4.6	5.1	7.9×10^3	6.3×10^3
$\tau_{1/2,\text{tel}}$ (s)[b]	73		3.0×10^5	

[a]Taken from Ref. [29].
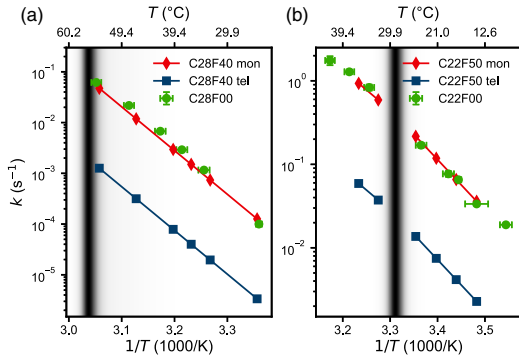[b]Half-exchange time calculated for $T = 25$ °C via Eq. (2).

FIG. 3. Arrhenius representation of the rate constants of C_{28} and C_{22} monofunctional (mon) and telechelic (tel) polymers, obtained via a simultaneous fit of all temperatures. For comparison, previous data of the pure monofunctional samples (F00) are included [29]. The gray shades are contour plots of differential scanning calorimetry traces, indicating the melting transitions of the micellar cores.

FIG. 4. Relaxation curves of C28F40 measured at $T = 37\,°C$ and three different polymer volume fractions. (Inset) Respective rate constants obtained by fitting Eq. (5). The fast process is concentration independent, while the slow process exhibits a $k \sim \phi$ dependence.

are in good agreement with values obtained earlier for pure diblock polymer exchange [21,29], see Table I. Because of the exponential dependence, the obtained attempt times τ_0 are rather uncertain, but still similar to previous results. Following the assumptions made above, we can unambiguously rule out the simultaneous escape of the two core blocks, as this would correspond to twice the activation energy.

From the above results, we can already conclude that the exchange of telechelic chains proceeds via a consecutive release of the two chain ends. Either the two hydrophobic blocks are released stepwise and then diffuse freely [scenario (ii)] or short-lived clusters are formed [scenario (iii)]. Now, in order to distinguish between the two mechanisms, we have measured C_{28} relaxation curves at different concentrations because the latter mechanism is collision based and therefore concentration dependent. Figure 4 shows relaxation curves of C_{28}-PEO5 and C_{28}-PEO10-C_{28} micelles measured at three different polymer volume fractions, $\phi = 0.5$, 1.0, and 2.5 vol%.

As seen, the three relaxation curves superimpose at short times, indicating a concentration-independent escape of monofunctional PEO chains, whereas the telechelic chains show a distinct acceleration of chain exchange with increasing ϕ. The kinetic data were quantitatively analyzed by fitting with Eq. (5) and the obtained rate constants extracted for the fast and slow process are plotted vs ϕ in the inset of Fig. 4. The rate constant of the fast process, associated with k_{mon}, is basically constant, which confirms that the exchange is not affected by micellar collisions. However, the slow process, associated with k_{tel}, on the other hand, scales linearly with ϕ, suggesting that collision-induced chain exchange is the dominating mechanism for telechelic chain exchange. To further confirm the proposed
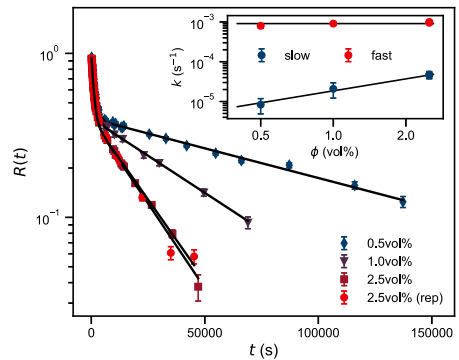
exchange mechanism, we performed concentration- and temperature-dependent measurements on C28F40—compare Figs. S4 and S5 in the Supplemental Material [22]. We were able to fit all relaxation curves with one set of parameters, in agreement with the values given in Table I. As expected, E_a is constant for all three concentrations, proving that the collision-induced exchange is the dominant exchange mechanism for telechelic micelles.

The proposed mechanism is similar to the walking diffusion suggested by Yokoyama *et al.* [23,24] in polymer melts, but differs by the lack of micellar crystalline order. Instead, the exchange events are triggered by random collisions between micelles where at least one chain is in an "activated state," i.e., with one chain end outside the micelle. It also resembles collision-based exchange mechanisms recently found in lipid nanodisks [32]. For the present case of telechelic molecules in solution, we propose the three-step kinetic model sketched in Fig. 5. This can be written as (1) expulsion of one telechelic hydrophobic
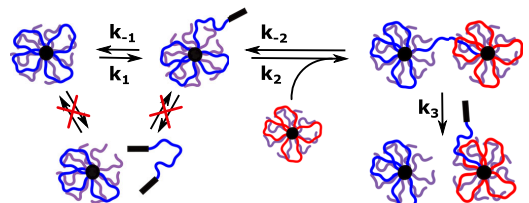

FIG. 5. Visualization of the exchange mechanism of telechelic chains in flowerlike micelles and clusters of micelles via a sequence of consecutive equilibrium steps involving collision-induced exchange. Diffusion of free telechelic chains as an important pathway is excluded.

chain end while the other one is still buried in the micellar core,

$$P \underset{k_{-1}}{\overset{k_1}{\rightleftharpoons}} P^*, \tag{6a}$$

(2) insertion of the free chain end into another micelle, i.e., bridging

$$P^* + M \underset{k_{-2}}{\overset{k_2}{\rightleftharpoons}} P^{**}, \tag{6b}$$
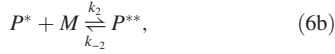
and (3) release of the second chain end that was still in the original micelle,

$$P^{**} \overset{k_3}{\rightarrow} M + \bar{P}^*. \tag{6c}$$

Here, P represents telechelic polymer molecules that have not exchanged yet and both chain ends are buried in the original micelle. P^* are molecules that are also still attached to their original micelle but with one chain end free in solution and M is an arbitrary micelle. P^{**} is a molecule that bridges between its original micelle and another one and $\bar{P}^*$ is a chain that has exchanged at least once and has one free chain end.

Applying a steady-state approximation for the unstable intermediates P^* and P^{**}, this leads to a single exponential (see Supplemental Material [22] for a more detailed discussion)

$$[P](t) = [P]_0 \exp(-k_{\text{eff}} t), \tag{7}$$

with the concentration-dependent decay constant $k_{\text{eff}} = k_1 k_2 [M] / (2 k_{-1} + k_2 [M])$. $[M] = \phi / (N_{agg} N_{avo} V_p)$ where N_{agg} is the aggregation number, V_p is the volume of a chain and N_{avo} is Avagadros number. For low micelle concentrations and $k_2 \le k_{-1}$, a Taylor expansion in $[M]$ yields $k_{\text{eff}} = k_1 k_2 [M] / (2 k_{-1}) + \mathcal{O}([M]^2)$. Thus, in the leading order, the rate constant depends linearly on $[M]$, concurring with our experimental data shown in the inset of Fig. 4, as well as Figs. S4 and S5 in the Supplemental Material [22]. Since k_{-1} and k_2 have approximately the same enthalpic contribution, the temperature dependence is governed by k_1. Moreover, the equilibrium constant $K = k_1/k_{-1} \ll 1$, which controls release of a single chain end. This naturally describes the effective reduction of the exchange rate of telechelic chains, $k_{\text{eff}} = K k_2 [M] / 2$. These findings are in perfect agreement with our experimental results. In addition, the telechelic PEO block is longer than the corresponding monofunctional one, which is known to slow down chain exchange [19,33].

In conclusion, we have shown that the molecular exchange of telechelic polymers in flowerlike micelles and clusters of micelles proceeds in consecutive steps via a collision-induced single-chain exchange mechanism that so far has not been reported experimentally. TR-SANS in combination with the KZAC contrast variation method was applied to monitor the chain exchange in a well-defined model system for self-assembly. By carefully analyzing the TR-SANS data at different temperatures and concentrations, we can rule out a simultaneous release of the two chain ends. In addition, we have developed a kinetic model that explains the experimental findings and provides a rather complete picture of the equilibration mechanism and diffusion processes in such systems. The discovered collision-induced exchange mechanism is relevant also to other self-assembled structures, in which multivalency plays a role, e.g., in supramolecular networks, lipid membranes, multidomain proteins, lipoproteins, and conventional hydrogels.

*l.willner@fz-juelich.de
†reidar.lund@kjemi.uio.no

[1] T. Annable, R. Buscall, R. Ettelaie, and D. Whittlestone, The rheology of solutions of associating polymers: Comparison of experimental behavior with transient network theory, J. Rheol. **37**, 695 (1993).

[2] A. N. Semenov, J.-F. Joanny, and A. R. Khokhlov, Associating polymers: Equilibrium and linear viscoelasticity, Macromolecules **28**, 1066 (1995).

[3] E. Alami, M. Almgren, W. Brown, and J. François, Aggregation of hydrophobically end-capped poly(ethylene oxide) in aqueous solutions. fluorescence and light-scattering studies, Macromolecules **29**, 2229 (1996).

[4] E. Beaudoin, O. Borisov, A. Lapp, L. Billon, R. C. Hiorns, and J. François, Neutron scattering of hydrophobically modified poly(ethylene oxide) in aqueous solutions, Macromolecules **35**, 7436 (2002).

[5] J. Berret, Fluorocarbon associative polymers, Curr. Opin. Colloid Interface Sci. **8**, 296 (2003).

[6] X.-X. Meng and W. B. Russel, Rheology of telechelic associative polymers in aqueous solutions, J. Rheol. **50**, 189 (2006).

[7] T. Koga, F. Tanaka, R. Motokawa, S. Koizumi, and F. M. Winnik, Theoretical modeling of associated structures in aqueous solutions of hydrophobically modified telechelic PNIPAM based on a neutron scattering study, Macromolecules **41**, 9413 (2008).

[8] J. Sprakel, E. Bartscherer, G. Hoffmann, M. A. C. Stuart, and J. van der Gucht, Dynamics of polymer bridge formation and disruption, Phys. Rev. E **78**, 040802 (2008).

 [9] J. Sprakel, E. Spruijt, M. A. C. Stuart, N. A. M. Besseling, M. P. Lettinga, and J. van der Gucht, Shear banding and rheochaos in associative polymer networks, Soft Matter **4,** 1696 (2008).

[10] T. Zinn, L. Willner, and R. Lund, Telechelic polymer hydrogels: Relation between the microscopic dynamics and macroscopic viscoelastic response, ACS Macro Lett. **5,** 1353 (2016).

[11] G. W. Park and G. Ianniruberto, A new stochastic simulation for the rheology of telechelic associating polymers, J. Rheol. **61,** 1293 (2017).

[12] R. Lund, L. Willner, and D. Richter, Kinetics of block copolymer micelles studied by small-angle scattering methods, Adv. Polym. Sci. **259,** 51 (2013).

[13] R. Lund, L. Willner, D. Richter, and E. E. Dormidontova, Equilibrium chain exchange kinetics of diblock copolymer micelles: Tuning and logarithmic relaxation, Macromolecules **39,** 4566 (2006).

[14] S.-H. Choi, T. P. Lodge, and F. S. Bates, Mechanism of Molecular Exchange in Diblock Copolymer Micelles: Hypersensitivity to Core Chain Length, Phys. Rev. Lett. **104,** 047802 (2010).

[15] T. Zinn, L. Willner, R. Lund, V. Pipich, and D. Richter, Equilibrium exchange kinetics in n-alkyl-PEO polymeric micelles: Single exponential relaxation and chain length dependence, Soft Matter **8,** 623 (2012).

[16] J. Lu, F. S. Bates, and T. P. Lodge, Chain exchange in binary copolymer micelles at equilibrium: Confirmation of the independent chain hypothesis, ACS Macro Lett. **2,** 451 (2013).

[17] Z. Li and E. E. Dormidontova, Equilibrium chain exchange kinetics in block copolymer micelle solutions by dissipative particle dynamics simulations, Soft Matter **7,** 4179 (2011).

[18] A. Prhashanna, S. A. Khan, and S. B. Chen, Kinetics of chain exchange between diblock copolymer micelles, Macromol. Theory Simul. **25,** 383 (2016).

[19] A. Halperin and S. Alexander, Polymeric micelles: Their relaxation kinetics, Macromolecules **22,** 2403 (1989).

[20] A. Halperin, On micellar exchange: The role of the insertion penalty, Macromolecules **44,** 5072 (2011).

[21] T. Zinn, L. Willner, V. Pipich, D. Richter, and R. Lund, Effect of core crystallization and conformational entropy on the molecular exchange kinetics of polymeric micelles, ACS Macro Lett. **4,** 651 (2015).

[22] See Supplemental Material at http://link.aps.org/supplemental/10.1103/PhysRevLett.124.197801 for additional TR-SANS data, differential scanning calorimetry curves as well as a detailed discussion of exchange scenarios (ii) and (iii).

[23] H. Yokoyama and E. J. Kramer, Diffusion of triblock copolymers in a spherical domain structure, Macromolecules **33,** 954 (2000).

[24] H. Yokoyama, E. J. Kramer, and G. H. Fredrickson, Simulation of diffusion of asymmetric diblock and triblock copolymers in a spherical domain structure, Macromolecules **33,** 2249 (2000).

[25] F. Tanaka and S. F. Edwards, Viscoelastic properties of physically crosslinked networks. 1. Transient network theory, Macromolecules **25,** 1516 (1992).

[26] J. Lu, F. S. Bates, and T. P. Lodge, Remarkable effect of molecular architecture on chain exchange in triblock copolymer micelles, Macromolecules **48,** 2667 (2015).

[27] F. Laflèche, D. Durand, and T. Nicolai, Association of adhesive spheres formed by hydrophobically end-capped PEO. 1. Influence of the presence of single end-capped PEO, Macromolecules **36,** 1331 (2003).

[28] T. Zinn, L. Willner, K. D. Knudsen, and R. Lund, Self-assembly of mixtures of telechelic and monofunctional amphiphilic polymers in water: From clusters to flowerlike micelles, Macromolecules **50,** 7321 (2017).

[29] N. König, L. Willner, V. Pipich, T. Zinn, and R. Lund, Cooperativity During Melting and Molecular Exchange in Micelles with Crystalline Cores, Phys. Rev. Lett. **122,** 078001 (2019).

[30] L. Willner, A. Poppe, J. Allgaier, M. Monkenbusch, and D. Richter, Time-resolved SANS for the determination of unimer exchange kinetics in block copolymer micelles, Europhys. Lett. **55,** 667 (2001).

[31] König, L. Willner, and R. Lund, Structure and thermodynamics of mixed polymeric micelles with crystalline cores: Tuning properties via co-assembly, Soft Matter **15,** 7777 (2019).

[32] R. Cuevas Arenas, B. Danielczak, A. Martel, L. Porcar, C. Breyton, C. Ebel, and S. Keller, Fast collisional lipid transfer among polymer-bounded nanodiscs, Sci. Rep. **7,** 45875 (2017).

[33] T. Zinn, L. Willner, V. Pipich, D. Richter, and R. Lund, Molecular exchange kinetics of micelles: Corona chain length dependence, ACS Macro Lett. **5,** 884 (2016).

[34] A. Radulescu, N. K. Szekely, and M.-S. Appavou, KWS-2: Small angle scattering diffractometer, J. Large-Scale Res. Facil. **1,** A29 (2015).

[35] R. Lund, N. König, N. Mahmoudi, L. Willner, and L. Willner, *Tuning the Molecular Exchange Kinetics of Self-Assembled Antimicrobial Peptide- Polymer Conjugates* (STFC ISIS Neutron and Muon Source, 2019), https://doi .org/10.5286/ISIS.E.RB1910106.

[36] R. Lund, N. König, L. Cavalcanti, L. Willner, H. Sørensen, and L. Willner, *Exchange Kinetics of Telechelic Cn-PEO-Cn Micelles: Effect of Conformation and Crystallinity* (STFC ISIS Neutron and Muon Source, 2019), https://doi .org/10.5286/ISIS.E.RB1920656.

218

Supplementary Information

for

A Tale of Two Tails: Molecular Exchange Kinetics of Telechelic Polymer Micelles

Nico König,[1,2] Lutz Willner,[2,*] Vitaliy Pipich,[3] Najet Mahmoudi,[4] and Reidar Lund[1,†]

[1]*Department of Chemistry, University of Oslo, P.O. Box 1033, Blindern, 0315 Oslo, Norway*
[2]*Jülich Centre for Neutron Science (JCNS) and Institute for Complex Systems (ICS),*
Forschungszentrum Jülich GmbH, 52425 Jülich, Germany
[3]*Jülich Centre for Neutron Science (JCNS) at Heinz Maier-Leibnitz Zentrum (MLZ),*
Forschungszentrum Jülich GmbH, 85747 Garching, Germany
[4]*ISIS-STFC, Rutherford Appleton Laboratory, Chilton, Oxon OX11 0QX, United Kingdom*
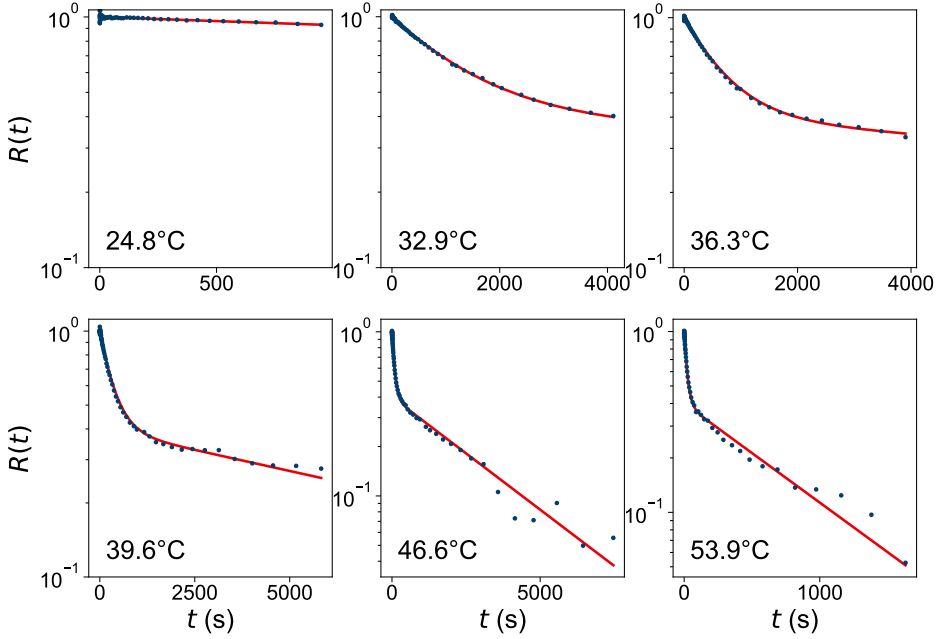
FIG. S1: Experimental relaxation functions of C28F40 at different temperatures, corresponding to Fig. 3a) in the main manuscript. The red lines are a simultaneous fit of all datasets according to Eqs. (2) and (5) in the main manuscript, where only E_a, $\tau_{0,\mathrm{mon}}$ and $\tau_{0,\mathrm{tel}}$ were free fit parameters.
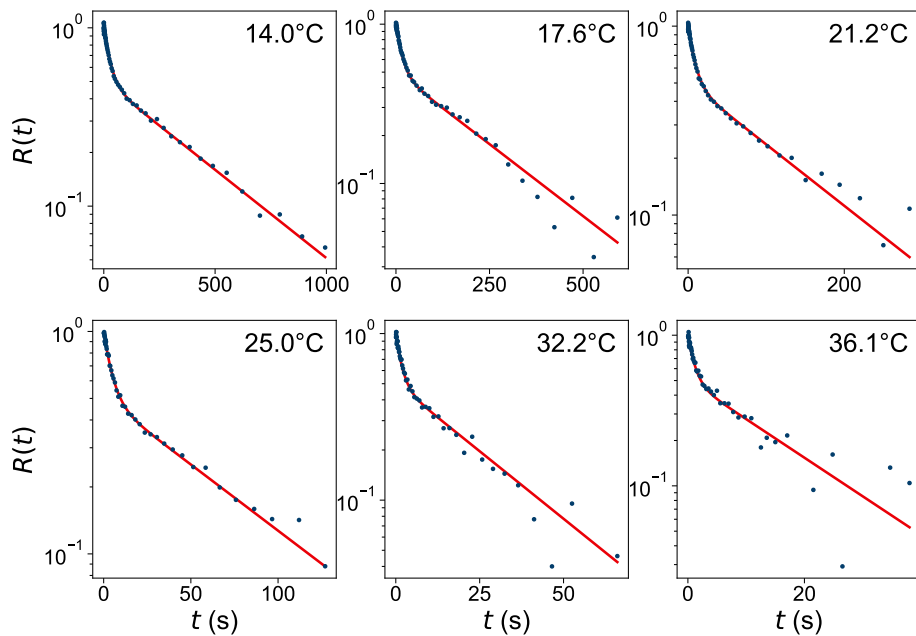
FIG. S2: Experimental relaxation functions of C22F50 at different temperatures, corresponding to Fig. 3b) in the main manuscript. The red lines are a simultaneous fit of all datasets according to eqs. (2) and (5) in the main manuscript, where only E_a, $\tau_{0,\mathrm{mon}}$ and $\tau_{0,\mathrm{tel}}$ were free fit parameters.
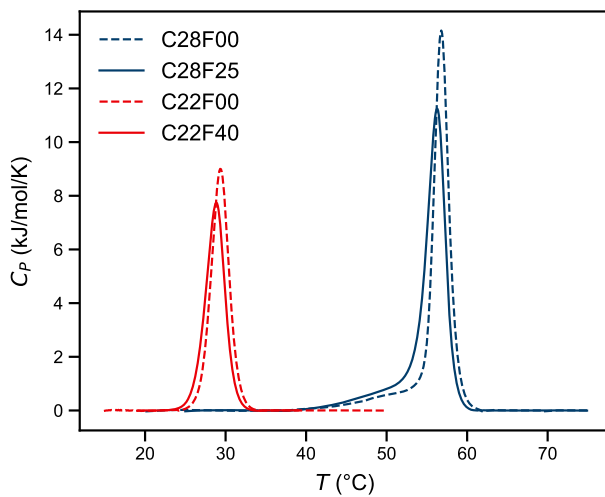
FIG. S3: Differential scanning calorimetry curves of $\phi = 1\,\mathrm{vol}\%$ samples obtained with a TA Instruments NanoDSC. Melting points and enthalpies are given in Tab. I in the main manuscript.
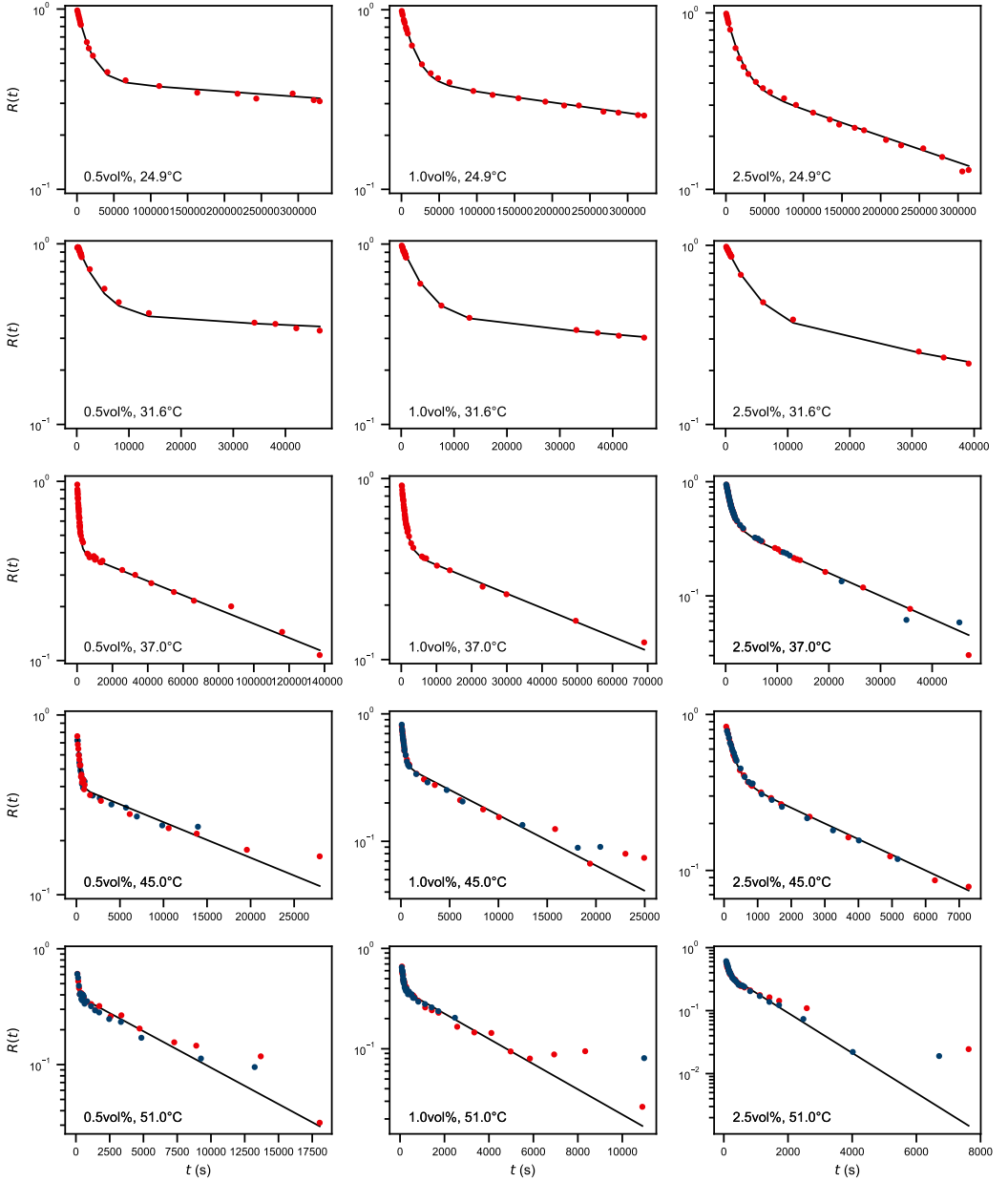
FIG. S4: Experimental relaxation functions of C28F40 at different temperatures and concentrations, blue symbols represent repeated measurements. The black lines are a simultaneous fit of all datasets according to eqs. (2) and (5) in the main manuscript, where only E_a, $\tau_{0,\mathrm{mon}}$ and $\tau_{0,\mathrm{tel}}(\phi)$ were free fit parameters. The $\tau_{0,\mathrm{tel}}(\phi)$ were kept at a fixed ratio of 0.5:1.0:2.5, according to the sample concentrations. The fit parameters are shown in Tab. S1.
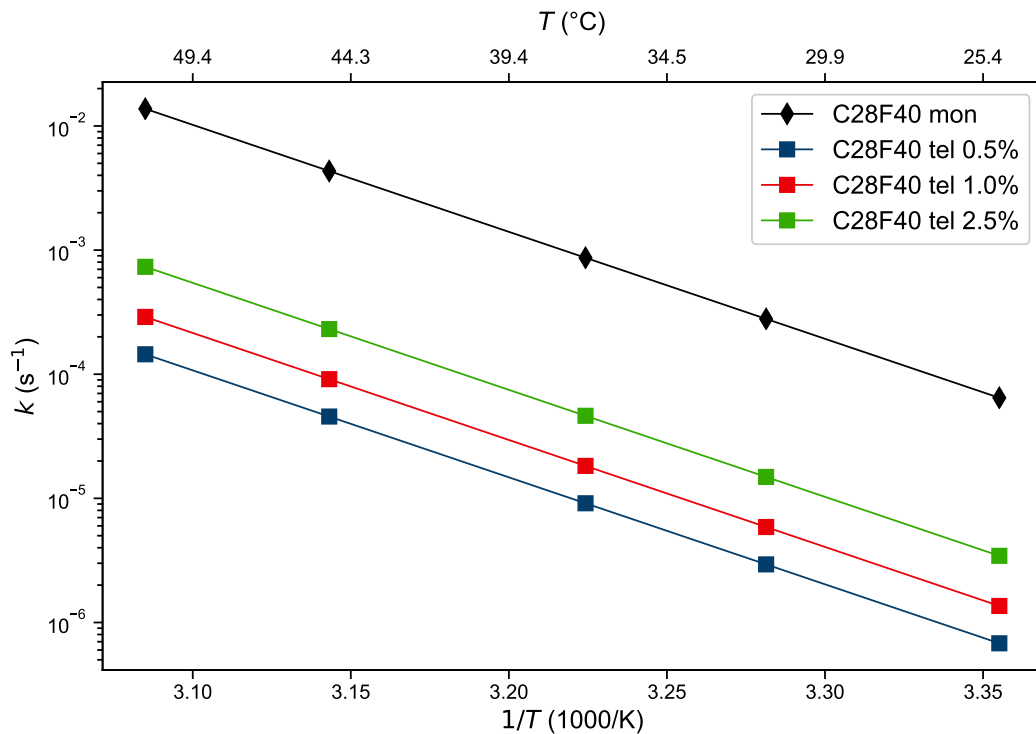
FIG. S5: Arrhenius representation of the rate constants of C_{28} monofunctional (mon) and telechelic (tel) polymers, obtained via a simultaneous fit of all temperatures and concentrations as shown in Fig. S4. The fit parameters are shown in Tab. S1.

TABLE S1: Parameters of the simultaneous fits of C28F40 at different temperatures and concentrations shown in Figs. S4 and S5.

$\tau_{0,\mathrm{mon}}(\mathrm{s})$	4.0×10^{-19}
$\tau_{0,\mathrm{tel}}(0.5\,\mathrm{vol\%})(\mathrm{s})$	3.8×10^{-17}
$\tau_{0,\mathrm{tel}}(1.0\,\mathrm{vol\%})(\mathrm{s})$	1.9×10^{-17}
$\tau_{0,\mathrm{tel}}(2.5\,\mathrm{vol\%})(\mathrm{s})$	7.5×10^{-18}
$E_a\ (\mathrm{kJ\,mol}^{-1})$	125

DISCUSSION OF THE MULTI-STEP KINETIC PROCESS INCLUDING COLLISION-INDUCED EXCHANGE

The kinetic model we propose for the molecular exchange of C_{28} telechelic molecules, which is sketched in Fig. 5 in the main manuscript, consists of multiple steps:

1) Expulsion of one hydrophobic chain end while the other one is still buried in the micellar core.

$$P \underset{k_{-1}}{\overset{k_1}{\rightleftharpoons}} P^* \tag{1a}$$

2) Insertion of the free chain end into another micelle, i.e., bridging.

$$P^* + M \underset{k_{-2}}{\overset{k_2}{\rightleftharpoons}} P^{**} \tag{1b}$$

3) Release of the second chain end that was still in the original micelle.

$$P^{**} \overset{k_3}{\rightarrow} M + \bar{P}^* \tag{1c}$$

Here, P represents telechelic polymer molecules that have not exchanged yet and both chain ends are buried in the original micelle, P^* are molecules that are also still attached to their original micelle but one chain end is free in solution, M is an arbitrary micelle, P^{**} is a molecule that bridges between its original micelle and another one, and $\bar{P}^*$ is a telechelic molecules that has exchanged at least once, with one free chain end. k_1 and k_2 describe reversible steps where no complete chain exchange has occurred yet. The third step, however, signifies the completion of the exchange process and thus no further steps (e.g., $\bar{P}^* \rightarrow \bar{P}$ or re-bridging to the original micelle) need to be considered. This gives the following rate equations

$$\frac{\mathrm{d}[P]}{\mathrm{d}t} = -k_1[P] + k_{-1}[P^*], \tag{2a}$$

$$\frac{\mathrm{d}[P^*]}{\mathrm{d}t} = +k_1[P] - k_{-1}[P^*] - k_2[P^*][M] + k_{-2}[P^{**}], \tag{2b}$$

$$\frac{\mathrm{d}[P^{**}]}{\mathrm{d}t} = +k_2[P^*][M] - k_{-2}[P^{**}] - k_3[P^{**}]. \tag{2c}$$

k_{-2} and k_3 are equivalent steps and thus $k_{-2} = k_3$. Furthermore, polymer bridges as in P^{**} are, at least for C_{28}, thermodynamically unfavourable and solvent-exposed chain ends as in P^* are generally unfavourable. Hence, these two states can be considered as transient and we can apply the steady-state approximation: $\frac{\mathrm{d}[P^*]}{\mathrm{d}t} \approx \frac{\mathrm{d}[P^{**}]}{\mathrm{d}t} \approx 0$. The solution is:

$$[P](t) = [P]_0 \cdot \exp(-k_{\mathrm{eff}} t), \tag{3}$$

with the concentration-dependent decay constant $k_{\mathrm{eff}} = k_1 k_2[M]/(2k_{-1} + k_2[M])$. For low micelle concentrations and $k_2 \le k_{-1}$, a Taylor expansion in $[M]$ yields

$$k_{\mathrm{eff}} = \frac{k_1 k_2[M]}{2k_{-1}} + \mathcal{O}([M]^2). \tag{4}$$

DISCUSSION OF HYPOTHETICAL SEQUENTIAL CHAIN END EXPULSION WITH FREE CHAIN DIFFUSION
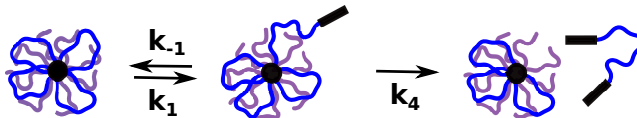

FIG. S6: Schematic to illustrate the sequential expulsion of chain ends with free chain diffusion.

Fig. S6 depicts a sequential chain end expulsion whereupon the telechelic chain diffuses freely, which we named scenario ii) in the main manuscript. The first equilibrium k_1/k_{-1} is the same as in the collision-induced mechanism, i.e., scenario iii), discussed in the main manuscript and in more detail in the previous section. But in scenario ii), this step is followed by the expulsion of the second chain end with rate constant k_4, so that the molecule is completely disconnected from the micelle. The freely diffusing telechelic chain, which we label $\bar{P}^\dagger$, can then insert into a random micelle which completes the chain exchange. We thus obtain the following reaction scheme:

$$P \underset{k_{-1}}{\overset{k_1}{\rightleftharpoons}} P^*, \tag{5a}$$

$$P^* \overset{k_4}{\rightarrow} \bar{P}^\dagger, \tag{5b}$$

which yields the rate equations

$$\frac{\mathrm{d}[P]}{\mathrm{d}t} = -k_1[P] + k_{-1}[P^*], \tag{6a}$$

$$\frac{\mathrm{d}[P^*]}{\mathrm{d}t} = +k_1[P] - k_{-1}[P^*] - k_4[P^*]. \tag{6b}$$

$$\frac{\mathrm{d}[\bar{P}^\dagger]}{\mathrm{d}t} = +k_4[P^*]. \tag{6c}$$

Since exposition of the solvophobic chain ends to the solvent is highly unfavourable, we can assume that $k_{-1} \gg k_1 \approx k_4$. Hence, we can once more apply the steady-state approximation $\frac{\mathrm{d}[P^*]}{\mathrm{d}t} \approx 0$, yielding a single-exponential form

$$[P](t) \approx [P]_0 \cdot \exp(-k_{\mathrm{eff}}\, t) \tag{7}$$

for the not-yet-exchanged chains. The effective rate constant is $k_{\mathrm{eff}} = k_1 k_4/(k_{-1} + k_4) \approx k_1 k_4/k_{-1}$. This result is not in agreement with our experimental findings. Firstly, k_{eff} is not expected to exhibit the same temperature-dependence as its monofunctional counterpart k_{mon}. Secondly, this scenario does not involve any concentration dependence. The model can therefore be ruled out as principle mechanism of chain exchange in C_{28} telechelic polymer micelles in aqueous solution.

––––––––––

[*] l.willner@fz-juelich.de
[†] reidar.lund@kjemi.uio.no